Investigation of liquid-film characteristics in downwards co-current gas-liquid annular flows with laser-induced fluorescence techniques

Jae Sik An

Academic Supervisors:

Professor Christos N. Markides

Emeritus Professor Geoffrey F. Hewitt

A thesis submitted to Imperial College London in fulfilment of the requirements for the degree of Doctor of Philosophy

Department of Chemical Engineering, Imperial College London

2020

List of Publications

An, J.S., Morgan, R.G., Hale, C.P., Zadrazil, I., Hewitt, G.F. & Markides, C.N. (2016) A three-phase slug flow investigation by tomographic dual-beam X-ray imaging: Slug frequency measurement and lessons for correlation development and application. *Multiphase Science and Technology*. 28, 71-98. Available from: doi:10.1615/MultScienTechn.2016018538

An, J.S., Cherdantsev, A.V., Zadrazil, I. & Markides, C.N. (2020) Study of disturbance wave development in downwards annular flows with a moving frame-of-reference brightness-based laser induced fluorescence method. *Experiments in Fluids*. *Submitted for publication*.

Charogiannis, A., An, J.S. & Markides, C.N. (2015) A simultaneous planar laser-induced fluorescence, particle image velocimetry and particle tracking velocimetry technique for the investigation of thin liquid-film flows. *Experimental Thermal and Fluid Science.* 68, 516–536. Available from: doi:10.1016/j.expthermflusci.2015.06.008

Charogiannis, A., An, J.S., Voulgaropoulos, V. & Markides, C.N. (2019) Structured planar laser-induced fluorescence (S-PLIF) for the accurate identification of interfaces in multiphase flows. *International Journal of Multiphase Flow*, 118, 193-204. Available from: doi:10.1016/j.ijmultiphaseflow.2019.06.002

Cherdantsev, A.V., An, J.S., Charogiannis, A. & Markides C.N. (2019) Simultaneous application of two laser-induced fluorescence approaches for film thickness measurements in annular gas-liquid flows. *International Journal of Multiphase Flow*. 119, 237-258. Available from: doi:10.1016/j.ijmultiphaseflow.2019.07.013

Declaration of Originality

The work presented in this thesis was carried out in the Clean Energy Processes (CEP) Laboratory, which is based in the Department of Chemical Engineering at Imperial College London, under the supervision and guidance of Professor Christos N. Markides and Emeritus Professor Geoffrey F. Hewitt.

I hereby declare that the work in this thesis, "Investigation of liquid-film characteristics in downwards co-current gas-liquid annular flows with laser-induced fluorescence techniques", is entirely my own, and where I have incorporated the work of others, it has been acknowledged and referenced appropriately.

Copyright Declaration

The copyright of this thesis rests with the author. Unless otherwise indicated, its contents are licensed under a Creative Commons Attribution-NonCommercial 4.0 International Licence (CC BY-NC).

Under this licence, you may copy and redistribute the material in any medium or format. You may also create and distribute modified versions of the work. This is on the condition that: you credit the author and do not use it, or any derivative works, for a commercial purpose.

When reusing or sharing this work, ensure you make the licence terms clear to others by naming the licence and linking to the licence text. Where a work has been adapted, you should indicate that the work has been changed and describe those changes.

Please seek permission from the copyright holder for uses of this work that are not included in this licence or permitted under UK Copyright Law.

The thesis is dedicated to:

My cherished family and friends

Emeritus Professor Geoffrey F. Hewitt.

Abstract

Liquid-film thickness is one of the key flow quantities to measure in downwards gas-liquid annular flows. However, reliable space and time-resolved measurements are highly challenging to perform due to the presence of complex and three-dimensional interfaces. Non-intrusive optical methods based on the principles of laser-induced fluorescence (LIF) are widely used, and the two main types are planar laser-induced fluorescence (PLIF) and brightness-based laser-induced fluorescence (BBLIF). PLIF uses the fluorescence emission to directly image the axial cross-section of the film; while BBLIF uses the fluorescence intensity signals or 'brightness' to recover the film-thickness. While both PLIF and BBLIF have their own distinct advantages, measurement limitations exist with each approach due to the various optical effects at the film free-surface.

In order to better understand the optical effects, new measurements from the simultaneous application of PLIF and BBLIF were performed at the same region of interrogation (ROI) to measure the film-thickness of the identical film region in downwards annular flows. PLIF and BBLIF were directly compared to evaluate and acquire fresh insight into the capability of each approach to reliably recover the film-thickness of smooth and rough liquid-films. Based on the observations in this set of measurements, an innovative adaption of PLIF known as structured planar laser-induced fluorescence (S-PLIF) was developed and demonstrated in falling-film flows. S-PLIF relies on structured rather than uniform illumination to substantially improve the reliability of the film-thickness data in comparison with other experimental methods.

Finally, an inherent characteristic of standard annular flow measurements is the static ROI position, which can limit the interrogation time of individual disturbance waves. A unique moving-frame-of-reference brightness-based laser-induced fluorescence (MFoR-BBLIF) method was developed to generate a dynamic ROI in order to significantly increase the interrogation time of individual waves; and demonstrated in downwards annular flows to obtain pioneering data on the individual disturbance wave velocities as a function of downstream distance.

Acknowledgements

First, I would like to thank Professor Christos N. Markides and Emeritus Professor Geoffrey F. Hewitt for giving me an opportunity to work on this amazing experimental project. I am sincerely grateful for their continuous supervision and encouragement during my PhD.

I would like to also thank Dr Andrey V. Cherdantsev from the Kutateladze Institute of Thermophysics (Novosibirsk, Russia) for the collaboration in a number of experiments. Special thanks to Dr Alexandros Charogiannis and Dr Ivan Zadrazil for their guidance on experimental work in multiphase flows. This research project would not have gone smoothly without the help from: Mr Pim Amrit, Mr Bob Brace, Dr Colin P Hale, Mr Ben Kistnah, Mr Tony Meredith, Dr Severine Toson, Ms Susi Underwood, and Mr Richard Wallington.

My time at Imperial College London would not have been as memorable without my friends at the Department of Chemical Engineering: Mark Allenby, Assen Batchvarov, Diego Baresch, Alba Ramos, Shane Cadogan, Marco De Corato, James Freeman, Ilaria Guarracino, Ajay Gupta, Baptiste Heiles, Axel Huerre, Roberto Ibarra, Akaki Jamburidze, Lyes Kahouadji, Christoph Kirmse, Niccolò Le Brun, Richard Mathie, Claudia Menichini, Oyeniyi A Oyewunmi, Vincent Poulichet, Paul Sapin, Aly Taleb, Christiana Udoh, Stuart Wright, and Maria Herrando.

I am truly grateful for the undying love and support throughout my life from my loving parents and younger brother. Finally, I would like to express my sincere gratitude to my most dearest friends for always being there for me in times of both hardship and joy: Joon Ho Choi, Justin Jihong Chung, Younseop Chung, Boram Gu, Jaehyun Hong, Jiun Im, Joohyung Jeon, Doyeon Kim, Eunjung Kim, Jeong Kim, Seung Hyun Kim, Younshin Kim, Tae Hyuk Kim, Taekang Kim, Yong Ryun Kim, Changgun Lee, Hong Gyu Lee, Ho Sung Lee, Ji Young Lee, Joon-ser Lee, Jin Woo Oh, Jinny Pae, Ki Joo Pahk, Kyeong Hyeon Park, Sang Joon Park, Sungkyun Park, Yong Ha Park, Jiho Rhew, Daniel Shin, Hyukmin Son, Jinyung Yoon, and Ah Ryoon Yun.

Table of Contents

Abstract 7

Acknowledgements 8

Table of Contents 9

Table of Figures 13

List of Tables 25

Nomenclature 27

1. Introduction 33

    1.1. Background 34

    1.2. Motivation 37

    1.3. Principal objectives 41

    1.4. Thesis outline 43

2. Literature Review 44

    2.1. Downwards gas-liquid annular flows 45

        2.1.1. Disturbance waves and ripple waves 48

        2.1.2. Gas and liquid entrainment 52

    2.2. Experimental methods 55

        2.2.1. Conductance probes 57

        2.2.2. High-speed visualisation 59

2.2.3. Laser-focus displacement (LFD) 61

2.2.4. LIF-based optical methods 63

2.3. Summary 66

3. Flow Facility & Experimental Methods 67

3.1. Flow facility: DAFLOF 68

3.1.1. Gas-line (air) 73

3.1.2. Liquid-line (water) 75

3.1.3. Gas inlet (GI) 79

3.1.4. Liquid injector (LI) 81

3.1.5. Test-section (TS) 83

3.1.6. Linear actuator system (LA) 87

3.2. Experimental methodologies 90

3.2.1. Graticule correction technique 90

3.2.2. Simultaneous PLIF & BBLIF 94

3.2.3. S-PLIF 98

3.2.4. MFoR-BBLIF 103

4. Simultaneous PLIF & BBLIF 109

4.1. Introduction and problem statement 110

4.2. BBLIF image processing 117

4.3. PLIF image processing 122

4.3.1. Solid-liquid interface 122

4.3.2. Gas-liquid interface 124

4.4. Comparisons of PLIF & BBLIF 128

4.4.1. Flow regime map 128

4.4.2. Flat and smooth liquid-films 133

4.4.3. Agitated and rough liquid-films 135

4.4.4. Optical effects at the film free-surface 138

4.4.5. Effect of the PLIF camera observation angle 146

4.4.6. Entrained gas bubbles 151

4.5. Quantitative analysis 154

4.5.1. Statistical moments 154

4.5.2. Probability density distributions 158

4.6. Summary 164

5. S-PLIF 166

5.1. Introduction and problem statement 167

5.2. S-PLIF image processing 176

5.2.1. Solid-liquid interface 177

5.2.2. Gas-liquid interface 179

5.3. Quantitative analysis 181

5.3.1. Statistical moments 181

5.3.2. Probability density distributions 187

5.4. Liquid-films with gas-shear 190

5.5. Uncertainty considerations 194

5.6. Summary 196

6. MFoR-BBLIF 198

6.1. Introduction and problem statement 199

6.2. MFoR-BBLIF image processing 205

6.3. Qualitative analysis 209

6.4. Disturbance wave velocities 212

6.5. Summary 217

7. Conclusions 218

References 224

Table of Figures

Chapter 1: Introduction

Figure 1-1 Illustrations of the flow patterns or regimes of downwards co-current gas-liquid flows in vertically orientated pipes: (a) bubbly flow; (b) slug flow; (c) churn flow; and (d) annular flow. For a given Re_L, the flow regime transitions from bubbly to annular flow as Re_G increases. 36

Chapter 2: Literature Review

Figure 2-1 Illustration of adiabatic and non-reacting downwards co-current gas-liquid annular flows in vertical pipes. The main features of the flow are: (i) continuous gas-core; (ii) continuous liquid-film; (iii) large amplitude interfacial disturbance waves; (iv) small amplitude ripple waves; (v) substrate-film; (vi) entrained liquid droplets in the gas-core; and (vi) entrained gas bubbles in the liquid-film. 47

Figure 2-2 Primary configurations of the two electrodes in conductance or conductivity probes: (a) 'flush-mounted'; and (b) 'parallel-wire' or 'twin-wire'. 58

Figure 2-3 General optical configuration of high-speed visualisation with back-lit illumination: (i) white-light source; (ii) optical-diffuser; and (iii) high-speed camera. A refractive index matching approach can be applied to the design of the test-section to minimise optical distortions in the collected images due to the curvature of the pipe. 60

Figure 2-4	General configuration of the main components in the laser-focus displacement (LFD) method: (i) semiconductor laser; (ii) beam splitter; (iii) pinhole; (iv) light-receiving element; (v) vibration source; (vi) collimating lens; and (vii) oscillating objective lens.	62

Chapter 3: Flow Facility & Experimental Methods

Figure 3-1	Schematic diagram of the modified air-water flow facility, DAFLOF: (a) gas-line (air); (b) liquid-line (water); (c) test-section (TS); and (d) linear actuator system (LA).	70
Figure 3-2	Photographs of the: (a) pressure regulator with air filter (PR01); and (b) thermal mass flow-controller (F3).	74
Figure 3-3	Internal configuration of the HDPE conical tank (TS01): (a) side-view; (b) top-view; and (c) photograph	77
Figure 3-4	Photographs of the: (a) vertical multi-stage centrifugal pump (J01); (b) turbine flow-meter (F1); and (c) Coriolis mass flow-controller (F2).	78
Figure 3-5	Gas inlet (GI): (a) axial cross-section; (b) photograph; (c) front-face of female-flange; and (d) front-face of male-flange.	80
Figure 3-6	Conical liquid injector (LI): (a) axial cross-section; (b) photograph; (c) front-face of female-flange; (d) front-face of male-flange; and (e) axial cross-section of each component.	82
Figure 3-7	Axial cross-section of the: (a) FEP pipe; (b) assembled acrylic anti-distortion boxes; and (c) assembled the test-section (TS).	84
Figure 3-8	Female-flange: (a) front-face view; (b) cross-sectional view; and (c) exploded view. Male-flange: (d) front-face view; (e) cross-sectional	85

view; and (f) exploded view.

Figure 3-9 DAFLOF test-section (TS): (a) assembly; (b) cross-sectional view of the connections; and (c) exploded view of the connections. 86

Figure 3-10 Photographs of the linear actuator system (LA): (a) fixed to a 50 × 50 aluminium profile frame; and (b) set-up vertically to a 50 × 50 aluminium profile frame affixed to the wall. 88

Figure 3-11 Photographs of the 30 × 30 aluminium profile frame mounted on the carriage of the linear actuator system (LA-C): (a) at position P2, and (b) in motion. 89

Figure 3-12 Graticule correction technique: (a) target with a cross pattern; (b) target with a square pattern; (c) photograph of the calibration-target used for the calibration procedure prior to the simultaneous PLIF and BBLIF measurements; and (d) implementation of the method. 92

Figure 3-13 In the application of the graticule correction technique prior to the simultaneous PLIF and BBLIF experiments, sample calibration-target images collected by the pair of cameras of : (a) PLIF90 (left) and BBLIF (right); and (b) PLIF70 (left) and BBLIF (right). 93

Figure 3-14 Experimental set-up of simultaneous PLIF90 and BBLIF to measure the thickness of films in the same region of interrogation (ROI): (a) side-view; and (b) top-view. 96

Figure 3-15 Experimental set-up of simultaneous PLIF70 and BBLIF to measure the thickness of films in the same region of interrogation (ROI): (a) side-view; and (b) top-view. 97

Figure 3-16 Experimental set-up of S-PLIF70 and S-PLIF90 to measure the thickness of films in the same region of interrogation (ROI): (a) 101

side-view; and (b) top-view.

Figure 3-17 Illustrations of the employed method to collect 'reference' images for S-PLIF: (a) side-view; and (b) top-view. 102

Figure 3-18 Experimental set-up of the calibration exercises for MFoR-BBLIF to recover the velocity profiles of the optical measurement system: (a) side-view; and (b) top-view. 106

Figure 3-19 The velocity profiles of the carriage of the linear actuator system, and hence, the optical system (u_{AC}) as a function of: (a) downstream distance from the test-section inlet (s); and (b) time (t). The acceleration and deceleration of the motor was set constant. The different colours and markers represent the different set motor speeds. 107

Figure 3-20 Experimental set-up of MFoR-BBLIF to measure the individual disturbance wave velocities (u_{DW}) as a function downstream distance (s): (a) side-view, and (b) top-view 108

Chapter 4: Simultaneous PLIF & BBLIF

Figure 4-1 Photograph of simultaneous PLIF and BBLIF to measure liquid-film thickness in downwards co-current air-water annular flows (Re_G = 0 – 85,100 and Re_L = 140 – 1330) generated in the vertical test-section of DAFLOF. 116

Figure 4-2 For different values of the absorption coefficient (α_{dye}), a plot of: (a) the normalized fluorescence intensity signal ($J(\delta)/J(\delta_0)$) as a function of the real liquid-film thickness (δ_{real}); and (b) corresponding ratio of BBLIF and real film-thickness as a function 121

of δ_{real}. The values of α_{dye} are α_{dye} = 0.25 mm^{-1} (solid black-line), α_{dye} = 0.25 mm^{-1} ± 5 % (dashed-lines) and α_{dye} = 0.25 mm^{-1} ± 10 % (solid-lines). Positive and negative errors are in blue and red, respectively.

Figure 4-3 PLIF image processing routine to identify the position of the gas-liquid interface in each PLIF image ($I_P(x, y, t)$): (a) sample raw PLIF70 image at Re_G = 0 and Re_L = 520; (b) a binarized image of (a); (c) a processed image of (a); and (d) a processed PLIF70 image of a flow at Re_G = 43,700 and Re_L = 1330 127

Figure 4-4 Raw PLIF70 (top) and BBLIF (bottom) images of interfacial waves in flows at Re_L = 300 and: (a) Re_G = 34,900; (b) Re_G = 43,700; and (c) Re_G = 52,400. In each PLIF frame, the dashed blue-line indicates the position of the solid-liquid interface. 131

Figure 4-5 A flow regime map of downward co-current gas-liquid annular flow: (i) 'ripple' regime; (ii) 'dual-wave' regime; (iii) 'thick ripple' regime; and (iv) 'regular wave' regime. The dashed black-lines represent the transitions in the wave pattern as proposed by Webb & Hewitt (1975), which was based on their study in a D_P = 38.2 mm pipe. The red-line represents the transition in the wave pattern as reported by Alekseenko et al. (2015b) in a D_P = 15.0 mm pipe. 132

Figure 4-6 For flat and smooth liquid-films at Re_G = 0 and Re_L = 300, the identified location of the gas-liquid interface by BBLIF and: (a) PLIF90; and (b) PLIF70. In each sub-figure, the bottom and top frames are the BBLIF and PLIF images, respectively. The positions of the solid-liquid interface (dashed blue-line), the PLIF obtained 134

gas-liquid interface (solid green-line), and the gas-liquid interface acquired by BBLIF (solid red-line) are superimposed on each PLIF frame.

Figure 4-7 Instantaneous and raw PLIF70 (top) and BBLIF (bottom) frames of downwards annular flows at: (a) Re_G = 78,600 and Re_L = 300; and (b) Re_G = 52,400 and Re_L = 1330. The positions of the solid-liquid interface (dashed blue-line), and the PLIF70 obtained gas-liquid interface (solid green-line), and the gas-liquid interface acquired by BBLIF (solid red-line) are superimposed on each PLIF70 frame. 136

Figure 4-8 Instantaneous and raw PLIF90 (top) and BBLIF (bottom) frames of downwards annular flows at: (a) Re_G = 78,600 and Re_L = 300; and (b) Re_G = 52,400 and Re_L = 1330. The positions of the solid-liquid interface (dashed blue-line), and the PLIF90 obtained gas-liquid interface (solid green-line), and the gas-liquid interface acquired by BBLIF (solid red-line) are superimposed on each PLIF90 frame. 137

Figure 4-9 Effect of the reflection coefficient at the air-water interface (K): (a) a plot of K as a function of the incidence angle of the excitation light and interface (θ_i); and (b) a plot of the ratio of BBLIF and real film-thickness ($\delta_{BB}/\delta_{real}$) as a function of θ_i to estimate the effect of K on the BBLIF measurements of thickness. 140

Figure 4-10 Instantaneous and raw PLIF70 (top) and BBLIF (bottom) images of a flow at: (a) Re_G = 69,900 and Re_L = 140; and (b) Re_G = 43,700 and Re_L = 300. The positions of the solid-liquid interface (dashed blue-line), the PLIF70 obtained gas-liquid interface (solid green-line), and the gas-liquid interface acquired by BBLIF (solid red- 141

line) are superimposed on each PLIF70 frame. The frames highlight the errors in the film-thickness measurements of BBLIF due to the steep interfacial slopes at the front-slopes of waves.

Figure 4-11 In the PLIF70 images of smooth liquid-film regions, examples of the fluorescence intensity profiles in the y direction and the corresponding positions of the real gas-liquid interface (δ_{real}) observed as: (a) a peak in the profile; (b) a trough in the profile; or (c) no observation. 144

Figure 4-12 Illustrations of optical effects at the gas-liquid interface in the transverse direction: (a) overestimation by BBLIF due to non-collinear reflections; (b) overestimation by PLIF due to total internal refection (TIR) in circumferentially uniform film regions (i.e. absence of waves); and (c) underestimation by PLIF due to refraction or TIR in circumferentially non-uniform liquid-film regions (i.e. presence of waves). 145

Figure 4-13 Ray-tracing calculations to estimate the position of the false gas-liquid interface in the images of: (a) PLIF90 (θ_P = 90 °); and (b) PLIF70 (θ_P = 70 °). 149

Figure 4-14 For PLIF90 and PLIF70: (a) the overestimation of the PLIF liquid-film thickness ($\delta_{app}/\delta_{real}$) as a function of the real film-thickness (δ_{real}) based on $2R = D_P$ = 32.4 mm; and (b) the interfacial angle of incidence ($\theta_{AOB} + \theta_{OAB}$) as a function of δ_{real}. 150

Figure 4-15 Entrained gas bubbles in: (a) raw PLIF70 (top) and BBLIF (bottom) images of a liquid-film at Re_G = 43,700 and Re_L = 300 with entrained gas bubbles: B1 – ahead of the laser-sheet; B2 – behind 153

the laser-sheet; and B3 – inside the laser-sheet. Ray-tracing illustrations for: (b) B1 and B2, and (c) B1.

Figure 4-16 For the flows at Re_G = 0 – 52,400 and Re_L = 140 – 1330, BBLIF, PLIF70 and PLIF90 obtained: (a) mean liquid-film thickness ($\langle\delta\rangle$) as a function of Re_L; and (b) the ratios of $\langle\delta_P\rangle$ and $\langle\delta_{BB}\rangle$ ($\langle\delta_P\rangle/\langle\delta_{BB}\rangle$) as a function of Re_L. 156

Figure 4-17 For flows at Re_G = 0 – 52,400 and Re_L = 140 – 1330, BBLIF, PLIF70 and PLIF90 obtained: (a) standard deviation of the mean liquid-film thickness (σ_δ) as a function of Re_L; and (b) film roughness $\sigma_\delta/\langle\delta\rangle$ as a function of Re_L. 157

Figure 4-18 PLIF70 and BBLIF joint probability density distributions ($P(\delta_{P70}, \delta_{BB})$) of flows at Re_L = 300 and: (a) Re_G = 0; and (b) Re_G = 52,400. The colour-scale represents $P(\delta_{P70}, \delta_{BB})$, and the contours encompass 50 %, 80 %, 90 %, 95 %, 98 %, and 99 % of the data. The red and black-lines correspond to $\delta_{P70} = \delta_{BB}$ and predicted δ_{P70}, respectively. 160

Figure 4-19 PLIF70 and BBLIF joint probability density distributions ($P(\delta_{P70}, \delta_{BB})$) of flows at Re_L = 1330 and: (a) Re_G = 0; and (b) Re_G = 52,400. The colour-scale represents $P(\delta_{P70}, \delta_{BB})$, and the contours encompass 50 %, 80 %, 90 %, 95 %, 98 %, and 99 % of the data. The red and black-lines correspond to $\delta_{P70} = \delta_{BB}$ and predicted δ_{P70}, respectively. 161

Figure 4-20 PLIF90 and BBLIF joint probability density distributions ($P(\delta_{P90}, \delta_{BB})$) of flows at Re_L = 300 and: (a) Re_G = 0; and (b) Re_G = 52,400. The colour-scale represents $P(\delta_{P90}, \delta_{BB})$, and the contours 162

encompass 50 %, 80 %, 90 %, 95 %, 98 %, and 99 % of the data. The red and black-lines correspond to $\delta_{P90} = \delta_{BB}$ and predicted δ_{P90}, respectively.

Figure 4-21 PLIF90 and BBLIF joint probability density distributions ($P(\delta_{P90}, \delta_{BB})$) of flows at $Re_L = 1330$ and: (a) $Re_G = 0$; and (b) $Re_G = 52{,}400$. The colour-scale represents $P(\delta_{P90}, \delta_{BB})$, and the contours encompass 50 %, 80 %, 90 %, 95 %, 98 %, and 99 % of the data. The red and black-lines correspond to $\delta_{P90} = \delta_{BB}$ and predicted δ_{P90}, respectively. 163

Chapter 5: S-PLIF

Figure 5-1 For a falling liquid-film (i.e. $Re_G = 0$) at $Re_L = 1510$, sample raw image of: (a) PLIF70 image; and (b) PLIF90. The PLIF images have been superimposed with the position of the solid-liquid interface (dashed blue-line), and the location of the gas-liquid interface as obtained by PLIF70 (solid blue-line) and PLIF90 (solid cyan-line). 168

Figure 5-2 Illustrations of the main sources of errors in the liquid-film thickness measurements by the PLIF technique: (a) Error Source I (ES-I) – identification of a larger liquid-film thickness due to total internal reflection (TIR) in a circumferentially uniform liquid-films, (b) Error Source II (ES-II) – identification of a smaller liquid-film thickness due to refraction or TIR in a circumferentially non-uniform liquid-film. 170

Figure 5-3 Photograph of the application of S-PLIF to measure film-thickness 175

in falling liquid-film flows. The investigated range of flow conditions with the proposed methodology was $Re_G \approx 0 – 48{,}000$ and $Re_L \approx 150 – 1500$.

Figure 5-4 Identification of the solid-liquid interface in the S-PLIF images: (a) sample frame of a raw reference image; and (b) fluorescence intensity profile along the y axis of the reference image in (a). 178

Figure 5-5 Identification of the gas-liquid interface in the S-PLIF images: (a) median filter and laser-sheet correction applied on a raw S-PLIF70 frame of a falling film at $Re_L = 1150$; (b) a gradient-direction frame of (a); (c) absolute value of the difference between the frame in (b) and the gradient-direction frame of the reference image; and (d) frame (a) with the identified position of the gas-liquid (solid red-line) and solid-liquid (dashed blue-line) interfaces. 180

Figure 5-6 For falling liquid-films (i.e. $Re_G = 0$), comparison of the mean film-thickness ($\langle\delta\rangle$) data obtained by: (a) PLIF70, PLIF90, S-PLIF70, S-PLIF90 and BBLIF (Chapter 4); (b) PLIF70, PLIF90, S-PLIF70, S-PLIF90, Karapantsios et al. (1989), Karapantsios and Karabelas (1995), Zadrazil et al. (2014), and BBLIF (Chapter 4). 185

Figure 5-7 For falling liquid-films (i.e. $Re_G = 0$) at $Re_L \approx 150 – 1500$, a plot of the standard deviation of liquid-film thickness (σ_δ) as a function of Re_L, which includes the data acquired by PLIF70, PLIF90, S-PLIF70, S-PLIF90, and BBLIF (Chapter 4). 186

Figure 5-8 Contour plots of the joint probability distributions of the local and instantaneous film-thickness data obtained by S-PLIF70 (δ_{S70}) against: (a) S-PLIF70 (δ_{S90}); (b) PLIF90 (δ_{P90}); and (c) PLIF70 189

(δ_{P70}).

Figure 5-9 Raw S-PLIF70 frames of liquid-films with gas-shear at: (a) Re_G = 0 and Re_L = 1510; (b) Re_G = 22,100 and Re_L = 1360; and (c) Re_G = 48,300 and Re_L = 1360. The solid-liquid interface (dashed blue-line), and the gas-liquid interface obtained by S-PLIF70 (solid red-line) and S-PLIF90 (dashed black-line) are superimposed on each frame. 193

Chapter 6: MFoR-BBLIF

Figure 6-1 Photographs of the MRoF-BBLIF set-up to investigate the axial development of individual disturbance waves in downwards annular flows at Re_G = 39,500 – 79,000 and Re_L = 286 – 1320: (a) top-view; and (b) side-view. 203

Figure 6-2 Photographs of a MRoF-BBLIF measurement to investigate the axial development of individual disturbance wave velocities (u_{DW}) in downwards annular flows at Re_G = 39,500 – 79,000 and Re_L = 286 – 1320: (a) top-view; and (b) side-view. 204

Figure 6-3 In ER4 of a flow at Re_G = 59,200 and Re_L = 286: (a) *x-t* matrix at *t* = 0.4469 s – 1.5190 s; (b) segments (*S*) represented as dashed red-squares; and (c) positions of the front-slope of identified waves (cyan cross-markers) in each *S*. 207

Figure 6-4 In ER4 of a downwards annular flow at Re_G = 59,200 and Re_L = 286: (a) *x-t* matrix at *t* = 0.6718 s – 0.8431 s, which shows an identical disturbance wave in the three consecutive segments and the identified positions of the front-slope of the wave; and (b) plot 208

of u_{DW} as a functions of s, which highlights (in the dashed black-square) the u_{DW} values extracted from the x-t matrix in (a).

Figure 6-5 For a flow at Re_G = 79,000 and Re_L = 1320, observation of disturbance wave coalescence in the x-t matrix of ER5 at t = 0.8324 s – 0.9619 s and the corresponding frames at: (a) t = 0.8481 s – DW1; (b) t = 0.8850 s – DW1 and DW2; (c) t = 0.9124 s – coalescence of DW1 and DW2; (d) t = 0.9324 s – DW3; and (e) t = 0.9524 s – DW3 and DW4. 211

Figure 6-6 Plots of u_{DW} as a function of s for downwards co-current gas-liquid annular flows at Re_L = 286 and: (a) Re_G = 39,500; (b) Re_G = 59,200; and (c) Re_G = 79,000. The different colours and markers indicate a different experimental run (ER), and the dashed-lines indicate an identical wave in each ER. 214

Figure 6-7 Plots of u_{DW} as a function of s for downwards co-current gas-liquid annular flows at Re_L = 826 and: (a) Re_G = 39,500; (b) Re_G = 59,200; and (c) Re_G = 79,000. The different colours and markers indicate a different experimental run (ER), and the dashed-lines indicate an identical wave in each ER. 215

Figure 6-8 Plots of u_{DW} as a function of s for downwards co-current gas-liquid annular flows at Re_L = 1320 and: (a) Re_G = 39,500; (b) Re_G = 59,200; and (c) Re_G = 79,000. The different colours and markers indicate a different experimental run (ER), and the dashed-lines indicate an identical wave in each ER. 216

List of Tables

Chapter 3: Flow Facility & Experimental Methods

Table 3-1 Naming convention of the main equipment and instrumentations in the air and liquid-lines shown in Figure 3-1. 71

Table 3-2 Naming convention of the main components of the test-section and linear actuator system shown in Figure 3-1 72

Chapter 4: Simultaneous PLIF & BBLIF

Table 4-1 List of the investigated gas flow conditions in the film-thickness measurements with simultaneous PLIF and BBLIF. 114

Table 4-2 List of the investigated liquid flow conditions in the film-thickness measurements with simultaneous PLIF and BBLIF. 115

Chapter 5: S-PLIF

Table 5-1 List of the investigated gas flow conditions in the film-thickness measurements with S-PLIF. 173

Table 5-2 List of the investigated liquid flow conditions in the film-thickness measurements with S-PLIF. 174

Chapter 6: MFoR-BBLIF

Table 6-1 List of the investigated gas flow conditions in the dynamic ROI 202

measurements with MFoR-BBLIF.

Table 6-2 List of the investigated liquid flow conditions in the dynamic ROI measurements with MFoR-BBLIF. 202

Nomenclature

Roman Symbols

a_{AC}	Acceleration of linear actuator carriage	m/s^2
d_{AC}	Deceleration of linear actuator carriage	m/s^2
$C(x)$	Compensation matrix	–
c_{dye}	Fluorescent dye concentration	mg/L
$D(x)$	Dark-current of camera	–
D_p	Internal pipe diameter	mm
E_{pulse}	Laser energy per pulse	mJ
F_D	Drag force on droplets	N
f_{camera}	Sampling frequency of camera	Hz
f_{DW}	Frequency of disturbance waves	Hz
$f_{d\text{-}s}$	Frequency of de-synchronization	Hz
f_{pulse}	Frequency of laser pulse	Hz
g	Gravitational force	N
H	Height	mm
h_c	Convective heat transfer coefficient	W/m^2K
$J(x)$	Fluorescence intensity signal at x	–
$J_{max}(x)$	Maximum fluorescence intensity signal at x	–
$J(\delta)/J(\delta_0)$	Normalized fluorescence intensity signal	–
$\langle J_0(x) \rangle$	Time-averaged intensity signal from known thickness	–
j_G	Gas superficial velocity	m/s
j_L	Liquid superficial velocity	m/s
K	Reflection coefficient at the air-water interface	–

k	Main fields of co-current gas-liquid annular flows in vertical pipes	−
L	Length	mm
L_{AC}	Motion length of linear actuator carriage	mm
L_p	Length of pipe	mm
L_{turb}	Development length for turbulent flow	mm
$\dot{m}_{gc}$	Mass flux of gas-core	kg/sm^2
$\dot{m}_{lf}$	Mass flux of liquid-film	kg/sm^2
$\dot{m}_{el}$	Mass flux of entrained liquid-phase	kg/sm^2
P_{lamp}	Power of halogen lamp	kW
P_{motor}	Power of linear actuator motor	kW
$P(\delta_P, \delta_{BB})$	Joint probability density distributions of PLIF and BBLIF δ data	−
p	Pressure	Barg
p_{out}	Discharge pressure	Barg
Q_G	Volumetric flow-rate of gas-phase	L/min
Q_L	Volumetric flow-rate of liquid-phase	L/min
R	Radius of pipe	mm
R_D	Deposition flux	kg/sm^2
R_E	Entrainment flux	kg/sm^2
Re_G	Reynolds number of gas-phase, $Re_G = 4Q_L/\pi D_p \upsilon_G$	−
Re_L	Reynolds number of liquid-phase, $Re_L = Q_L/\pi D_p \upsilon_L$	−
s	Downstream distance from channel inlet	m
t	Time	s
t_{pulse}	Laser pulse duration	ns
T_L	Temperature of liquid-phase	°C
u_{gc}	Local average velocity field of gas-core	m/s

u_{lf}	Local average velocity field of liquid-film	m/s
u_{el}	Local average velocity field of entrained liquid-phase	m/s
u_{AC}	Velocity of linear actuator carriage	m/s
u_{DW}	Velocity of disturbance wave	m/s
u_{DWR}	Relative velocity of disturbance wave	m/s
V_{tank}	Volume of the TS01 conical tank	L
V_L	Volume of liquid	L
W	Width	mm
x	Coordinate in the longitudinal (i.e. flow) direction	–
$Y(x)$	Linear array of interface coordinates at x	–
y	Coordinate in the radial direction	–
$y(x)$	Interface coordinate at x	–
z	Coordinate in the transverse direction	–

Greek Symbols

α_{dye}	Fluorescent dye absorption coefficient	m^{-1}
β_{gc}	Velocity correction factor of gas-core	–
β_{lf}	Velocity correction factor of liquid-film	–
β_{el}	Velocity correction factor of entrained liquid-phase	–
δ	Liquid-film thickness	mm
$\delta(x)$	Local liquid-film thickness at (x)	mm
δ_{app}	Apparent gas-liquid interface	mm
δ_{BB}	BBLIF obtained liquid-film thickness	mm
δ_{FS}	Film-thickness of substrate-film	mm
δ_{oe}	Overestimated film-thickness	mm

δ_P	PLIF obtained liquid-film thickness	mm
δ_{P70}	PLIF70 obtained liquid-film thickness	mm
δ_{P90}	PLIF90 obtained liquid-film thickness	mm
δ_{real}	Real or true gas-liquid interface	mm
δ_S	S-PLIF obtained liquid-film thickness	mm
δ_{S70}	S-PLIF70 obtained liquid-film thickness	mm
δ_{S90}	S-PLIF90 obtained liquid-film thickness	mm
δ_{WP}	Wave peak film-thickness	mm
$\langle\delta\rangle$	Mean liquid-film thickness	mm
$\langle\delta_{BB}\rangle$	BBLIF obtained mean liquid-film thickness	mm
$\langle\delta_P\rangle$	PLIF obtained mean liquid-film thickness	mm
$\langle\delta_{P70}\rangle$	PLIF70 obtained mean liquid-film thickness	mm
$\langle\delta_{P90}\rangle$	PLIF90 obtained mean liquid-film thickness	mm
$\langle\delta_S\rangle$	S-PLIF obtained mean liquid-film thickness	mm
$\langle\delta_{S70}\rangle$	S-PLIF70 obtained mean liquid-film thickness	mm
$\langle\delta_{S90}\rangle$	S-PLIF90 obtained mean liquid-film thickness	mm
ε_{gc}	Cross-sectional area occupied by gas-core	m^2
ε_{lf}	Cross-sectional area occupied by liquid-film	m^2
ε_{el}	Cross-sectional area occupied by entrained liquid-phase	m^2
η_{air}	Refractive index of air	–
η_{FEP}	Refractive index of fluorinated ethylene propylene (FEP)	–
η_{water}	Refractive index of water	–
λ_{DW}	Wavelength of disturbance wave	nm
λ_{laser}	Laser wavelength	nm
υ_G	Kinematic viscosity of gas-phase	m^2/s

υ_L	Kinematic viscosity of liquid-phase	m^2/s
θ	Angle between camera axis and perpendicular plane to laser-sheet	°
θ_{AOB}	Angle AOB in Figure 4-13	°
θ_{BB}	BBLIF camera observation angle relative to the excitation plane	°
θ_i	Angle of incidence	°
θ_{OAB}	Angle OAB in Figure 4-13	°
θ_P	PLIF camera observation angle relative to the excitation plane	°
θ_r	Angle of reflection	°
θ_S	S-PLIF camera observation angle relative to the excitation plane	°
θ_{TIR}	Critical angle for total internal reflection	°
θ_t	Angle of refraction	°
σ_δ	Standard deviation of the liquid-film thickness	mm
$\sigma_\delta\langle\delta\rangle$	Liquid-film roughness	–
τ_i	Interfacial shear stress	N/m^2
τ_w	Wall shear stress	N/m^2
φ_{box}	Thickness of laser-sheet	mm
φ_{laser}	Thickness of laser-sheet	mm
φ_{tube}	Thickness of tube	mm

Abbreviations

BBLIF	Brightness-based laser-induced fluorescence
FOV	Field-of-view
GI	Gas inlet of DAFLOF
LA	Linear actuator system
LA-C	Carriage of linear actuator

LA-M	Motor of linear actuator
LA-R	Rail of linear actuator
LFD	Laser-focus displacement
LI	Liquid injector of DAFLOF
LIF	Laser-induced fluorescence
MTF	Modulation transfer function
PLIF	Planer laser-induced fluorescence
PLIF70	Planer laser-induced fluorescence with $\theta_P = 70$ °
PLIF90	Planer laser-induced fluorescence with $\theta_P = 70$ °
ROI	Region of interrogation
S-PLIF70	Structured planer laser-induced fluorescence with $\theta_S = 70$ °
S-PLIF90	Structured planer laser-induced fluorescence with $\theta_S = 70$ °
TIR	Total internal reflection
TS	DAFLOF test-section

CHAPTER

1. Introduction

In Chapter 1, the main flow regimes of downwards co-current gas-liquid flows in vertical pipes are briefly introduced, and the industrial significance of the characteristics of liquid-films in the annular flow regime is discussed. In addition, the motivation of the project, the principal project objectives, and the outline of thesis is also provided in this Chapter.

1.1. Background

Multiphase flows, which are flows with more than a single phase, are encountered in nature (e.g. sediment transport in rivers) and are an essential element to a wide range of industrial applications. For a multiphase flow in a given channel, the interfacial behaviour is dependent on numerous factors: (i) axial distance downstream from the inlet of the channel; (ii) channel geometry and orientation; (iii) chemical and physical properties of each phase; (iv) flow-rates of each phase; (v) imposed heat flux on the flow; (vi) number of phases; (vii) method of phase introduction into the channel; and (viii) phase transitions and chemical reactions. The different types of multiphase flows are categorized into flow patterns or regimes, which are commonly based on the visually observed behaviour and structure of the interfaces.

For adiabatic and non-reacting downwards co-current gas-liquid flows in vertical pipes, the flow direction is in the same direction as gravity (Zadrazil et al., 2014), and the accepted flow regimes in literature are mainly (Bouyahiaoui et al., 2020): (a) bubbly flow; (b) slug flow; (c) churn flow; and (d) annular flow. For a given liquid Reynolds number (Re_L), the flow regime transitions from bubbly to annular flow as the gas Reynolds number (Re_G) increases. Illustrations of the four flow regimes are provided in Figure 1-1, and a brief description of each flow pattern are given below:

- **Bubbly flow** – In a liquid-phase continuum, the gas-phase is dispersed as discrete gas bubbles that can experience slippage between the two phases (Bouyahiaoui et al., 2020). The motions of gas bubbles are complex, and the bubble sizes are non-uniform. Gas bubbles tend to concentrate at the centre of the channel, which has been referred to as 'coring' (e.g. Bhagwat & Ghajar, 2012; Enrique Julia et al., 2013; Usui & Sato, 1989). The coalescence of bubbles, and consequently, the formation of larger 'cap' bubbles can occur as Re_G increases (Enrique Julia et al., 2013).

- **Slug flow** – In a continuous liquid-phase, the gas-phase primarily flows as 'Taylor bubbles' with bullet-like shapes and cross-sectional areas similar to the pipe. In contrast to upwards flow, the nose of Taylor bubbles is orientated in the opposite direction of the bulk flow, and has a more flat-shape (Bouyahiaoui et al., 2020). Complete deformation of the base of the large bubbles occur due to the flow of liquid-films around and in the opposite direction of Taylor bubbles (Usui & Sato, 1989). Taylor bubbles are separated by 'liquid slugs', which can be entrained with small gas bubbles (Spedding et al., 1998). This type of gas-liquid flow is inherently intermittent due to the alternating flow of 'Taylor bubbles' and 'liquid slugs'.
- **Churn flow** – The flow becomes agitated as Re_G increases, and Taylor bubbles become less stable, which eventually results in the break-down of these large gas bubbles (Bouyahiaoui et al., 2020). The axial length of liquid slugs decreases and appear frothy (Bouyahiaoui et al., 2020). Furthermore, liquid slugs frequently fragment into smaller liquid bodies (Enrique Julia et al., 2013). The momentum of the gas-phase is insufficient to completely push the liquid-phase around the periphery of the channel to form a near-symmetric liquid-film (Bouyahiaoui et al., 2020).
- **Annular flow** – The liquid-phase flows as a continuous thin wavy liquid-film on the inner pipe wall, and the gas-phase flows through the centre of the pipe as a continuous gas-core. Liquid droplets can be entrained in the gas-core, and gas bubbles can be entrained in the liquid-film. In downwards flows, liquid-films can still form on the inner surface of the pipe wall in the absence of gas flow (i.e. $Re_G = 0$), which is referred to as falling liquid-films. The surface of the film is covered with a multi-scale system of interfacial waves, and the main types waves are disturbance (large amplitude) waves and ripple (small amplitude) waves.

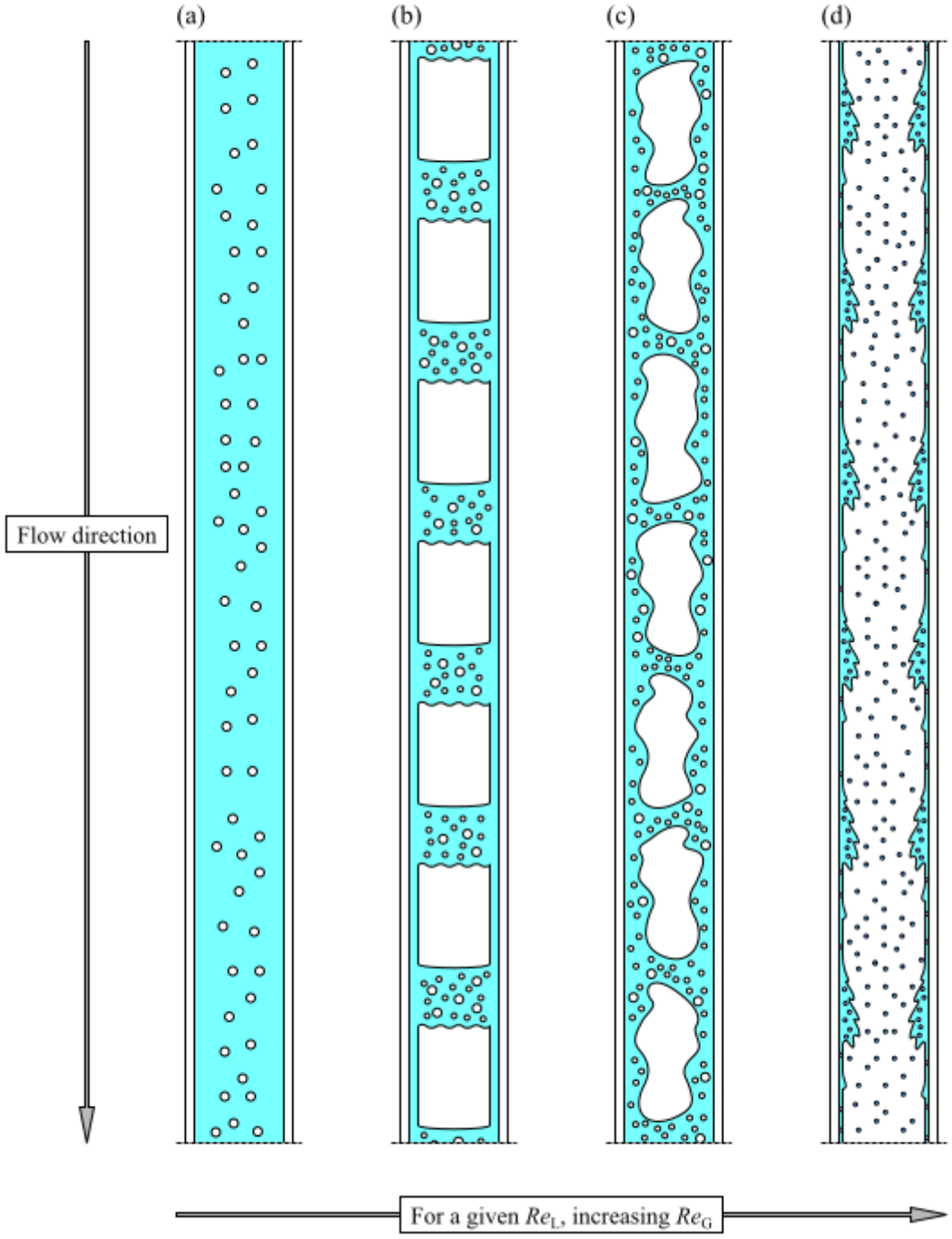


Figure 1-1 – Illustrations of the flow patterns or regimes of downwards co-current gas-liquid flows in vertically orientated pipes: (a) bubbly flow; (b) slug flow; (c) churn flow; and (d) annular flow. For a given Re_L, the flow regime transitions from bubbly to annular flow as Re_G increases.

1.2. Motivation

Downwards co-current gas-liquid annular flows are found in many important industrial process units (e.g. chemical reactors. condensers, distillation columns, evaporators); since the continuous liquid-films of the flow have a high surface-to-volume ratio, and the surface instabilities (i.e. wave activity) of the films have a strong influence on the heat and mass transfer capabilities. For example, film surface instabilities can increase the mass transfer by up to 170 % during the absorption of carbon dioxide by liquid-films of water (Nakoryakov et al., 1976); while the presence of large amplitude interfacial waves initiated nucleate boiling for flows in heated pipes (Barbosa et al., 2003). However, the same flow characteristics are also associated with a number of challenges in the design and operation of relevant process systems.

Interfacial waves on liquid-films increase the surface roughness and frictional pressure drop in the channel (Wolf, 1995; Schubring & Shedd, 2011). The entrainment of liquid droplets in the gas-core are attributed to large amplitude disturbance waves (Hewitt & Hall Taylor, 1970), and entrained liquid droplets with sufficient size and velocity can cause the inner wall of the channel to sustain physical damages through corrosion and erosion (Azzopardi, 2006). Film regions can become non-existent (i.e. dry-out phenomena) at high entrainment and low deposition rates, which can cause problems for non-isothermal systems (Jepson et al., 1989). The gas-phase becomes in contact with the channel wall, and the convective heat transfer coefficient (h_c) deteriorates, which leads to efficiency losses in temperature-controlled systems. However, the significance of dry-out conditions becomes far greater in heat flux controlled systems due to the rise in the temperature of the channel wall to remove heat, which can result in hazardous conditions and impact safety.

The ability to accurately and reliably predict the integral liquid-film characteristics (e.g. film-thickness, wave frequency, wave velocity) in downwards gas-liquid annular flows is crucial for

the correct design and operation of relevant industrial process systems. This necessitates detailed qualitative and quantitative experimental data on the various interfacial phenomena of the flow to assist in the development and validation of advanced models. For example, the basic mass and momentum balances of annular flows highlight a number of the required closure relationships (Azzopardi, 2006). For co-current gas-liquid annular flows in vertical pipes, the main fields can be divided into three categories: (i) gas-core; (ii) liquid-film; and (iii) entrained liquid-phase. The time-varying mass balances of the three fields for a time-invariant adiabatic annular flow are as follows (Azzopardi, 2006):

$$d\dot{m}_{\mathrm{gc}}/dx = 0 \qquad \text{Equation 1-1}$$

$$d\dot{m}_{\mathrm{lf}}/dx = 4\left(D_{\mathrm{p}} - 2\delta\right)/{D_{\mathrm{p}}}^{2} \cdot \left(R_{\mathrm{D}} - R_{\mathrm{E}}\right) \qquad \text{Equation 1-2}$$

$$d\dot{m}_{\mathrm{el}}/dx = 4\left(D_{\mathrm{p}} - 2\delta\right)/{D_{\mathrm{p}}}^{2} \cdot \left(R_{\mathrm{E}} - R_{\mathrm{D}}\right) \qquad \text{Equation 1-3}$$

where k, D_{p}, $\dot{m}_{\mathrm{k}}$, R_{D}, R_{E}, u_{k}, x, and δ are the main field, internal pipe diameter, mass flux, deposition flux, entrainment flux, local average field velocity, direction of the flow and liquid-film thickness, respectively. In addition, the time-varying momentum balances of the three fields for steady-state conditions are as follows (Azzopardi, 2006):

$$d\left(\beta_{\mathrm{gc}}{\dot{m}_{\mathrm{gc}}}^{2}/\varepsilon_{\mathrm{gc}}\rho_{\mathrm{G}}\right)/dx + \varepsilon_{\mathrm{gc}} \cdot dp/dx + 4\tau_{\mathrm{i}}\left(D_{\mathrm{p}} - 2\delta\right)/{D_{\mathrm{p}}}^{2} + \rho_{\mathrm{G}} \cdot g \cdot \varepsilon_{\mathrm{gc}} + F_{\mathrm{D}} = 0 \qquad \text{Equation 1-4}$$

$$d\left(\beta_{\mathrm{lf}}{\dot{m}_{\mathrm{lf}}}^{2}/\varepsilon_{\mathrm{lf}}\rho_{\mathrm{L}}\right)/dx + \varepsilon_{\mathrm{lf}} \cdot dp/dx + 4\tau_{\mathrm{w}}/D_{\mathrm{p}} - 4\tau_{\mathrm{i}}\left(D_{\mathrm{p}} - 2\delta\right)/{D_{\mathrm{p}}}^{2} + \rho_{\mathrm{L}} \cdot g \cdot \varepsilon_{\mathrm{lf}} + 4\left(D_{\mathrm{p}} - 2\delta\right)/{D_{\mathrm{p}}}^{2} \cdot \left(R_{\mathrm{E}}u_{\mathrm{FD}} - R_{\mathrm{D}}u_{\mathrm{DF}}\right) = 0 \qquad \text{Equation 1-5}$$

$$d\left(\beta_{\mathrm{el}}{\dot{m}_{\mathrm{el}}}^{2}/\varepsilon_{\mathrm{el}}\rho_{\mathrm{L}}\right)/dx + \varepsilon_{\mathrm{el}} \cdot dp/dx + \rho_{\mathrm{L}} \cdot g \cdot \varepsilon_{\mathrm{el}} + 4\left(D_{\mathrm{p}} - 2\delta\right)/{D_{\mathrm{p}}}^{2} \cdot \left(R_{\mathrm{D}}u_{\mathrm{DF}} - R_{\mathrm{E}}u_{\mathrm{FD}}\right) - F_{\mathrm{D}} = 0 \qquad \text{Equation 1-6}$$

where g, p, F_{D}, u_{DF}, u_{FD}, β_{k}, ε_{k}, ρ_{G}, ρ_{L}, τ_{i}, and τ_{w} are gravitational force, pressure, drag force on

droplets, velocity difference between droplets and film, velocity difference between film and droplets, velocity profile correction factor, fraction of pipe cross-sectional area occupied by each field, density of gas-phase, density of liquid-phase, interfacial shear stress, and wall shear stress, respectively. Based on Equations 1-1 to 1-6, one of the essential flow quantities to measure is the liquid-film thickness (δ).

The collection of accurate and reliable liquid-film thickness data is a significant challenge with gas-liquid annular flows due to the three-dimensional (3-D) flow and the presence of highly complex gas-liquid interfaces. Many experimental techniques based on various principles have been developed to measure film-thickness, however, advantages and limitations exist with each method. Non-intrusive optical methods based on the principles of laser-induced fluorescence (LIF) have been frequently employed to perform film-thickness measurements in annular flows. In LIF-based optical methods, the liquid-phase is initially seeded with a chosen soluble fluorescent dye in order to emit fluorescent-light upon laser-light excitation. The dye selection is mainly based on the difference between the laser-light absorption and fluorescence emission spectra. A laser-sheet is used to excite the liquid-film in the region of interrogation (ROI), which is usually along the axial plane of the channel. The different types of LIF-based optical methods primarily vary in the approach to the collection of the emitted fluorescence, and hence, the raw data treatment.

The two most commonly used types are planar laser-induced fluorescence (PLIF), and brightness-based laser-induced fluorescence (BBLIF). In PLIF, a camera is used to directly image an axial cross-section of the liquid-film, and the film boundaries in the imaged domain are identified to determine film-thickness (Farias et al., 2012; Schubring et al., 2010; Zadrazil et al., 2014). In BBLIF, fluorescence intensity signals or 'brightness' from the excited film region with a camera, and the intensity signals are converted to film-thickness in accordance with the Beer-Lambert law (Alekseenko et al., 2009; 2013; 2014; 2015b). The main benefit of the PLIF approach is the ability to integrate with other similar measurement approaches to simultaneously investigate

different flow quantities in the same ROI (Charogiannis & Markides, 2014; 2017; 2019; Mathie et al., 2014; Zadrazil and Markides, 2014); while the ability to perform three-dimensional (3-D) measurements of the flow is the main advantage of BBLIF (Alekseenko et al., 2012; Cherdantsev et al., 2014).

While both LIF-based optical methods have been used in numerous studies to conduct liquid-film thickness measurements in annular flows, PLIF and BBLIF have limitations due to the light phenomena that occur at the gas-liquid interface between the film and gas-core. In PLIF, total internal reflection (TIR) of the emitted fluorescent-light at the circumferential interface between the excitation and imaging planes cause liquid-films to appear thicker in the collected images (Häber et al., 2015). This leads to overestimations of film-thickness, which is ≈ 30 % in film regions with smooth and uniform circumferential surfaces (Häber et al., 2015). In BBLIF, light reflections occur at the gas-liquid interface and contribute to the collected fluorescence intensity signals in the images (Cherdantsev et al., 2019). The degree of reflections is dependent on the angle of incident-light from the normal to the interface, and hence, the interfacial slope steepness. Errors in the BBLIF thickness measurements increase gradually as the incidence angle approaches the critical angle of TIR, and becomes significant when the critical angle is exceeded (Cherdantsev et al., 2019).

Experimental investigations into the limitations of both PLIF and BBLIF is crucial in order to better understand the issues with each approach, and further develop the methods for future use. An inherent characteristic of the vast majority of flow measurements is the fixed or static ROI to investigate the characteristics of interfacial wave phenomena with large development lengths (e.g. disturbance waves), which can be a limitation due to the unknown instantaneous information before-and-after the ROI position and the short interrogation time of individual waves. Therefore, the implementation of a dynamic or moving ROI position can be beneficial in the investigation of individual interfacial phenomena characteristics as a function of downstream distance.

1.3. Principal objectives

The focus of the project was to develop LIF-based optical methods to investigate the liquid-film characteristics in downwards co-current gas-liquid annular flows in vertical pipes. The first main project aim was to better understand the limitations with the application of PLIF and BBLIF to measure liquid-film thickness (δ). In order to maintain the advantages of direct flow imaging, the second aim was to develop a variation of PLIF to improve the reliability of the approach. The final aim of the project was to develop a novel experimental method in order to overcome the inherent limitation associated with the use of a static region of interrogation (ROI) to investigate interfacial phenomena with large development lengths. Based on the aforementioned aims, the objectives of the project were divided in the following manner:

1) Re-construction of the air-water flow facility known as Downwards Annular Flow Laser Observation Facility (DAFLOF) to incorporate a new test-section and a linear actuator system. Apply a refractive index matching approach to the design and manufacture of the entire test-section length in order to minimize perspective distortions in the flow images collected with the employed non-intrusive LIF-based optical methods at any given ROI position. Employ the linear actuator system to physically move optical measurement systems, and hence, the ROI along the entire length of the test-section. Utilize DAFLOF to generate adiabatic and non-reacting downwards co-current air-water annular flows ($Re_G \approx 0 – 90{,}000$, $Re_L \approx 0 – 1500$) in a vertical pipe.

2) Conduct a set of liquid-film thickness measurements on downwards annular flows ($Re_G \approx 0 – 85{,}000$, $Re_L \approx 140 – 1330$) with the application of simultaneous PLIF and BBLIF at the same ROI. The capability of both PLIF and BBLIF to recover the thickness of the same film region was directly compared to better understand the effects of the light phenomena at the gas-liquid interface on each method. This set of simultaneous PLIF and BBLIF experiments was in collaboration with Dr Andrey Cherdantsev from

the Kutateladze Institute of Thermophysics (Novosibirsk. Russian).

3) Based on the findings of the simultaneous PLIF and BBLIF experiments, develop a variation of the PLIF technique to improve the reliability of this specific method. This novel variation of PLIF uses a structured illumination rather than the conventional uniform illumination to enhance the identification of the gas-liquid interface between the liquid-film and gas-core. Therefore, the approach is referred to as structured planar laser-induced fluorescence (S-PLIF). Conduct a set of film-thickness measurements on falling liquid-film flows ($Re_G \approx 0$, $Re_L \approx 150 - 1500$) to demonstrate and validate the benefits of the S-PLIF approach.

4) Develop a novel non-intrusive optical method which integrates a moving frame-of-reference (MFoR) approach to overcome the limitations of standard flow measurements with fixed ROI positions to investigate interfacial phenomena characteristics with large axial development lengths. In a MFoR measurement, the optical measurement system physically moves along the entire test-section length to have a dynamic ROI in order to investigate the axial development of individual interfacial phenomena as a function of downstream distance from the channel inlet. Perform a set of dynamic ROI measurements on large amplitude disturbance waves in downwards annular flows ($Re_G \approx$ 39,000 – 80,000, $Re_L \approx 250 - 1300$) to demonstrate and validate the potential of the MFoR approach.

1.4. Thesis outline

A brief review of the current literature on downwards co-current gas-liquid annular flows and a review of the most commonly employed experimental techniques in gas-liquid annular flow studies to measure liquid-film thickness (δ) are presented in Chapter 2. Detailed descriptions of the air-water flow facility known as DAFLOF and the optical configurations of the employed non-intrusive LIF-based optical methods are given in Chapter 3. In Chapter 4, the film-thickness measurements with simultaneous PLIF and BBLIF are discussed; while the liquid-film thickness measurements with the S-PLIF are discussed in Chapter 5. The dynamic ROI measurements with MFoR-BBLIF to recover the velocities of individual disturbance waves (u_{DW}) as a function of downstream distance from the channel inlet are discussed in Chapter 6. Finally, the main conclusions of each set of experiments and areas for further work are highlighted in Chapter 7.

CHAPTER

2. Literature Review

In Chapter 2, a brief of the current literature on downwards gas-liquid annular flows in vertical pipes is presented. Further, a review of the most widely used experimental techniques to measure thickness of liquid-films in gas-liquid annular flows is also provided in this Chapter.

2.1. Downwards gas-liquid annular flows

The primary gas-liquid interface in downwards co-current gas-liquid annular flows is defined by the continuous liquid-film, which flows on the surface of the inner pipe wall, and the gas-core, which flows through the centre of the channel. In downwards annular flows, liquid-films can still form on the inner pipe wall in the absence of gas flow (i.e. $Re_G \approx 0$). Additional gas-liquid interfaces can be present in the flow at sufficiently high gas and liquid Reynolds numbers due to the entrainment of liquid droplets in the gas-core and the entrainment of gas bubbles in the liquid-film. The size of the entrained gas bubbles and liquid droplets are non-uniform. The entrained liquid droplets in the gas-core can either deposit back onto the film or continue to travel within the gas-core in the direction of the bulk flow. A multi-scale system of interfacial waves cover the surface of the film, and the dominant types are large amplitude 'disturbance waves' and small amplitude 'ripple waves'. The smooth liquid-film regions between disturbance waves are commonly referred to as the film-substrate or substrate-film. An illustration of downwards co-current gas-liquid annular flows in vertical pipes is provided in Figure 2-1. In the 1960s and 1970s, the basis of the current understanding of this flow regime was pioneered (e.g. Chu & Dukler, 1974; 1975; Telles & Dukler, 1970; Webb & Hewitt, 1975). For downwards annular flows, Webb and Hewitt (1975) identified four different sub-regimes based on the characteristics of the interfacial wave activity on liquid-films: (i) 'ripple' regime; (ii) 'dual-wave' regime; (iii) 'thick ripple' regime; and (iv) 'regular wave' regime. Zadrazil et al. (2014) identified an additional 'disturbance wave' regime, however, the study did not observe the ripple regime due to gas and liquid flow-rate control limitations of the used flow-loop system. Based on the observations of Webb & Hewitt (1975) and Zadrazil et al. (2014), a brief description of each sub-regime is provided below:

i. **'Ripple' regime ($Re_G \geq 0$, $Re_L \leq 121$)** – Liquid-films are covered with a pattern of small amplitude ripple waves.

ii. **'Dual-wave' regime ($Re_G \leq 21{,}100$, $Re_L \approx 306 - 613$)** – Films with ripple waves and low frequency disturbance waves (i.e. < 1 Hz). Entrainment of gas bubbles and liquid droplets is negligible, and disturbance waves are separated by long regions of film-substrate with smooth surfaces.

iii. **'Thick ripple' regime ($Re_G \leq 21{,}100$, $Re_L \approx 919 - 1226$)** – Thick liquid-films covered completely with small amplitude ripple waves. The continuous alternation of interfacial waves and film-substrate regions cause the gas-liquid interface to have a near-sinusoidal shape.

iv. **'Disturbance wave' regime ($Re_G \leq 21{,}100$, $Re_L \geq 1532$)** – Liquid-films with both disturbance and ripple waves. The local thickness of individual disturbance waves can be in order of ≈ 5 mm, which is several times larger than the mean film-thickness. The disturbance wave frequency is greater than in the dual-wave regime, and hence, the rate of gas and liquid entrainment is higher. Similar to the dual-wave regime, the length of film-substrate regions is larger than individual disturbance waves.

v. **'Regular wave' regime ($Re_G \leq 42{,}300$, $Re_L \geq 0$)** – Thin liquid-films with highly agitated surfaces due to the presence of high frequency small and large amplitude interfacial waves. Furthermore, the entrainment of gas bubbles in the film and liquid droplets in the gas-core is significant.

In a number of studies, disturbance waves and ripple waves have been referred to as 'roll' (or 'rolling') waves and 'capillary' waves, respectively (Asali et al., 1985; Ishii & Grolmes, 1975; Yu et al., 2006). In addition, the accepted definitions of different interfacial waves are to a degree ambiguous, which can lead to discrepancies in the distinction of the waves, and hence, the flow regimes. A detailed description of disturbance ripple waves are presented in Section 2.1.1. The mechanisms of gas bubble and liquid droplet entrainment are explained in Section 2.2.2.

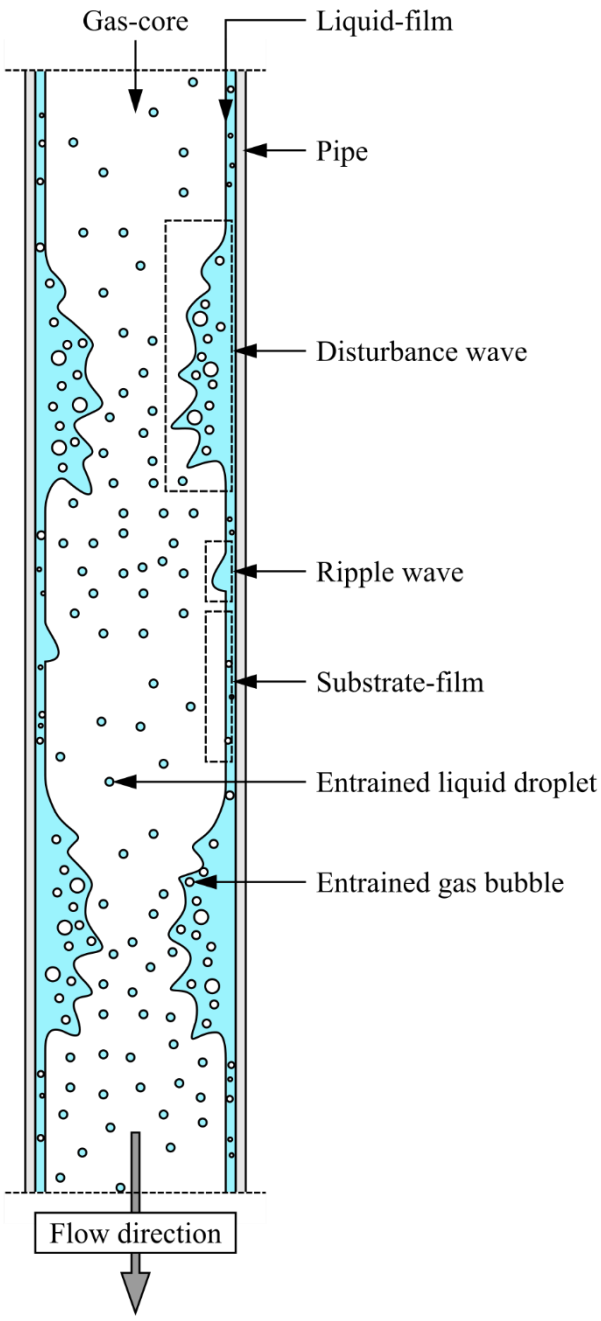


Figure 2-1 – Illustration of adiabatic and non-reacting downwards co-current gas-liquid annular flows in vertical pipes. The main features of the flow are: (i) continuous gas-core; (ii) continuous liquid-film; (iii) large amplitude interfacial disturbance waves; (iv) small amplitude ripple waves; (v) substrate-film; (vi) entrained liquid droplets in the gas-core; and (vi) entrained gas bubbles in the liquid-film.

2.1.1. Disturbance waves and ripple waves

The presence of large amplitude disturbance waves in gas-liquid annular flows is dependent on both the gas and liquid Reynolds numbers. This type interfacial wave is considered a major interfacial phenomena in gas-liquid annular flows as the waves are a necessary element for liquid droplet entrainment in the gas-core (Azzopardi, 1997), and hence, significant effort has been invested in numerous studies to investigate the disturbance wave characteristics. Disturbance waves have long lifespans and carry liquid mass (Han et al., 2006) as they propagate through the channel with high speeds (Chu & Dukler., 1974; 1975). The large amplitude interfacial waves are circumferentially coherent around the periphery of the channel (Hewitt & Lovegrove, 1969; Zhao et al., 2013), and the local thickness of disturbance waves can be ≈ 5 times larger than the mean liquid-film thickness (Hewitt & Nicholls, 1969; Zadrazil et al., 2014). However, the local circumferential film-thickness is non-uniform due to the presence of small amplitude ripple waves with varying amplitudes, wave frequencies, and circumferential sizes on the surface of disturbance waves (Alekseenko et al., 2012). While the circumferential coherence of disturbance waves do not occur instantaneously, the circumferential coherence strengthens with downstream distance from the channel inlet (Zhao et al., 2013). This behaviour can be attributed to periodic circumferential velocity variations within the liquid-film (Kline et al., 1967). Local disturbance waves assimilate liquid mass and expand circumferentially as they flow through the channel. Disturbance waves are more localised and circumferentially incoherent interfacial wave phenomena in larger diameter pipes (Azzopardi et al., 1983).

In gas-liquid annular flows, the frequency of disturbance waves (f_{DW}) increases with both gas and liquid superficial velocities, however, the disturbance waves frequency is independent of the gas superficial velocity below a critical gas flow-rate (Hall Taylor et al., 1963; Webb & Hewitt, 1975; Karimi & Kawaji, 2000). In a study of falling liquid-film flows ($Re_G = 0$, $Re_L \approx 1500$), Karapantsios et al. (1989) found that the amplitude of disturbance waves (λ_{DW}) increased with

increasing liquid Reynolds number (Re_L) for $Re_L \leq 1250$; while Re_L had no considerable effect on the frequency. Furthermore, the amplitude and frequency of disturbance waves were constant for $Re_L \geq 1250$, however, the thickness of substrate-film regions gradually increased with increasing Re_L. The Re_L values reported by Karapantsios et al. (1989) were based on the bulk-mean film velocity and the mean liquid-film thickness ($\langle\delta\rangle$). The internal diameter of the channel influences the disturbance wave frequency as the frequency decreases with increasing internal pipe diameter (Martin, 1983). The frequency of disturbance waves is high near the point of liquid-film formation, however, decreases to an asymptotic value further downstream of the channel. This can be attributed to the coalescence of disturbance waves due to variations in the disturbance wave velocities (Hall Taylor & Nedderman, 1968). A linear relationship exists between the disturbance wave amplitude and disturbance wave velocity (Pashniak, 1969), and the velocities of disturbance waves (u_{DW}) are dependent on both gas and liquid flow-rates (Hall Taylor et al., 1963). Disturbance wave velocities have a normal distribution about a mean value, and the standard deviation is not dependent on the mean wave velocities (Hall-Taylor & Nedderman, 1968). Therefore, the coalescence of disturbance waves can occur between fast and slow-moving large amplitude interfacial waves. In addition, Hall Taylor et al. (1963) reported that after disturbance wave coalescence, the consequent coalesced disturbance wave continues to travel with the velocity of the faster moving disturbance wave.

The mechanism of disturbance wave formation in annular flows is not yet known, however, interfacial instabilities and turbulent bursts have been suggested in literature (Azzopardi, 2006). Imbalances between inertial, pressure, surface tension and viscous forces acting on local liquid-film regions typically cause interfacial instabilities. Turbulent bursts are a feature of turbulence, and the term refers to the sequence of events associated with the sudden motion of low momentum fluid from the channel wall to the gas-liquid interface and the inrush of high momentum fluid (Kline et al., 1967). The sudden wall-to-interface movement of liquid in the turbulent boundary layer of the liquid-film causes the gas-liquid interface to bulge and protrude into the gas-core.

This interface bulge and the inrush of high momentum gas leads to the formation of disturbance waves (Wolf, 1995). The frequency of this phenomenon is independent of distance from the channel wall and dimensionless film-thickness (Azzopardi, 2006). Thwaites et al. (1976) and van Maanen & Fortuin (1983) reported that drag reducing agents decrease the frequency of disturbance waves in annular flows and turbulent bursts in single-phase flows, respectively. Based on the observations in these two studies, Martin & Azzopardi (1985) suggested a similarity in the frequencies of both flow phenomena to support the turbulent burst mechanism of disturbance wave formation.

The governing mechanism for wall-to-interface mass and momentum transfer in wavy liquid-films may be largely attributed to the possible presence of large-scale circulating eddies or recirculation zones in liquid-films. Brauner et al. (1987) predicted the existence of circulating eddies within interfacial waves and the formation of interfacial stagnation points (in a coordinate system moving with the waves); when the interfacial velocity is greater than the wave velocity and the ratio of wave peak to film-substrate thickness is higher than $\delta_{WP}/\delta_{FS} \approx 2.5 - 3.0$. Zadrazil & Markides (2014) found recirculation zones within disturbance waves, and observed an increase in of wave complexity with increasing δ_{WP}/δ_{FS} values. Furthermore, disturbance waves began to feature multiple recirculation zones, and hence, stagnation points. Multiple recirculation zones within a wave is possible, since the length-scales of a given wave is greater than the recirculation zones (Karimi & Kawaji, 1999). In addition, Alekseenko et al. (2009) predicted that the presence of stagnation points is essential for the generation of ripples at the rear-slope of disturbance waves, and the entrainment gas and liquid at the wave-front.

In contrast to large amplitude disturbance waves, ripple waves or ripples are small amplitude interfacial waves that are omnipresent on the surface of liquid-films in gas-liquid annular flows. Extensive experimental studies on ripple waves have been limited previously due to the poor spatial resolution of the employed experimental techniques. Nevertheless, Alekseenko et al. (2009)

recently reported the generation of fast and slow-moving ripple waves are generated at the rear-slope of disturbance waves. Slow-moving ripples slide to the film-substrate region behind the 'parent' disturbance wave, and eventually become absorbed by the following disturbance wave; while fast-moving ripples accelerate over the top of the parent disturbance wave, and either decay near the wave-front or fragment into liquid droplets due to the gas-shear (Azzopardi, 1983; Cherdantsev et al., 2014; Pham et al., 2014; Woodmansee & Hanratty, 1969). Based on the aforementioned observations, Alekseenko et al. (2009) assumed that the stagnation point exists on the rear-slope of disturbance waves. The liquid-film surface region between the stagnation point and wave-front moves in the direction of the flow; while the film surface region between the stagnation point and wave-tail moves in the opposite direction. Therefore, the generation of fast or slow-moving ripples is dependent on the relative location of ripple generation to the stagnation point. This assumption could not be verified by Zadrazil & Markides (2014) due to the low temporal resolution of the measurements.

2.1.2. Gas and liquid entrainment

In gas-liquid annular flows, the presence of large amplitude disturbance waves is necessary for the entrainment of liquid droplets in the gas-core. Several liquid droplet entrainment mechanisms have been proposed or reported in literature. Hall Taylor et al. (1963) observed liquid entrainment during the coalescence of disturbance waves due to the normal distribution of disturbance wave velocities. Furthermore, the consequent coalesced disturbance wave continued to travel through the channel with the velocity of the faster disturbance wave. Based on this observation, Wilkes et al. (1983) suggested that the volume of liquid in the slower disturbance wave becomes completely entrained in the gas-core, since there is a linear relationship between the wave amplitude and wave velocity (Pashniak, 1969). If the liquid volumes between the two disturbance waves coalesce, the wave height and wave velocity of the coalesced disturbance wave would be greater than the fast-moving wave (Wilkes et al., 1983).

Woodmansee & Hanratty (1969) were one of the first to observe liquid droplet entrainment due to the acceleration of ripple waves over the surface of disturbance waves in co-current gas-liquid flows in a horizontal rectangular duct. Based on high-speed observations through the axis of vertical upwards annular flows, Azzopardi (1983) proposed ‘bag break-up’ and ‘ligament break-up’ mechanisms. Pham et al. (2014) also observed the same mechanisms for liquid-films with gas-shear on the outer pipe wall. In a study of liquid-films with gas-shear in a horizontal duct, Cherdantsev et al. (2014) associated both liquid entrainment mechanisms to the fast-moving ripple waves on disturbance waves. In the bag break-up mechanism, a liquid arc or liquid bag appears in front of the disturbance wave. The liquid arc protrudes forward and expands until it fragments into droplets. In the ligament break-up mechanism, a liquid jet or ligament appears in front of the disturbance wave. The ligament protrudes forward and elongates along its own axis until it atomises into droplets. Liquid droplets from ligament break-up are larger and slower than from bag break-up (Cherdantsev et al., 2014). Ishii & Grolmes (1975) described three additional

mechanisms of liquid droplet entrainment for co-current gas-liquid annular flows: (i) 'wave under-cut' – the gas flow under-cuts the liquid film; (ii) 'bubble burst' – entrained gas bubbles in the film rise to the surface and burst; and (iii) 'liquid impingement' – entrained liquid droplets in the gas-core deposit onto to the film and generate more droplets during impact. A number of the aforementioned mechanisms were observed by Zadrazil et al. (2014) for downwards annular flows: (i) 'wave under-cut'; (ii) 'bubble burst'; (iii) 'liquid impingement'; and (iv) 'ligament break-up'.

In the gas-core, the entrained liquid droplets have a distribution of sizes that vary in space and time (Azzopardi, 1997). Droplet sizes are dependent on both the gas superficial velocity and entrained liquid mass flux (Azzopardi, 1985). The sizes of liquid droplets decrease with increasing gas superficial velocities due to the greater shear forces acting on the liquid-film; while droplet sizes increase with increasing droplet concentration or entrained liquid mass fluxes due to the increase in the probability of droplet coalescence that leads to larger droplets (Azzopardi, 1985). In comparison with large entrained liquid droplets, small droplets have higher axial velocities (i.e. in the flow direction), however, have a wider axial velocity distribution (Azzopardi, 1997). This can be attributed to the greater influence of the gas turbulence on smaller entrained droplets, which cause these liquid droplets to accelerate or decelerate in the radial direction. The upper limit of the axial droplet velocity is dependent on the superficial velocity of the gas-phase; while the lower limit is assumed to be dependent on the interfacial wave velocity (Azzopardi, 1997).

The entrained droplets in the turbulent gas-core can deposit onto the liquid-film. James et al. (1980) observed the radial behaviour of droplets, and identified two different mechanisms of liquid droplet deposition based on droplet momentum and size: (i) 'diffusion'; and (ii) 'direct impact'. In the diffusion mechanism, liquid droplets with small momentum and size have random motions due to the gas turbulence; while the trajectory of droplets with large momentum and size are not influenced by the gas-phase, and hence, have a near-straight radial motion in the direct

impact' mechanism (James et al., 1980). In the study of Zadrazil et al. (2014), the diffusion mechanism was observed for entrained droplets generated from the ligament break-up mechanism; while the direct impact mechanism was observed for liquid droplets created from the bubble burst, liquid impingement and wave under-cut mechanisms. In a study of liquid-films with gas-shear in a duct, Cherdantsev et al. (2017) found two distinct liquid droplet deposition mechanisms based on the type of liquid-film perturbation: (i) 'craters'; and (ii) 'furrows'. In the crater mechanism, large droplet impact angles cause circular craters with possible asymmetric rims on the leeward side, and occasionally generate more entrained droplets; while small droplet impact angles create long and narrow or furrows covered with radial wrinkles, which lead to entrained gas (Cherdantsev et al., 2017). The impact angle of entrained droplets is the angle between the droplet trajectory and local interfacial slope. Craters and furrows occur predominantly at the film-substrate and disturbance waves, respectively.

The volumetric density of gas bubbles and the mean bubble chord length increases with both gas and liquid flow-rates (Hann et al., 2018; Zadrazil et al., 2014;). The bubble size has an exponential distribution, which is mainly dependent on air flow-rate (Rodríguez & Shedd, 2004). The majority of entrained bubbles with sizes equal or smaller than the film-thickness are located in the substrate-film due to the deposition of liquid droplets through the furrow mechanism, however, bubbles sizes can be larger in disturbance waves than the substrate-film (Hann et al., 2018). Disturbance waves assimilate bubbles in the substrate-film, and bubbles inside the disturbance waves move faster than the ones in substrate-film (Hann et al., 2018). Bubbles can move from an interfacial wave to the substrate-film due to lower liquid velocity within waves than the interfacial velocity (Hann et al., 2018; Rodríguez & Shedd, 2004). If such a bubble gets into the film layer with thickness less than the bubble's size, it may collapse when trapped between the wall and the film surface, possibly due to action of gas-shear (Hann et al., 2018).

2.2. Experimental methods

The highly complex gas-liquid interfaces and three-dimensional (3-D) nature of gas-liquid annular flows create significant challenges to experimentally investigate the characteristics of the liquid-film topology (e.g. liquid-film thickness, wave frequency, wave velocity). Therefore, the employed experimental methods/techniques must encompass a number of rigorous requirements to obtain reliable data:

- **High temporal resolution** – The velocities of interfacial waves can be in the order of several metres per second.
- **High spatial resolution** – The wavelength of small amplitude interfacial waves can be in the order of a few millimetres.
- **High dynamic range** – The variation of the liquid-film thickness can be in the range of several micrometres to several millimetres for a given flow condition.
- **Space and time resolved** – The co-existence and interaction of interfacial waves with varying length and time-scales.
- **Longitudinally and azimuthally/circumferentially resolved** – The gas-liquid flows and interfacial wave phenomena are three-dimensional (3-D).
- **Large interrogation regions and time durations** – The interaction of interfacial waves vary in space and time.
- **Non-intrusive** – The use of intrusive methods can physically disturb the flow and lead to the collection of unreliable data.
- **Adaptable/flexible** – Simultaneous application of independent techniques is beneficial for simultaneously measurements of various flow quantities in the same interrogation region (e.g. species concentration, temperature variations, velocity fields).

A wide range of experimental methodologies with different physical principles have been developed or adapted from other research fields to measure the liquid-film thickness (δ) in gas-liquid annular flows, however, the various techniques do not necessarily encompass all the listed requirements. The most commonly employed experimental methods, which are described in detail in Sections 2.2.1 to 2.2.4, are the following: (i) conductance/conductivity probes; (ii) high-speed visualisation; (iii) laser-focus displacement (LDF); and (iv) laser-induced fluorescence (LIF) based optical methods. More complex experimental methods with diverse principles have been used, such as: (i) cold neutron tomography (Takenaka et al., 1998); (ii) gamma densitometry (Sharaf et al., 2011); (iii) nuclear magnetic resonance (NMR) tomography (Bonn et al., 2008); (iv) ultrasonic-based methods (Chen et al., 2005); and (v) X-ray tomography (Fischer & Hampel, 2010). However, the wide application of the aforementioned experimental methods is limited due to a combination of factors: (i) limited spatial or temporal resolution which effects the reliability of measurements in thin liquid-film regions; (ii) inability to resolve measurements in more than one dimension; (iii) considerable financial burden to purchase and maintain relevant equipment and instrumentation; and (iv) significant safety hazards.

2.2.1. Conductance probes

In the application of conductance or conductivity probes, the electrical conductivity of liquid-films passing between two electrodes is measured in order to recover film-thickness. Conductance probes are inexpensive and relatively easy to manufacture. The primary configurations of the two electrodes are either: (i) 'flush-mounted' (Azzopardi, 1986; Belt et al., 2010; Chu & Dukler, 1974; Damsohn and Prasser, 2009; Sekoguchi et al., 1985; Webb & Hewitt, 1975; Zhao et al., 2013); or (ii) 'parallel-wire' or 'twin-wire' (Han et al., 2006; Karapantsios et al., 1989). The general configurations of both the flush-mounted and twin-wire conductance probes are illustrated in Figure 2-2.

In the flush-mounted configuration, the electrodes are manufactured to be flush with the inner pipe wall (Wang & Gabriel, 2005). The main limitations with this method are the spatial-averaging and low spatial resolution at the point of liquid-film interrogation, which can lead to underestimations of interfacial wave wavelengths comparable to the probe size. In addition, an inherent limitation with this type of probe is the insensitive response to thick film regions (Zhao et al., 2013). The measured conductance increases linearly with film-thickness, however, this asymptotes to a constant value after a certain thickness. Miniaturization of flush-mounted probes can partially address the issue with spatial-averaging and resolution, however, this also results in smaller linear relationship regions between conductance and film-thickness (Zhao et al., 2013).

In the twin-wire configuration, the two electrodes extend across the channel, and the distance between the electrodes can be reduced to improve spatial resolution due to the linear sensitivity dependence on film-thickness (Karapantsios et al., 1989). Nevertheless, this type of probe is intrusive and disturbs the flow. Another limitation of twin-wire probes is the possible formation of capillary menisci between the electrodes, which is most likely to occur in films with high entrained gas bubble concentrations (van der Meulen, 2012). Overall, conductance probes must be calibrated

to liquid-films with known thicknesses prior to flow measurements, and simultaneous measurements with the application of multiple conductance probes must be cautious of the interference between neighbouring probes (Karapantsios et al., 1989; Zhao et al., 2013).

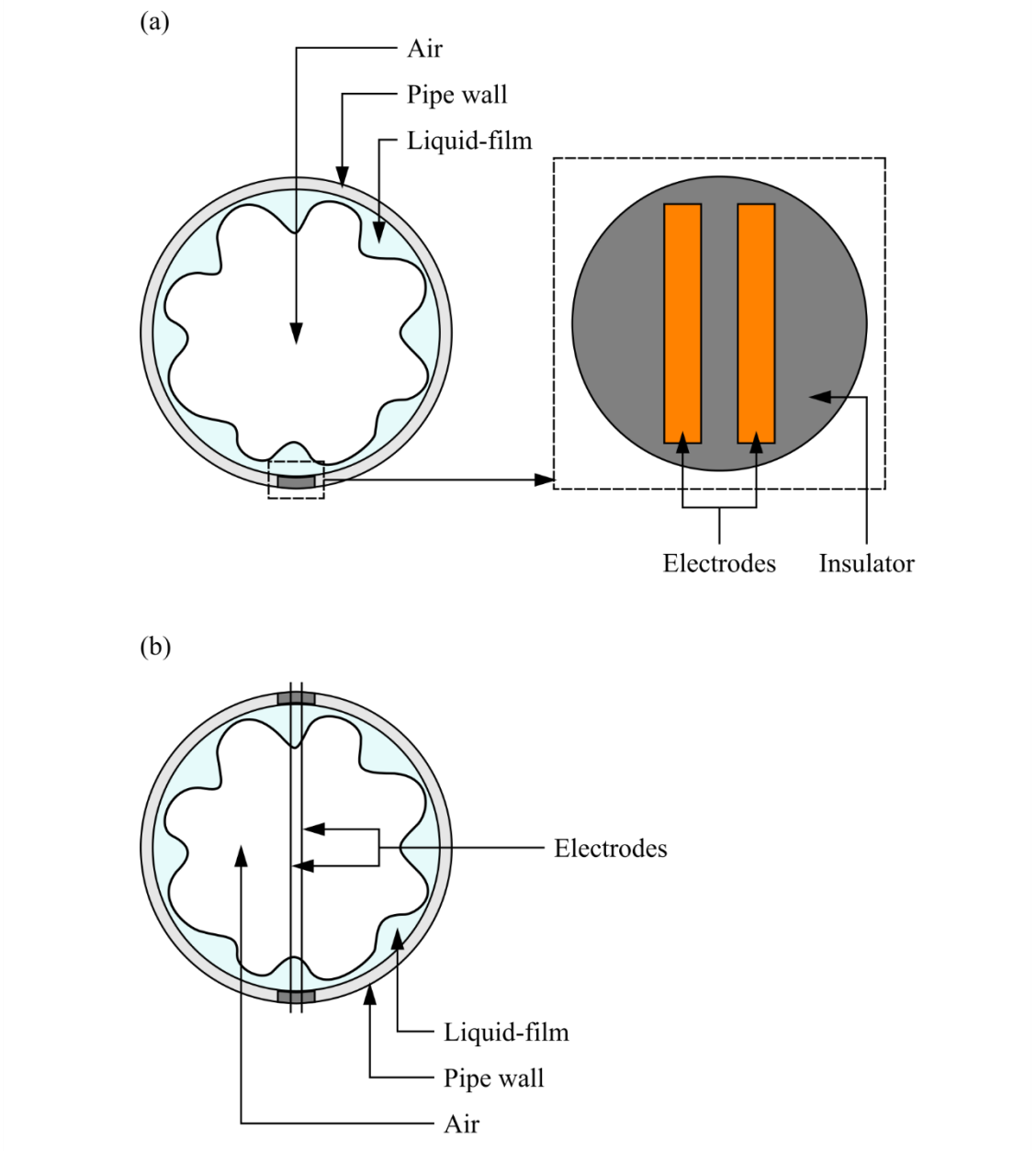


Figure 2-2 – Primary configurations of the two electrodes in conductance or conductivity probes: (a) 'flush-mounted'; and (b) 'parallel-wire' or 'twin-wire'.

2.2.2. High-speed visualisation

High-speed visualisation is a simple non-intrusive optical-based method that is extensively used in annular flow studies to qualitatively investigate the flow phenomena in both the axial (Lin et al., 2020; Setyawan et al., 2016) and radial (Arnold & Hewitt, 1967; James et al., 1980) directions of the flow. Nevertheless, a number of studies have implemented the technique to recover the film-thickness in annular flows along the flow direction (Hewitt et al., 1990; Pan et al., 2015; Pham et al., 2014). For this type of application, the general optical configuration is based on the principles of the shadowgraph photography, which is widely used for fluid visualisation studies in other research fields (Castrejón-García et al., 2011; Settles, 2001). Differences in refractive indices at an interface between different media are accentuated in shadowgraph photography (Settles, 2001), and in the employment of back illumination, interfaces appear dark (i.e. shadows) in the collected images, since refracted light disperse at the interfaces (Castrejón-García et al., 2011). The general set-up of the method for annular flows in pipes is shown in Figure 2-3.

A refractive index matching approach can be applied to the test-section design in order to minimise optical distortions due to the pipe curvature. The flow interrogation region is back-lit with a white-light source, and an optical-diffuser is used to diffuse or scatter the white-light to create a near-homogenous background illumination. A camera is set-up on the opposite side of the flow channel from the light source to directly image the axial cross-section of the flow. The observation angle of the camera is usually perpendicular to the horizontal and vertical planes. Prior to the measurements, a calibration procedure is necessary for the employed camera to obtain the spatial resolution. The collected instantaneous flow images can be processed to identify the gas-liquid and solid-liquid interfaces, and hence, recover the liquid-film thickness. High-speed visualisation is a relatively inexpensive method, and offers high temporal resolution. However, one of the main limitations with this optical method for film-thickness measurements is the spatial averaging of the local liquid-film thickness in the transverse direction.

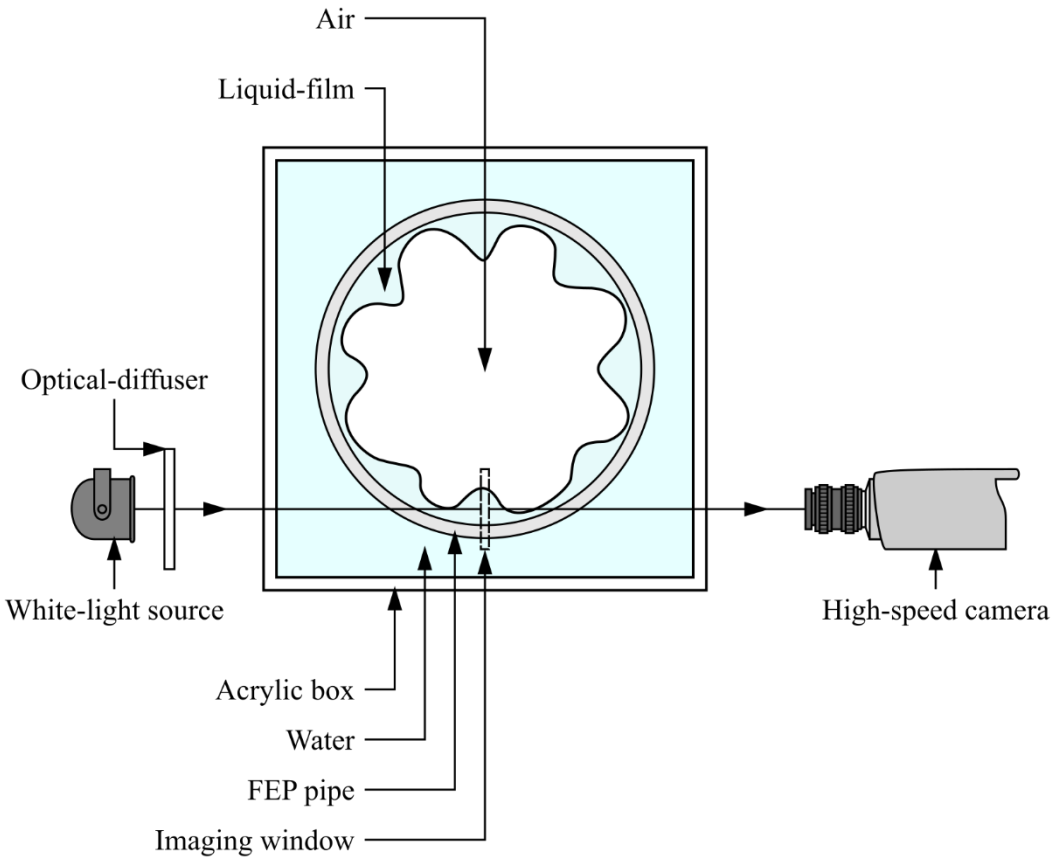


Figure 2-3 – General optical configuration of high-speed visualisation with back-lit illumination: (i) white-light source; (ii) optical-diffuser; and (iii) high-speed camera. A refractive index matching approach can be applied to the design of the test-section to minimise optical distortions in the collected images due to the curvature of the pipe.

2.2.3. Laser-focus displacement (LFD)

The laser-focus displacement (LFD) method is a non-intrusive laser-based technique, which was originally developed to detect scratches on electrical devices, and currently employed to verify the quality of products that require either a fine surface finish or material thickness (e.g. contact-lenses, glasses, vehicle break-discs) in various industries (Wegener & Drallmeier, 2010). LFD has been used in a number of studies to measure the thickness of liquid-films in various flow configurations. Takamasa & Hazuku (2000) and Takamasa & Kobayashi (2000) used the LFD method to perform film-thickness measurements in falling liquid-film flows on a vertical plate and inner pipe wall, respectively. In addition, Hazuku et al. (2008) implemented LFD to measure the liquid-film thickness in upwards gas-liquid annular flows.

In order to determine the location of the gas-liquid interface (i.e. film free surface) in annular flows, an instrument of the LFD method uses the confocal principle with laser-light (Wegener & Drallmeier, 2010). The general configuration of the main components of the laser-focus displacement (LFD) method is shown in Figure 2-4. The focal-point of a converging laser-beam oscillates with a known frequency and amplitude in the radial direction of the flow; and when the focal-point of the laser is at the gas-liquid interface, peaks in the reflected light intensity are detected by the instrument (Wegener & Drallmeier, 2010). LFD instruments include a sensor to measure the position of the relevant optics for the converging laser-beam in order to determine the focal point location at light intensity peaks, and hence, the surface of liquid-films (Wegener & Drallmeier, 2010). Prior to the film-thickness measurements, the instrument must be calibrated to known liquid-film thicknesses. While the LFD method offers good spatial resolution, it can only be implemented to conduct point-wise thickness measurements of liquid-films. In addition, the reliability of the LFD method is dependent on the absence of entrained gas bubbles and interfacial slopes must be $< 33\ ^{\circ}$ (Hazuku et al., 2008).

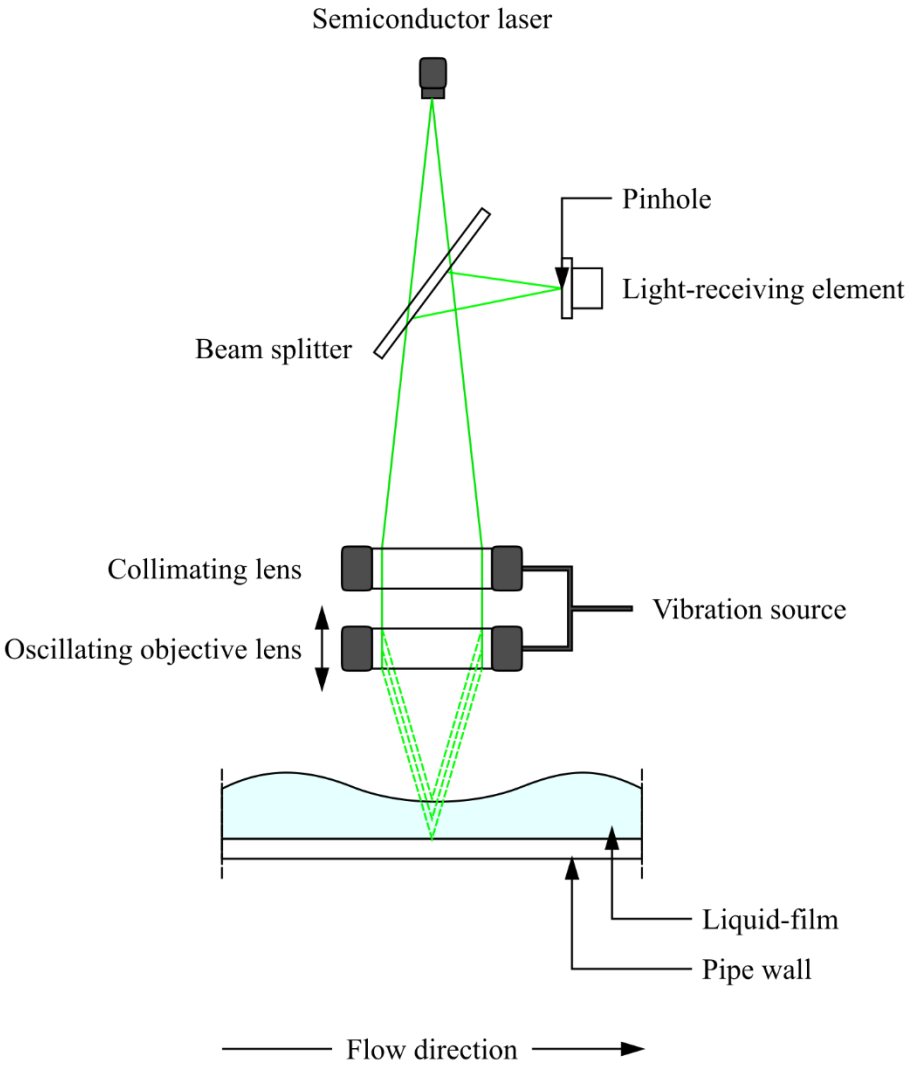


Figure 2-4 – General configuration of the main components in the laser-focus displacement (LFD) method: (i) semiconductor laser; (ii) beam splitter; (iii) pinhole; (iv) light-receiving element; (v) vibration source; (vi) collimating lens; and (vii) oscillating objective lens.

2.2.4. LIF-based optical methods

In the application of optical methods based on the principles of laser-induced fluorescence (LIF) for annular flow studies, a soluble fluorescent dye is added to the liquid-phase in order for the film to emit fluorescence upon excitation. The dye is carefully selected to ensure the spectral range of the emitted fluorescent-light is different to the spectrum of the excitation or laser-light. The fluorescence emitted from the excited liquid-film in the region of interrogation (ROI) is collected with a camera, which is typically equipped with an optical filter to only collect light in the fluorescence emission spectrum. Since the chosen chemical or particle additives (i.e. fluorescent dye) do not affect the main fluid properties or flow characteristics, the LIF-based optical methods are considered non-intrusive. The difference between variations of this method is mainly in the approach to the fluorescence emission collection, and hence, the treatment of collected raw flow images. The two main types of non-intrusive LIF-based optical methods are: (i) planar laser-induced fluorescence (PLIF); and (ii) brightness-based laser-induced fluorescence (BBLIF). The spatial and temporal resolutions of both techniques can often be adjusted to meet the requirements of a particular application. Various interfacial phenomena (gas bubble entrainment, liquid droplet entrainment, liquid droplet deposition) can be detected in the collected images of both PLIF and BBLIF, and hence, the complex interactions between bubbles, droplets, and waves can be investigated (Cherdantsev et al., 2017; Hann et al., 2018; Zadrazil et al., 2014).

In the standard PLIF approach, a laser-sheet and a camera with an observation angle of $\theta_P = 90\ °$ relative to the excitation plane is used to directly image an axial cross-section of the liquid-film. The near-wall and far-wall boundaries of the fluorescence domain in the PLIF images correspond to the solid-liquid and gas-liquid interfaces, respectively. Therefore, the images are processed to identify the locations of the interfaces and recover the liquid-film thickness. PLIF has been used to investigate the film characteristics in annular flows (Farias et al., 2012; Lecompte et al., 2017; Schubring et al., 2010; Zadrazil et al., 2014), and in other flow configurations

(Charogiannis & Markides, 2017; Charogiannis et al., 2018a; 2018b).

The main advantage of PLIF is the ability to integrate similar measurement approaches to investigate other film characteristics in the same ROI, such as: (i) particle image or tracking velocimetry (PIV/PTV) to obtain velocity field information in the liquid-film (Charogiannis & Markides, 2014; Charogiannis et al., 2015); and (ii) infrared (IR) tomography to obtain two-dimensional (2-D) free-surface temperature (Charogiannis & Markides, 2017; 2019; Mathie et al., 2014). In addition, the circumferential or transverse film-thickness profiles can be obtained with PLIF by changing the alignment of the laser-sheet (Farias et al., 2012). A limitation of the standard PLIF technique is the inherently 2-D nature of the measurements, and three-dimensional (3-D) measurements are a challenge to perform. However, 3-D measurements with PLIF may be possible with further development, such as the integration of laser-sheet scanning (Knutsen et al., 2017). Another limitation with PLIF is the 'mirror effect' due to total internal reflection (TIR) of the emitted fluorescent-light at the circumferential gas-liquid interface (i.e. film free-surface) between the excitation and imaging planes (Häber et al., 2015).

In contrast to PLIF, BBLIF is a line-of-sight technique, and hence, the camera is aligned near-adjacent to the laser to minimise the observation angle of the camera (i.e. $\theta_{BB} \approx 15$ °). In the standard BBLIF approach, the emitted fluorescence intensity signals or 'brightness' from the liquid-film excited with a laser-sheet is collected with a camera. The collected intensity signals are converted to film-thickness in accordance with the Beer-Lambert law (Alekseenko et al., 2014). BBLIF has been used in various configurations for different flow configurations: (i) point-wise (Hewitt et al., 1964; Lel et al., 2005); (ii) 2-D (Alekseenko et al., 2009; 2013; 2014; 2015b; Liu et al., 1993; Vasques et al., 2018; Vlachogiannis & Bontozoglou, 2001); and (iii) 3-D (Adomeit & Renz, 2000; Alekseenko et al., 2005; 2012; 2015a; Cherdantsev et al., 2014; Kharlamov et al., 2015).

The advantage of BBLIF is that it can be more easily resolved in two spatial coordinates simultaneously in order to obtain the 3-D shape of the gas-liquid interface. A limitation of the

BBLIF approach arises when the steepness of interfacial slopes increase, which introduces a measurement error that increases gradually with slope steepness. This error becomes significant when the critical angle of TIR is approached, which is approximately 48 ° for an air-water interface (Lindon et al., 2010). While entrained gas bubbles are still detectable and measurable with BBLIF, the local thickness of the film encompassing the bubble can only be approximated. In contrast to PLIF, BBLIF does not directly image the film in the radial direction, and hence, the method cannot be integrated readily with other similar measurement approaches, such as PIV/PTV. Many other methods similar measurement approaches to BBLIF, such as: (i) light absorption (Clark et al., 2001); (ii) pigment luminance (Ohba & Nagae, 1993); and (iii) near-infrared attenuation (Dupont et al., 2016). However, to the best of our knowledge, these techniques are not widely employed in annular flow studies.

2.3. Summary

Accurate and reliable film-thickness measurements of liquid-films in downwards gas-liquid annular flows are highly challenging to perform due to the various complex and three-dimensional (3-D) interfacial phenomena present within the flow: (i) gas bubble entrainment in the liquid-film; (ii) liquid droplet entrainment into the gas-core; (iii) wave activity (e.g. disturbance and ripple waves) on the surface of the film; and (iv) varying length and time-scales of individual phenomena. Numerous experimental techniques based on different physical principles have been employed to measure the liquid-film thickness in previous annular flow studies. Due to a number of factors (e.g. simpler implementation, less financial burden, less safety hazards), the most commonly used methods have been the following: (i) conductance probes; (ii) high-speed visualisation; (iii) laser-focus displacement (LFD); and (iv) LIF-based optical methods.

LIF-based optical methods, such as planar laser-induced fluorescence (PLIF) and brightness-based laser-induced fluorescence (BBLIF), have been extensively implemented in recent studies as both PLIF and BBLIF can be employed to perform high spatiotemporal film-thickness measurements, and the measurements can be resolved in more than one dimension. In addition, each approach has its own distinct benefits. For example, the main advantages of PLIF are the ability to directly image the film cross-section and integrate other similar measurement approaches (e.g. particle image or tracking velocimetry) at the same region of interrogation (ROI); while the ability to perform 3-D flow measurements is the main benefit of BBLIF. Nevertheless, both PLIF and BBLIF film-thickness measurements are susceptible to errors due to the optical effects encountered at the gas-liquid interfaces. Therefore, a better understanding of these optical effects is necessary in order to further develop each LIF-based optical method and improve the reliability of the acquired liquid-film thickness data.

CHAPTER

3. Flow Facility & Experimental Methods

In Chapter 3, an in-depth description is provided of DAFLOF, which is the air-water flow facility used to generate adiabatic and non-reacting downwards co-current air-water annular flows in vertical pipes ($Re_G \approx 90{,}000$, $Re_L \approx 1500$). Furthermore, the optical configurations of the applied non-intrusive laser-based optical techniques (i.e. simultaneous PLIF and BBLIF, S-PLIF, and MFoR-BBLIF) are described in detail in this Chapter. For each method, a set of experiments were performed to measure either liquid-film thickness (δ), or individual disturbance wave velocities (u_{DW}) as a function of downstream distance (s).

3.1. Flow facility: DAFLOF

The Downwards Annular Flow Laser Observation Facility (DAFLOF) is an air-water flow-loop system that was used in several studies (e.g. Cherdantsev et al., 2018; Zadrazil et al., 2014; Zadrazil & Markides, 2014) to generate downwards co-current air-water annular flows with adiabatic and non-reacting conditions in vertical pipes, and to investigate the liquid-film characteristics with non-intrusive laser-based optical techniques. The working fluids of the flow facility are air and water as these fluids are: (i) abundant and cheap; (ii) chemically non-hazardous; and (iii) commonly employed in gas-liquid annular flow studies. After the use of the facility in the work of Zadrazil & Markides (2014), the flow-loop was dismantled and re-built to add extensive modifications:

- **Fluid-lines** – Installation of new equipment and instrumentation for the air and water-lines. The maximum possible air and water volumetric flow-rates of the flow-loop are $Q_G \approx 2000$ L/min and $Q_L \approx 9.0$ L/min, respectively

- **Test-section** – Incorporation of a new test-section with a length of $L_{TS} \approx 4200$ mm. A refractive index matching approach was applied in the design and manufacture of the test-section to minimise optical/perspective distortions in the collected flow images due to the curvature of the pipe (Zadrazil et al., 2014). The visualisation-section length was $L_{IS} \approx 4000$ mm to maximise the available axial flow interrogation length.

- **Linear actuator system** – Integration of a vertically orientated linear actuator system to the facility. The optical measurement systems can be installed on the carriage of the system to physically move the optics along the entire test-section length. Therefore, the flow interrogation point can be set either at a specific downstream distance from the test-section inlet to conduct static measurements, or in linear motion to implement a moving frame-of-reference (MFoR) approach and perform dynamic measurements.

- **Laser safety enclosure** – Construction of a laser safety enclosure around the DAFLOF. The employed optical methods are laser-based, and hence, the environment must meet the laser safety standards of the Department and the College.

The rebuild of DAFLOF with the aforementioned modifications was accomplished over a time period of ≈ 16 months with the assistance of the Mechanical Workshop in the Department of Chemical Engineering. A schematic diagram of the DAFLOF is shown in Figure 3-1. A large frame was assembled with aluminium profiles (KJN Aluminium Profiles) to mount the numerous components of the air-water flow-loop. The overall dimensions of DAFLOF was ≈ 3000 mm × 3000 mm × 6500 mm ($L \times W \times H$), and hence, a one-person scaffold tower (MiTOWER, HSS Hire) was necessary to operate and maintain the facility. The laser safety enclosure (Lasermet Ltd) was assembled with laser safety compliant panels and curtains. The use of curtains was specific to the current enclosure design due to bridge crane in the laboratory, and the interlock control system on the curtains prevented the use of the laser systems when the curtains were open to either enter the safety enclosure or use the crane. Nevertheless, the overall dimensions of the laser safety enclosure was ≈ 7000 mm × 6000 mm × 6500 mm ($L \times W \times H$), which encompassed the entire flow facility.

As depicted in the schematic diagram of Figure 3-1, the main elements of DAFLOF are the: (a) gas-line (air); (b) liquid-line (water); (c) test-section (TS); and (d) linear actuator system (LA). The naming convention of the equipment and instrumentations in the gas and liquid-lines is provided in Table 3-1; while the naming convention of the components of the test-section and linear actuator system is provided in Table 3-2. The air and water-lines are described in Sections 3.1.1 and 3.1.2, respectively. The design of the gas inlet (TS-GI), liquid injector (TS-LI) and test-section (TS-IS) are explained in Sections 3.1.3, 3.1.4, and 3.1.5, respectively. Finally, a description of the linear actuator (LA) is given in Section 3.1.6.

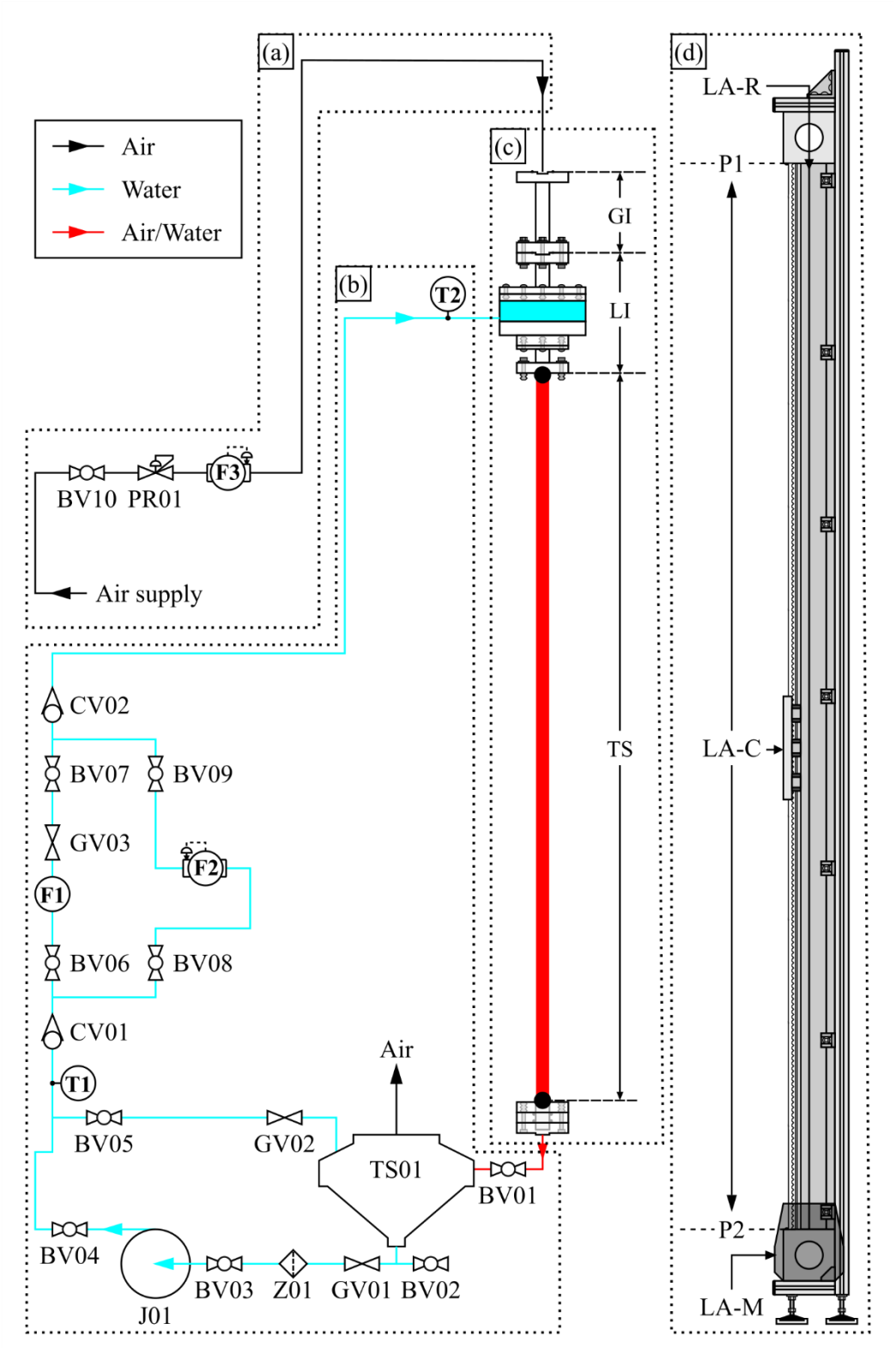


Figure 3-1 – Schematic diagram of the modified air-water flow facility, DAFLOF: (a) gas-line (air); (b) liquid-line (water); (c) test-section (TS); and (d) linear actuator system (LA).

Table 3-1 – Naming convention of the main equipment and instrumentations in the air and liquid-lines shown in Figure 3-1.

GAS-LINE (AIR)	
LABEL	**EQUIPMENT/INSTRUMENT**
BV10	Ball valve (one-piece) – 22 mm brass compression fittings
PR01	Pressure regulator with filter (≥ 40 μm) – p_{out} = 0.3 – 10 Barg
F3	Thermal mass flow-controller (horizontal orientation) – Q_G = 0 – 2000 L/min

LIQUID-LINE (WATER)	
LABEL	**EQUIPMENT/INSTRUMENT**
BV01 – BV07	Ball valve (two-piece) – 3/4 " stainless steel compression fittings
BV08 – BV09	Ball valve (one-piece) – 1/4 " stainless steel compression fittings
CV01 – CV02	Check valve (one-piece) – 18 mm brass compression fittings
GV01 – GV03	Gate valve (one-piece) – 18 mm or 22 mm brass compression fittings
F1	Turbine flow-meter (vertical orientation) – Q_L = 3.0 – 9.0 L/min
F2	Coriolis mass flow-controller (horizontal orientation) – Q_L = 0 – 3.0 L/min
J01	Vertical multi-stage centrifugal pump – p_{out} = 0 – 7.0 Barg
Z01	y-strainer (≥ 100 μm) – 28 mm brass compression fittings
T1 – T2	K-type thermal couple – T = 0 – 50 °C (± 0.1 °C)
TS01	High-density polyethylene (HDPE) conical tank – V = 40 L

Table 3-2 – Naming convention of the main components of the test-section and linear actuator system shown in Figure 3-1.

TEST-SECTION (TS)	
LABEL	**COMPONENT**
GI	Gas inlet – Acrylic pipe, D_p = 32.4 mm (± 0.4 mm), L_p = 400 mm
LI	Liquid injector – Conical injection system, D_p = 32.4 mm (± 0.4 mm)
TS	Test-section – Fluorinated ethylene propylene (FEP) pipe × 1, D_p = 32.4 mm (± 0.4 mm), L_p = 4200 mm; and acrylic anti-distortion boxes ($L \times W \times H \approx$ 70 mm × 60 mm × 1320 mm) × 3
LINEAR ACTUATOR SYSTEM (LA)	
LABEL	**COMPONENT**
LA-R	Linear actuator rail – Anodized and extruded aluminium structure ($L \times W \approx$ 6000 mm × 220 mm), and a transmission with a polyurethane steel re-enforced driving belt
LA-C	Linear actuator carriage – Rectangular unit ($L \times W \approx$ 500 mm × 300 mm) with multiple recirculating ball bearing runner blocks
LA-M	Motor of the linear actuator – P_{motor} = 1.5 kW
P1 – P2	Linear motion length of the carriage – L_{AC} = 5000 mm
P1	Position of the carriage at the top of the test-section
P2	Position of the carriage at the bottom of the test-section

3.1.1. Gas-line (air)

The compressed air mains-supply (p = 5.0 – 6.0 Barg) of the College was the source of the gas-phase for DAFLOF. The air-line was assembled with a system of 22 mm and 28 mm copper tubing and brass compression fittings to connect the mains-supply to the gas inlet (GI). The PR01 pressure regulator with filter (Norgren Olympian B15-F3) was used to regulate the air pressure and to remove impurities (≥ 40 μm) in the air. A photograph of the pressure regulator is provided in Figure 3-2(a). The air flow-rate was controlled and measured with a thermal mass flow-controller (M14, Bronkhorst UK Ltd), which had a range of Q_G = 0 – 2000 L/min. The accuracy of this instrument was ± 0.2 % of full-scale as stated by the supplier. A number of software tools (Bronkhorst FlowWare) were provided by the supplier to digitally communicate with the flow-controller. A photograph of the instrument is given in Figure 3-2 (b).

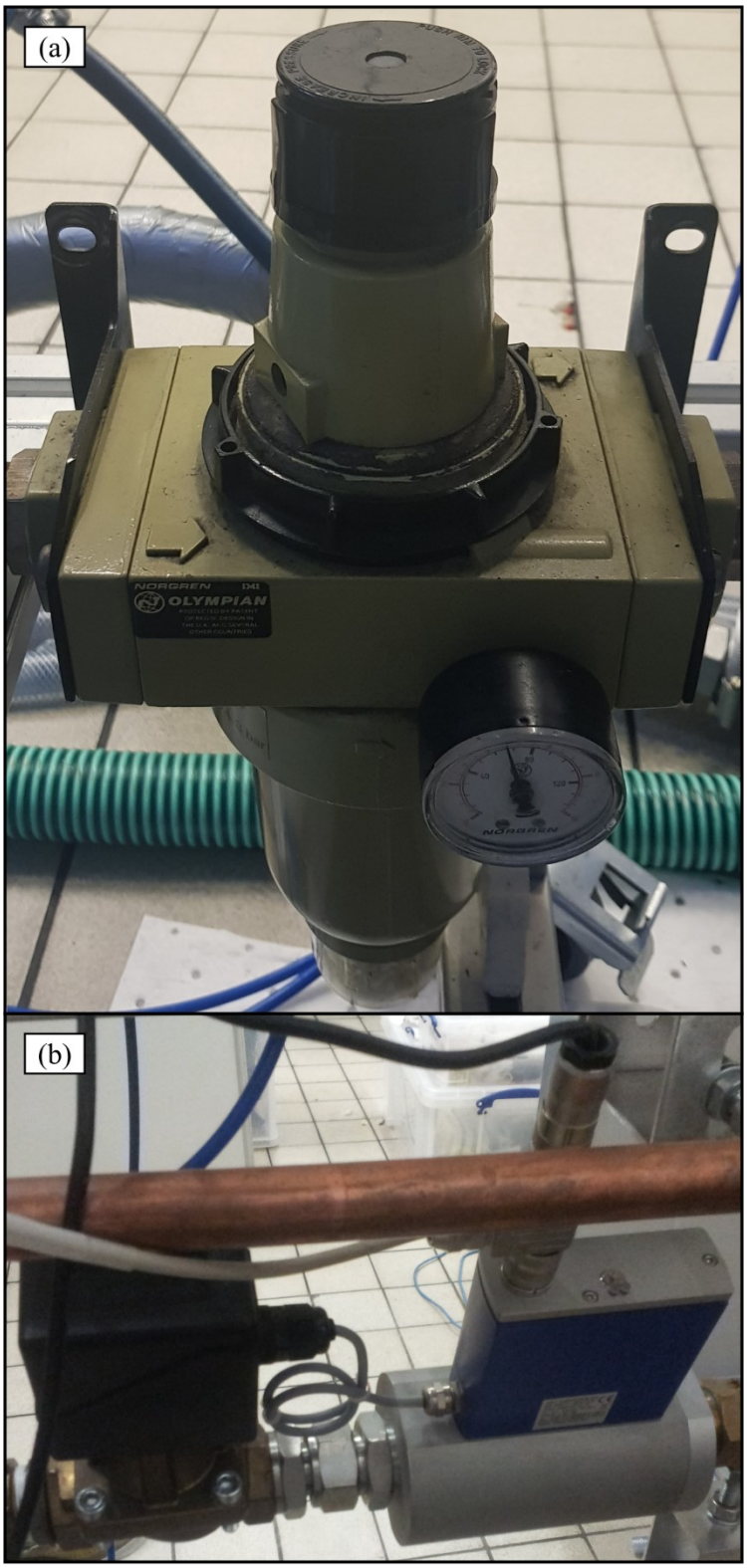


Figure 3-2 – Photographs of the: (a) pressure regulator with air filter (PR01); and (b) thermal mass flow-controller (F3).

3.1.2. Liquid-line (water)

The source of the water-line was a high density polyethylene (HDPE) conical tank (Tanks Direct Ltd) with a maximum volume capacity of V_{tank} = 40 L. Due to the flow-loop configuration and the physical restrictions of the available laboratory space, the conical tank (TS01) was modified to also function as an air-water separator. The maximum volume of water permitted in the tank was $V_L \approx 20$ L to maintain an optimum water level in TS01 during the operation of DAFLOF. A lay-out and a photograph of the modified tank is provided in Figure 3-3. As depicted in Figure 3-3(a), the TS01 conical tank consists of several inlet and outlets: (i) a 22 mm inlet for the water from the bypass-line; (ii) a 2 " inlet for the air-water mixture from the test-section (TS) outlet; (iii) a 3/4 " outlet for the water; and (iv) a 250 mm outlet for the air. The separation of the water from the air was based on cyclonic separation. Therefore, the tubing of the 2 " air-water inlet was set-up as shown in Figures 3-3(a) and 3-3(b) to allow the gas-liquid mixture to flow in a helical pattern, and due to centrifugal forces, drive the water to the inner wall of the tank. The majority of the water was collected in TS01, and the air was vented into the atmosphere through the 250 mm outlet. Since residual water droplets can be carried by the vented air, a wire-mesh was attached over this outlet. A stainless steel tube was installed in the tank to act as a baffle in order to prevent swirling. By opening valve BV02, the conical tank can be drained in order to perform maintenance procedures.

The liquid-line of DAFLOF connected from the water supply (i.e. TS01) to the liquid injector (LI). The line was assembled with a complex system of 18 mm and 22 mm copper tubing and brass compression fittings, and 1/4 " and 3/4 " stainless steel tubing and compression fittings. Initially, the water from TS01 flowed through a y-strainer (Z01) to remove solid impurities ($\geq$ 100 μm) in the water to prevent damages to the impeller of the J01 pump, which was used to circulate the water around the closed-loop. J01 was a vertical multi-stage centrifugal pump (CRiE3-15, Grundfos Pumps Ltd) equipped with a variable speed motor to vary the constant

discharge pressure (p_{out} = 0 – 7.0 Barg). In addition, wireless communication with the pump was possible with a remote to control the pump over a distance of ≈ 3.0 m. A photograph of the centrifugal pump is given in Figure 3-4(a). Whenever a new batch of water was added to the tank, J01 was primed before fully operating the pump. A bypass-line with a gate valve (GV02) was added to partially direct the flow back into the tank. This prevented the accidental build-up of pressure within the water-line, and ensured there was sufficient volumetric flows through the pump for cooling and lubrication in order to avoid pump failures or malfunctions.

The water flow-rate to the liquid injector (LI) was measured with either a turbine flow-meter (F110-X LCD, Fluidwell Ltd), or a Coriolis mass flow-controller (M15, Bronkhorst UK Ltd), which was dependent on the desired water flow-rate. The range of water flow-rates covered by the turbine flow-meter (F1) and the Coriolis mass flow-controller (F2) were Q_L = 3.0 – 9.0 L/min and Q_L = 0 – 3.0 L/min, respectively. The accuracies of the F1 and F2 instruments as stated by the different suppliers were ± 0.5 % of full-scale and ± 0.2 % of full-scale, respectively. As shown in Figure 3-1, ball valves BV06 and BV07 were opened to direct the water through F1, while BV08 and BV09 were opened to direct the water through F2. When the turbine flow-meter was used, the water flow-rate was regulated with a manual gate valve (GV03) downstream of the meter. GV03 was positioned downstream of F1 as this configuration provided more steady flow-rate measurements. The Coriolis mass flow-controller was coupled to a control valve with a pneumatic actuator to control the flow-rate. Software tools (Bronkhorst FlowWare) were provided by the supplier to digitally communicate with the flow-controller. Photographs of the turbine flow-meter and the Coriolis mass flow-controller are given in Figures 3-4(b) and 3-4(c), respectively. Check valves CV01 and CV02 were installed in the line to ensure that the water was flowing in only one direction.

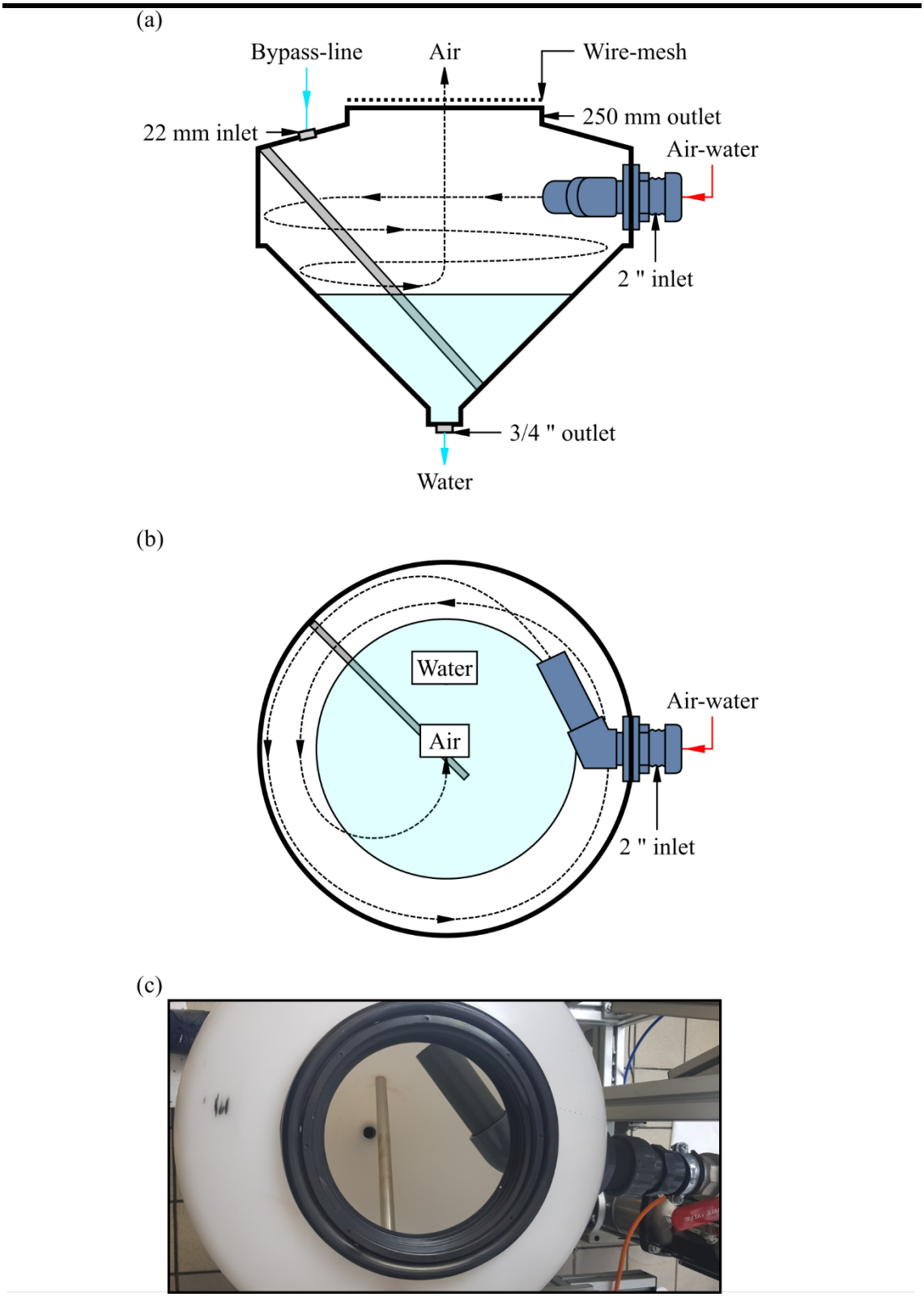


Figure 3-3 – Internal configuration of the HDPE conical tank (TS01): (a) side-view; (b) top-view; and (c) photograph.

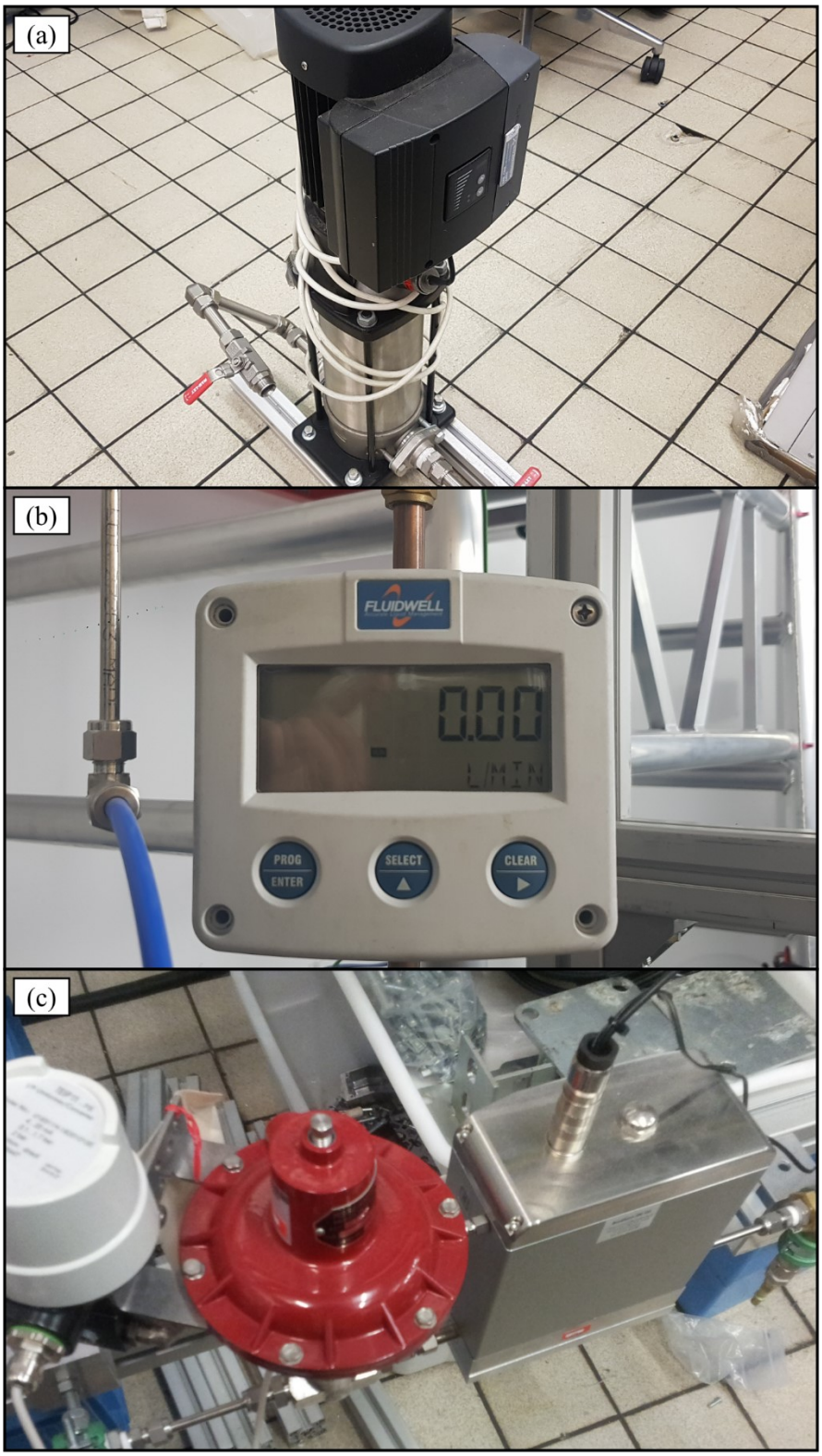


Figure 3-4 – Photographs of the: (a) vertical multi-stage centrifugal pump (J01); (b) turbine flow-meter (F1); and (c) Coriolis mass flow-controller (F2).

3.1.3. Gas inlet (GI)

The gas-phase was introduced into the test-section through a gas inlet (GI), which was a straight acrylic pipe with six-hole flanges. The design of the gas inlet is provided in Figure 3-5. The internal diameter and length of the pipe was D_p = 32 mm (± 0.4 mm) and L_p = 400 mm, respectively. An assumption was made that the gas flowing in the pipe was turbulent. For a turbulent flow of gas in a straight channel, the required minimum development length for a fully developed flow is (Cengel & Cimbala, 2006):

$$L_{\text{turb}} = 4.4 \times {Re_G}^{1/6} \times D_p \tag{3-1}$$

where D_p, L_{turb}, and Re_G are the internal diameter of the pipe, the required minimum development length for a fully developed flow of gas, and the gas Reynolds number, respectively. For a channel with D_p = 400 mm and Re_G = 90,000, a minimum development length of $L_{turb} \approx$ 9500 mm is necessary for the gas inlet. However, the maximum feasible pipe length was L_p = 400 mm due to the available physical space of the laboratory and the length of the test-section.

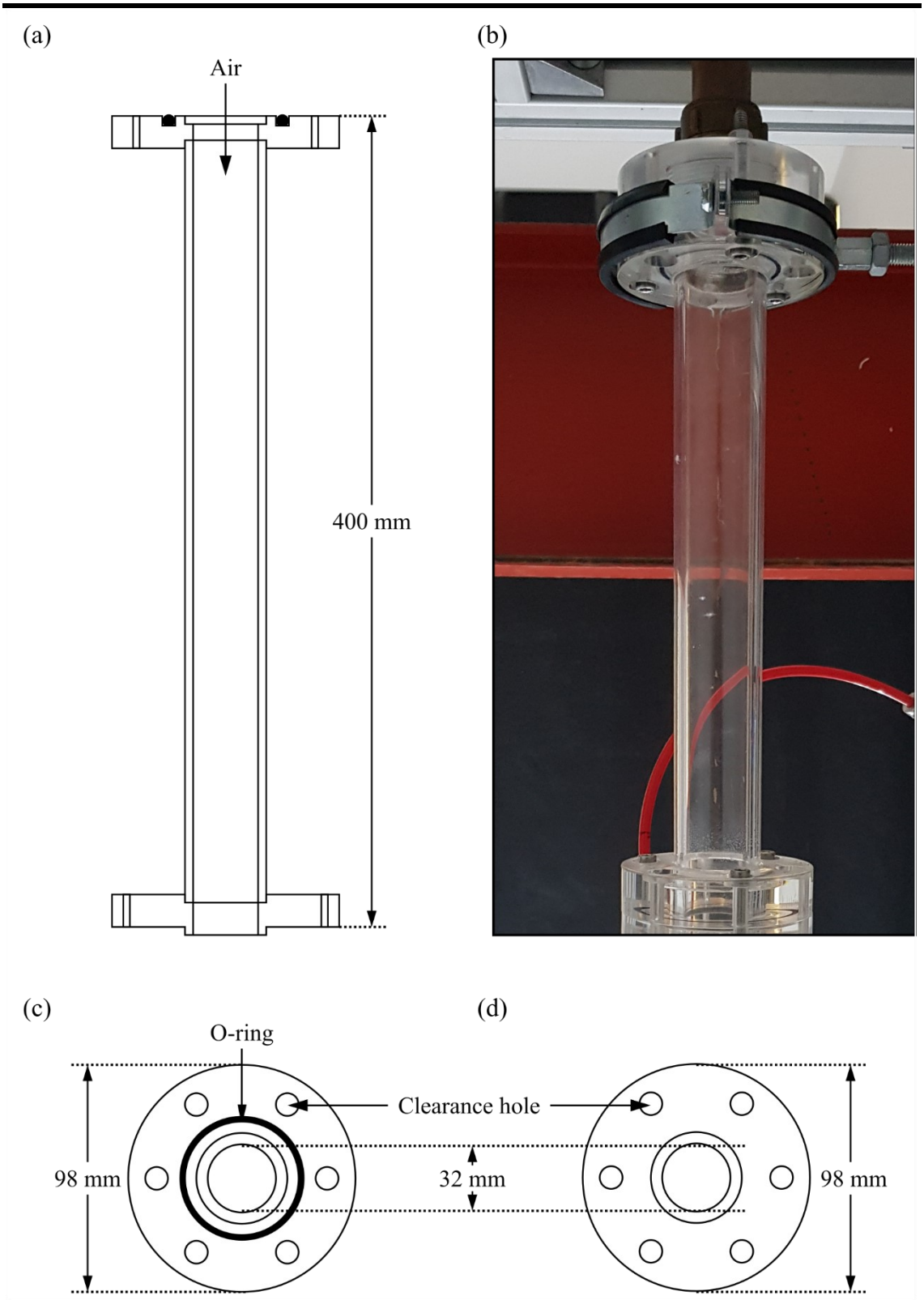


Figure 3-5 – Gas inlet (GI): (a) axial cross-section; (b) photograph; (c) front-face of female-flange; and (d) front-face of male-flange.

3.1.4. Liquid injector (LI)

Continuous liquid-films were established in the test-section with the use of a conical liquid injector (LI) at the top of the test-section (TS). The design of the liquid injector, which is given in Figure 3-6, was based on a conical injection system. This method of liquid injection was selected for three main reasons (Zhao et al., 2013): (i) conical injection is assumed to produce more uniform liquid-films on the periphery of the inner pipe wall; (ii) the liquid-films can be generated at a specific position in the test-section; and (iii) conical injection systems are a common practice in many industrial processes, such as the manufacture of detergents.

When the water-line became on-line during the operation of DAFLOF, water entered the settling chamber of the liquid injector through four 1/4 " inlets. The settling chamber was manually primed with a syringe via a gas bleed-line, which was connected from a 1/4 " outlet at the top of the chamber, to ensure that the chamber was absent of air bubbles. This was an important step in the operating procedure of the flow-loop as any compressible gas bubbles in the settling chamber could cause unsteady liquid-film flows. The point of liquid injection into the test-section, and hence, liquid-film formation was at the conical outlet. As demonstrated in Figure 3-6(c), the injector was composed of three components: LI-1, LI-2, and LI-3. In an assembled state, LI-3 could be rotated within LI-2 to adjust the width of the exit: a clockwise rotation to narrow the width and vice versa. A single revolution of LI-3 was equivalent to an alteration of ≈ 1.0 mm. The ability to adjust the width was incorporated in the design to regulate flow contractions and prevent hydraulic jumps or gas entering the settling chamber (Charogiannis et al., 2015). The 1/4 " outlet at the bottom of the chamber was connected to a liquid bleed-line, which was only used to drain the settling chamber in order to remove the injector from the test-section for disassembly and maintenance.

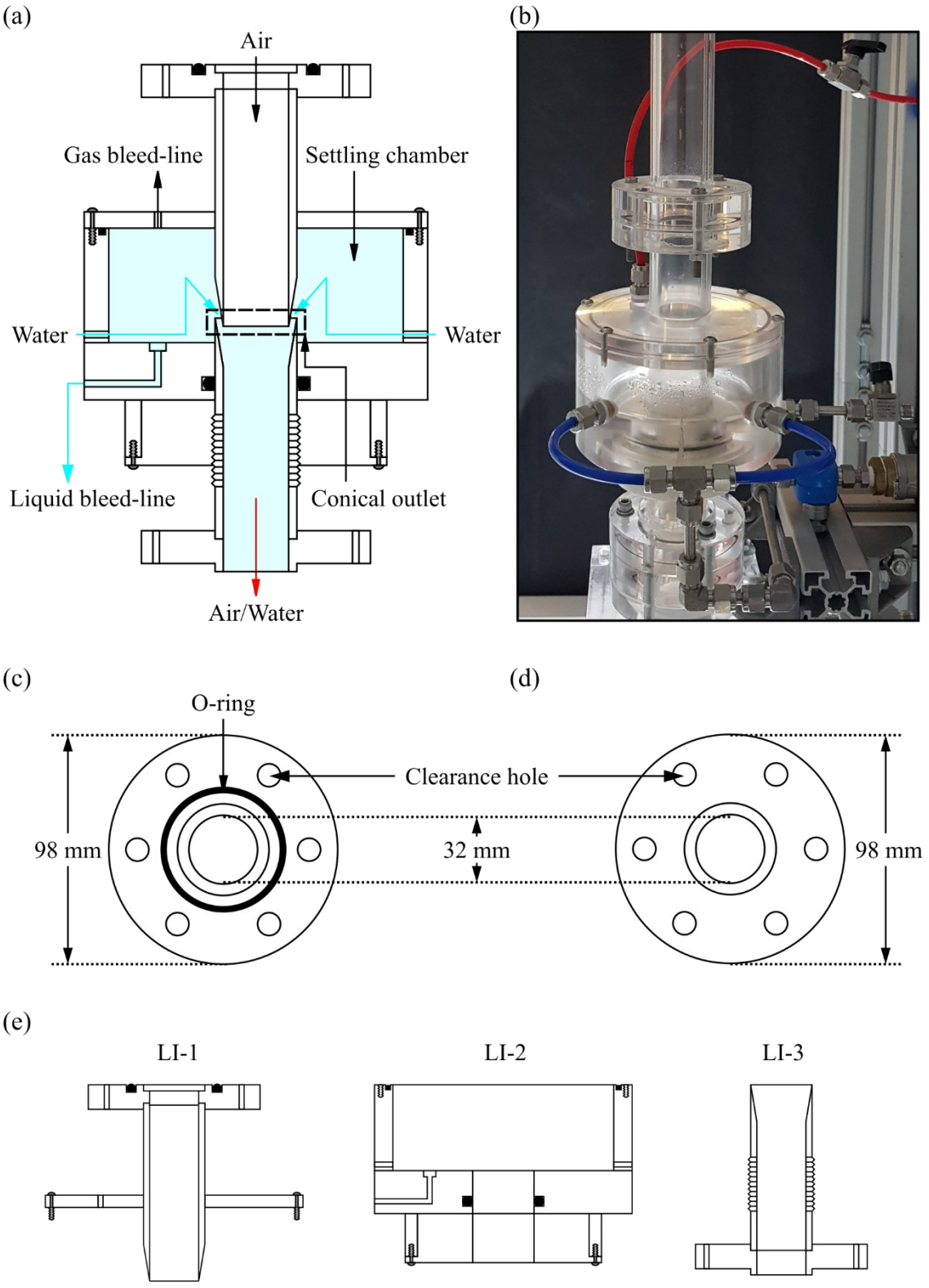


Figure 3-6 – Conical liquid injector (LI): (a) axial cross-section; (b) photograph; (c) front-face of female-flange; (d) front-face of male-flange; and (e) axial cross-section of each component.

3.1.5. Test-section (TS)

A refractive index matching approach was applied to the design and the manufacture of the new test-section to minimize perspective distortions due to the curvature of the pipe (Zadrazil et al., 2014). A schematic diagram of the test-section is shown in Figure 3-7. One of the main elements of the test-section was the fluorinated ethylene propylene (FEP) pipe, which was composed of a FEP tube, an acrylic female-flange, and an acrylic male-flange. The dimensions of the FEP tube were the following: an internal diameter of D_p = 32 mm (± 0.4 mm), a tube wall thickness of φ_{tube} = 1.5 mm, and a length of $L_p \approx$ 4200 mm. The selected material for the tube was FEP to match the refractive index of water, since the refractive indices of FEP and water at ambient conditions are η_{FEP} = 1.34 and η_{water} = 1.33, respectively (Zadrazil et al., 2014). The acrylic flanges were attached to the FEP tube as demonstrated in Figure 3-8. Each flange was an assembly of three acrylic pieces and two O-rings. The O-rings were compressed between the surfaces of the tube and flanges, and the degree of compression was sufficient to fix the flanges to the tube and to create a seal. It should be noted that the O-ring compressions did not deform the tube, which was avoided to not disrupt the gas-liquid flow.

The FEP pipe was enclosed in a series of three acrylic anti-distortion boxes (Barkston Plastics Engineering Ltd) and immersed in water as depicted in Figure 3-7(c). The internal dimensions of each acrylic box were ≈ 70 mm × 60 mm × 1320 mm ($L \times W \times H$), and the wall thickness was φ_{box} = 10 mm. As shown in Figure 3-9, additional acrylic pieces were required to: (a) assemble the test-section in a similar approach to the FEP pipe assembly; (b) position the FEP pipe within the centre of the boxes; and (c) fill and drain the boxes. The assembled test-section was set-up vertically on to a 50 × 50 aluminium frame ($L \times W \times H \approx$ 300 mm × 300 mm × 6500 mm), and the vertical orientation was checked with the use of a laser plumb-line.

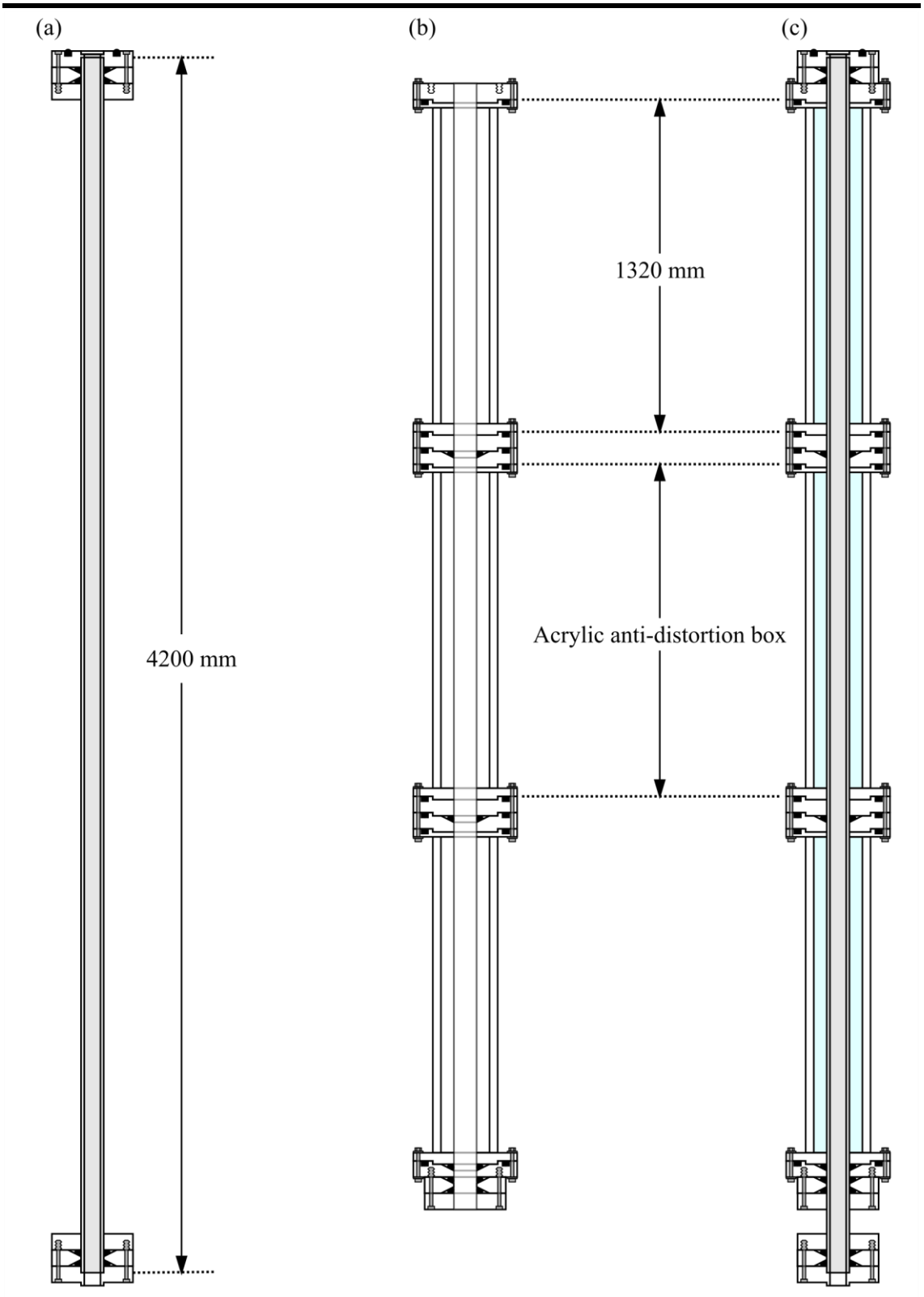


Figure 3-7 – Axial cross-section of the: (a) FEP pipe; (b) assembled acrylic anti-distortion boxes; and (c) assembled the test-section (TS).

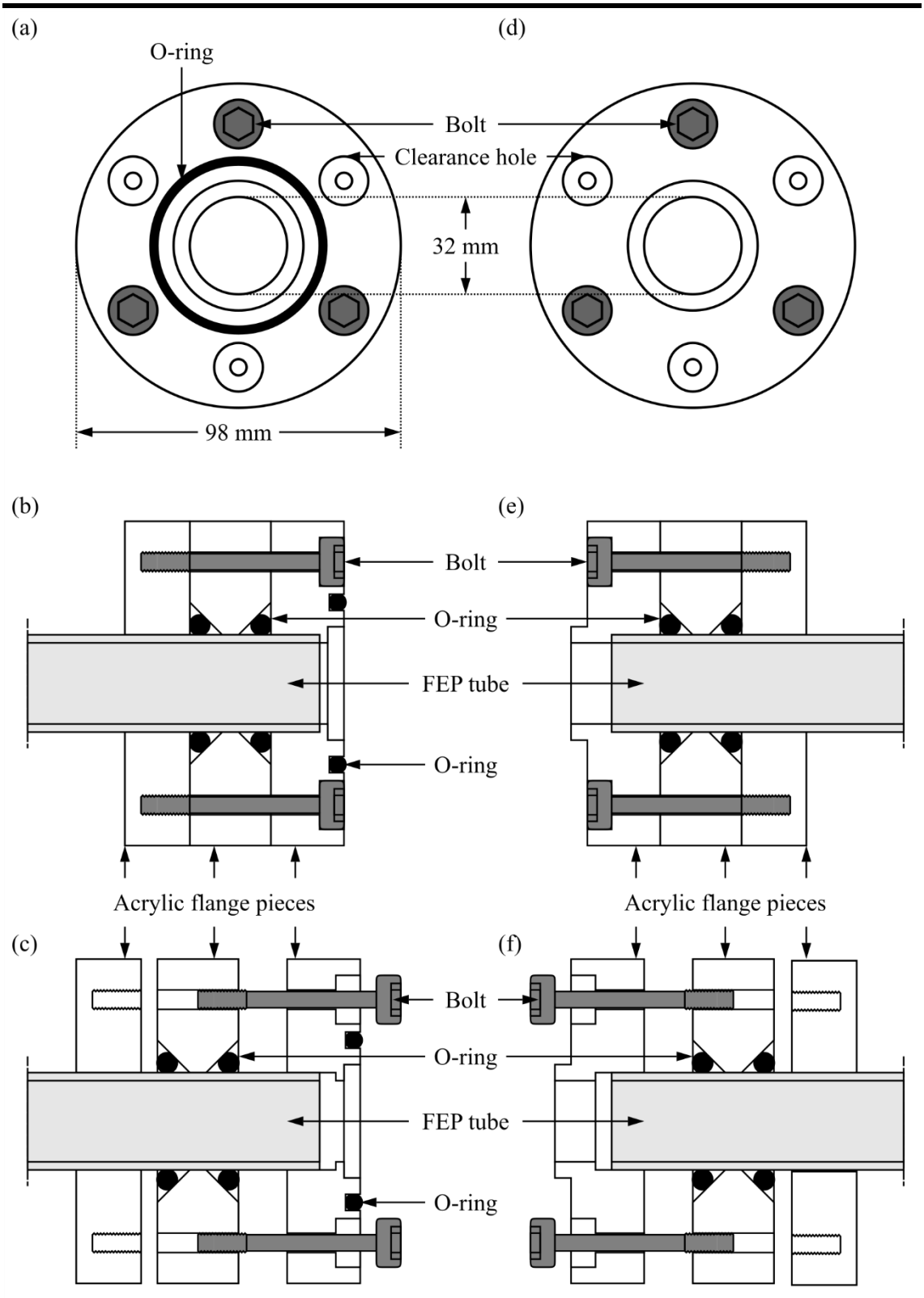


Figure 3-8 – Female-flange: (a) front-face view; (b) cross-sectional view; and (c) exploded view. Male-flange: (d) front-face view; (e) cross-sectional view; and (f) exploded view.

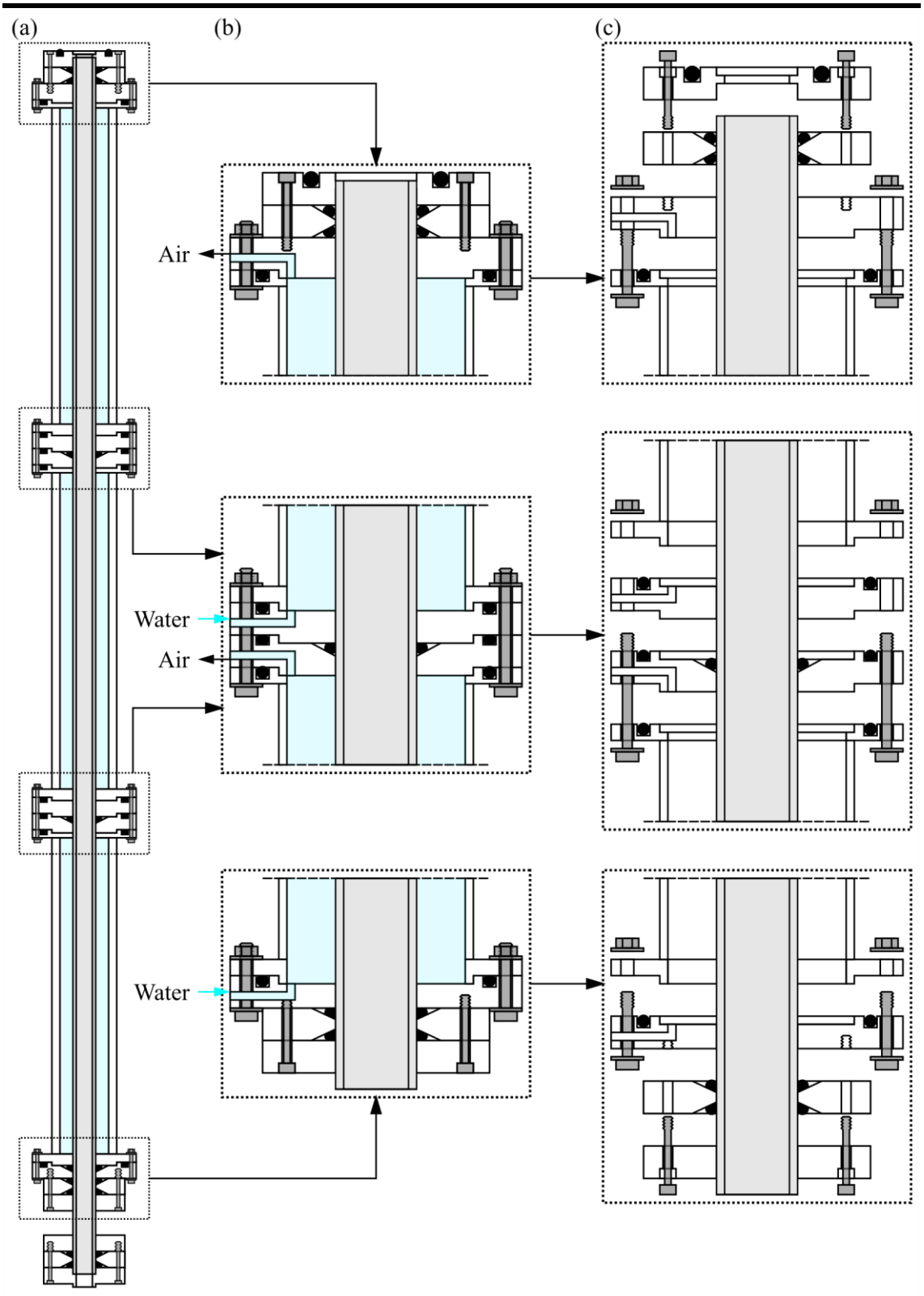


Figure 3-9 – DAFLOF test-section (TS): (a) assembly; (b) cross-sectional view of the connections; and (c) exploded view of the connections.

3.1.6. Linear actuator system (LA)

A linear actuator system (R-SMART, ROLLON Ltd) was added to the facility to physically move optical measurement systems along the entire length of the test-section in order to set the flow interrogation point either at a specific downstream distance from the test-section inlet to conduct static measurements, or in linear motion to use a moving frame-of-reference (MFoR) approach and perform dynamic measurements. A photograph of the linear actuator is provided in Figure 3-10(a). The dimensions of the actuator rail (LA-R) with an anodized and extruded aluminium structure and the actuator carriage (LA-C) with multiple recirculating ball bearing runner blocks were ≈ 6000 mm × 220 mm ($L \times W$) and ≈ 500 mm × 300 mm ($L \times W$), respectively. LA-R, which had a polyurethane steel re-enforced driving belt transmission, was coupled with a 1.5 kW motor (MAC1500, JVL Industri Elektronik A/S). A software (MacTalk) was provided by the supplier to digitally communicate with the motor (LA-M) in order to control LA-C: (i) acceleration; (ii) deceleration; (iii) position; and (iv) speed. The maximum LA-C motion properties were: (i) acceleration of a_{AC} = 50.0 m/s^2; (ii) velocity of u_{AC} = 4.0 m/s; and (iii) motion length of L_{AC} = 5000 mm (± 0.1 mm), which corresponds to the length between Positions P1 and P2 in Figure 3-1.

As shown in Figure 3-10, LA was attached to a 50 × 50 aluminium frame ($L \times W$ = 6000 mm × 300 mm) and then set-up vertically on to another 50 × 50 aluminium frame ($L \times W$ = 6500 mm × 300 mm) affixed to the laboratory wall. The bridge (or overhead) crane available in the laboratory was used for this procedure, and the vertical orientation of LA was evaluated with a laser plumb-line. The linear deviation between the test-section and the actuator system was estimated to be ± 1 mm. To install optical measurement systems on to LA-C, a small 30 × 30 aluminium profile frame was connected to LA-C as shown in Figure 3-11. A cable carrier was set along the linear actuator to guide and protect relevant cables, such as fibre optic (i.e. for the laser-sheet optics) and ethernet (i.e. for the collection optics) cables.



Figure 3-10 – Photographs of the linear actuator system (LA): (a) fixed to a 50 × 50 aluminium profile frame; and (b) set-up vertically to a 50 × 50 aluminium profile frame affixed to the wall.

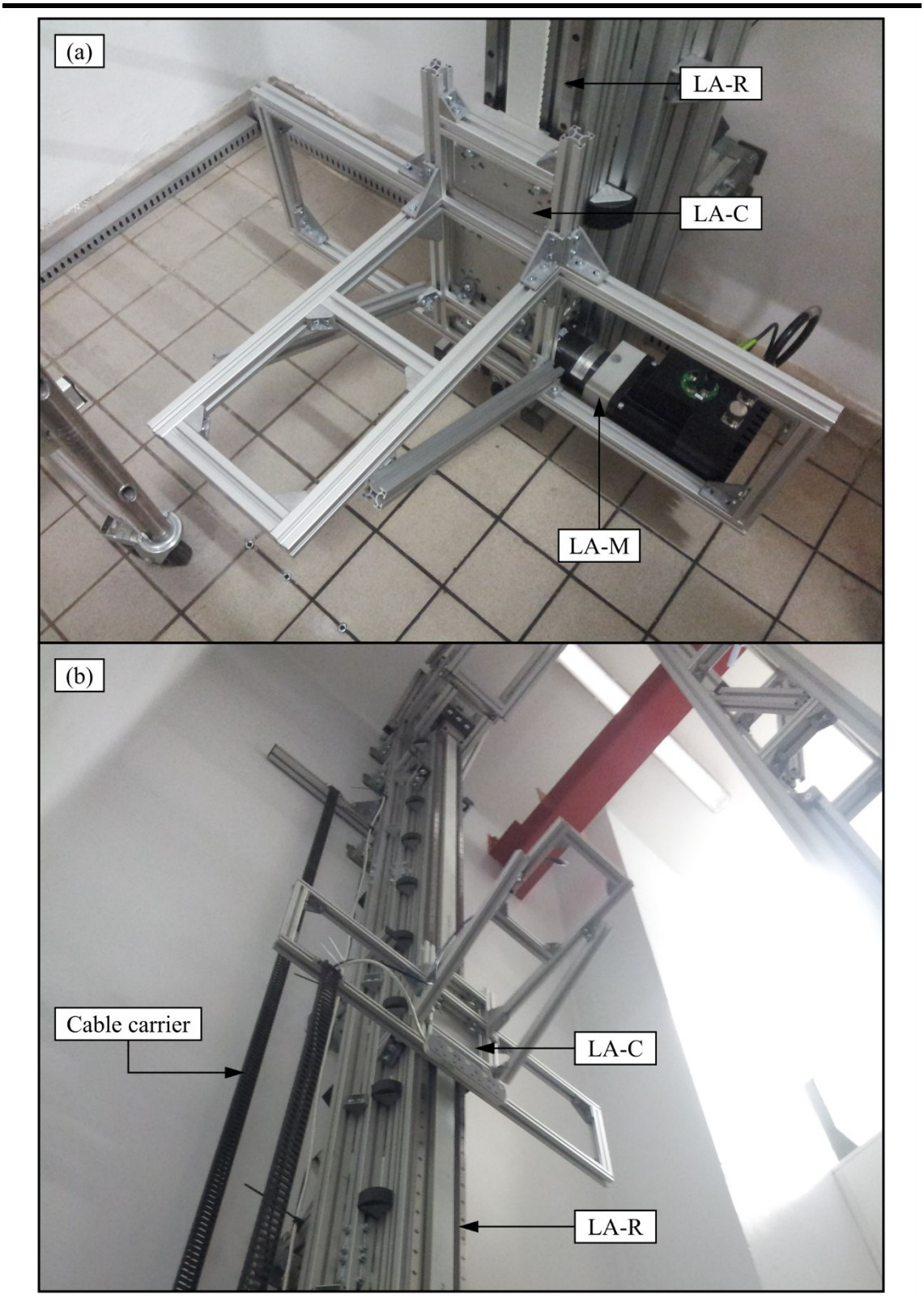


Figure 3-11 – Photographs of the 30 × 30 aluminium profile frame mounted on the carriage of the linear actuator system (LA-C): (a) at position P2, and (b) in motion.

3.2. Experimental methodologies

Spatial calibration procedures are necessary for optical measurement systems prior to any flow characteristic measurements. In Section 3.2.1, the calibration procedure implemented prior to each set of measurements in the current work is described. In addition, the optical system configurations of simultaneous planar laser-induced fluorescence (PLIF) and brightness-based laser-induced fluorescence (BBLIF), structured planar laser-induced fluorescence (S-PLIF), and moving frame-of-reference brightness-based laser-induced fluorescence (MFoR-BBLIF) are discussed in detail in Sections 3.2.2, 3.2.3, and 3.2.4, respectively.

3.2.1. Graticule correction technique

Prior to each set of experiments, a spatial calibration procedure, which can be referred to as the graticule correction technique (Charogiannis et al., 2015), was essential for the different optical systems to: (i) assist in the alignment of the laser-sheet along the axial plane of the test-section; (ii) recover the spatial resolution of the utilized cameras in the axial and radial directions of the flow; (iii) correct for optical or perspective distortions in the collected flow images; and (iv) ensure the field-of-view (FOV) was near-identical when a pair of cameras was employed (i.e. simultaneous PLIF and BBLIF, S-PLIF). For the procedure, a calibration-target or graticule with either a pattern of crosses or squares with known dimensions was attached to the segment section surface of a cylindrical-device in order to align the surface of a target along axis of the pipe. Examples of a target with either a cross or square pattern are shown in Figures 3-12(a) and 3-12(b), respectively. In addition, a photograph of the device and target used for the spatial calibration procedure is provided in Figure 3-12(a). The target surface dimensions were ≈ 70 mm × 32.4 mm ($L \times W$); while the dimensions of each black cross or square was 1 mm × 1 mm with

a pitch of 2 mm. A horizontal line within the target pattern was added to determine the relative locations of imaging windows when a pair of cameras was employed.

In the application of the graticule correction method as shown in Figure 3-12(d), the device was inserted into the test-section and positioned within the imaging window. The surface of the target was aligned with the excitation plane, and the pipe was flooded with the working liquid-phase (i.e. water). The test-section was flooded from the bottom and at a low liquid flow-rate to prevent gas bubble entrainment on the target surface. Finally, images of the calibration-target were collected with cameras and processed with the LaVision DaVis software to determine the spatial resolution, and later, correct for perspective distortions in the collected flow images. Examples of calibration-target images collected by the pair of cameras used in the simultaneous PLIF and BBLIF experiments are presented in Figure 3-13.

In the simultaneous PLIF and BBLIF experiments, the effect of the camera observation angle relative to the excitation plane on liquid-film thickness measurements with PLIF was investigated. The PLIF camera observation angles were set either at $\theta_P = 90\,^\circ$ (referred to as PLIF90) or $\theta_P = 70\,^\circ$ (referred to as PLIF70). The instantaneous images in Figures 3-13(a) and 3-13(b) were acquired by the PLIF90 and BBLIF cameras and the PLIF90 and BBLIF cameras, respectively. In each subfigure, the PLIF images are on the left and the BBLIF images are on the right. Furthermore, the inner wall of the FEP pipe is located on the left of each frame. The field-of-view (FOV) of the cameras did not overlap completely, however, the region of overlap covered a sufficiently large image domain. The transform used to relate the FOV of the two cameras was acquired by a linear approximation of the coordinates (units in pixels) of several squares in the target images. In the PLIF90 and BBLIF set-up, the length of overlap region was ≈ 34.3 mm; while the length was ≈ 31.5 mm in PLIF70 and BBLIF.

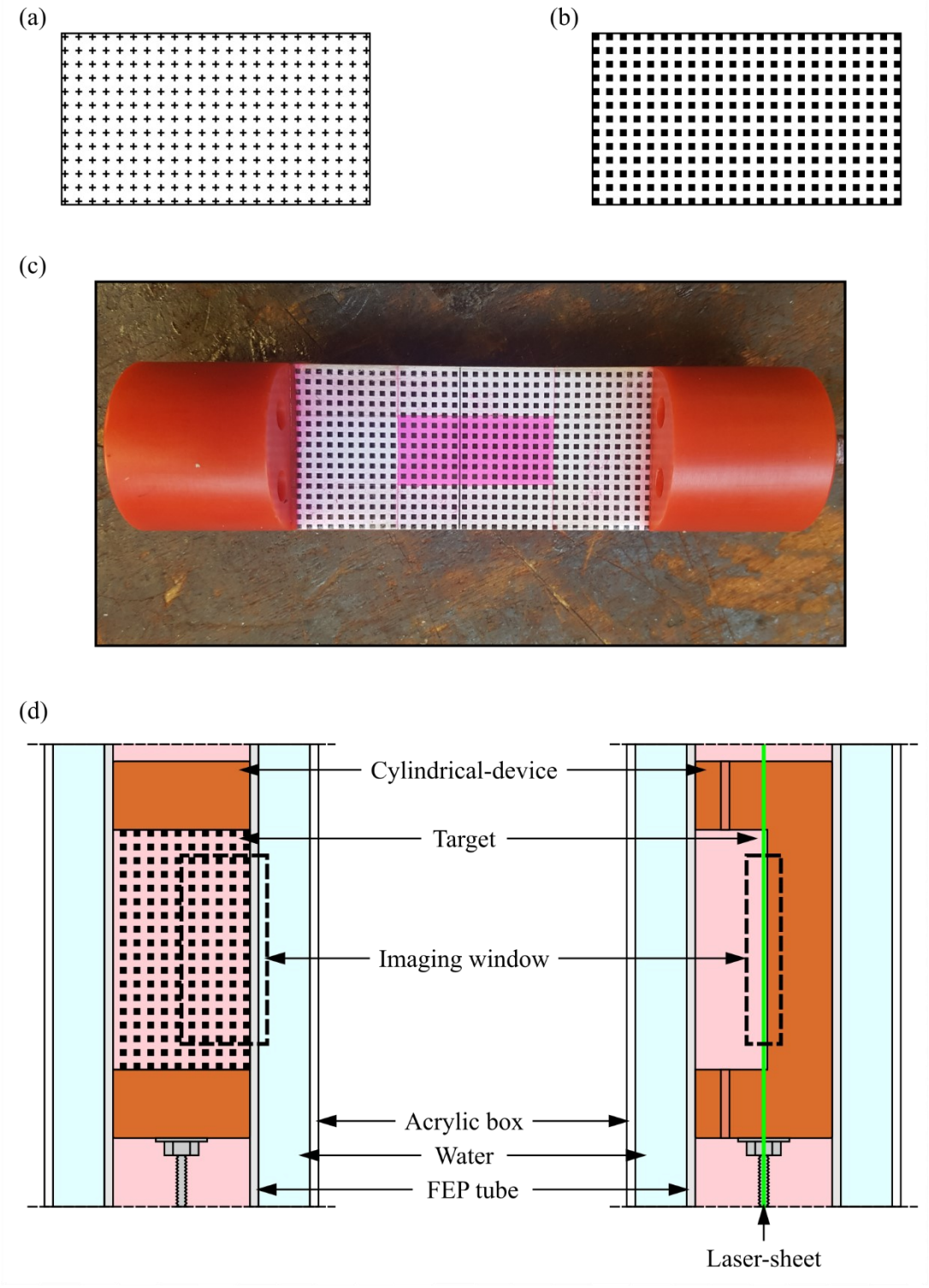


Figure 3-12 – Graticule correction technique: (a) target with a cross pattern; (b) target with a square pattern; (c) photograph of the calibration-target used for the calibration procedure prior to the simultaneous PLIF and BBLIF measurements; and (d) implementation of the method.

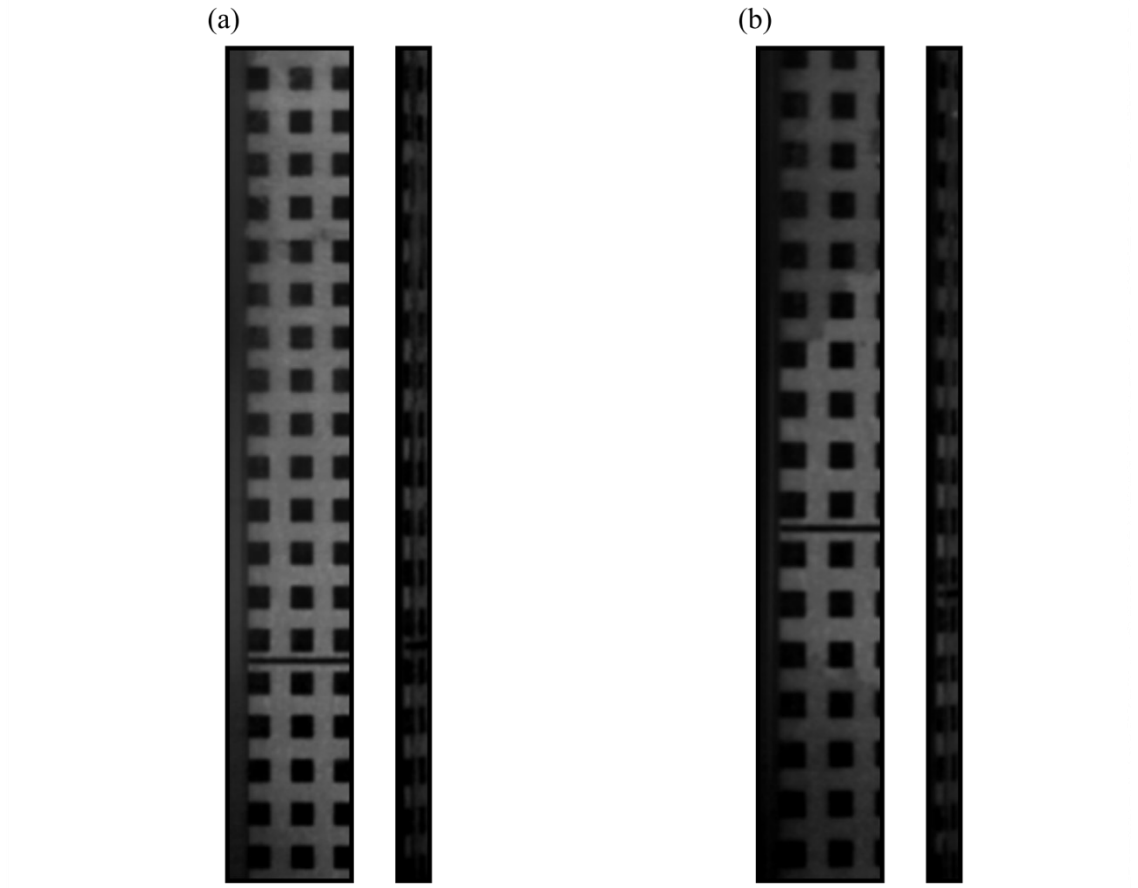


Figure 3-13 – In the application of the graticule correction technique prior to the simultaneous PLIF and BBLIF experiments, sample calibration-target images collected by the pair of cameras of : (a) PLIF90 (left) and BBLIF (right); and (b) PLIF70 (left) and BBLIF (right). The horizontal line within the square pattern was used to determine the relative positions of the field-of-view (FOV) of each camera. The position of the pipe wall is on the left-side of each frame.

3.2.2. Simultaneous PLIF & BBLIF

The experimental set-up of the simultaneous PLIF and BBLIF film-thickness measurements are illustrated in Figures 3-14 and 3-15. The water in DAFLOF was seeded with Rhodamine 6G dye at a concentration of $c_{dye} \approx 8.0$ mg/L. A two-dimensional (2-D) plane along the flow axis was excited with a laser-sheet ($\varphi_{laser} \approx 0.5$ mm), which was generated with a pulsed Nd:YAG laser (Nano-L-50-100PV, Litron Lasers Ltd, $\lambda_{laser} = 532$ nm, $E_{pulse} = 50$ mJ, $f_{pulse} = 100$ Hz, $t_{pulse} = 10$ ns) and dedicated laser-sheet optics. The laser was focused at the inner-wall of the FEP pipe, and the sheet optics were inclined at an angle of ≈ -15 ° along the vertical plane to limit the occurrence of reflections at the gas-liquid interface of the flow. A pair of 8-bit CMOS cameras (VC-Imager Pro HS 500, LaVision Ltd, 1024 × 1280 pixels) were used to collect the fluorescence emitted by the liquid-film in the region of interrogation (ROI). The flow interrogation position was $\approx 100\ L/D$ (i.e. ≈ 3.24 m) from the test-section inlet, and the field-of-view (FOV) of both cameras was near-identical. Each camera was equipped with a Sigma 105 mm f/2.8 macro lens and a 540 nm long-pass filter. The observation angle of the BBLIF camera was $\theta_{BB} \approx 15$ ° relative to the excitation plane to avoid the overlap of fluorescent signals from the ROI and other regions of the flow.

In order to investigate the effect of the PLIF camera observation angle on the liquid-film thickness measurements, one set of experiments was conducted with a PLIF camera observation angle of $\theta_P = 90$ °, which is referred to as PLIF90, and another set was conducted with an observation angle of $\theta_P = 70$ °, which is referred to as PLIF70. The alignment of the BBLIF camera and laser-sheet optics were not altered in both sets of experiments. The cameras and laser system were synchronized with the LaVision High-Speed Controller (HSC) and operated with the LaVision DaVis software. The frame-rate of each camera was $f_{camera} = 100$ Hz due to the specifications of the available cameras and laser system. While the camera frame-rate was not sufficient to conduct a comprehensive investigation of the spatiotemporal evolution of liquid-films in downwards annular flows, the primary objective of the simultaneous PLIF and BBLIF

experiments was to simultaneously collect instantaneous PLIF and BBLIF images of the film in the same ROI.

For each liquid-film thickness measurement of a given gas and liquid flow condition, 1000 images were collected by the pair of PLIF and BBLIF cameras, which corresponds to a flow interrogation time of $t = 10$ s. The overlap between the FOV of each camera was ≈ 90 %. Furthermore, the physical extent of the overlap region was ≈ 34.3 mm in the PLIF90 and BBLIF set-up, and ≈ 31.5 mm in the PLIF70 and BBLIF set-up. The spatial resolution of the PLIF90 camera was 30.6 μm/pixel in the axial and radial flow directions; while the spatial resolution of the PLIF70 camera was 26.6 μm/pixel and 28.0 μm/pixel in the axial and radial directions of the flow, respectively. The spatial resolution of the BBLIF camera was 26.7 μm/pixel.

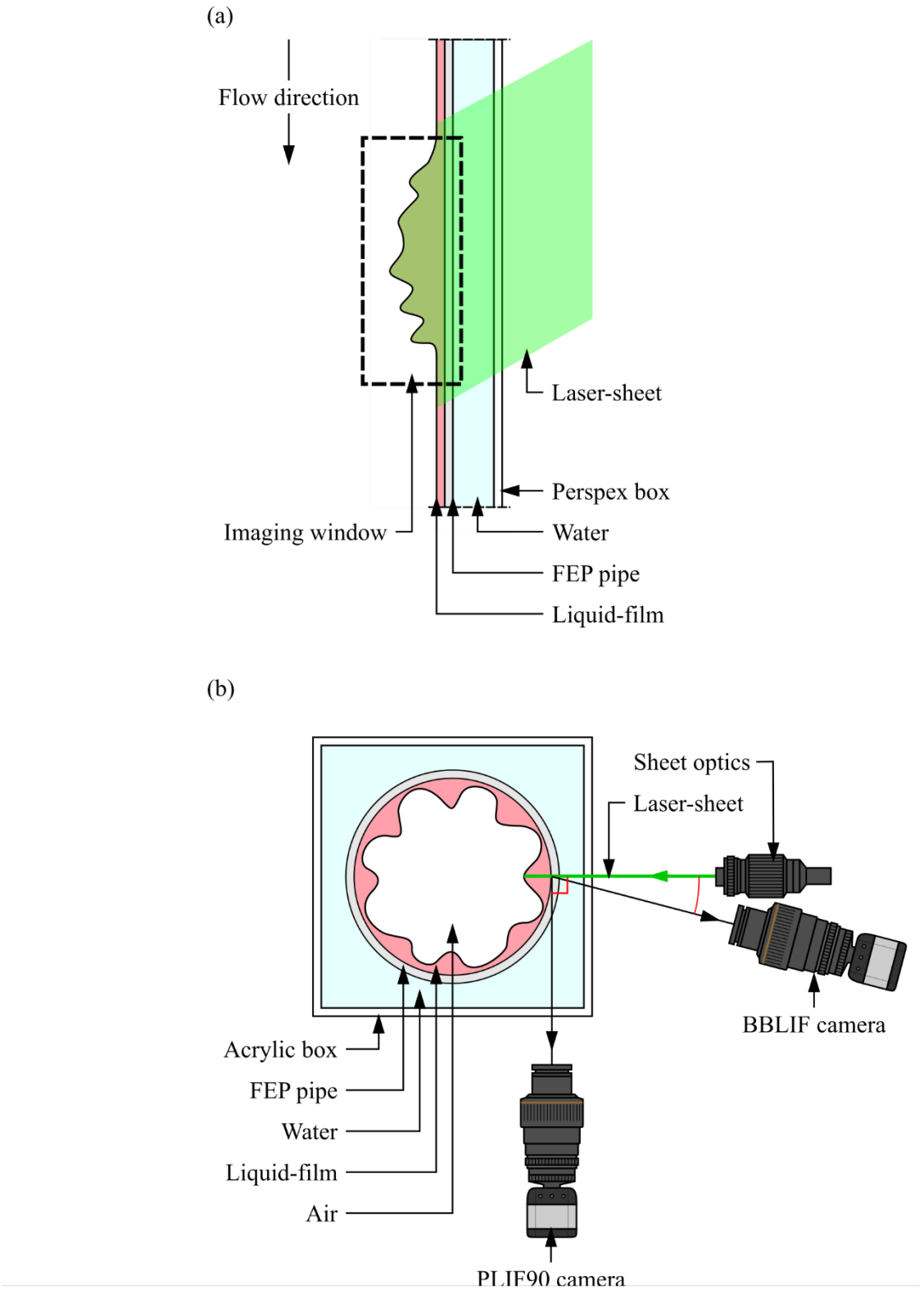


Figure 3-14 – Experimental set-up of simultaneous PLIF90 and BBLIF to measure the thickness of films in the same region of interrogation (ROI): (a) side-view; and (b) top-view.

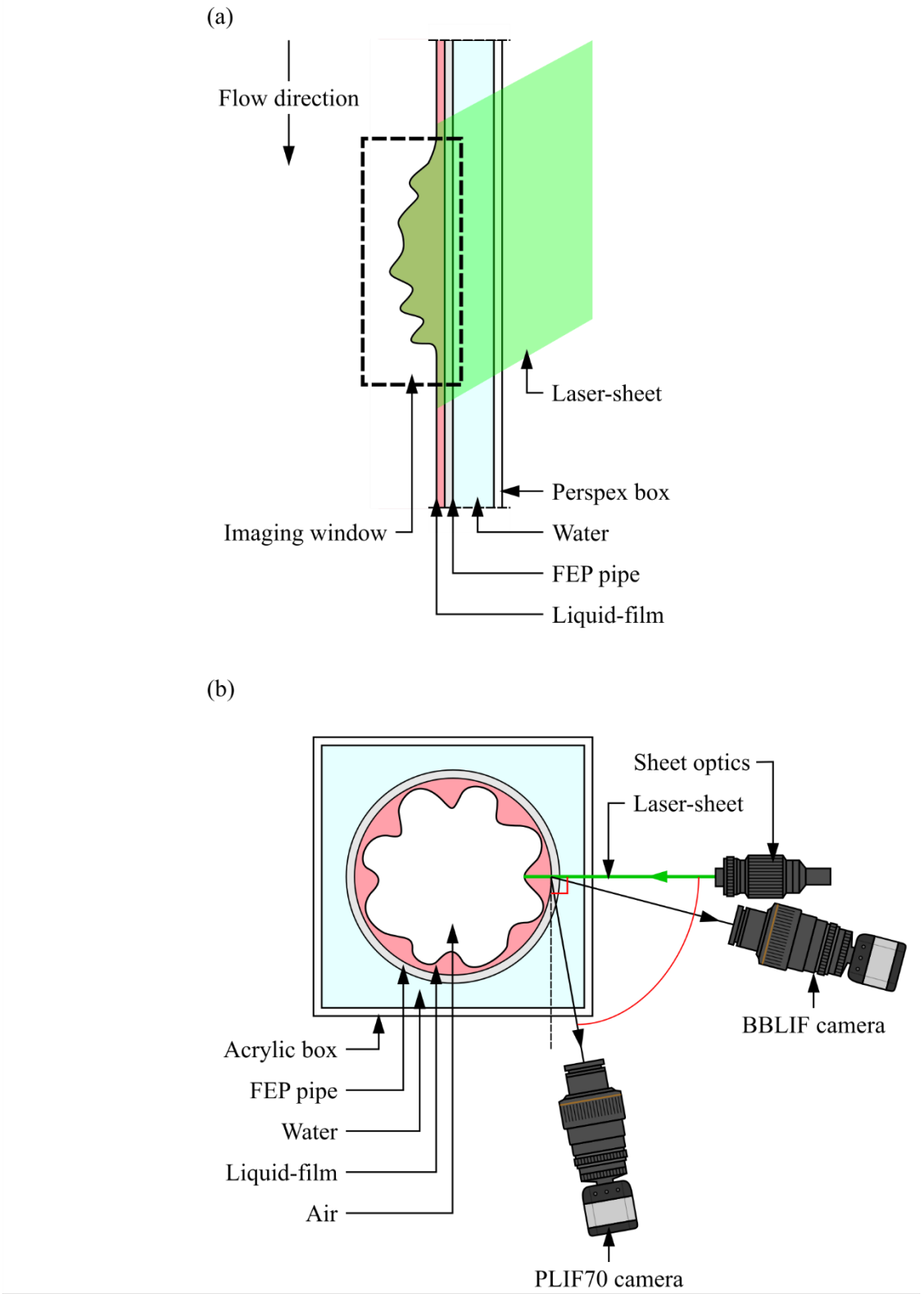


Figure 3-15 – Experimental set-up of simultaneous PLIF70 and BBLIF to measure the thickness of films in the same region of interrogation (ROI): (a) side-view; and (b) top-view.

3.2.3. S-PLIF

The experimental set-up of the S-PLIF film-thickness measurements is illustrated in Figure 3-16. The water in DAFLOF was seeded with Rhodamine 6G dye at a concentration of $c_{dye} \approx 4.0$ mg/L. A two-dimensional (2-D) plane along the flow axis was excited with a laser-sheet ($\varphi_{laser} \approx 0.5$ mm), which was generated with a pulsed Nd:YAG laser (Nano-L-50-100PV, Litron Lasers Ltd, λ_{laser} = 532 nm, f_{pulse} = 100 Hz, E_{pulse} = 50 mJ, t_{pulse} = 10 ns) and dedicated laser-sheet optics. To create the structured illumination, the sheet optics, and hence, the laser-sheet was aligned at a negative inclination angle of ≈ 30 ° along the vertical plane and directed through a Ronchi ruling plate with 5 line-pairs per mm, which was attached to the wall of the acrylic anti-distortion box.

In contrast with the work of van Eckeveld et al. (2018), the laser-sheet was negatively inclined to limit the occurrence of reflections of the intensity-modulated fluorescence at the gas-liquid interface of the flow and the shift in the observed pattern, which would occur at interfacial slope angles of ≈ 0 ° (i.e. flat liquid-film). In comparison with the optical arrangement used by van Eckeveld et al. (2018), a Ronchi ruling plate was employed in the current experiments to generate the modulation of the fluorescence emission, which allows the recovery of liquid-film thickness measurements with high spatial resolutions in the axial direction of the flow. A sparse grid was positioned in front of the laser-sheet in the set-up of van Eckeveld et al. (2018) to track the deflections (due to total internal reflection) of the cast shadows. This resulted in thin dark-lines that were separated by larger bright emission intervals, which significantly reduced the obtained spatial resolution (i.e. one measurement per mm). Nevertheless, the study demonstrated the advantages of using structured rather than uniform illumination for reliable identification of the gas-liquid interface in upward annular flow in smooth and corrugated pipes.

In the current set of experiments, the amplitude of the laser-light modulation (peak-to-peak value divided by the mean) was ≈ 20 %, which provided sufficient contrast to conduct S-PLIF

measurements, however, also allowed enough laser-light through the dark-regions, and hence, only partially obstructing visualisation in these regions. The degree of modulation was mainly limited by the use of a translucent material (i.e. FEP) for the pipe, which diffuses both the excitation-light and emitted fluorescent-light. The modulation amplitude can be tuned by varying the distance between the Ronchi plate and flow interrogation region due to the divergence of the laser-sheet.

In order to investigate the effect of the camera observation angle on the S-PLIF film-thickness measurements, a pair of 8-bit CMOS cameras (VC-Imager Pro HS 500, LaVision Ltd, 1024 × 1280 pixels) were used to collect the fluorescence emitted by the liquid-film in the same region of interrogation (ROI). The observation angle of one S-PLIF camera was $\theta_S = 90$ °, which is referred to as S-PLIF90, and the other camera observation angle was $\theta_S = 70$ °, which is referred to as S-PLIF70. The flow interrogation position was ≈ 125 L/D (i.e. ≈ 4.05 m) from the test-section inlet, and the field-of-view (FOV) of both cameras was identical. Each camera was equipped with a Sigma 105 mm f/2.8 macro lens and a 540 nm long-pass filter. A LaVision High-Speed Controller (HSC) was used to synchronize the cameras and laser system, which was operated with the LaVision DaVis software. The frame-rate of each camera was $f_{camera} = 100$ Hz due to the specifications of the available system. While the camera frame-rate was not sufficient to conduct a comprehensive investigation of the spatiotemporal evolution of the liquid-films in downwards annular flows, the primary objective of the current experiments was to simultaneously collect instantaneous S-PLIF70 and S-PLIF90 flow images in the same ROI. In each measurement of a given flow condition, 1000 images were collected by the pair of S-PLIF70 and S-PLIF90 cameras, which corresponds to a flow interrogation time of $t = 10$ s. The spatial resolution of the collection optics was ≈ 27.0 μm/pixel, and consequently, a line-pair occupied ≈ 8 pixels along the imaged domain.

In the current set of experiments, ‘reference’ images were also collected to locate the position

of the solid-liquid interface (i.e. pipe wall), and later, use in the image processing steps of the collected S-PLIF flow images to identify the position of the gas-liquid interface. The importance of these images for the SPLIF image processing routine is discussed further in Section 5.2 of Chapter 5 on page 176. To collect the reference images, the test-section was flooded with the dye-seeded working liquid (i.e. the water seeded with Rhodamine 6G dye) and excited with the structured illumination as depicted in Figure 3-17. A sequence of 100 reference images were collected with the pair of S-PLIF70 and S-PLIF90 cameras.

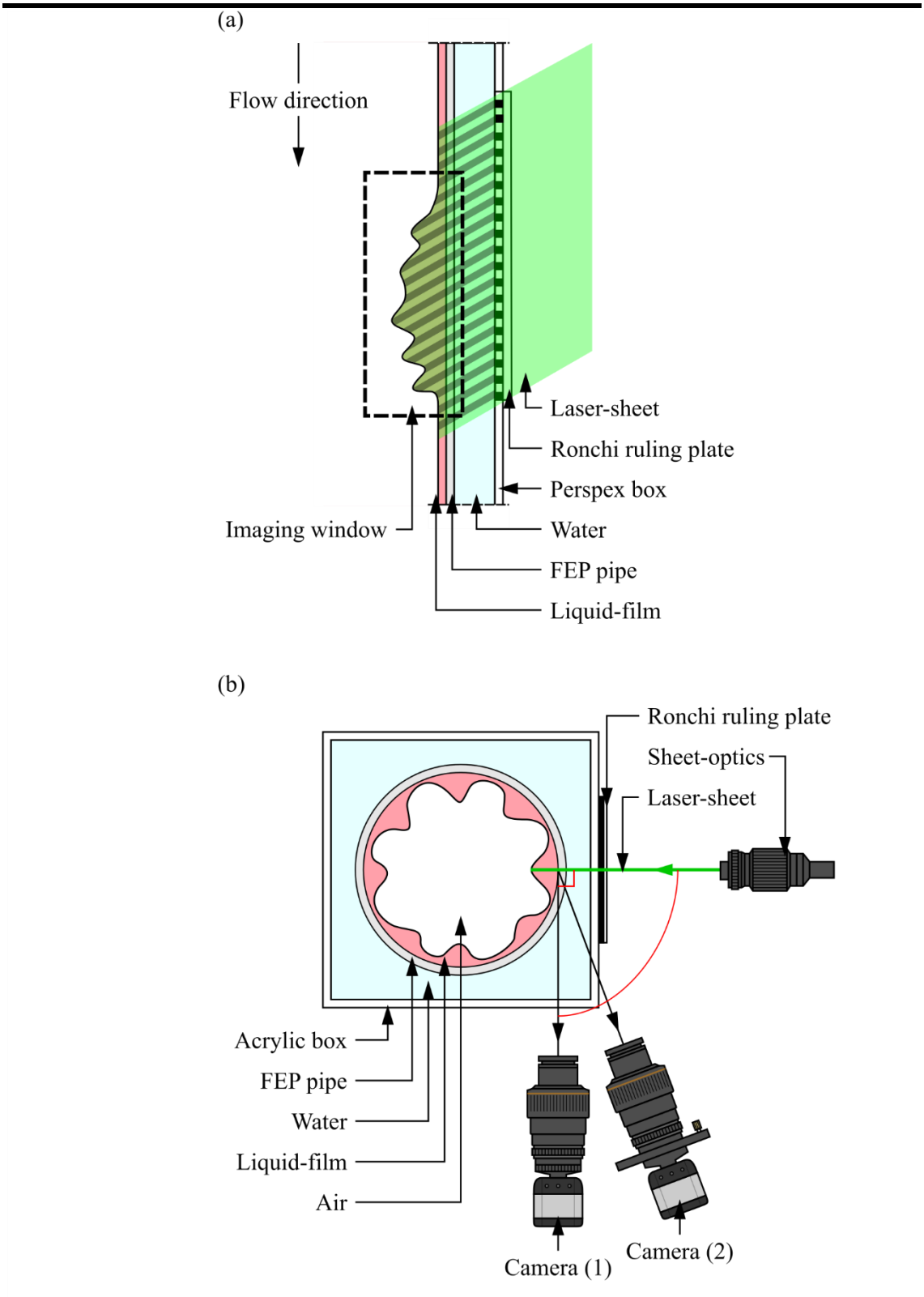


Figure 3-16 – Experimental set-up of S-PLIF70 and S-PLIF90 to measure the thickness of films in the same region of interrogation (ROI): (a) side-view; and (b) top-view.

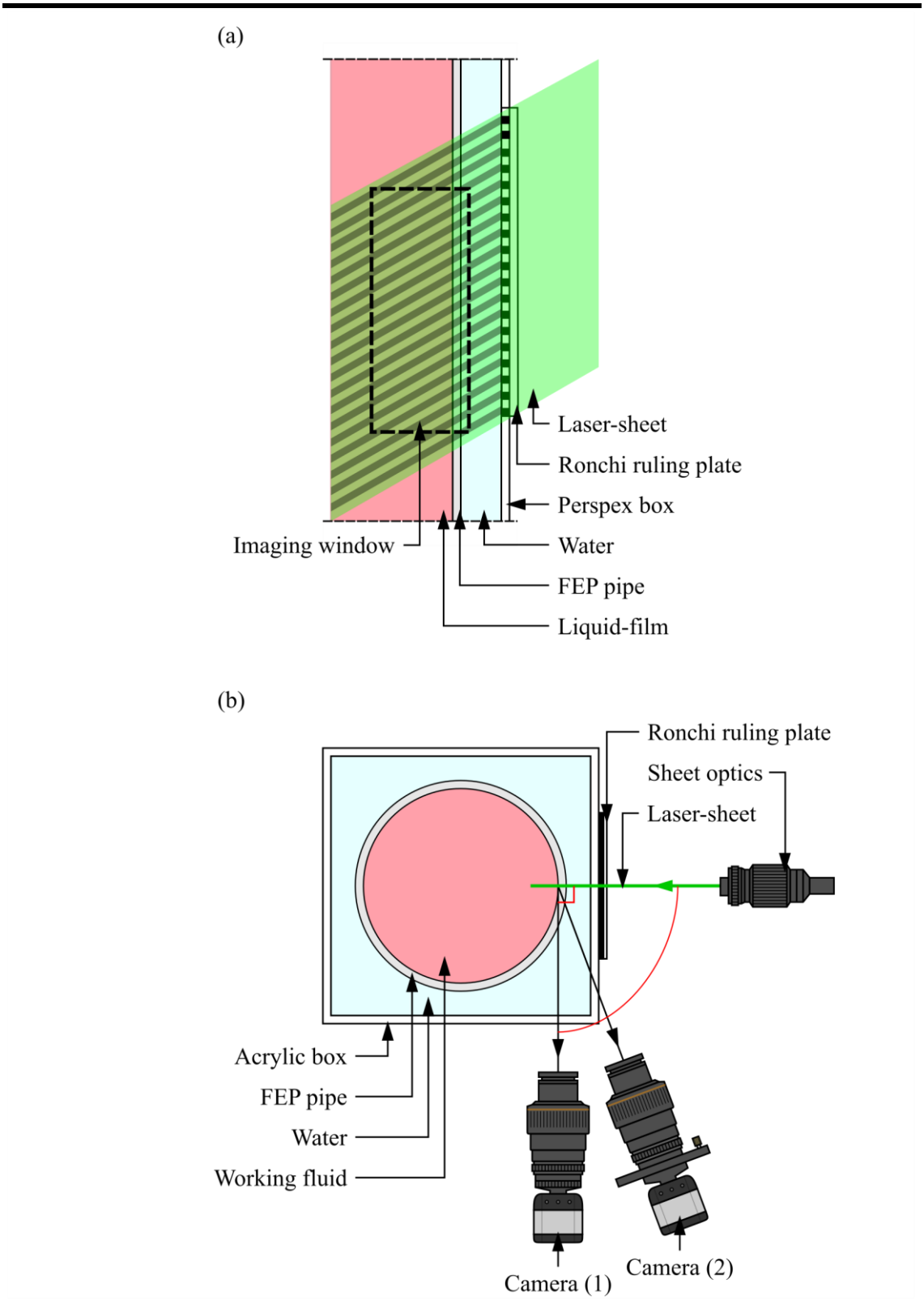


Figure 3-17 – Illustrations of the employed method to collect 'reference' images for S-PLIF: (a) side-view; and (b) top-view.

3.2.4. MFoR-BBLIF

The moving-frame-of-reference brightness-based laser-induced fluorescence (MFoR-BBLIF) method involves the use of a linear actuator system (ROLLON Ltd) to employ the BBLIF method in a moving-frame-of-reference (MFoR) approach. The details of the linear actuator system is provided in Section 3.1.6 of Chapter 3 on page 87. The relevant BBLIF optics were installed on the 30 × 30 aluminium profile frame mounted on the carriage of the linear actuator (LA-C) as illustrated in Figure 3-20. A two-dimensional (2-D) plane along the flow axis was excited with a laser-sheet ($\varphi_{laser} \approx 0.2$ mm), which was generated with a Cu-vapour laser system (LS20-10, Oxford Lasers Ltd, $\lambda_{laser} = 510.6$ nm, $E_{pulse} = 6$ mJ, $f_{pulse} = 10{,}000$ Hz, $t_{pulse} = 5 – 60$ ns) and a dedicated laser-sheet generator. The connection between the laser and sheet-generator was via a fibre-optic cable ($L_{fibre} = 20.0$ m). The emitted fluorescence was collected with a high-speed camera (i-SPEED 3, i-X Cameras), which was also operated at a frame-rate of $f_{camera} = 10{,}000$ Hz with the i-SPEED software suite. The camera was equipped with Nikon AF NIKKOR 50mm f/1.4D lens and a 540 nm long-pass optical filter. The BBLIF camera was positioned at an observation angle of $\theta_{BB} \approx 15$ ° relative to the excitation plane. The high-speed camera and linear actuator were not synchronized due to the lack of necessary electronic components.

Prior to the MFoR-BBLIF measurements, calibration exercises on the linear actuator system (LA) were performed to obtain velocity profiles of the carriage, and hence, the optical measurement system as a function of downstream distance (i.e. from Positions P1 to P2 in Figure 3-1 on page 70) and time. The experimental set-up of the calibration exercises are illustrated in Figure 3-18, which consisted of the following steps:

1) Markers with a spacing of 10 mm were placed along the left-edge of the entire test-section length, and the region of interrogation (ROI) was illuminated with a halogen lamp ($P_{lamp} = 1$ kW) installed on the 30 × 30 aluminium profile frame of LA-C.

2) For a set LA-M motor speed, instantaneous images of the markers were collected with the camera (f_{camera} = 2000 Hz) as the carriage and optical system physically traversed down the test-section (i.e. from Positions P1 to P2). The acceleration and deceleration of LA-C were kept constant at a_{AC} = 8.58 m/s^2 and d_{AC} = 8.06 m/s^2, respectively.

3) The collected images were analysed to extract the velocity profile of the optical system for a range of motor speeds. Plots of the LA-C carriage velocity (u_{AC}) as a function of downstream distance from the test-section inlet (s) and as a function of time (t) are provided in Figures 3-19(a) and 3-19(b), respectively.

The u_{AC} data was used in the processing routine of the MFoR-BBLIF images to obtain the wave velocities of individual disturbance waves (u_{DW}), which is discussed further in Section 6.2 of Chapter 6 on page 205. The MFoR-BBLIF measurements were performed once the preliminary exercises were completed. For each investigated gas and liquid flow condition, ≈ 10 experimental runs (ER) were necessary to ensure that a sufficient number of disturbance waves were observed in the ROI or imaging window of the MFoR-BBLIF camera. An experimental run of a MFoR-BBLIF measurement comprised of the following steps:

1) First, the water in DAFLOF was seeded with Rhodamine 6G dye (c_{dye} ≈ 4.0 mg/L), and a downwards co-current air-water annular flow with the desired flow conditions was established in the vertical test-section of DAFLOF.

2) The optical measurement system was slowly elevated from Positions P2 to P1 (Figure 3-1 on page 70). The acceleration, deceleration, and speed of LA-C were set at Position P2. While the acceleration and deceleration of LA-C was always set at a_{AC} = 8.58 m/s^2 and d_{AC} = 8.06 m/s^2, respectively, the set speed of LA-C was dependent on the investigated flow condition and based on the disturbance wave velocity data of Webb and Hewitt (1975).

3) Both the actuator and optical systems were triggered separately as the systems were not digitally connected due to the lack of necessary electronic components. Therefore, the optical system was initiated first and subsequently the linear actuator. Instantaneous raw MFoR-BBLIF images of the flow were collected as the measurements optics physically moved from Positions P1 to P2.

In each experimental run, ≈ 15,000 – 25,000 images were collected by the MFoR-BBLIF camera, which corresponds to a flow interrogation time of $t \approx 1.5 – 2.5$ s. Variations in the number of collected frames was due to the set velocity profile of LA-C, and hence, the optical system. The size of the imaging window was ≈ 129 mm × 32 mm, and the spatial resolution of the camera was ≈ 245 μm/pixel. Since the triggering of the MFoR-BBLIF measurements were random and the velocities of u_{AC} and u_{DW} were not matched completely, a large imaging window was implemented to increase the probability of observing disturbance waves in the moving ROI.

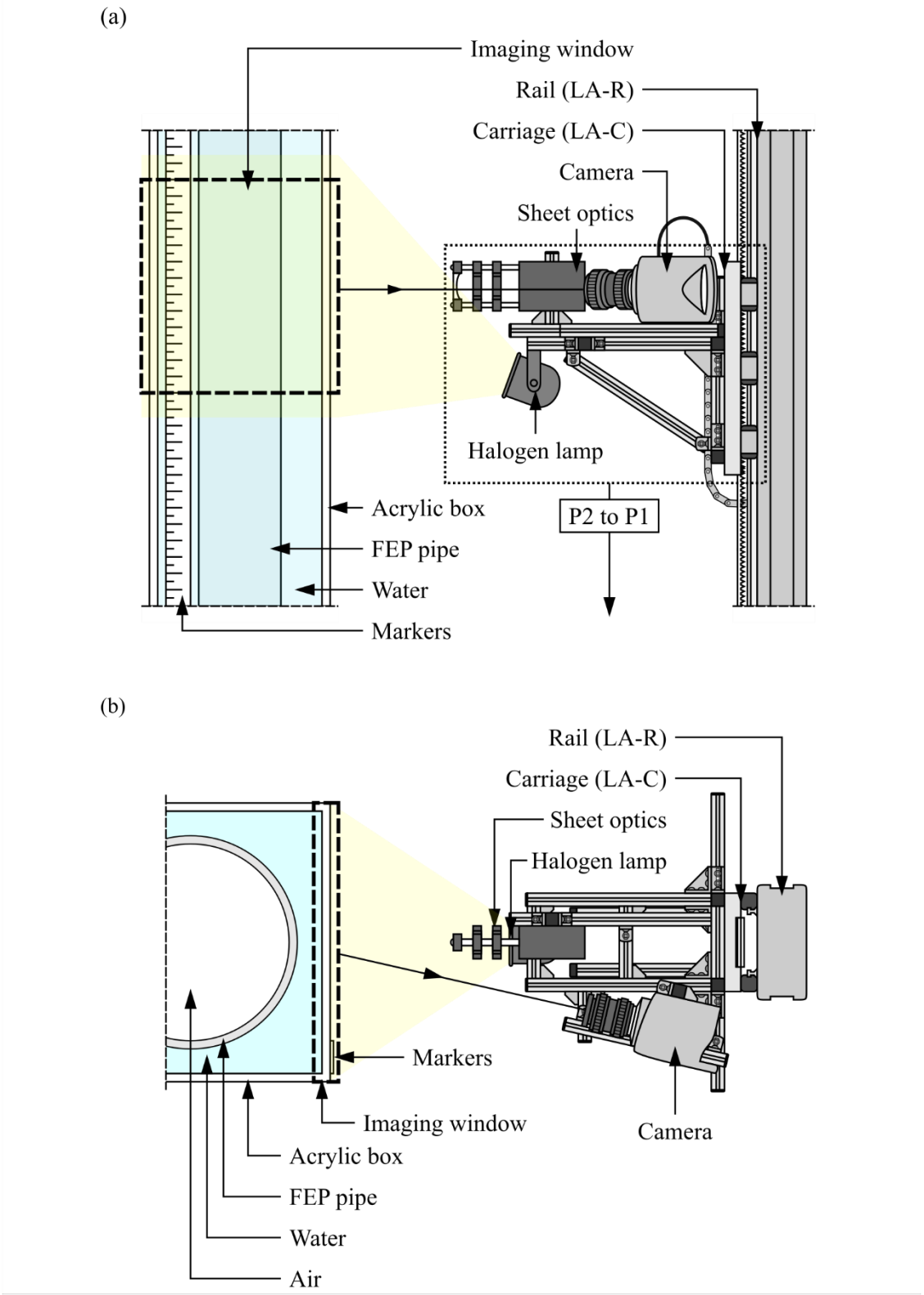


Figure 3-18 – Experimental set-up of the calibration exercises for MFoR-BBLIF to recover the velocity profiles of the optical measurement system: (a) side-view; and (b) top-view.

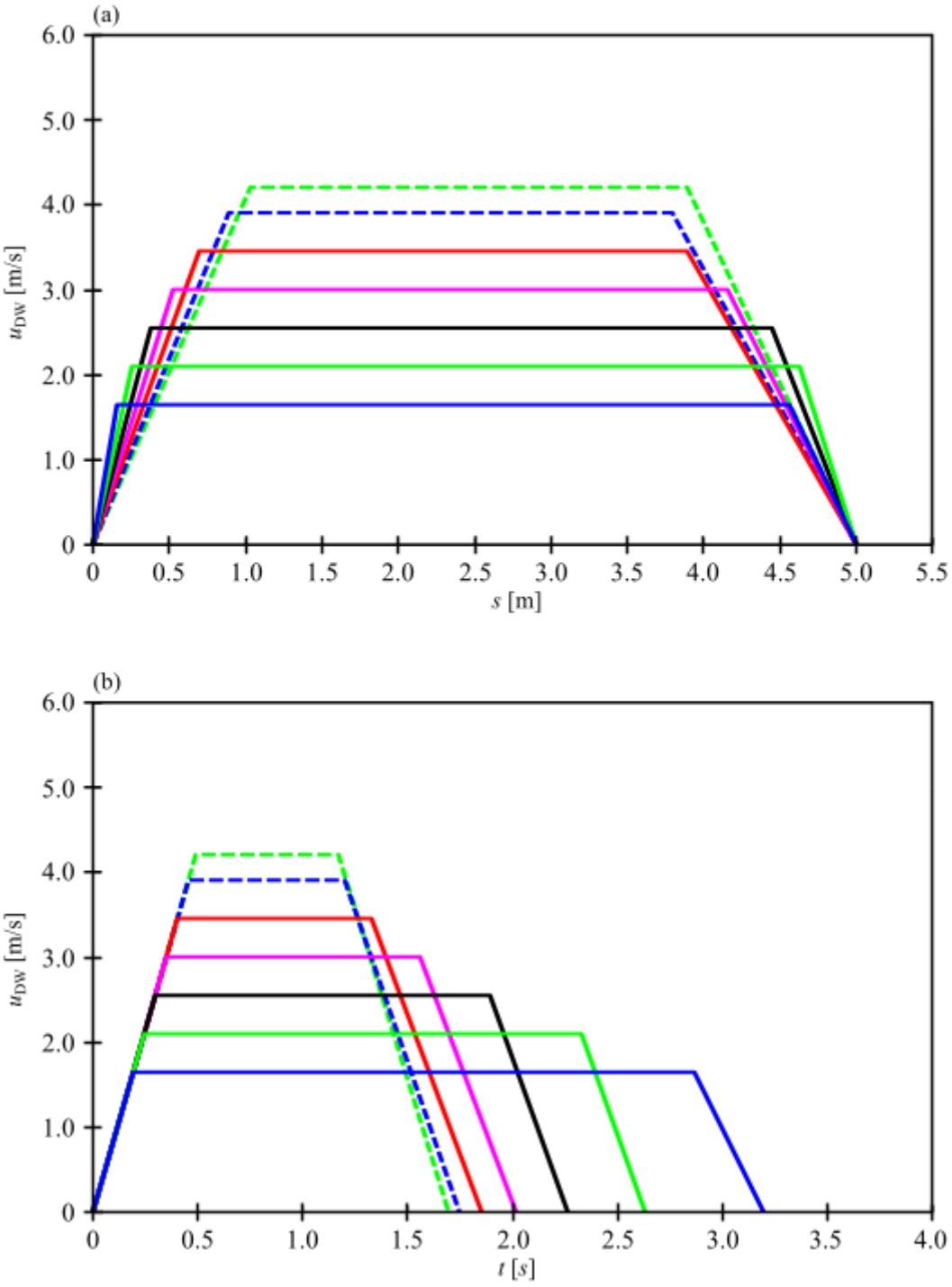


Figure 3-19 – The velocity profiles of the carriage of the linear actuator system, and hence, the optical system (u_{AC}) as a function of: (a) downstream distance from the test-section inlet (s); and (b) time (t). The acceleration and deceleration of the motor was set constant. The different colours and markers represent the different set motor speeds.

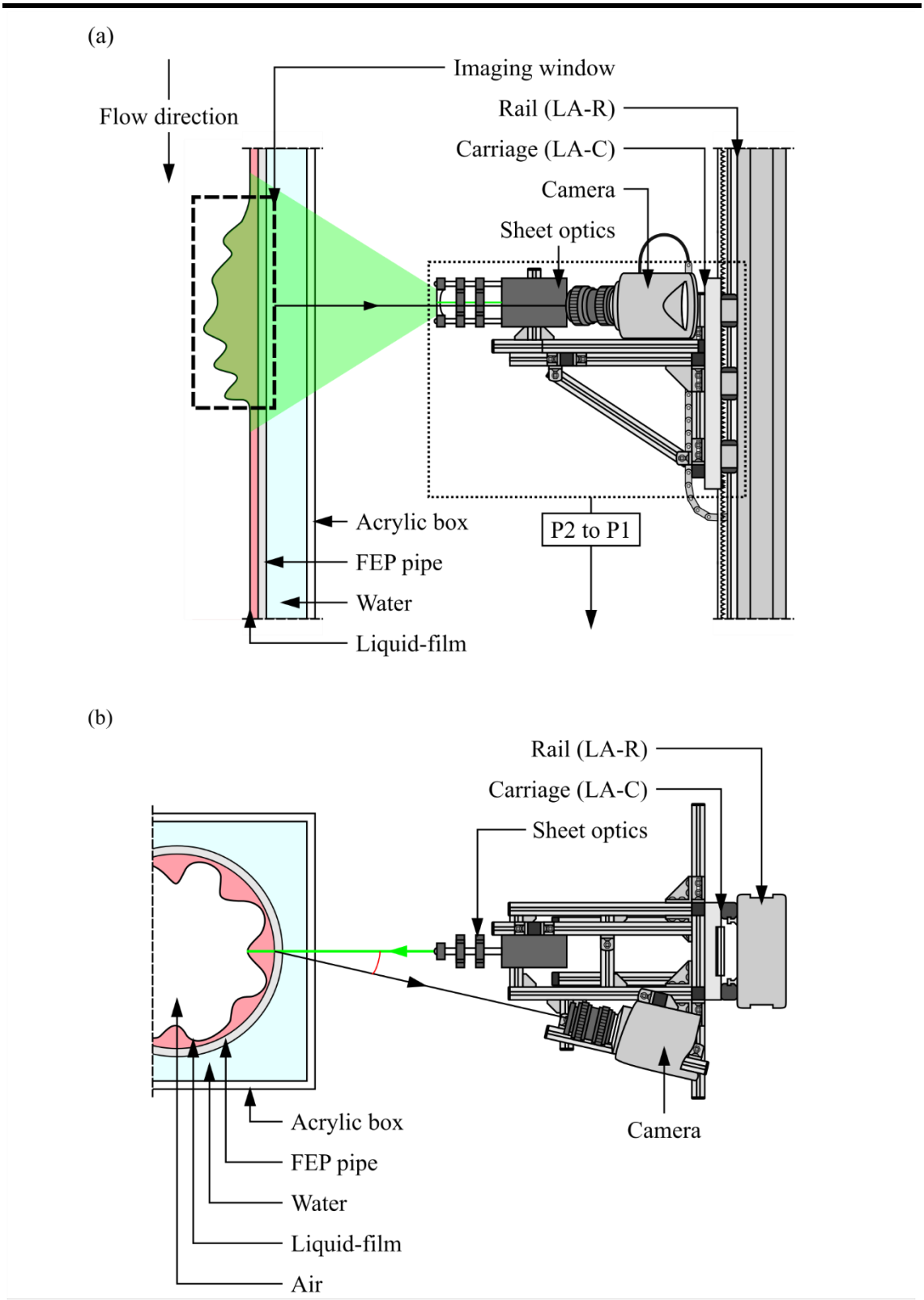


Figure 3-20 – Experimental set-up of MFoR-BBLIF to measure the individual disturbance wave velocities (u_{DW}) as a function downstream distance (s): (a) side-view, and (b) top-view

CHAPTER

4. Simultaneous PLIF & BBLIF

In this Chapter, results are provided for the set of liquid-film thickness (δ) measurements on downwards air-water annular flows (Re_G = 0 – 85,000, Re_L = 140 – 1330) with the simultaneous application of PLIF and BBLIF at the same region of interrogation (ROI). PLIF and BBLIF were directly compared to better understand the limitations with each approach. The experimental work in this Chapter was in collaboration with Dr Andrey V. Cherdantsev from the Kutateladze Institute of Thermophysics (Novosibirsk, Russia), who gratefully shared his expertise in the BBLIF approach. The film-thickness measurements, data processing and analysis were performed jointly with Dr Cherdantsev in order to successfully achieve the objectives of the current set of experiments.

4.1. Introduction and problem statement

In gas-liquid annular flow studies, planar laser-induced fluorescence (PLIF) and brightness-based laser-induced fluorescence (BBLIF) are two non-intrusive optical methods based on the principles of laser-induced fluorescence (LIF) that are extensively used to measure the liquid-film thickness (δ). In standard applications of both PLIF and BBLIF, the liquid-phase is seeded with a soluble fluorescent dye, and an axial plane of the flow is excited/illuminated with a laser-sheet. The selection of the fluorescent dye is mainly dependent on the excitation and fluorescence emission spectra. The spectra must be distinct to be able to distinguish between the two wavelengths. The fluorescence emission is collected with a camera equipped with an optical filter to only collect light in the spectral range of the fluorescence emission. PLIF and BBLIF mainly differ in the camera alignment due to the use of different approaches in fluorescence collection, and hence, raw data treatment.

In standard PLIF, the common observation angle of the camera relative to the excitation plane is $\theta_P = 90$ ° to directly image the axial liquid-film cross-section in the x (longitudinal) and y (radial) directions. Therefore, the near-wall and far-wall boundaries of the fluorescence domain in the PLIF images ($I_P(x, y, t)$) represent the solid-liquid and gas-liquid interfaces of the film. The images are processed to determine the interface positions and determine the film-thickness. A spatial calibration procedure for the camera is performed prior to the measurements in order to: (i) correct for perspective distortions in the collected images; and (ii) recover the spatial resolution in the axial and radial directions of the flow. In standard BBLIF, the camera alignment is near-adjacent to the laser-sheet optics to minimise the angle between the excitation and imaging planes, since BBLIF uses a line-of-sight approach for the fluorescence emission collection. Therefore, the typical observation angle of the BBLIF camera is $\theta_{BB} \approx 10 - 15$ °. In the BBLIF images ($I_{BB}(x, z, t)$), the fluorescence intensity signals or 'brightness' in the x and z directions of the film are collected, and converted to liquid-film thickness according to the Beer-Lambert law

(Alekseenko et al., 2014). BBLIF requires calibration procedures due to the: (i) unknown specific fluorescent dye concentration; (ii) non-uniform laser energy distribution; and (iii) spatially non-uniform camera sensor response.

A number of challenges are associated with the application of both PLIF and BBLIF for film-thickness measurements due to errors caused by optical effects at the gas-liquid interface (i.e. film free-surface). Häber et al. (2015) performed a ray-tracing analysis of the emitted fluorescent-light in the PLIF approach, and reported that part of the fluorescent-light emitted along the film region in the y (i.e. radial) direction travels to the gas-liquid interface region between the excitation and imaging planes. Fluorescent-light with incidence angles greater than the critical angle undergo total internal reflection (TIR), which are detected by the PLIF camera and cause liquid-films to appear thicker in PLIF images of circumferentially smooth and uniform film regions. In this type of film surfaces, Häber et al. (2015) reported an overestimation of ≈ 30 % in film-thickness with PLIF. BBLIF is known to be sensitive to light reflections at the film free-surface as the reflections contribute to the fluorescence intensity signals collected by the BBLIF camera (Cherdantsev et al., 2019). Reflections rise with increasing interfacial curvature due to the consequent increase in the incidence angles at the gas-liquid increase. In BBLIF, the errors in the measurements increase progressively with increasing interfacial curvature, and hence, the incidence angle approaches the critical angle of TIR, which is $\theta_{TIR} \approx 48\,^{\circ}$ for an air-water interface (Lindon et al., 2010). Furthermore, errors become significant when the interfacial curvature causes the incidence angle to exceed the critical angle.

In order to better understand the optical effects, and hence, the limitations of both PLIF and BBLIF, the two methods were simultaneously implemented to measure the film-thickness in downwards annular flows at the same region of interrogation (ROI). Direct comparison of PLIF and BBLIF were made to evaluate their ability to obtain reliable liquid-film thickness data. Downwards annular flows were generated in DAFLOF, which is described in detail in Section

3.1 on page 68. The lists of the investigated gas and liquid flow conditions are provided in Tables 4-1 and 4-2, respectively. The experimental matrix was comprised of 66 data-points: 11 gas flow-rates and 6 liquid flow-rates.

The investigated gas volumetric flow-rate range was $Q_G = 0 – 1950$ L/min. This corresponds to gas superficial velocities of $j_G = 0 – 39.4$ m/s and gas Reynolds numbers of $Re_G = 0 – 85{,}100$. The superficial gas velocity was defined as $j_G = 4Q_L/\pi D_p^2$, which is approximately equivalent to the bulk gas-phase velocity in annular flows with thin liquid-films; while the gas Reynolds number was defined as $Re_G = 4Q_L/\pi D_p \upsilon_G$, where υ_G is the kinematic viscosity of air. The investigated range of the liquid volumetric flow-rates was $Q_L = 0.8 – 8.4$ L/min, which corresponds to liquid superficial velocities and liquid Reynolds numbers of $j_L = 0.02 – 0.17$ m/s and $Re_L = 140 – 1330$, respectively. The definition of the liquid superficial velocity was $j_L = 4 Q_L/\pi D_p^2$; while liquid Reynolds number was $Re_L = Q_L/\pi D_p \upsilon_L$, where υ_L is the kinematic viscosity of water. Slight variations were observed in liquid flow-rates at high gas flow-rates, which was in the order of ≈ 5 % of liquid flow-rates in falling-films. The temperature of the liquid-phase was $T_L \approx 18$ ° for the majority of the measurements, however, the temperature did approach a maximum of $T_L \approx 25 – 27$ ° due to the work done by the pump.

A photograph of the simultaneous application of PLIF and BBLIF to measure the thickness of liquid-films in downwards annular flows is given in Figure 4-1. The ROI position, and hence, the location of the PLIF and BBLIF optics was ≈ 100 L/D (i.e. ≈ 3.24 m) downstream of the test-section inlet. The description of the configuration of relevant optics is provided in Section 3.2.2 on page 94. The optics include a pair of cameras to collect images of the flow: one camera for PLIF and the other for BBLIF. The effect of the PLIF camera observation angle (θ_P) on the PLIF approach was investigated by performing two separate sets of simultaneous PLIF and BBLIF measurements in order to employ a different observation angle in each set. In the first set, the PLIF camera was set-up with the standard observation angle of $\theta_P = 90$ °, which is referred to as

PLIF90; and in the second set, the observation angle was $\theta_P = 70$ °, which is referred to as PLIF70. Based on the spatial calibration procedure described in Section 3.2.1 on page 90, the overlap between the field-of-views (FOV) of the PLIF and BBLIF cameras was ≈ 90 %. The physical extent of the overlap region was ≈ 34.3 mm and ≈ 31.5 mm with PLIF90 and PLIF70, respectively.

In Section 4.2, an in-depth explanation is provided for the BBLIF image processing routine applied to recover the film-thickness in the BBLIF images from the fluorescence intensity signals. For the PLIF images, the method used to obtain the solid-liquid interface position and the PLIF image processing routine applied to identify the gas-liquid interface position are explained in Section 4.3. Direct comparisons of the PLIF and BBLIF derived liquid-film thickness profiles in non-uniform and uniform film regions and the liquid-film thickness statistics (i.e. first and second moments, probability densities) obtained with PLIF and BBLIF are presented in Sections 4.4 and 4.5, respectively. Finally, a summary of the experiments with simultaneous PLIF and BBLIF is given in Section 4.6.

Table 4-1– List of the investigated gas flow conditions in the film-thickness measurements with simultaneous PLIF and BBLIF.

Gas volumetric flow-rate	**Gas superficial velocity**	**Gas Reynolds number**
Q_G	j_G	Re_G
L/min	**m/s**	**–**
0	0.0	0
200	4.1	8700
400	8.1	17,500
600	12.1	26,200
800	16.2	34,900
1,000	20.2	43,700
1,200	24.3	52,400
1,400	28.3	61,100
1,600	32.4	69,900
1,800	36.4	78,600
1,950	39.4	85,100

Table 4-2 – List of the investigated liquid flow conditions in the film-thickness measurements with simultaneous PLIF and BBLIF.

Liquid volumetric flow-rate	**Liquid superficial velocity**	**Liquid Reynolds number**
$\boldsymbol{Q}_{\mathrm{L}}$	$\boldsymbol{j}_{\mathrm{L}}$	$\boldsymbol{Re}_{\mathrm{L}}$
L/min	**m/s**	**–**
0.8	0.02	140
1.7	0.03	300
3.2	0.07	500
5.1	0.10	800
6.6	0.14	1040
8.4	0.17	1330

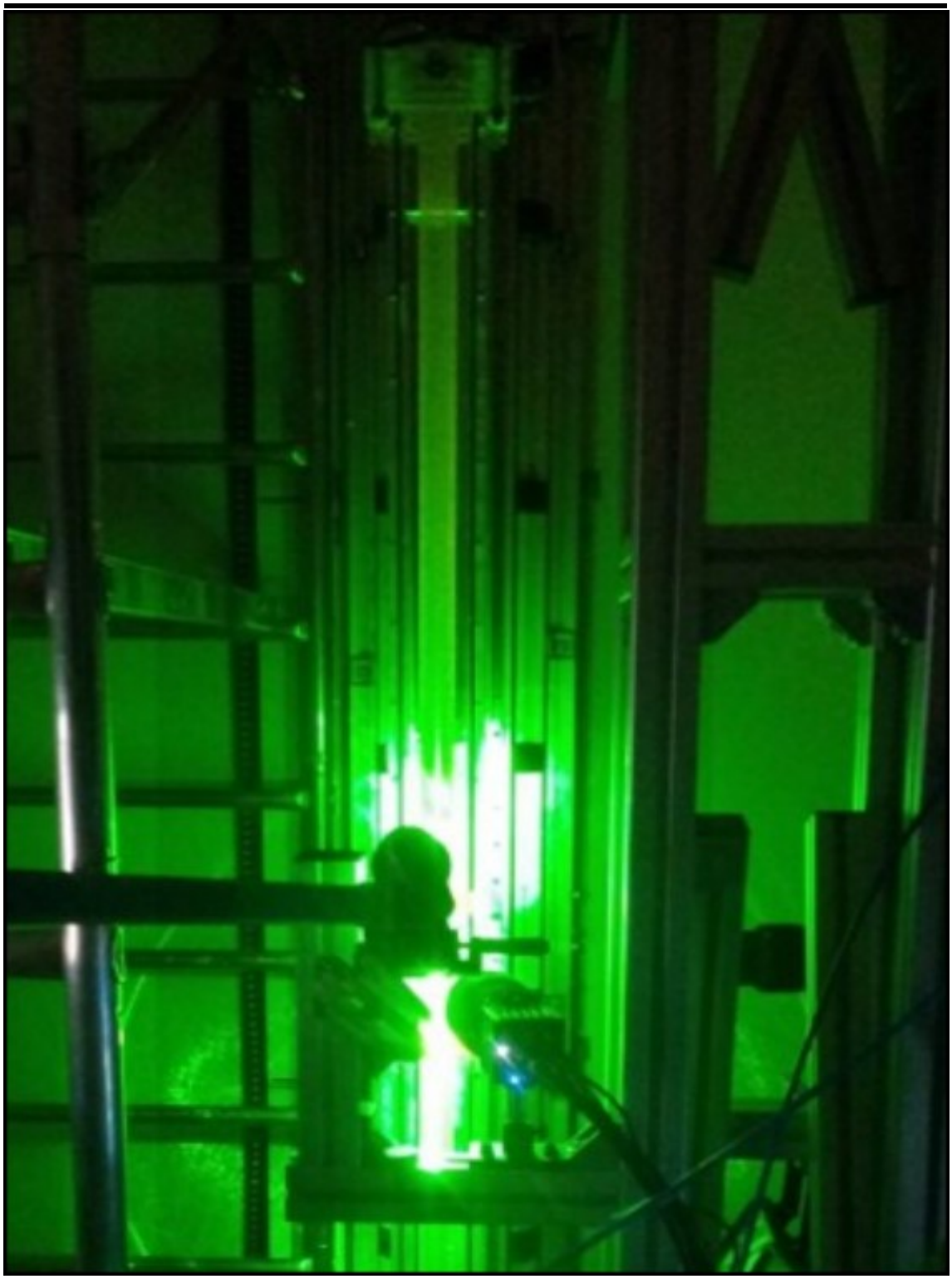


Figure 4-1 – Photograph of simultaneous PLIF and BBLIF to measure liquid-film thickness in downwards co-current air-water annular flows (Re_G = 0 – 85,100 and Re_L = 140 – 1330) generated in the vertical test-section of DAFLOF.

4.2. BBLIF image processing

In the BBLIF images ($I_{BB}(x, z, t)$), the fluorescence signals represent the liquid-film region in the x (longitudinal) and z (transverse) directions. The conversion of fluorescence intensity signals to liquid-film thickness is based on the Beer-Lambert law, which describes the absorption of light (i.e. laser-light) through a medium with uniform distributions of light absorbing material (i.e. fluorescent dye). The BBLIF image processing routine was custom built with the MATLAB software, and involves two major steps. The first step of the BBLIF image processing is to identify the central-line of the illuminated film region and to form a spatiotemporal (x-t) matrix of the raw fluorescence intensity signals from the entire set of collected images for a given flow condition. In the second step, each value of the instantaneous and local intensity is converted into film-thickness value by using the Beer-Lambert law, and in the procedure described by Alekseenko et al. (2014), leads to the equation:

$$J(x) = C(x)\left(1 - e^{-\alpha_{\mathrm{dye}}\delta(x)}\right)\left(1 + K\mathrm{e}^{-\alpha_{\mathrm{dye}}\delta(x)}\right) + D(x) \qquad \text{Equation 4-1}$$

where x, $J(x)$, $C(x)$, α_{dye}, K, $\delta(x)$, and $D(x)$ are position in the flow direction, fluorescence intensity signal registered in a single camera pixel, compensation matrix, selected fluorescent dye absorption coefficient, reflection coefficient at the air-water interface, local film-thickness at x, dark-current of the camera. Instead of using the intensity at a single pixel at the central-line, an average intensity over a number of pixels in the y direction can be implemented to improve the signal-to-noise ratio. However, this would lead to a loss of resolution in the x direction, and the choice depends on the application of the approach and the desirable outcomes from the measurements.

In BBLIF, a fraction of the excitation or laser-light is reflected at the gas-liquid interface (i.e. film free-surface), and the laser-light is reflected back towards the pipe wall, which re-excites the liquid-film. Therefore, primary and secondary fluorescence emissions are collected by the BBLIF camera, which is taken into account in Equation 4-1 by assuming the original and reflected

laser-light rays are collinear and completely overlap. This is not the case in reality, and hence, off-axis reflections will cause a different volume of the film to be excited. If the secondary laser-light does not cross the original optical path, underestimation of the local film-thickness of ≈ 2 % can occur, which is considered negligible. However, a more significant overestimation of the local thickness may occur due to the local re-excitation of the film by off-axis reflections. The overestimation is dependent on the interfacial slope steepness, which is discussed in Section 4.4.4 on page 138.

The reflection coefficient at the air-water interface (K) in Equation 4-1 was set to a constant value of $K = 0.02$; while the absorption coefficient of the fluorescent dye (α_{dye}) is dependent on the dye concentration (c_{dye}), and hence, the value is typically obtained through a set of calibration exercises (Alekseenko et al., 2014). The emitted fluorescence intensity signals were measured from the dye-seeded water in two cuvettes with known thicknesses. The obtained signal intensity values were inserted into Equation 4-1 with the path lengths to yield a system of two equations, which was subsequently transformed into a single equation of α_{dye} and solved numerically. In the current set of measurements, a Rhodamine 6G dye concentration of $c_{dye} = 8.0$ mg/L was used, which gave a dye absorption coefficient of $\alpha_{dye} \approx 0.25$ mm^{-1} with an estimated error of ≈ 10 %. The contribution of this error to the film-thickness measurements is illustrated in Figure 4-2(a). In Figure 4-2(a), a plot of the normalised fluorescence intensity signal ($J(\delta)/J(\delta_0)$) as a function of film-thickness (δ_{real}) for values of $\alpha_{dye} = 0.25$ mm^{-1} (solid black-line), $\alpha_{dye} = 0.25$ mm^{-1} ± 5 % (dashed-lines), and $\alpha_{dye} = 0.25$ mm^{-1} ± 10 % (solid-lines). When the intensity signals are calculated from Equation 4-1, the thickness deviation due to the uncertainty in the value of α_{dye} results increases as the films become thicker as demonstrated in Figure 4-2(b). For example, the thickness deviation was ≈ 6 % and ≈ 18 % for films with a thickness of $\delta = 3.0$ mm and $\delta = 6.0$ mm, respectively. Furthermore, the sensitivity of the measurement decreases at progressively thicker films which eventually leads to signal saturation. This is expected of any type of absorption method, and hence, an appropriate

selection of the measurement sensitivity and dynamic range is necessary during the set-up of the experiments.

The compensation matrix ($C(x)$) is used to (Alekseenko et al., 2014): (i) relate the measured signal intensity in the BBLIF image to the corresponding local liquid-film thickness; (ii) compensate for the non-uniform energy distribution along the laser-sheet; (iii) compensate for the spatially non-uniform response of the camera sensor. An in-situ reference signal, such as a time-averaged signal intensities ($\langle J_0(x) \rangle$), emitted from the dye-seeded water with a known thickness (δ_0) is required to obtain $C(x)$:

$$C(x) = \langle J_0(x) \rangle - D(x)/(1 - e^{-\alpha\delta_0})(1 + Ke^{-\alpha\delta_0}) \qquad \text{Equation 4-2}$$

In previous applications of BBLIF (e.g. Alekseenko et al., 2013; 2014), the reference signal was obtained in falling-film flows ($Re_G = 0$, $Re_L \approx 20 - 40$), since the δ_0 value is comparable to the Nusselt film-thickness (Nusselt, 1916) as the films are flat and smooth. This method was not applicable to the current measurements as the pipe wall material was fluorinated ethylene propylene (FEP), which is highly hydrophobic and dry-out regions were found in falling-films at $Re_L < 100$. Therefore, the average liquid-film thickness of a film at $Re_L = 140$ was used (i.e. $h_0 \approx 0.33$ mm), since the Nusselt formula was assumed to still provide a reasonable prediction of h_0 in this flow condition. Even though the temperature of the liquid-phase varied to a degree during the measurements, the fluorescence emission of Rhodamine 6G dye is only slightly sensitive to temperature variations, and hence, errors due to the use of a reference signal at a different temperature to the flow is negligible.

The dark-current of the camera ($D(x)$) must be corrected as $D(x)$ increases over time, and hence, camera dark-current measurements is recommended during the experiments. The overall systematic error due to the aforementioned dependencies of $J(x)$ (in the absence of optical distortions associated with interfacial curvature) is estimated at ≈ 5 %. Random errors are induced by multiple factors: (i) camera noise; (ii) pulse-to-pulse variation in the laser power; and (iii) long

term laser energy drift. The total random error of BBLIF in the current experiments was estimated at ≈ 10 %. One reason for this error is due to the low dynamic range of the employed camera which was 8-bit, which can be minimised by using a 12-bit camera (Alekseenko et al., 2014).

The maximum measurable liquid-film thickness with BBLIF is dependent on the geometrical configuration of the BBLIF camera observation angle (θ_{BB}) relative and the excitation plane. The illuminated liquid volume in the z direction can be approximated as a rectangle with a height equivalent to the instantaneous and local film-thickness (δ) and a width equivalent to the thickness of the laser-sheet (φ_{laser}). In the present measurements, laser-sheet thickness was $\varphi_{laser} \approx 0.5$ mm to improve the spatial resolution of the thickness measurements in the axial direction of the flow. For a BBLIF camera observation angle of $\theta_{BB} = 15$ °, which was used in the simultaneous PLIF and BBLIF measurements, the maximum measurable film-thickness is $\delta = \varphi_{laser}/\tan(15\ °) \approx 2.0$ mm. A further increase in the liquid-film thickness will not contribute to the collected fluorescence intensity signals and the signals will appear to saturate, which results in underestimations in the BBLIF derived thickness data. This type of error can be reduced by either increasing the thickness of the laser-sheet, which increases the spatial averaging in the z direction of the flow, or the use of the three-dimensional (3-D) configuration of BBLIF (Alekseenko et al., 2012; Cherdantsev et al., 2014). However, light reflections at complex 3-D interfaces and their aforementioned influences on the total fluorescence emission will become worse.

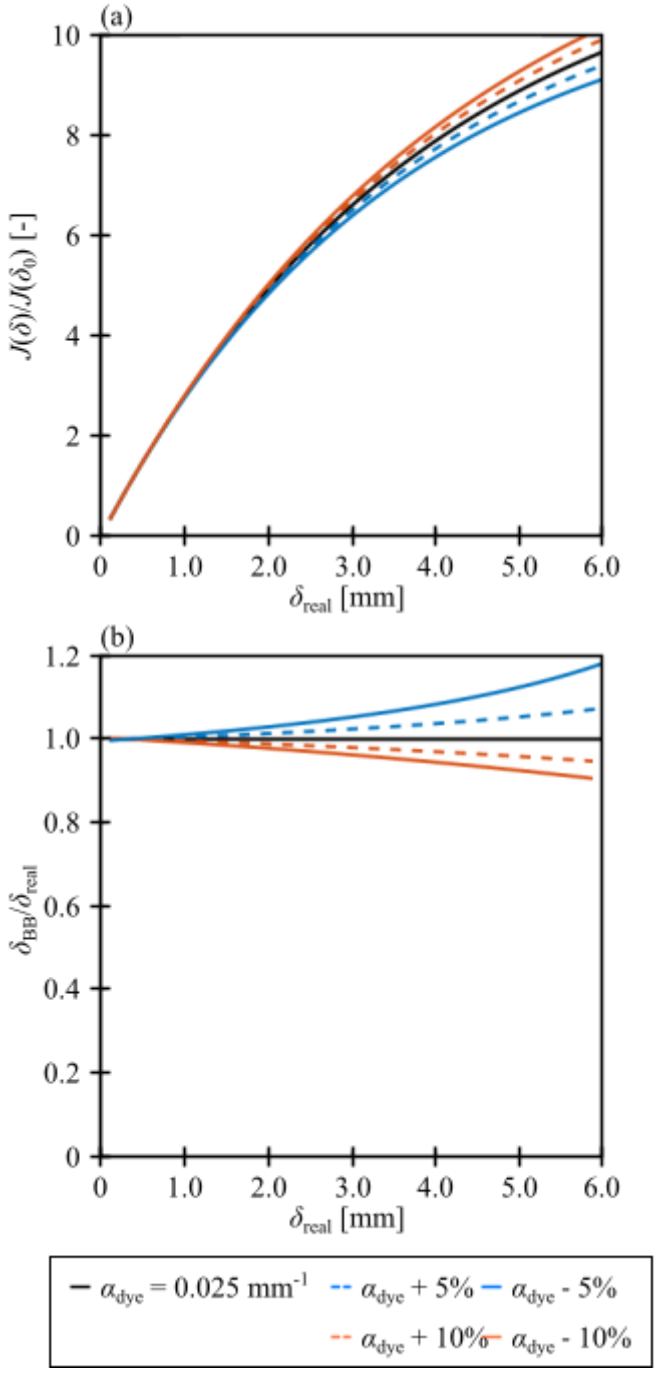


Figure 4-2 – For different values of the absorption coefficient (α_{dye}), a plot of: (a) the normalized fluorescence intensity signal ($J(\delta)/J(\delta_0)$) as a function of the real liquid-film thickness (δ_{real}); and (b) corresponding ratio of BBLIF and real film-thickness as a function of δ_{real}. The values of α_{dye} are $\alpha_{dye} = 0.25$ mm^{-1} (solid black-line), $\alpha_{dye} = 0.25$ mm^{-1} ± 5 % (dashed-lines) and $\alpha_{dye} = 0.25$ mm^{-1} ± 10 % (solid-lines). Positive and negative errors are in blue and red, respectively.

4.3. PLIF image processing

In the PLIF images ($I_P(x, y, t)$), the fluorescence domain represent the axial liquid-film cross-section in the x (longitudinal) and y (radial) directions. The edges of the fluorescence domain indicate the location of the gas-liquid and solid-liquid interfaces. A sample raw instantaneous PLIF70 image of a falling-film at $Re_L = 520$ is given in Figure 4-3(a). The extraction of liquid-film thickness profiles from the images is based on the ability to locate the position of the interfaces. The employed method to locate the solid-liquid interface is discussed in Section 4.3.1; while the image processing routine applied on the PLIF images to identify the gas-liquid interface is discussed in Section 4.3.2. The PLIF image processing algorithm was developed in-house with the MATLAB software, and the LaVision DaVis software was used to initially correct for perspective distortions in the raw PLIF images. The spatial resolution of the PLIF90 frames was 30.6 μm/pixel in both axial and radial directions; while the spatial resolution of the PLIF70 frames was 26.6 μm/pixel and 28.0 μm/pixel in the axial and radial directions, respectively.

4.3.1. Solid-liquid interface

In the PLIF images, the solid-liquid interface corresponds to the position of the inner pipe wall of the test-section. The position of this interface can be located by using either: (i) the images of calibration target, which were collected during the application of the graticule correction method; or (ii) the actual PLIF flow images, which were collected during the measurements. The graticule correction technique, which is described in Section 3.2.1 on page 90, was employed prior to the simultaneous BBLIF and PLIF measurements. In this method, a calibration-target was inserted into the test-section and the test-section was flooded with the liquid-phase (i.e. the water). The surface of the target was aligned with the excitation plane, and images of the target were collected

with the cameras.

The images were primarily employed to: (i) assist in the alignment of the cameras to the same region of interrogation (ROI); (ii) to ensure sufficient overlap between the field-of-views (FOV) of the PLIF and BBLIF cameras; and (iii) to obtain the spatial resolution of the collection optics in both the axial and radial directions of the flow. Nevertheless, the same images can be also used to locate the edge of the target, which is assumed to be the position of the solid-liquid interface. However, systematic errors in the location of the solid-liquid boundary can be induced in this approach due to the possible misalignment of the target and the excitation plane, or the edge of the target and the inner wall of the test-section. Therefore, in the application of simultaneous PLIF and PTV by Charogiannis et al. (2015) and Charogiannis et al. (2017) to investigate the hydrodynamic characteristics of falling liquid-films over an inclined plane, the fluorescence intensity profiles in the PLIF images of the flow were directly used to locate the solid-liquid interface.

In the current set of experiments, the solid-liquid interface was recovered with the images of the calibration target. The approach applied by Charogiannis et al. (2015) and Charogiannis et al. (2017) was not reliable as the acquired position of the solid-liquid boundary varied with the investigated range of flow conditions, despite the use of identical identification criterions. Incorrect identification of the solid-liquid interface can lead to systematic errors in the measurements of liquid-film thickness; and the errors increase with thinner films. In the current optical configuration, an offset of 1 – 2 pixels corresponds to 25 – 50 μm, or a local relative error of ≈ 0 – 10 % in a liquid-film with a thickness of 500 μm. This type of systematic error can be overcome by zooming into the liquid-film and increasing the spatial resolution of the images, however, this reduces the ROI in the direction of the flow.

4.3.2. Gas-liquid interface

In previous applications of PLIF, the image processing algorithms applied on the PLIF images to locate the position of the gas-liquid interface (i.e. film free-surface) were based on either: (i) the fluorescence intensity threshold (Farias et al., 2012; Kokomoor & Schubring, 2014; Schubring et al., 2010; Zadrazil et al., 2014), or (ii) the local gradient of the fluorescence intensity profile (Charogiannis et al., 2015; 2017; Markides et al., 2016). One of the major challenges with the first method is the selection of an appropriate intensity threshold due to variations in the fluorescence intensity across the liquid-film over time, which can be caused by the: (i) excitation energy variation along the illumination plane due to the pulse-to-pulse variation in laser power and the possible long-term laser energy drift; (ii) thickness of the liquid-film (Schubring et al., 2010) due to the scatter of the laser-light at the optical section and the consequent enlarged liquid volume illumination in the azimuthal direction; and (iii) local fluorescence intensity affected by the presence of entrained gas bubbles or steep interfacial slopes. In order to address this issue, Zadrazil et al. (2014) manually identified the interface to adjust the intensity threshold along the excitation plane (i.e. x direction); while Schubring et al. (2010) and Farias et al. (2012) linearly 'stretched' the intensity distribution between the maximum and minimum levels at each x. Another challenge with the development of PLIF image processing algorithms is the presence of out-of-plane features due to the fluorescence emitted from film regions outside of the excitation plane. Smooth interface criteria (Schubring et al., 2010) and manual identification and removal of outliers (Kokomoor & Schubring, 2014) have been used to identify these out-of-plane features in the PLIF images and remove them from the recovered liquid-film thickness data.

In the current set of measurements, a combination of the fluorescence intensity threshold method and the local signal gradient method was implemented to identify the gas-liquid interface. In the present set of PLIF images, the following PLIF image processing algorithm was developed to identify the location of the gas-liquid interface:

1) An intensity threshold value ($J(x, y)$) was determined by the average of the maximum and minimum intensity at each x-coordinate in each PLIF image. The raw PLIF images were binarized with the set of intensity threshold values and morphologically closed to reduce the effect of random noise.

2) In each binarized image, the signs of the local intensity gradients ($J(y+1) - (y-1)$) were obtained at each x-coordinate, and border-lines were identified at y-coordinates with a sign-change in order to obtain a linear array of interface coordinates, $Y(x)$.

3) The lines were sorted according to the sum of the signs of the gradients along their length. The discarding process was initiated at this stage, which started with the longest lines with the most stable negative sign. When more than one y-coordinate was assigned to a given x-coordinate, the lowest y-coordinate (i.e. near-wall position) was selected as the position of the gas-liquid interface.

4) When a sub-range of x values belonging to a border-line of $Y(x)$ was already obtained in the previous steps, the next $y(x)$ was compared to the previous $y(x)$ that has been already assigned to the interface location, and the larger values were discarded. This process allowed us to eliminate most out-of-plane features.

5) If the entire range of x values belonging to a border-line was already written in $Y(x)$, the new line was discarded completely. This step removed any border-lines corresponding to the borders of entrained gas bubbles in the liquid-film. The processing routine was terminated when the sum of the signs of a line reached a positive value.

In the assessment and the validation of the PLIF image processing algorithm, raw PLIF images were superimposed with the identified gas-liquid boundaries. Examples are presented in Figures 4-3(c) and 4-3(d) for a flow at $Re_G = 0$ and $Re_L = 520$, and $Re_G = 43{,}700$ and $Re_L = 1330$, respectively. In the sample images, the red-lines mark the gas-liquid interface identified by

utilizing the described edge-detection technique and the green-lines mark the final $Y(x)$ values. For each investigated flow condition, a large number of images were visually inspected, which showed good agreement between the identified gas-liquid interfaces and the visible edges of the film fluorescence domain. In smooth liquid-films, for example in Figure 4-3(c), the processing algorithm was effective in the removal of liquid structures that resemble 'over-turning waves', which are non-physical aspects in this type of flow. In more agitated or rough films, for example in Figure 4-3(d), the processing routine neglects a significant number of out-of-plane features.

For liquid-film thicknesses in the range of $\delta \leq 150 - 200$ μm, a larger uncertainty was found in the PLIF90 images; since the fluorescence signal emitted from the film occupied smaller regions of the resulting images, and the fluorescence intensity across the image was reduced locally to similar levels as the background signals. This occurred rarely in the PLIF70 images, and mostly arose in the presence of entrained gas bubbles with sizes similar to the film-thickness. In contrast, the occurrence of this was more frequent in the PLIF90 images; even in films with absence of entrained gas bubbles. This lead to appearances of 'dry-out' regions, which were not observed in the PLI70 images. In order to address this issue in the PLIF90 image processing, the intensity threshold was adjusted in cases where the PLIF90/BBLIF film thickness ratio were low. If the maximum intensity fell below the adjusted threshold value, the corresponding PLIF90 data were not processed further, and the film thickness was set to $\delta = 150$ μm. In future applications of the PLIF technique, this issue can be overcome by using a higher: (i) dye concentration; (ii) laser excitation intensity; and/or (iii) laser-sheet thickness. Furthermore, zooming closer to the liquid-film and increasing the spatial resolution are additional considerations.

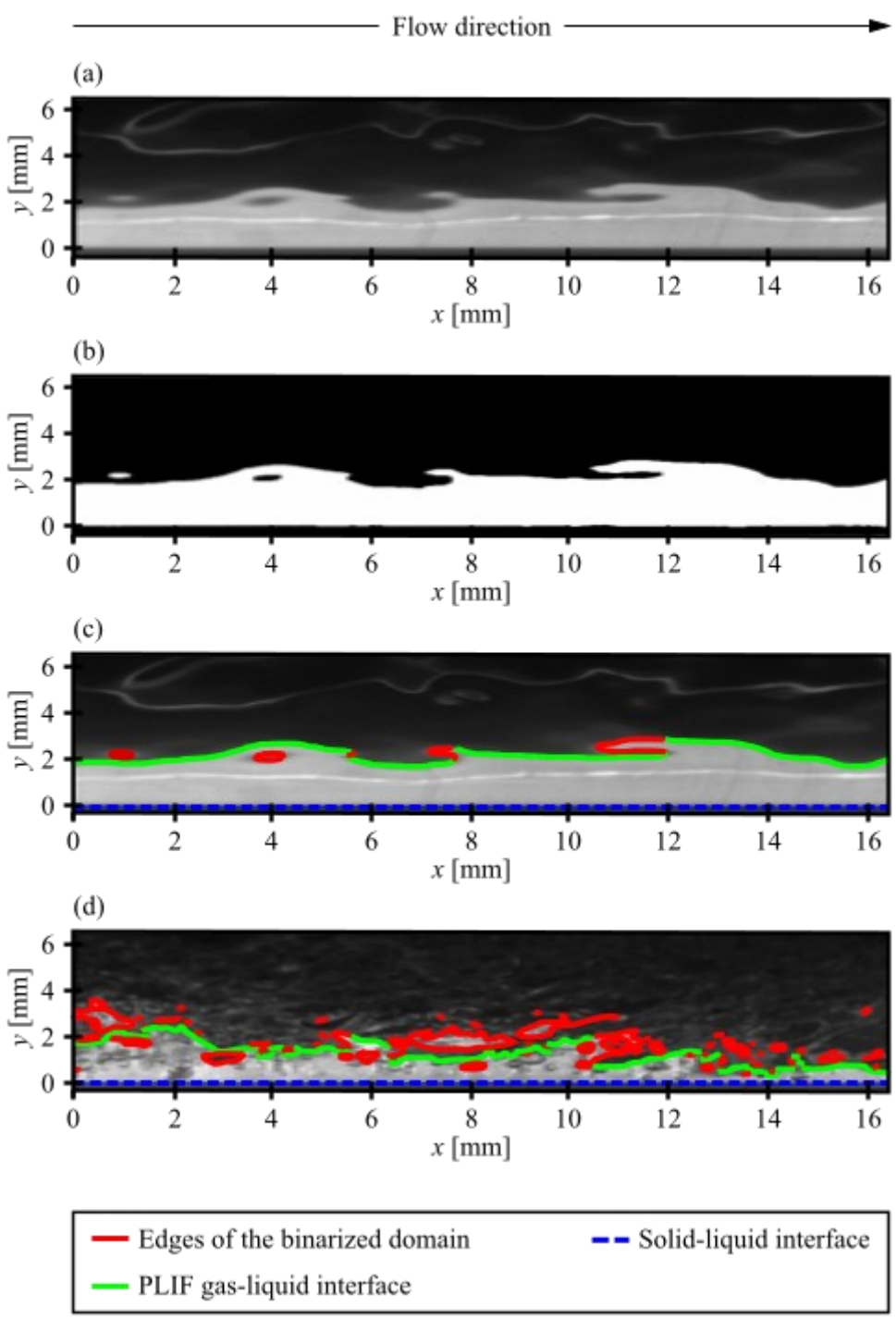


Figure 4-3 – PLIF image processing routine to identify the position of the gas-liquid interface in each PLIF image ($I_P(x, y, t)$): (a) sample raw PLIF70 image at $Re_G = 0$ and $Re_L = 520$; (b) a binarized image of (a); (c) a processed image of (a); and (d) a processed PLIF70 image of a flow at $Re_G = 43{,}700$ and $Re_L = 1330$

4.4. Comparisons of PLIF & BBLIF

For the investigated range of flow conditions, the BBLIF and the PLIF images were qualitatively compared frame-by-frame to attain a better understanding of the effectiveness and limitations of each approach. First, a flow regime map of downwards co-current air-water annular flows generated with the current set of collected images is presented in Section 4.4.1. The discrepancy between the liquid-film thickness profiles obtained with the instantaneous images in smooth and rough film regions are discussed in Sections 4.4.2 and 4.4.3, respectively. In Section 4.4.4, the optical effects at the gas-liquid interface are described in detail. The effect of the observation angle of the PLIF camera on the resultant PLIF images and the effect of entrained gas bubbles on PLIF and BBLIF derived film-thickness profiles are discussed in Sections 4.4.5 and 4.4.6, respectively.

4.4.1. Flow regime map

Webb & Hewitt (1975) were the first to present a flow regime map for downwards co-current gas-liquid annular flows in vertical pipes, and identified four distinct sub-regimes based on the wave patterns on the surface of liquid-films: (i) 'ripple' regime, (ii) 'dual-wave' regime, (iii) 'thick ripple' regime, and (iv) 'regular wave' regime. Webb & Hewitt (1975) used the temporal spectra of film-thickness to distinguish transitions from one wave pattern to another. Similar to Zadrazil et al. (2014), raw BBLIF and PLIF images were visually inspected to identify individual wave patterns in this flow regime. In addition, the qualitative image analysis was supplemented with the evaluation of liquid-film roughness. For the investigated range of flow conditions, the most pertinent and prominent wave pattern transition was from the dual-wave to regular wave regime. The dual wave to regular wave regime transition was characterised by highly agitated gas-liquid

interfaces due to the presence of disturbance waves, and hence, entrained gas bubbles in the film. For flows at Re_G = 34,900 – 52,400 and Re_L = 300, raw BBLIF and PLIF70 images are shown in Figure 4-4 to demonstrate this transition. In each sub-figure, the PLIF70 frame is at the top and the corresponding BBLIF frame is at the bottom. The dashed blue-line in each PLIF70 image indicates the position of the solid-liquid interface (i.e. the surface of the pipe wall).

A flow regime map was constructed with the current set of experiments and the map is shown in Figure 4-5, which has been superimposed with the flow regime map presented by Webb & Hewitt (1975). In the range of the investigated flow conditions, two types of interfacial wave behaviours were predominant, which is represented as empty-circle markers and filled-circle markers in the flow regime map. The empty-circle markers indicate flows with large amplitude waves, however, the gas-liquid interface is relatively smooth and the dimensionality of the flow is small. The filled-circle markers indicate flows with highly complex gas-liquid interfaces, and the presence of large amplitude and fast-moving interfacial waves (i.e. disturbance waves) with highly agitated surfaces. This lead to frequent gas bubble entrainment in the liquid-film and liquid droplet entrainment in the gas-phase.

Another observed wave pattern was the ‘thick ripple’ regime, which was described by Webb & Hewitt (1975) and Zadrazil et al. (2014). The wave pattern is represented by the square-markers in Figure 4-4. The mean liquid-film thickness ($\langle\delta\rangle$) of the flows is larger and the distribution of the film thickness is narrow, which is approximately symmetrical about the average. Finally, the triangle-markers indicate flows in transition. In comparison with the flow regime map presented by Webb & Hewitt (1975), the ‘dual wave’ to ‘regular wave’ regime transition is shifted slightly towards lower gas and liquid flow-rates in the current set of experiments. The discrepancy between the two flow regime maps may be attributed to the difference in the identification criteria of the wave pattern transitions. Another reason for the discrepancy could be the different pipe diameters used in the experiments. For the current work, downwards annular flows were

generated in a D_P = 32.0 mm pipe, while Webb & Hewitt employed a D_P = 38.2 mm pipe. Further support of the second argument can be provided by the findings of Alekseenko et al. (2015b). In the study by Alekseenko et al. (2015b), spatiotemporal film thickness data were used to find the wave pattern transitions in a D_P = 15.0 mm pipe; and identified the same wave pattern transition at even lower flow conditions, which is depicted by the dashed red-line in Figure 4-5.

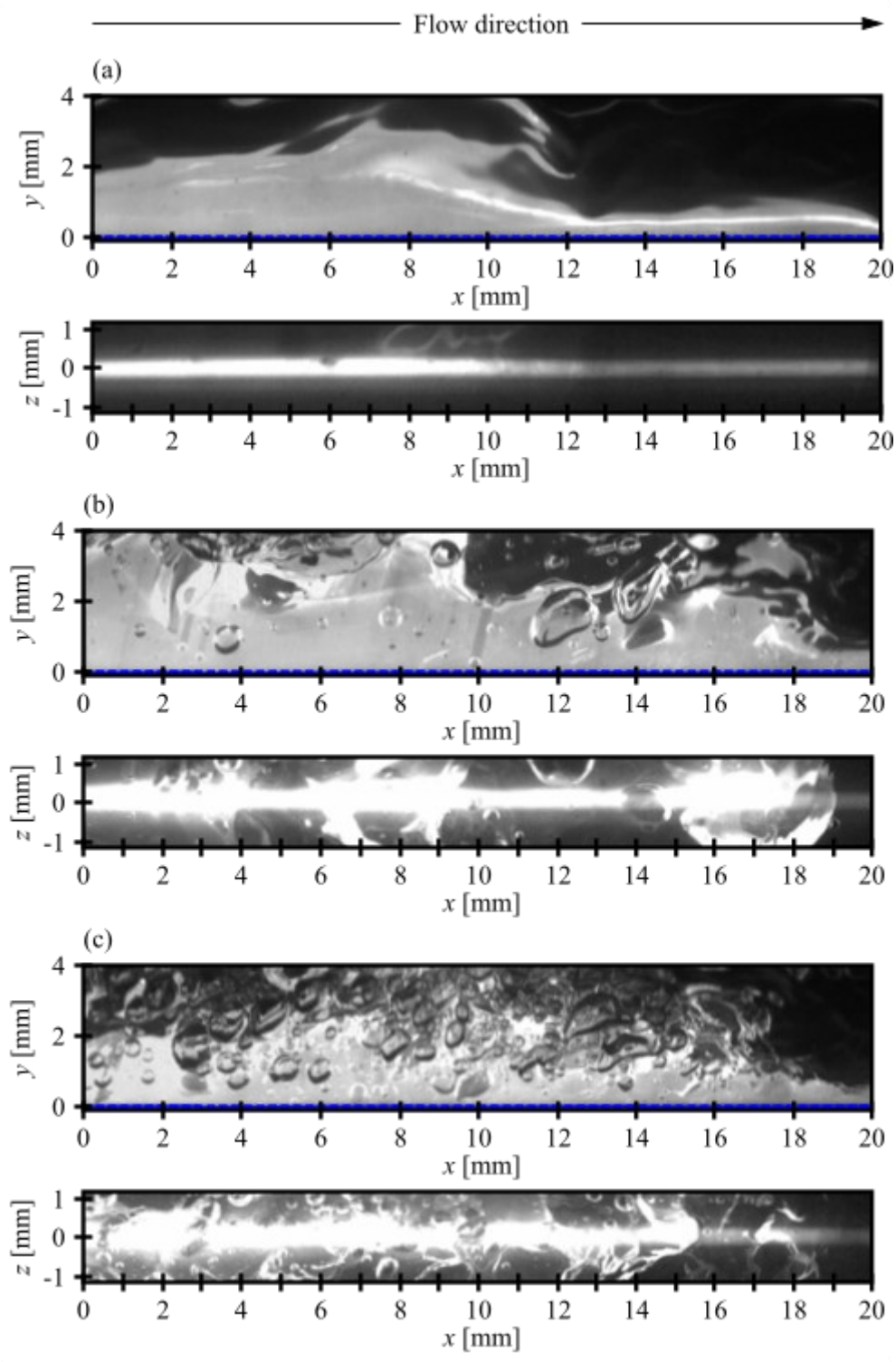


Figure 4-4 – Raw PLIF70 (top) and BBLIF (bottom) images of interfacial waves in flows at Re_L = 300 and: (a) Re_G = 34,900; (b) Re_G = 43,700; and (c) Re_G = 52,400. In each PLIF frame, the dashed blue-line indicates the position of the solid-liquid interface.

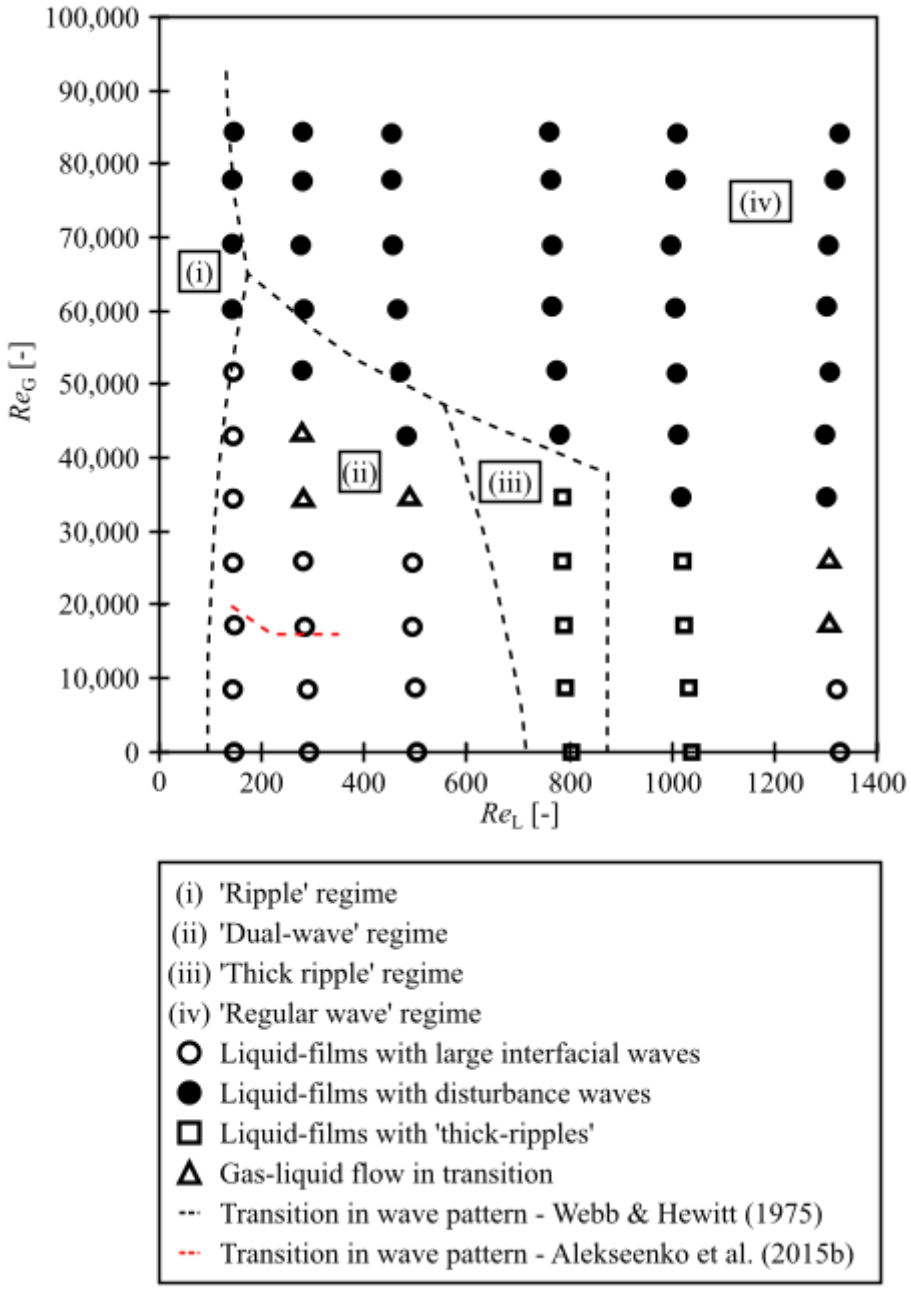


Figure 4-5 – A flow regime map of downward co-current gas-liquid annular flow: (i) 'ripple' regime; (ii) 'dual-wave' regime; (iii) 'thick ripple' regime; and (iv) 'regular wave' regime. The dashed black-lines represent the transitions in the wave pattern as proposed by Webb & Hewitt (1975), which was based on their study in a $D_P = 38.2$ mm pipe. The red-line represents the transition in the wave pattern as reported by Alekseenko et al. (2015b) in a $D_P = 15.0$ mm pipe.

4.4.2. Flat and smooth liquid-films

In Figure 4-6, examples of liquid-film regions with predominantly flat and smooth surfaces are shown in the instantaneous raw BBLIF and PLIF images of falling-films at $Re_G = 0$ and $Re_L = 300$. The PLIF frame at the top was collected by PLIF90 and the PLIF frame at the bottom was collected by PLIF70. The corresponding local liquid-film thickness profiles obtained with BBLIF and PLIF have been superimposed on the PLIF frames. Two major observations were made during the inspection of the images. The first major observation was the discrepancy in the profiles of film-thickness obtained each approach. In general, the location of the gas-liquid interface acquired by BBLIF is lower than PLIF. The difference between BBLIF and PLIF70 is greater than BBLIF and PLIF90. However, the local liquid-film thickness occasionally appears greater in BBLIF than PLIF90, such as the front-slope of an interfacial wave in Figure 4-6(a). This is related to the high interfacial slopes that effect BBLIF measurements (Cherdantsev et al., 2019).

The second major observation was the presence of distinct bright-lines (or occasionally dark-lines) in the illuminated liquid-film region along the x direction of the PLIF images. An identical trait was also visible in the PLIF images collected by Zadrazil et al. (2014). The position of this bright-line matches the position of the gas-liquid interface obtained by BBLIF, and hence, indicates the location of the 'true' gas-liquid interface. In addition, reflections of entrained gas bubbles are occasionally observed above the bright-lines. In the raw PLIF images, shadows cast by small non-uniformities of the pipe wall or acrylic anti-distortion box were visible as thin dark-lines in the illuminated film domain. The position of the thin dark-lines are fixed and the lines extend from the solid-liquid to gas-liquid boundaries (i.e. y direction). When the bright-line intersects the thin dark-lines, the thin dark-lines are interrupted at the bright-line position. The fluorescence emitted from the body of liquid above the bright-line could be related to the mirror effect due to total internal reflection (TIR) as demonstrated theoretically by Häber et al. (2015), which is discussed further in Section 4.4.4.

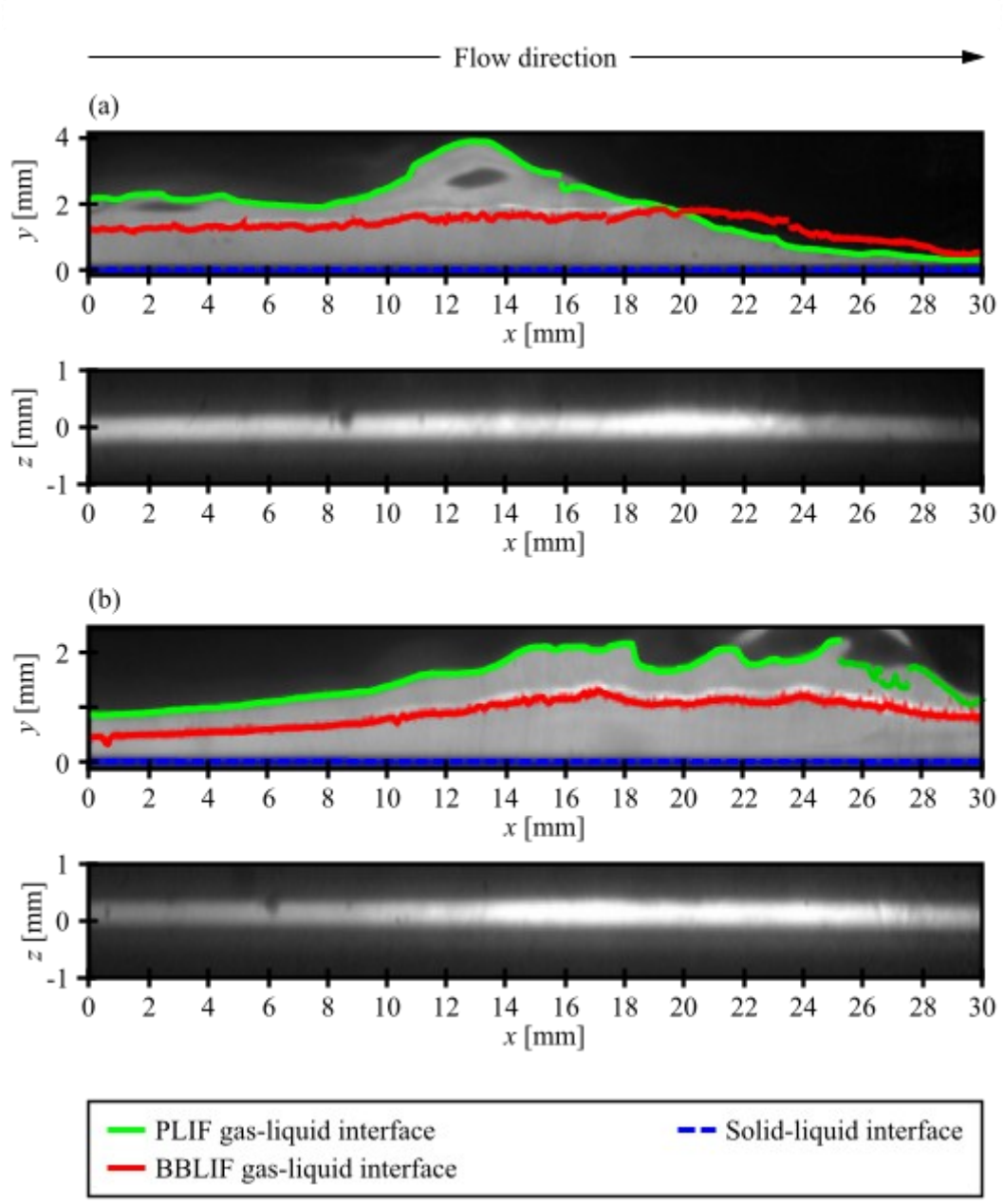


Figure 4-6 – For flat and smooth liquid-films at $Re_G = 0$ and $Re_L = 300$, the identified location of the gas-liquid interface by BBLIF and: (a) PLIF90; and (b) PLIF70. In each sub-figure, the bottom and top frames are the BBLIF and PLIF images, respectively. The positions of the solid-liquid interface (dashed blue-line), the PLIF obtained gas-liquid interface (solid green-line), and the gas-liquid interface acquired by BBLIF (solid red-line) are superimposed on each PLIF frame.

4.4.3. Agitated and rough liquid-films

For downwards annular flows at Re_G = 52,400 – 78,600 and Re_L = 300 – 1330, examples of liquid-films with gas-shear are shown in the instantaneous raw images of BBLIF and PLIF70 and BBLIF and PLIF90 in Figures 4-7 and 4-8, respectively. The corresponding local liquid-film thickness profiles obtained by both methods have been superimposed on the PLIF frames. As we can see in the images, the surfaces of liquid-films with gas-shear are highly agitated and rough. Large and small amplitude interfacial waves with three-dimensional (3-D) shapes and steep interfacial slopes cover the films. In addition, gas bubbles and liquid droplets are continuously entrained in the liquid-film and gas-core, respectively. Steep interfacial slopes were observed at the gas-liquid boundaries of: (i) entrained gas bubbles in the film; (ii) large amplitude disturbance waves; and (iii) fast-moving ripple waves on the surface of disturbance waves.

Cherdantsev et al. (2014) found that three-dimensional fast ripples with horseshoe-shaped front-slopes cause non-physically high amplitudes, and hence, incorrect peaks in the obtained local film-thickness with BBLIF. Similar to the observations of Cherdantsev et al. (2014), the liquid-film thickness profile acquired by BBLIF contain numerous narrow peaks due to steep interfacial slopes in the current set of images. For smooth regions of liquid-films, the local film-thickness obtained by PLIF is higher than BBLIF, such as the film-substrate region ($x \approx 24$ – 28 mm) ahead of the large amplitude disturbance wave in the PLIF70 frame of Figure 4-7(a). In addition, the loss of the fluorescence signal was found for very thin regions of the film, such as in the PLIF90 frame of Figure 4-8(a). For liquid-films with gas-shear, numerous optical effects are encountered due to the complexity of the gas-liquid interface. Therefore, errors are introduced in the liquid-film thickness data acquired by both BBLIF and PLIF.

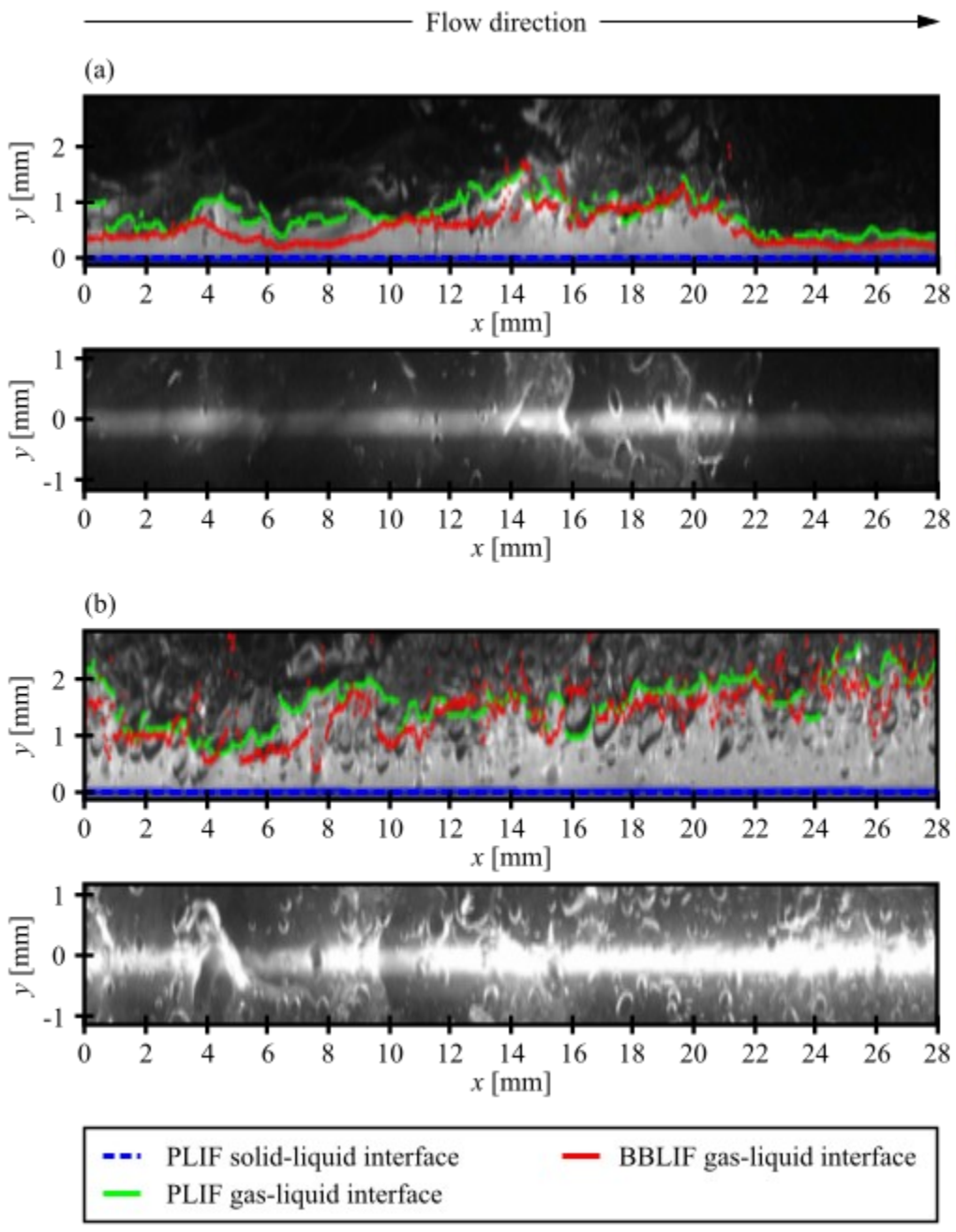


Figure 4-7 – Instantaneous and raw PLIF70 (top) and BBLIF (bottom) frames of downwards annular flows at: (a) $Re_G = 78{,}600$ and $Re_L = 300$; and (b) $Re_G = 52{,}400$ and $Re_L = 1330$. The positions of the solid-liquid interface (dashed blue-line), and the PLIF70 obtained gas-liquid interface (solid green-line), and the gas-liquid interface acquired by BBLIF (solid red-line) are superimposed on each PLIF70 frame.

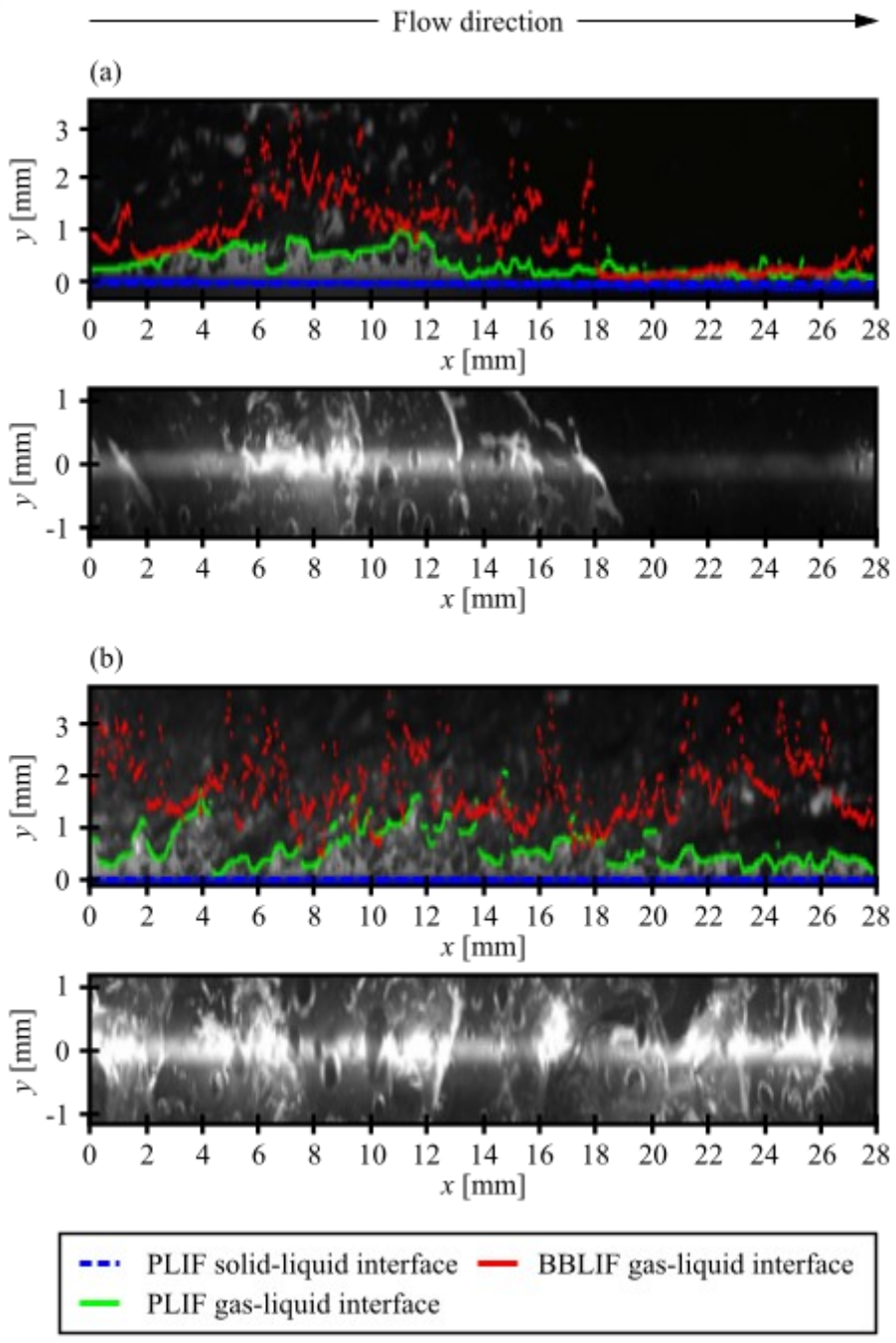


Figure 4-8 – Instantaneous and raw PLIF90 (top) and BBLIF (bottom) frames of downwards annular flows at: (a) Re_G = 78,600 and Re_L = 300; and (b) Re_G = 52,400 and Re_L = 1330. The positions of the solid-liquid interface (dashed blue-line) and the PLIF90 obtained gas-liquid interface (solid green-line), and the gas-liquid interface acquired by BBLIF (solid red-line) are superimposed on each PLIF90 frame.

4.4.4. Optical effects at the film free-surface

In BBLIF, the local intensity signal of the emitted fluorescence is directly proportional to the total excitation energy of the primary (i.e. incident) and secondary (i.e. reflected) lights. The primary light travels from the pipe wall to the liquid-film, and the secondary light travels from the gas-liquid interface to the pipe wall. The light reflections increase with steeper interfacial slope angles, and the light undergoes total internal reflection (TIR) at an angle of 48.5 ° in the current flows (Lindon et al., 2010). In the calculation of the BBLIF liquid-film thickness with Equation 4-1, the reflection coefficient (K) was set to a constant value. The effect of the actual value of K was evaluated for the simple case of collinear light paths. The value of K depends on the: (i) refractive indices of air ($\eta_{air} = 1$) and water ($\eta_{water} = 1.334$); (ii) incidence angle, which is the angle between the incident light and normal to the interface (θ_i); and (iii) the angle of refraction (θ_t). The incidence angle is related to the interfacial slope steepness and assumed that the angle does not change the light path. These factors are described by the Fresnel equations, and for an unpolarised light (i.e. fluorescent-light), the equations are (Duarte, 2003):

$$K = \frac{1}{2}\left[\left(\frac{\eta_{water}\cos\theta_i - n_{air}\cos\theta_t}{\eta_{water}\cos\theta_i + n_{air}\cos\theta_t}\right)^2 + \left(\frac{\eta_{water}\cos\theta_t - \eta_{air}\cos\theta_i}{\eta_{water}\cos\theta_t + \eta_{air}\cos\theta_i}\right)^2\right] \quad \text{Equation 4-3}$$

$$\cos\theta_t = \sqrt{1 - [(\eta_{water}/\eta_{air})\sin\theta_i]^2} \quad \text{Equation 4-4}$$

The value of K was set to a constant value of $K = 0.02$ as the interfacial slope is unknown, which corresponds to a flat film with $\theta_i = 0$. The value of K is ≈ 0.02 when the interfacial slope is relatively smooth, and hence, errors in the BBLIF measurements are primarily caused by camera noise, non-uniform sensitivity of the camera sensor, and pulse-to-pulse variations of the laser power. For flat and smooth films, the error in BBLIF was estimated to be ≈ 10 % in the current experiments. BBLIF is expected to be reliable for liquid-film thickness measurements of near-flat and smooth films as the contribution of the secondary light to the total excitation energy is small, also taken into account explicitly in Equation 4-1. However, the contributions of the light

reflections are not taken into account for steep interfacial slopes.

In Figure 4-9(a), a plot of K as a function of θ_i is provided, which demonstrates that $K \approx 0.02$ for a range of θ_i in flat films. However, the value of K starts to increase noticeably at $\theta_i \approx 30$ ° and becomes more significant as the angel approaches $\theta_i = 48.5$ °, which corresponds to the angle of TIR. For example, $K = 0.025$, $K = 0.060$, and $K = 0.500$ at $\theta_i = 30$ °, $\theta_i = 40$ °, and $\theta_i = 48$ °. In Figure 4-9(b), the effect of the increase in secondary light due to the rise in K values on the BBLIF derived film-thickness measurements is evaluated, since this is not taken into account in Equation 4-1. The average film-thickness is overestimated by ≈ 5 %, ≈ 10 – 15 %, and ≈ 40 – 50 % at $\theta_i =$ 40 °, $\theta_i = 45$ °, and $\theta_i = 48$ °. The light undergoes TIR at $\theta_i \geq 45$ °, and the secondary light contributions become comparable to the incident or primary light. Furthermore, the contributions of the reflections can exceed the excitation-light when the secondary light is focused locally by the curved interface. Therefore, the liquid-film thickness obtained with BBLIF can be significantly overestimated due to the non-linear relationship between the fluorescence intensity signals and the film-thickness.

In Figure 4-10, examples of overestimations in the local film-thickness obtained by BBLIF at steep interfacial slopes (e.g. front-slope of large amplitude waves). It should be noted that the steep interfacial slope appears to be in proximity of the bright-line within the liquid-film of the PLIF70 image. In smooth films, regions with $\theta_i \geq 48.5$ ° (i.e. TIR) can be identified in the liquid-film thickness profiles of BBLIF based on the high local gradients in $\delta_{BB}(x)$. However, film regions with $\theta_i \geq 48.5$ ° are common at higher Re_G and Re_L due to the agitated interface and entrained gas bubbles. Therefore, the ability to obtain reliable film-thickness measurements with BBLIF becomes very challenging. Furthermore, the interfacial slope in the z (i.e. transverse) direction should also be considered as illustrated in Figure 4-12. This leads errors due to out-of-plane light reflections that excite different volumes of liquid, which is unlike the assumption made for Equation 4-1 on page 117.

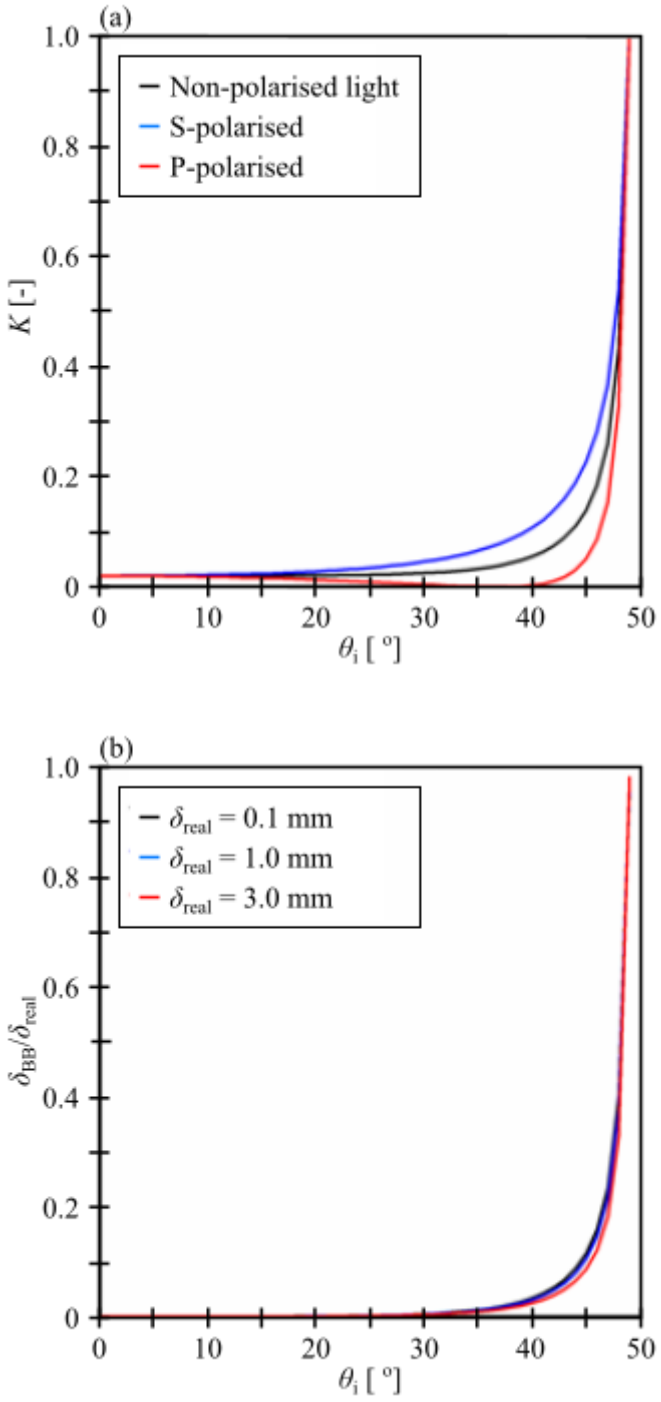


Figure 4-9 – Effect of the reflection coefficient at the air-water interface (K): (a) a plot of K as a function of the incidence angle of the excitation light and interface (θ_i); and (b) a plot of the ratio of BBLIF and real film-thickness ($\delta_{BB}/\delta_{real}$) as a function of θ_i to estimate the effect of K on the BBLIF measurements of thickness.

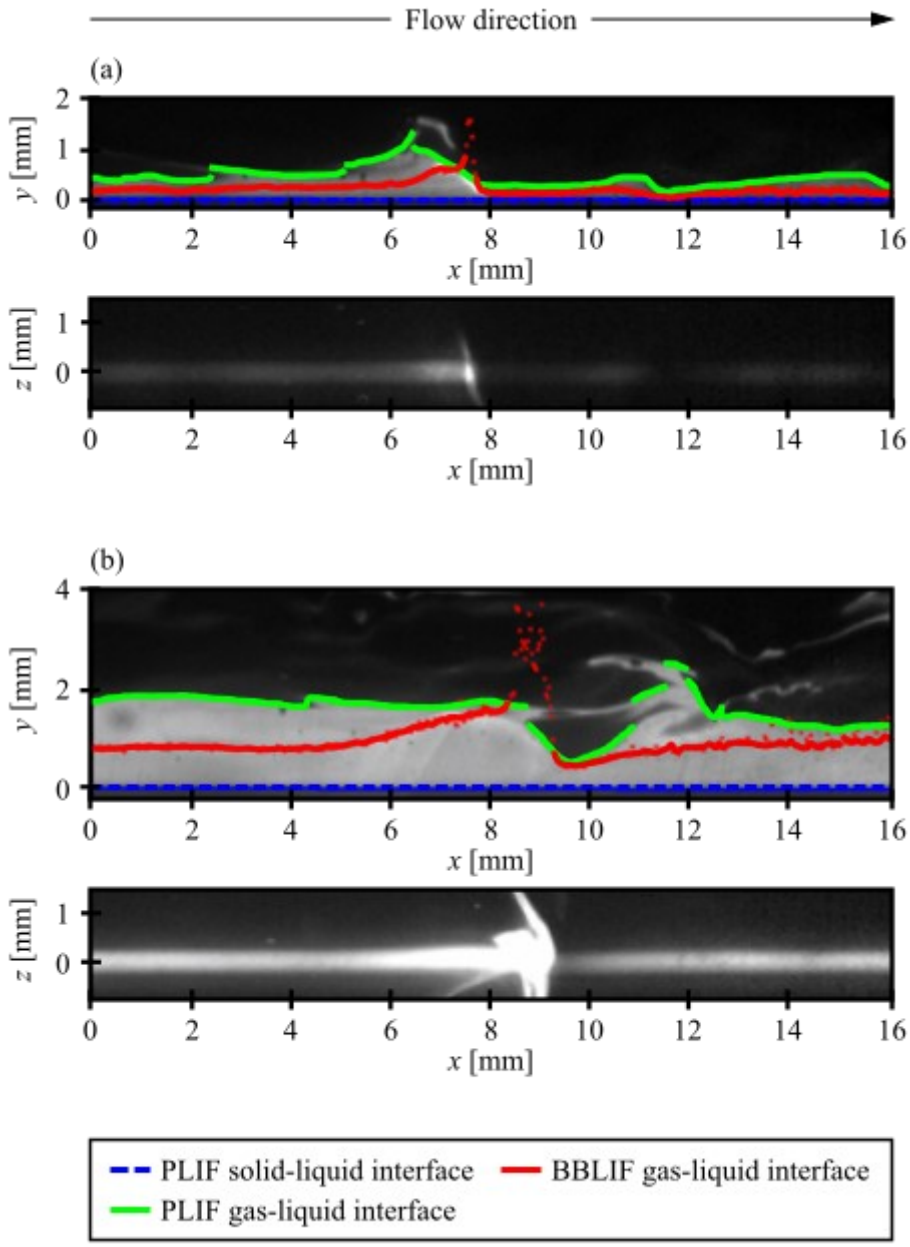


Figure 4-10 – Instantaneous and raw PLIF70 (top) and BBLIF (bottom) images of a flow at: (a) Re_G = 69,900 and Re_L = 140; and (b) Re_G = 43,700 and Re_L = 300. The positions of the solid-liquid interface (dashed blue-line), the PLIF70 obtained gas-liquid interface (solid green-line), and the gas-liquid interface acquired by BBLIF (solid red-line) are superimposed on each PLIF70 frame. The frames highlight the errors in the film-thickness measurements of BBLIF due to the steep interfacial slopes at the front-slopes of waves.

In the theoretical model of the PLIF approach by Häber et al. (2015), the emitted fluorescence from excited liquid-films travel in all directions. In smooth and uniform regions of the film, a portion of the fluorescence is directly collected by the PLIF camera to create the real or true image of the film; and a portion of the emitted fluorescence by the film endures total internal reflection (TIR) at the gas-liquid interface region between the excitation and imaging planes to create a false (second) image of the film above the true image. This optical effect at circumferentially uniform gas-liquid interfaces is illustrated in Figure 4-12(b). A major difference between the experimental observations and the predictions proposed by Häber et al. (2015) is the shape of the fluorescence intensity profiles across PLIF images of liquid-films in the *y* direction.

Examples of the intensity profiles from the collected PLIF images are shown in Figure 4-11, which differ with the 'ramp profile' predicted by Häber et al. (2015). When distinct bright-lines or dark-lines were not present in liquid-films, local intensity peaks or troughs are occasionally observed in the fluorescence intensity profiles. For flat and smooth liquid-film regions, the positions of the local peaks or troughs were in agreement with the location of the gas-liquid interface acquired by BBLIF, and hence, indicate the position of the true gas-liquid interface. For standard applications of PLIF, more reliable film-thickness statistics can be obtained with the integration of the aforementioned observations in the PLIF image processing algorithms: (i) local intensity peaks or troughs; (ii) gas bubble reflections; and (iii) shadows. However, these features are not present along the entire liquid-film in the *y* direction and only occur in select locations.

The local film-thickness profile obtained by PLIF (particularly PLIF90) was occasionally lower than BBLIF in flat and smooth liquid-film regions, such as the front-slope of the large amplitude disturbance wave shown in Figure 4-6(a) on page 134. This observation was possibly caused by the longitudinal and transverse slopes of the gas-liquid interface (i.e. the three-dimensionality of the interfacial waves). Interfacial waves with significant three-dimensional characteristics and negative transverse curvature are often found in falling-films (i.e. $Re_G = 0$).

For example, Kharlamov et al. (2015) describe horseshoe and streak waves. In addition, disturbance waves and ripple waves on liquid-films with gas-shear are highly three-dimensional (Cherdantsev et al., 2014). The circumferential span of the ripples are ≈ 5 – 10 mm, and the edges of the front-slope of the ripples could be found between the excitation plane and the PLIF camera.

The non-uniform circumferential curvature of the interface is expected to affect the measurements of the PLIF technique as demonstrated in the illustration in Figure 4-12(b), which shows a gas-liquid interface observed by the PLIF90 camera. In Figure 4-9, the collected PLIF90 image of the liquid-film is only attributed by the fluorescent-light rays A1 and B1 emitted from Points A and B, respectively. This leads to an underestimation of liquid-film thickness. Due to the refraction of the emitted fluorescence at very steep slopes of the gas-liquid interface or due to total internal reflection (TIR) at lower interfacial slopes, the liquid domain above Point B will be hidden to the PLIF camera. It should be noted that PLIF70 is expected to be less sensitive to this type of distortion than PLIF90, since the transverse slope of the gas-liquid interface will rarely attain large enough angles to hide the true interface.

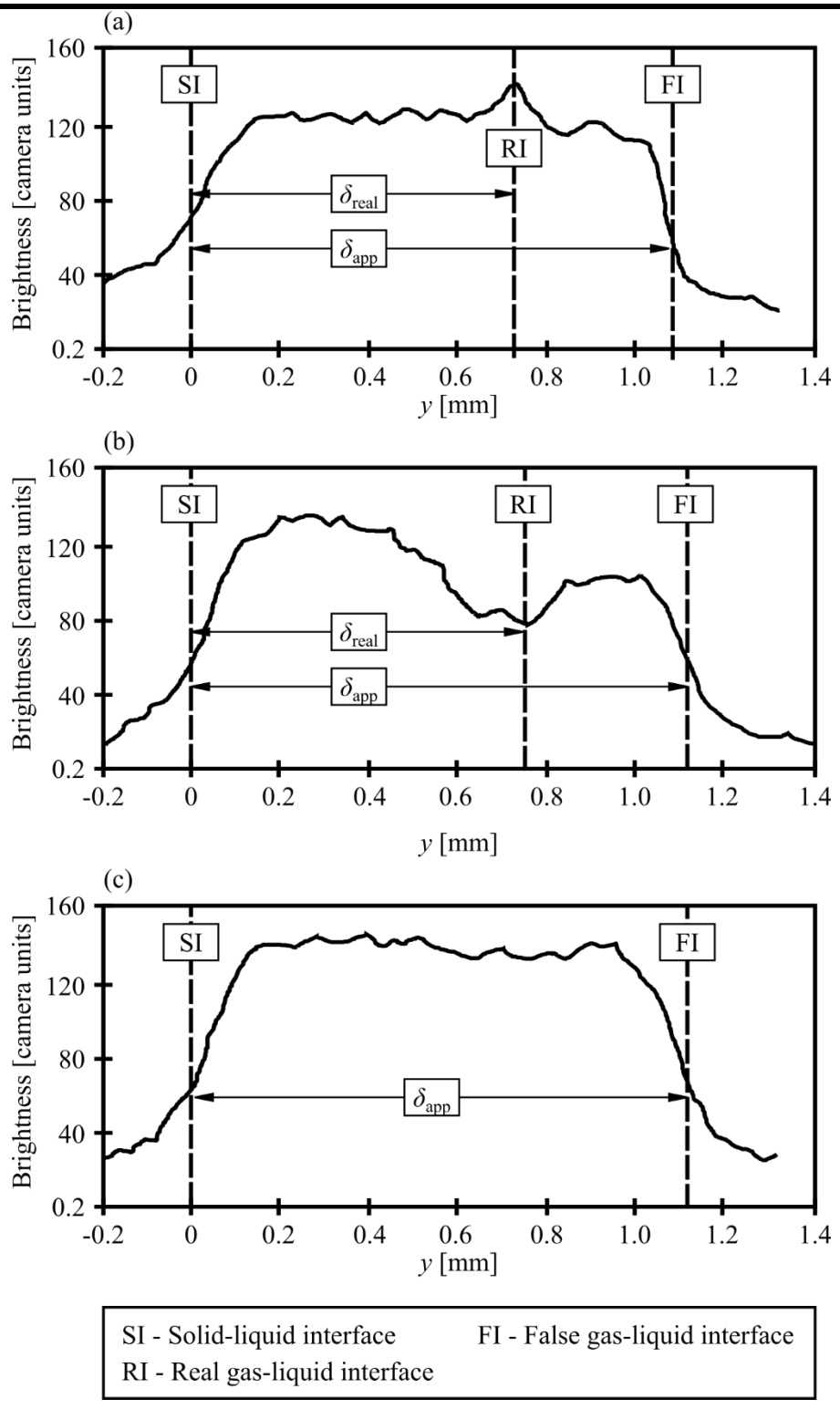


Figure 4-11 – In the PLIF70 images of smooth liquid-film regions, examples of the fluorescence intensity profiles in the y direction and the corresponding positions of the real gas-liquid interface (δ_{real}) observed as: (a) a peak in the profile; (b) a trough in the profile; or (c) no observation.

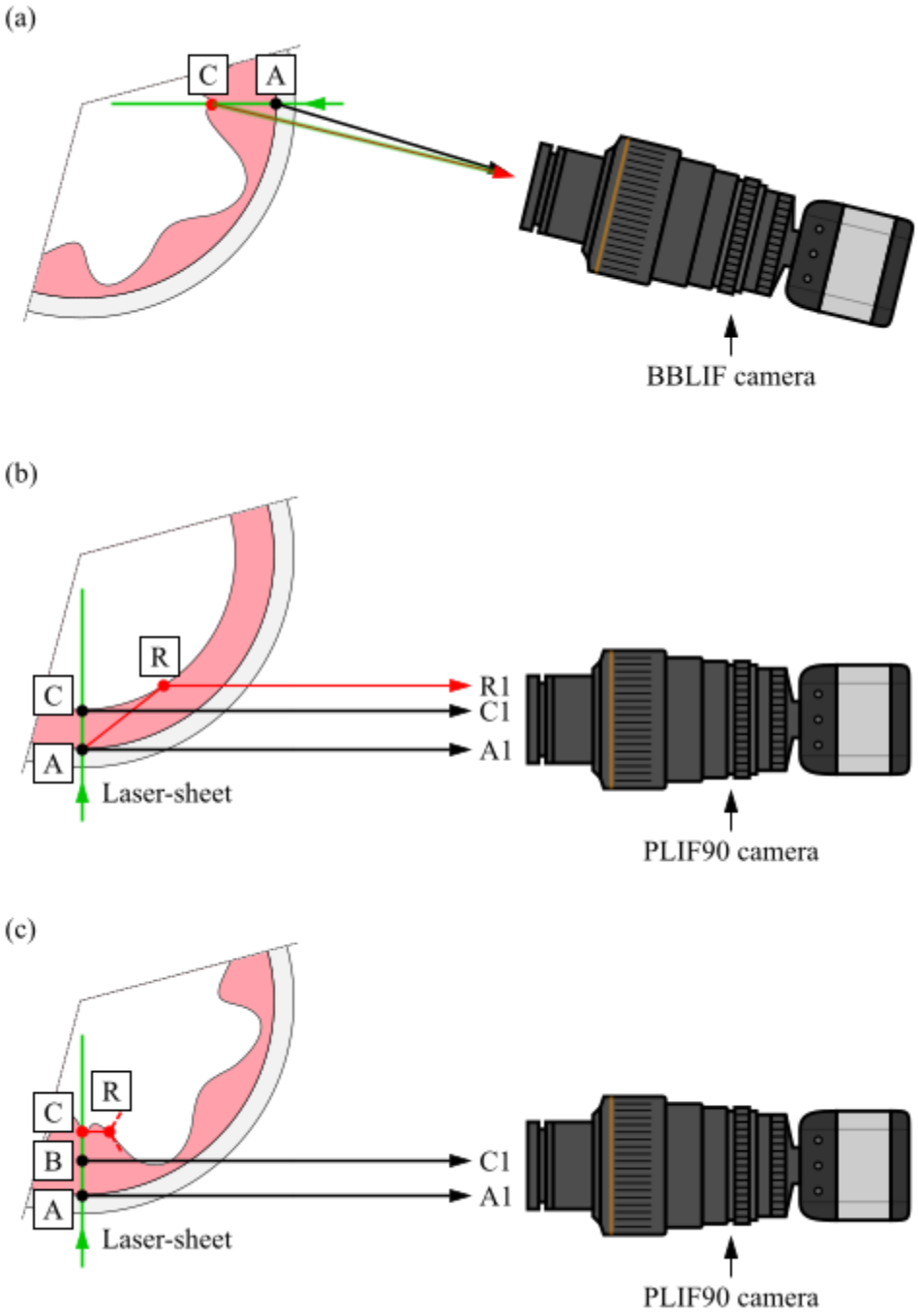


Figure 4-12 – Illustrations of optical effects at the gas-liquid interface in the transverse direction: (a) overestimation by BBLIF due to non-collinear reflections; (b) overestimation by PLIF due to total internal refection (TIR) in circumferentially uniform film regions (i.e. absence of waves); and (c) underestimation by PLIF due to refraction or TIR in circumferentially non-uniform liquid-film regions (i.e. presence of waves).

4.4.5. Effect of the PLIF camera observation angle

The effect of the PLIF camera observation angle (θ_P) was investigated as a lower θ_P was expected to cause the film to appear large in the images than θ_P = 90 °, and hence, increase the difference between the false and true gas-liquid interface positions. Therefore, the overestimation of PLIF70 would become larger than PLIF90 when left uncorrected. Ray-tracing calculations comparable to the one of Häber et al. (2015) were performed for non-wavy and uniform liquid-films. The geometries of the PLIF90 and PLIF70 model systems are presented in Figures 4-13(a) and 4-13(b), respectively.

In the PLIF90 model, a ray is emitted from adjacent to the wall of the pipe at Point A, and reflected at the gas-liquid interface at Point B. The direction of the ray becomes parallel to the axis of the PLIF90 camera and perpendicular to the illumination plane at Point B. This ray forms the upper boundary of the false liquid-film thickness in the PLIF90 image. In Figure 4-13(a), Line OA corresponds to the excitation plane, and c is the perpendicular distance between Point B and Line OA. In addition, δ_{oe} is the length between the true gas-liquid interface and c, and hence, corresponds to the overestimation of the true liquid-film thickness (δ_{real}). For PLIF90, the length of the total film image ($\delta_{real} + \delta_{oe}$) is obtained from the following set of equations:

$$\theta_r = \theta_{AOB} + \theta_{OAB} \quad \text{Equation 4-5}$$

$$\theta_r + \theta_{AOB} = \pi/2 \quad \text{Equation 4-6}$$

$$c = \sqrt{\delta_{oe}(2(R - \delta_{real}) - \delta_{oe})} \quad \text{Equation 4-7}$$

$$\tan(\theta_{AOB}) = c/(R - \delta_{real} - \delta_{oe}) \quad \text{Equation 4-8}$$

$$\tan(\theta_{OAB}) = c/(\delta_{real} + \delta_{oe}) \quad \text{Equation 4-9}$$

where R, θ_r, θ_{AOB}, and θ_{OAB} are the internal radius of the pipe, angle of reflection, angle of AOB, and angle of OAB. The interface incidence angle is equivalent to $\theta_{AOB} + \theta_{OAB}$, and hence, the

angle of reflection is $\theta_r = \theta_{AOB} + \theta_{OAB}$. For a given δ_{real} and a known R, the set of Equations 4-5 to 4-9 can be reduced to a single equation to solve numerically to find δ_{oe}:

$$\tan^{-1}\left(\frac{\sqrt{\delta_{oe}(2(R-\delta_{real})-\delta_{oe})}}{R-\delta_{real}-\delta_{oe}}\right) = \frac{\pi}{4} - \frac{1}{2}\tan^{-1}\left(\frac{\sqrt{\delta_{oe}(2(R-\delta_{real})-\delta_{oe})}}{\delta_{real}+\delta_{oe}}\right) \quad \text{Equation 4-10}$$

The overestimation of the true liquid-film thickness can be defined as the ratio of the apparent and the true liquid-film thicknesses, $\delta_{app}/\delta_{real}$ corresponds to:

$$\delta_{app}/\delta_{real} = (\delta_{real} + \delta_{oe})/\delta_{real} \quad \text{Equation 4-11}$$

A plot of $\delta_{app}/\delta_{real}$ as a function of δ_{real} is given in Figure 4-14(a). The overestimation matches the analytical approximation by Häber et al. (2015), which has been included in the plot (black-line).

In the geometry of the PLIF70 model system described in Figure 4-13(b), the length of the total film image ($\delta_{real} + \delta_{oe}$) is obtained from the following set of equations:

$$\theta_r = \theta_{AOB} + \theta_{OAB} \quad \text{Equation 4-12}$$

$$\theta_r + \theta_{AOB} + \theta = \pi/2 \quad \text{Equation 4-13}$$

$$c = \sqrt{\delta_{oe}(2(R-\delta_{real})-\delta_{oe})} \quad \text{Equation 4-14}$$

$$\tan(\theta_{AOB}) = c/(R-\delta_{real}-\delta_{oe}) \quad \text{Equation 4-15}$$

$$\tan(\theta_{OAB}) = c/(\delta_{real}+\delta_{oe}) \quad \text{Equation 4-16}$$

where θ is the angle between the camera axis and c. Therefore, Equation 4-11 becomes:

$$\tan^{-1}\left(\frac{\sqrt{\delta_{oe}(2(R-\delta_{real})-\delta_{oe})}}{R-\delta_{real}-\delta_{oe}}\right) = \frac{\pi}{4} - \frac{1}{2}\tan^{-1}\left(\frac{\sqrt{d(2(R-\delta_{real})-\delta_{oe})}}{\delta_{real}+\delta_{oe}}\right) - \frac{\theta}{2} \quad \text{Equation 4-17}$$

In the implementation of PLIF with an angle of $0 < \theta < 90$ ° between the imaging plane and plane perpendicular to the laser-sheet, $\delta_{app}/\delta_{real}$ becomes:

$$\delta_{app}/\delta_{real} = \delta_{real} + \delta_{oe} + \sqrt{\delta_{oe}(2(R-\delta_{real})-\delta_{oe})}\tan(\theta)/\delta_{real} \quad \text{Equation 4-18}$$

In Figure 4-14(a), the overestimation of the liquid-film thickness by PLIF70 is greater than PLIF90 with $\theta = 20$ °. For liquid-films with $\delta_{real} < 0.5$ mm, the overestimation is > 80 %. The overestimation is < 40 % for liquid-films with $\delta_{real} < 4.0$ mm.

A plot of the interface incidence angle ($\theta_{AOB} + \theta_{OAB}$) as a function of the liquid-film thickness is provided in Figure 4-14(b). For the examined range of film-thicknesses, incidence angles are consistently greater than the critical angle of total internal reflection (TIR) in both PLIF70 and PLIF90. Furthermore, incidence angles decrease with a higher θ, and hence, increasing θ further will cause the incidence angles to become lower than θ_{TIR}. Based on the calculations, $\theta \geq 45$ ° must be utilized for incidence angles to be lower than the critical TIR angle and avoid the appearance of false gas-liquid interfaces for approximately the entire film-thickness range of interest in annular flows. However, it should be noted that $\theta \geq 45$ ° would lead to poor spatial resolutions in PLIF. In the application of PLIF on planar falling liquid-films by Charogiannis et al. (2015; 2017), the observation angle was ≈ 52 – 56 °. False gas-liquid interfaces were found in the PLIF images, however, the intensities of the false interfaces were significantly lower than the real interfaces. This made it easier to distinguish between the two interfaces in the image processing algorithm. Therefore, false interfaces may not need to be avoided in the raw image as θ can be increased sufficiently (≥ 20 °) to produce a distinguishable difference between the intensities of false and true gas-liquid interfaces.

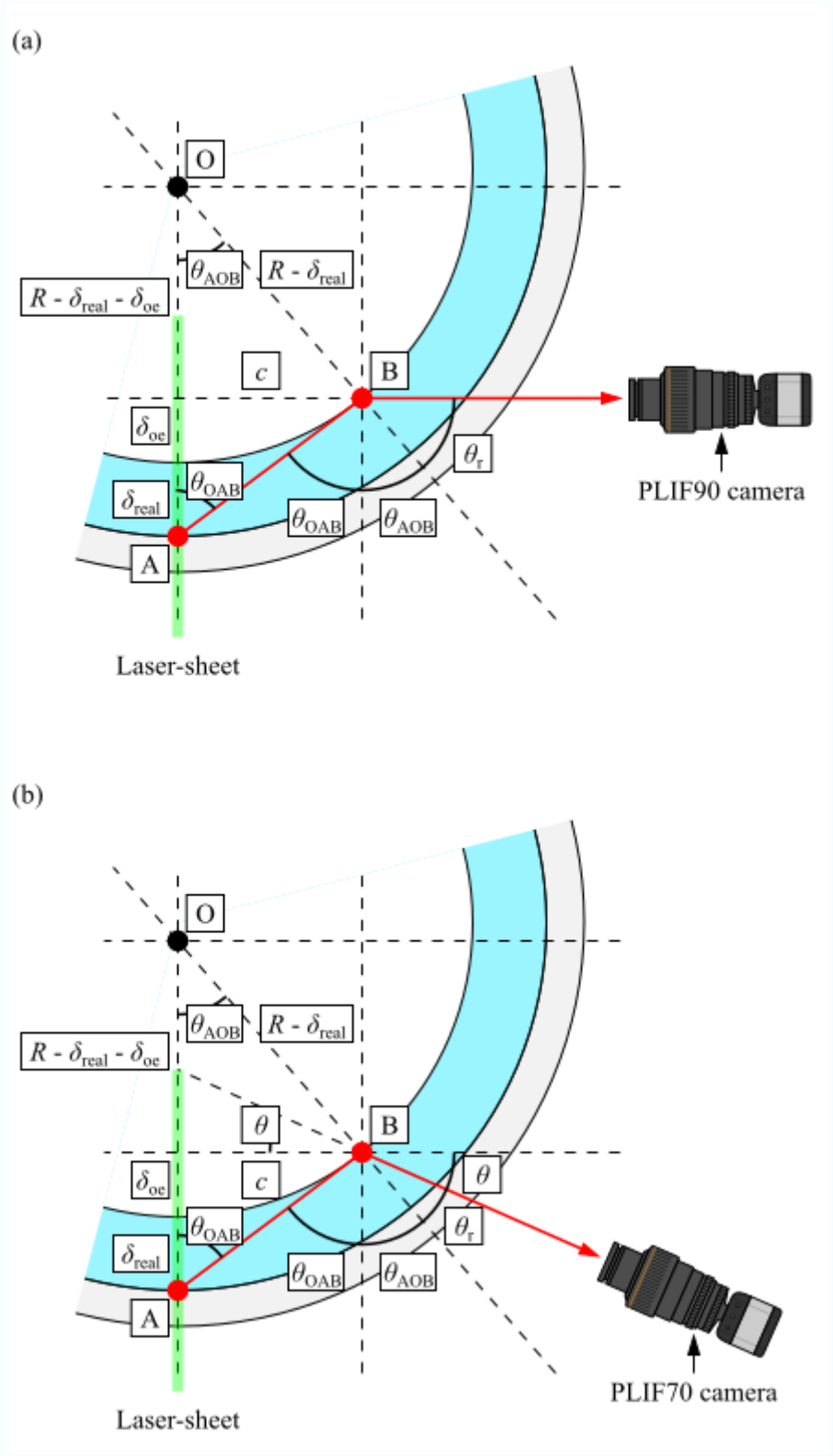


Figure 4-13 – Ray-tracing calculations to estimate the position of the false gas-liquid interface in the images of: (a) PLIF90 (θ_P = 90 °); and (b) PLIF70 (θ_P = 70 °).

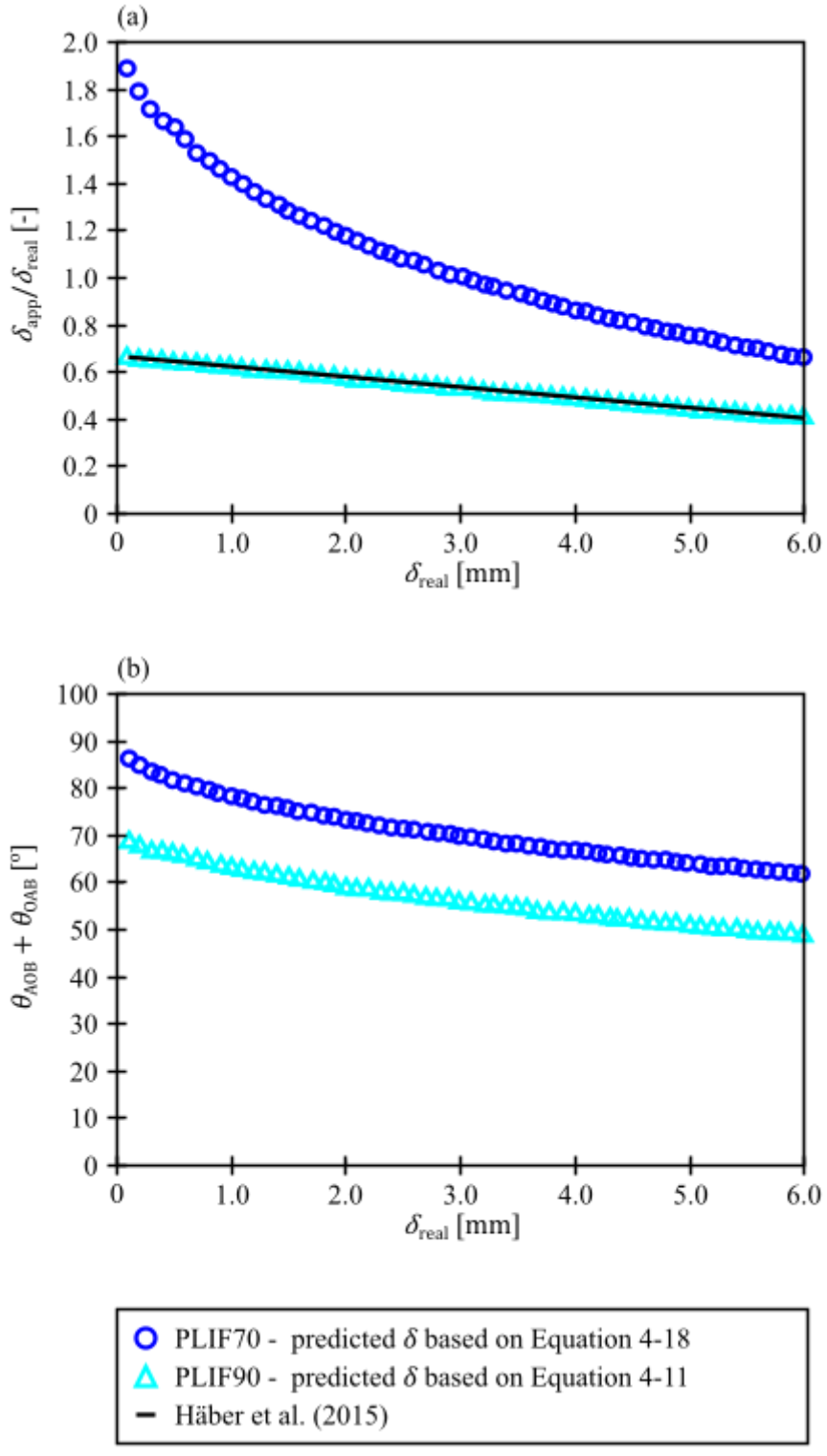


Figure 4-14 – For PLIF90 and PLIF70: (a) the overestimation of the PLIF liquid-film thickness ($\delta_{app}/\delta_{real}$) as a function of the real film-thickness (δ_{real}) based on $2R = D_P = 32.4$ mm; and (b) the interfacial angle of incidence ($\theta_{AOB} + \theta_{OAB}$) as a function of δ_{real}.

4.4.6. Entrained gas bubbles

Instantaneous frames of PLIF and BBLIF are presented of a liquid-film region with entrained gas bubbles in Figure 4-15. Based on a visual inspection of the frames, the majority of the gas bubbles found in the PLIF image are not located within the illumination plane. For example, the locations of Bubbles B1 to B3 in the PLIF images are: (i) B1 – ahead of the excitation plane; (ii) B2 – behind the excitation plane; and (iii) B3 – inside the excitation plane. In the PLIF frame, additional bubbles are found above the gas-liquid interface identified by BBLIF (i.e. red-line). These bubbles appear in the PLIF image due to the mirror effect, provided that BBLIF correctly identified the true interface in this smooth liquid-film. Therefore, visual evaluations of gas bubbles in PLIF images will lead to overestimations in the number of entrained gas bubbles.

Nevertheless, PLIF can still be used to obtain bubble frequencies with a thorough analysis of the intensity distributions within each bubble. Gas bubbles inside the excitation plane cause a substantial reduction in the local fluorescence intensity. Bubbles behind the excitation plane are visible as they reflect the fluorescence emitted from the excited liquid-film region as illustrated in Figure 4-12(b) (B2). The brightness at the centre of these bubbles is similar to the brightness of the fluorescing liquid-film, and the edges glow brighter as light from large portions of the fluorescing liquid-volume is reflected at this interface. Bubbles ahead of the laser-sheet are visible due to the passing and reflection of fluorescent light as illustrated in Figure 4-12(b) (B1). The reflected light is mostly visible along the edges of the bubbles in the axial direction of the flow, while the passing light creates an ellipsoid-shaped bright spot bound by darker regions at the upper and lower borders of the bubbles. These regions appear due to TIR of the transmitted light (Figure 4-12(c), B1). An alternative option can be the use of two or more PLIF cameras (i.e. one on either side of the illumination plane or otherwise) to identify common in and out-of-plane gas bubbles.

The entrained bubbles appear as thin bright rings in the BBLIF images. The centre of the bubbles are darker than the surrounding film as the fluorescent dye is absent in the bubbles, and the bright edges are attributed to TIR of the excitation-light at the bubble edges. If the curvature of the interfaces are neglected, the local BBLIF film-thickness at B1 corresponds to the 'residual' thickness of the film, which is the total thickness of the two liquid-layers above and below B1. Therefore, the red-line in the PLIF image at B1 is slightly above the lower bubble edge. Peaks in the local thickness at the edge of bubbles are found due to TIR of the excitation-light. The frequency of the peaks increases with the frequency of the presence of the entrained gas bubbles, which is shown in the images of Figures 4-7 and 4-8 on pages 136 and 137, respectively. BBLIF does not directly measure the thickness of the film surrounding the bubble or the size of the bubbles in the y direction, and hence, these quantities must be estimated by interpolating the thickness outside of the bubbles. In contrast to BBLIF, PLIF can perform such measurements as the illuminated film region is directly imaged, however, this is dependent on the suppression of the mirror effect and the absence of bubbles in the line-of-sight of the camera that conceal the location of the true gas-interface.

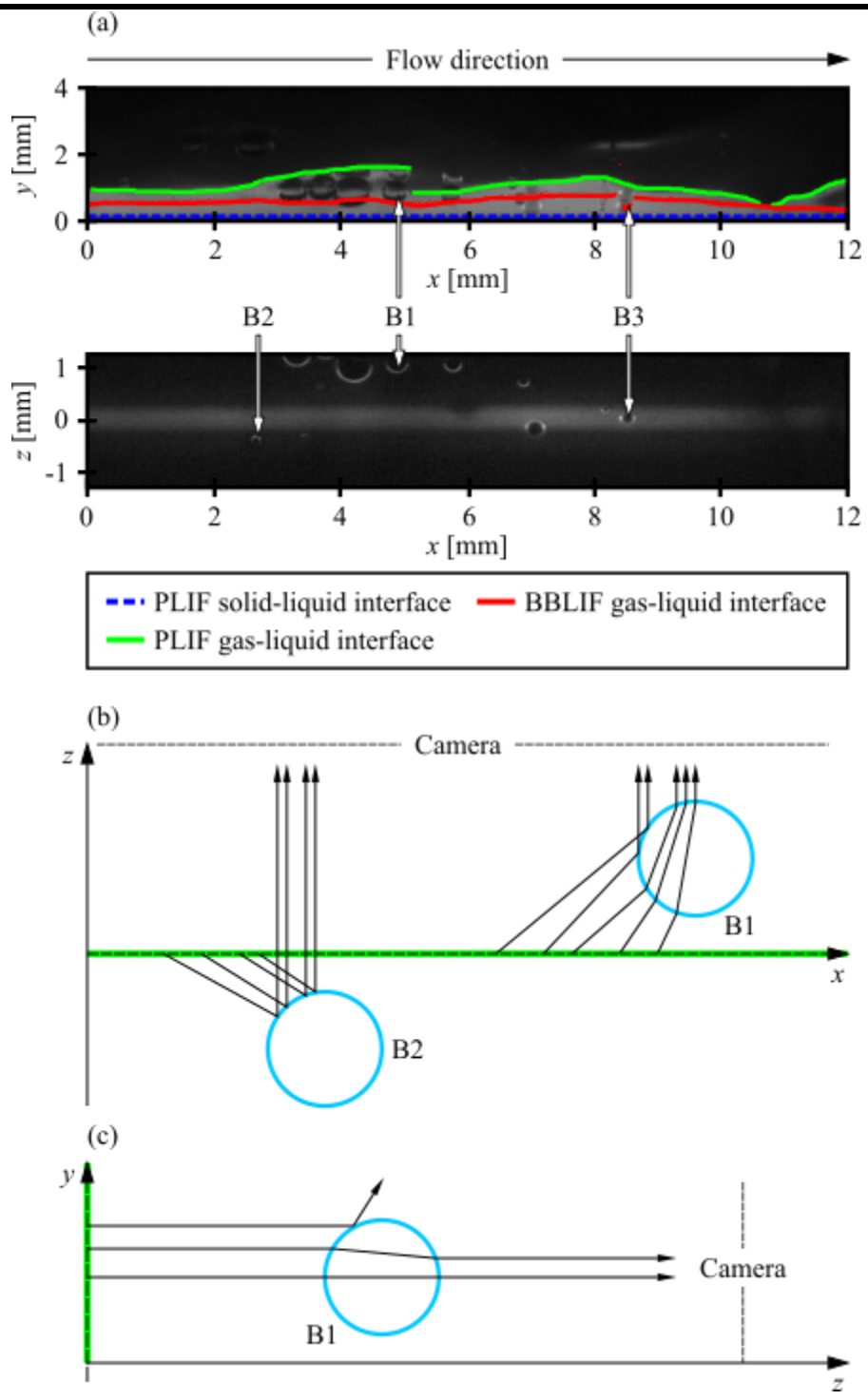


Figure 4-15 – Entrained gas bubbles in: (a) raw PLIF70 (top) and BBLIF (bottom) images of a liquid-film at Re_G = 43,700 and Re_L = 300 with entrained gas bubbles: B1 – ahead of the laser-sheet; B2 – behind the laser-sheet; and B3 – inside the laser-sheet. Ray-tracing illustrations for: (b) B1 and B2, and (c) B1.

4.5. Quantitative analysis

In this Section, direct comparison of the liquid film thickness data acquired by PLIF (δ_P) and BBLIF (δ_{BB}) are provided for the investigated range of flow conditions. The mean liquid-film thickness ($\langle\delta\rangle$), the standard deviation of the liquid-film thickness (σ_δ), and the liquid-film roughness ($\sigma_\delta/\langle\delta\rangle$) are compared in Section 4.5.1. In addition, the joint probability density distributions of the liquid-film thickness ($P(\delta_P, \delta_{BB})$) are given in Section 4.5.2.

4.5.1. Statistical moments

The liquid-film thickness statistics obtained by PLIF90, PLIF70 and BBLIF are presented in Figures 4-16 and 4-17. In the comparison of BBLIF and PLIF, two gas Reynolds numbers were selected: (a) $Re_G = 0$ (i.e. falling-films); and (b) $Re_G = 52{,}400$ (i.e. rough liquid-films). A plot of the mean film-thickness ($\langle\delta\rangle$) as a function of liquid Reynolds number (Re_L) is presented in Figure 4-16(a). For flows at $Re_G = 0$ and $Re_L \leq 500$, the flow is laminar with mostly smooth gas-liquid interfaces, and $\langle\delta_{BB}\rangle$ matches the predictions by the Nusselt solution to the Navier-Stokes equation. Therefore, the film-thickness data obtained by BBLIF can be considered reliable for these flow conditions. The effects of steep slopes or 3-D interfacial waves are less frequent in falling-films, and hence, the local errors will not significantly affect the $\langle\delta_{BB}\rangle$ data.

For higher Re_L, both the BBLIF and PLIF data increase slightly, which was also observed in other studies (e.g. Mudawar & El-Masri, 1986), and the behaviour has been attributed to the transition from laminar to turbulent flow. For the same flow conditions, the $\langle\delta\rangle$ data acquired by PLIF70 and PLIF90 are consistently higher than $\langle\delta_{BB}\rangle$ due to the mirror effect. For example, the $\langle\delta_{P90}\rangle$ data is ≈ 30 % higher than $\langle\delta_{BB}\rangle$, and the standard deviation of PLIF70 is higher. As demonstrated in Figure 4-16(b), $\langle\delta_P\rangle/\langle\delta_{BB}\rangle$ decreases with increasing Re_L and increasing δ, which

is in agreement with the prediction shown in Figure 4-14(a) on page 150. For higher Re_L, a general under-prediction of $\langle\delta\rangle$ by BBLIF is expected due to the limitations associated with the maximum measurable liquid-film thickness aforementioned in Section 4.2.

For liquid-films with gas-shear, a decrease in $\langle\delta\rangle$ is observed by all three LIF-based optical methods. In comparison with $\langle\delta_{BB}\rangle$, $\langle\delta_{P90}\rangle$ is higher at low Re_L and below at high Re_L. In addition, $\langle\delta_{P70}\rangle$ is higher than both $\langle\delta_{P90}\rangle$ and $\langle\delta_{BB}\rangle$. However, $\langle\delta_P\rangle/\langle\delta_{BB}\rangle$ decreases with increasing Re_L, which implies that the mirror effect is repressed by the three-dimensional (3-D) gas-liquid interface. This is primarily supported by the lower $\langle\delta_{P90}\rangle$ than $\langle\delta_{BB}\rangle$. Furthermore, the higher frequency of entrained gas bubbles is probably the main contributor to the substantial overestimations and underestimations of the local film-thickness obtained by BBLIF. This would affect the mean, and greatly impact the higher order statistics of the BBLIF liquid-film thickness data. Furthermore, $\langle\delta_{P90}\rangle/\langle\delta_{BB}\rangle$ falls to ≈ 0.75, which is below unity, at $Re_L = 1330$.

In Figure 4-17(a), a plot of the absolute standard deviation of the liquid-film thickness (σ_δ) as a function of Re_L is provided. At $Re_G = 0$, σ_δ of PLIF70 and PLIF90 show similar overall trends with increasing Re_L: (i) steep increase at $Re_L \approx 0 - 500$; (ii) fall at $Re_L \approx 800$; and (iii) further increase at $Re_L \geq 800$. In contrast, σ_δ of BBLIF increases gradually with increasing Re_L. The discrepancy between PLIF and BBLIF can be attributed to the 3-D gas-liquid interface. A plot of the liquid-film roughness ($\sigma_\delta/\langle\delta\rangle$) as a function of Re_L is given in Figure 4-17(b). For falling-films, $\sigma_\delta/\langle\delta\rangle$ obtained by all three methods have a relatively good agreement. Even though σ_δ acquired by BBLIF increased gradually with increasing Re_L, $\sigma_\delta/\langle\delta\rangle$ obtained by all three techniques reaches a maximum at an intermediate Re_L and sharp increase at the highest Re_L. For agitated liquid-films, σ_δ of the all the methods are similar, however, entrained gas bubbles and other interfacial complexities could lead to the higher $\sigma_\delta/\langle\delta\rangle$ found in BBLIF. The BBLIF obtained $\sigma_\delta/\langle\delta\rangle$ is higher than PLIF90, and nearly twice as high than PLIF70 for the same Re_L.

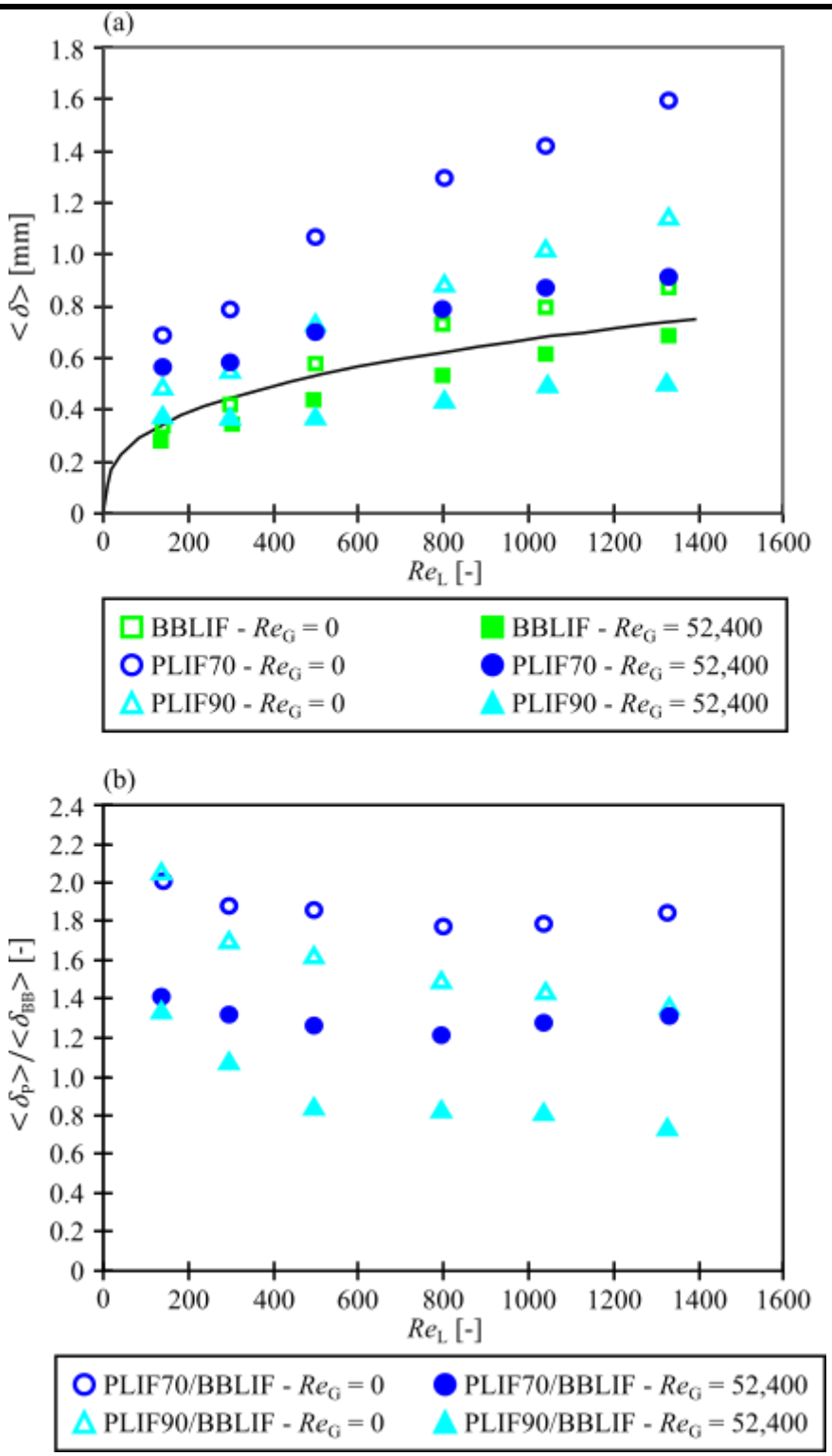


Figure 4-16 – For the flows at Re_G = 0 – 52,400 and Re_L = 140 – 1330, BBLIF, PLIF70 and PLIF90 obtained: (a) mean liquid-film thickness ($\langle\delta\rangle$) as a function of Re_L; and (b) the ratios of $\langle\delta_P\rangle$ and $\langle\delta_{BB}\rangle$ ($\langle\delta_P\rangle/\langle\delta_{BB}\rangle$) as a function of Re_L.

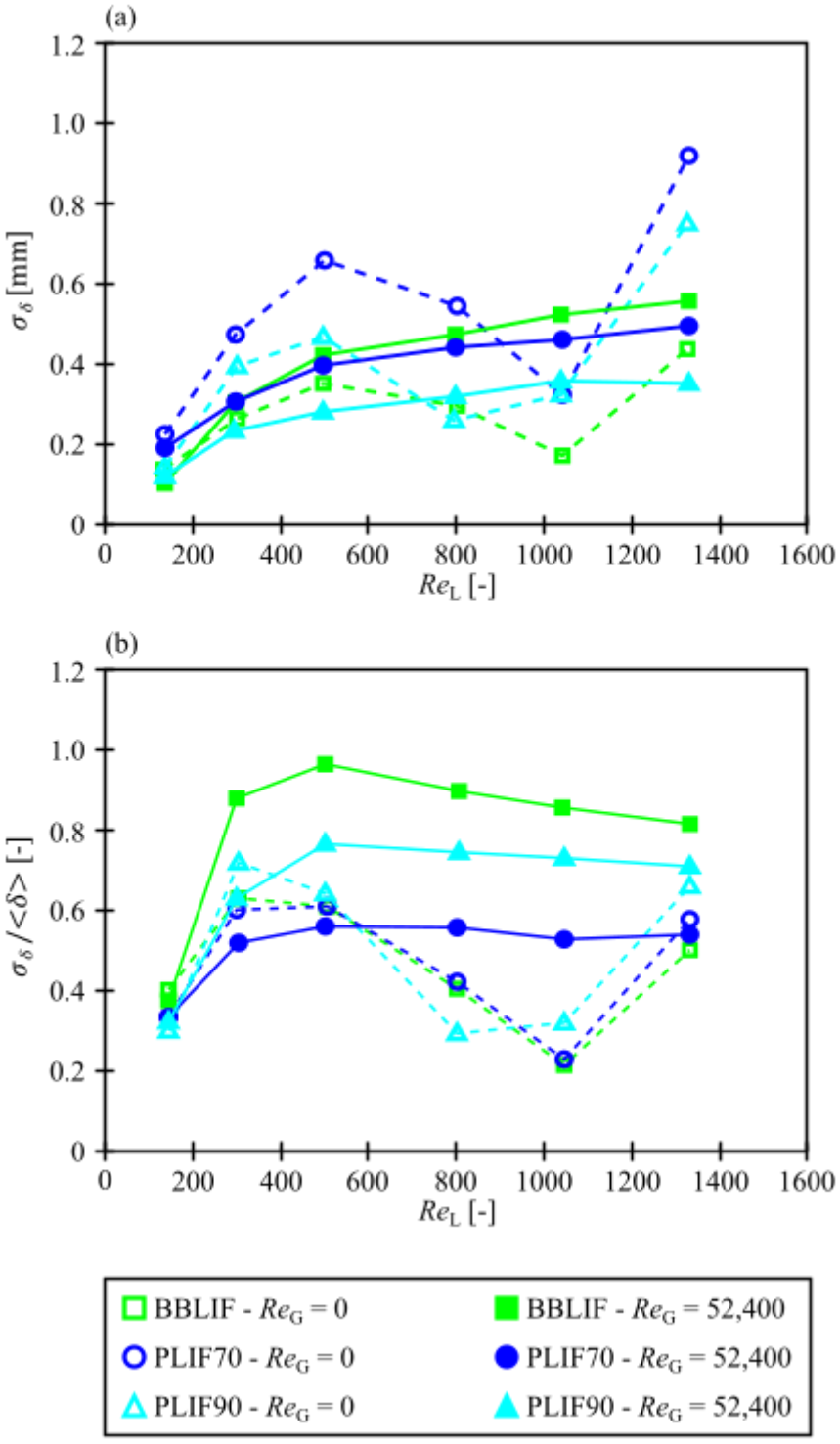


Figure 4-17 – For flows at Re_G = 0 – 52,400 and Re_L = 140 – 1330, BBLIF, PLIF70 and PLIF90 obtained: (a) standard deviation of the mean liquid-film thickness (σ_δ) as a function of Re_L; and (b) film roughness $\sigma_\delta/\langle\delta\rangle$ as a function of Re_L.

4.5.2. Probability density distributions

In Figures 4-18 to 4-21, joint probability density distributions, $P(\delta_P, \delta_{BB})$ are presented with $\{t, x\}$ combination in the liquid-film thickness records which contribute to the Nth measurement point in a two-dimensional (2-D) bin. In each plot, the x axis represents the δ_{BB} data, and the y axis represents the δ_P data. For $Re_G = 0 – 52{,}400$, the effect of the flow conditions on the distributions are evaluated by utilizing liquid-film thickness data of PLIF70 and BBLIF for flows at $Re_L = 300$ and $Re_L = 1330$ in Figures 4-18 and 4-19, respectively. In each plot, the red-line represents $\delta_{P70} = \delta_{BB}$, and the black-line represents the predicted liquid-film thickness for PLIF70 considering the overestimation due to the mirror effect in Figure 4-14(a) on page 150. For falling-films, good agreement was found between the data and prediction based on Equation 4-11. However, there is a large scatter in the data at higher Re_L and a deviation in thick liquid-films. For low Re_L and $Re_G = 0$, the general discrepancy between PLIF and BBLIF can be described by the mirror effect. This provides further evidence of the reliability of BBLIF for smooth liquid-film regions. In Figure 4-19(a), based on the local deviations at higher liquid-film thicknesses at $Re_G = 0$, an interesting observation was made on the saturation-like behaviour at $\delta_{BB} > 1.5$ mm. This behaviour is attributed to the narrow thickness of the laser-sheet and the BBLIF camera observation angle relative to the illumination plane due to the limitation on the maximum film-thickness that can be reliably measured in the used BBLIF set-up. Furthermore, the absorption that BBLIF relies upon is inherently non-linear and saturates progressively for thicker films.

In the range of $Re_G = 0 – 30{,}000$, the shapes of the distributions do not vary significantly with Re_L. In the transition to rough liquid-films, there is substantial scatter in the distributions. As shown in Figure 4-19(b), the majority of the data-points still tend to group around the black-line at higher Re_L and Re_G, however, a significant fraction approaches the red-line (i.e. $\delta_P = \delta_{BB}$). In these flow conditions, the mirror effect is suppressed due to the rough surface of disturbance waves, and the complexity of the gas-liquid interfaces lead to overestimations in δ_{BB}. Furthermore,

increasing Re_G for a given Re_L leads to a gradual reduction in the observed liquid-film thicknesses by BBLIF.

For Re_G = 0 – 52,400, the effect of the gas-liquid flow conditions on the distributions are evaluated by utilizing liquid-film thickness data of PLIF90 and BBLIF for flows at Re_L = 300 and Re_L = 1330 in Figures 4-20 and 4-21, respectively. In each plot, the red-line represents $\delta_{P90} = \delta_{BB}$, and the black-line represents the predicted liquid-film thickness for PLIF90 considering the overestimation due to the mirror effect in Figure 4-14(a) on page 150. For falling-films, most of the data lie between the black-lines and the red-lines. The exception is for the locally thick liquid-films in Figure 4-21(b), where BBLIF shows a saturation-like behavior similar to Figure 4-19(a). This is probably due to the weaker mirror effect and the stronger effect of the circumferential slopes of the film surface in the PLIF90 measurements compared to PLIF70. A significant fraction of the PLIF90 data lie below the red-line and a substantial scatter in the data is observed with increasing Re_G. Similar observations were found in Figure 4-19, which suggests an overestimation of the liquid film-thickness by BBLIF in the presence of multiple or complex gas-liquid interfaces, which are encountered more frequently in these highly three-dimensional (3-D) flows. Therefore, the agreement in the data between PLIF90 and BBLIF is reduced compared to that between PLIF70 and BBLIF.

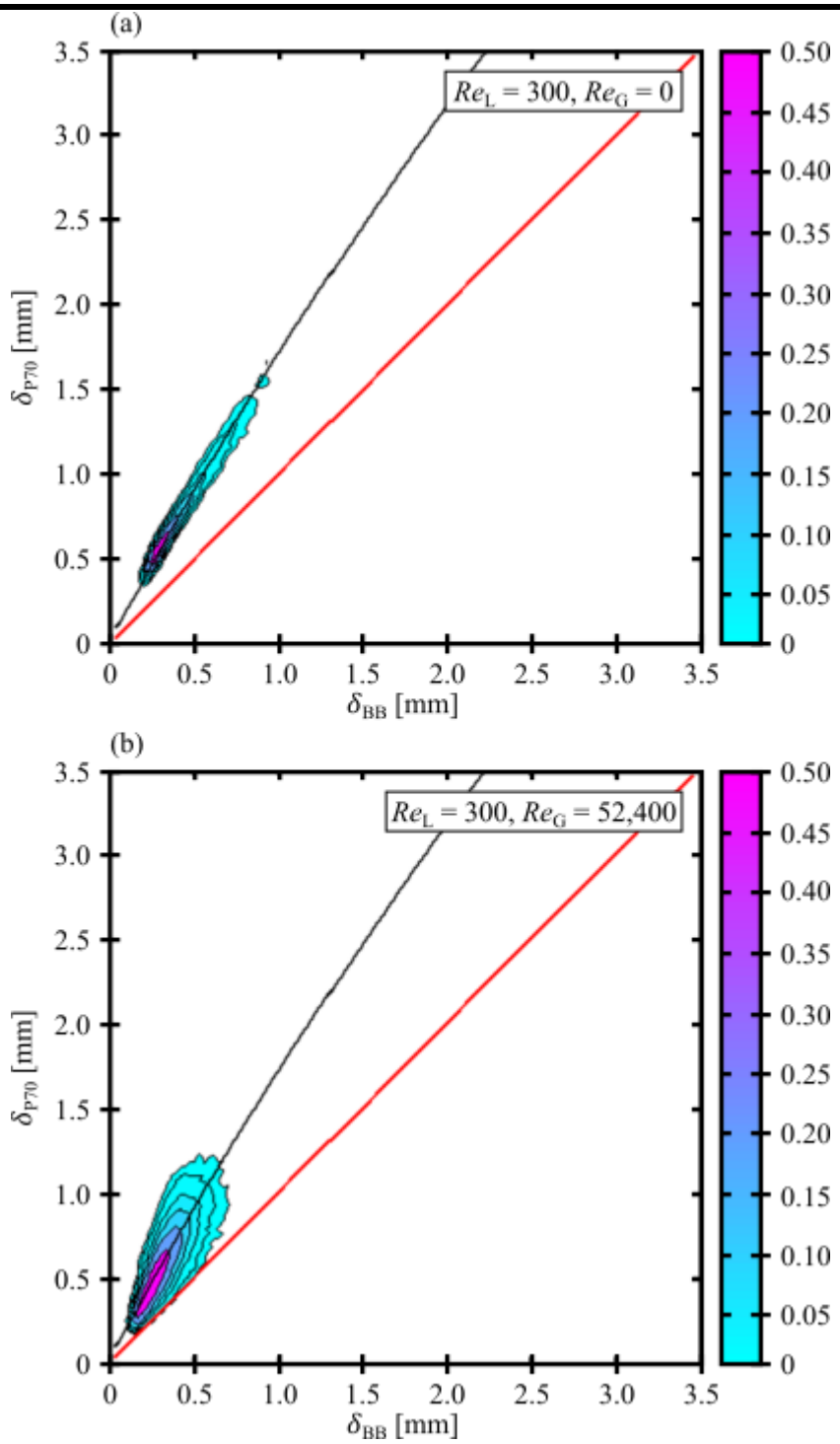


Figure 4-18 – PLIF70 and BBLIF joint probability density distributions ($P(\delta_{P70}, \delta_{BB})$) of flows at Re_L = 300 and: (a) Re_G = 0; and (b) Re_G = 52,400. The colour-scale represents $P(\delta_{P70}, \delta_{BB})$, and the contours encompass 50 %, 80 %, 90 %, 95 %, 98 %, and 99 % of the data. The red and black-lines correspond to $\delta_{P70} = \delta_{BB}$ and predicted δ_{P70}, respectively.

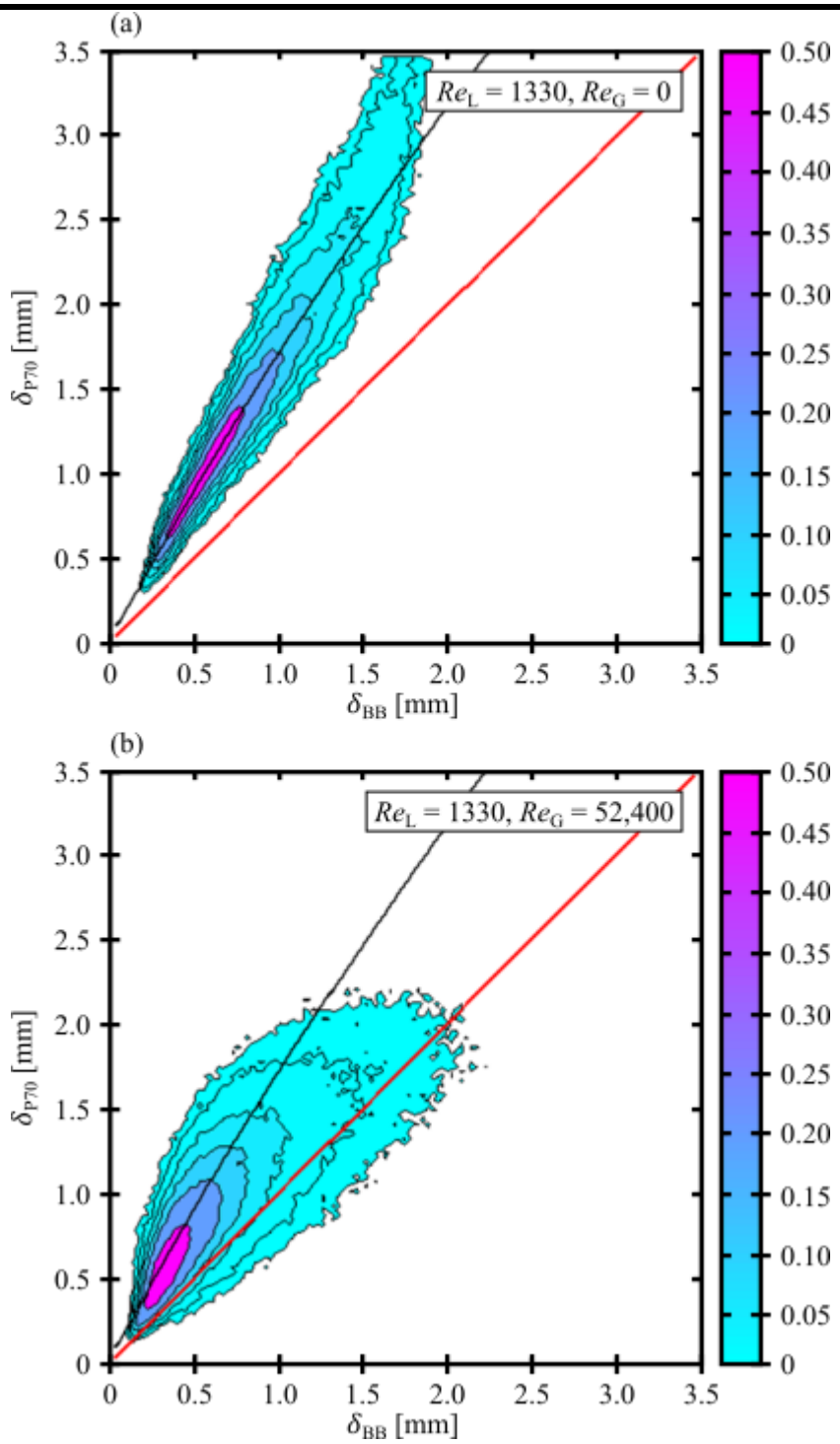


Figure 4-19 – PLIF70 and BBLIF joint probability density distributions ($P(\delta_{P70}, \delta_{BB})$) of flows at Re_L = 1330 and: (a) Re_G = 0; and (b) Re_G = 52,400. The colour-scale represents $P(\delta_{P70}, \delta_{BB})$, and the contours encompass 50 %, 80 %, 90 %, 95 %, 98 %, and 99 % of the data. The red and black-lines correspond to $\delta_{P70} = \delta_{BB}$ and predicted δ_{P70}, respectively.

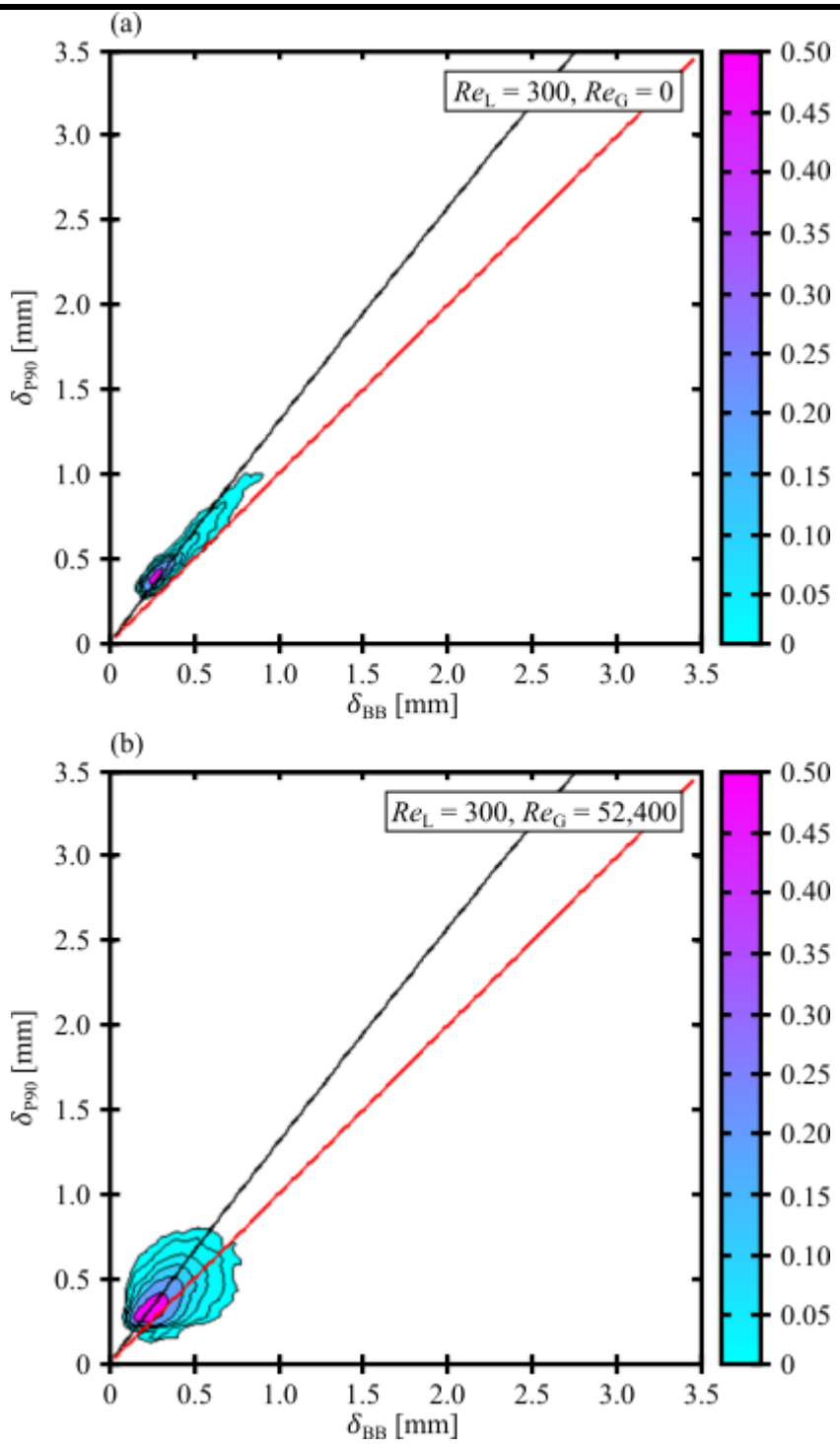


Figure 4-20 – PLIF90 and BBLIF joint probability density distributions ($P(\delta_{P90}, \delta_{BB})$) of flows at Re_L = 300 and: (a) Re_G = 0; and (b) Re_G = 52,400. The colour-scale represents $P(\delta_{P90}, \delta_{BB})$, and the contours encompass 50 %, 80 %, 90 %, 95 %, 98 %, and 99 % of the data. The red and black-lines correspond to $\delta_{P90} = \delta_{BB}$ and predicted δ_{P90}, respectively.

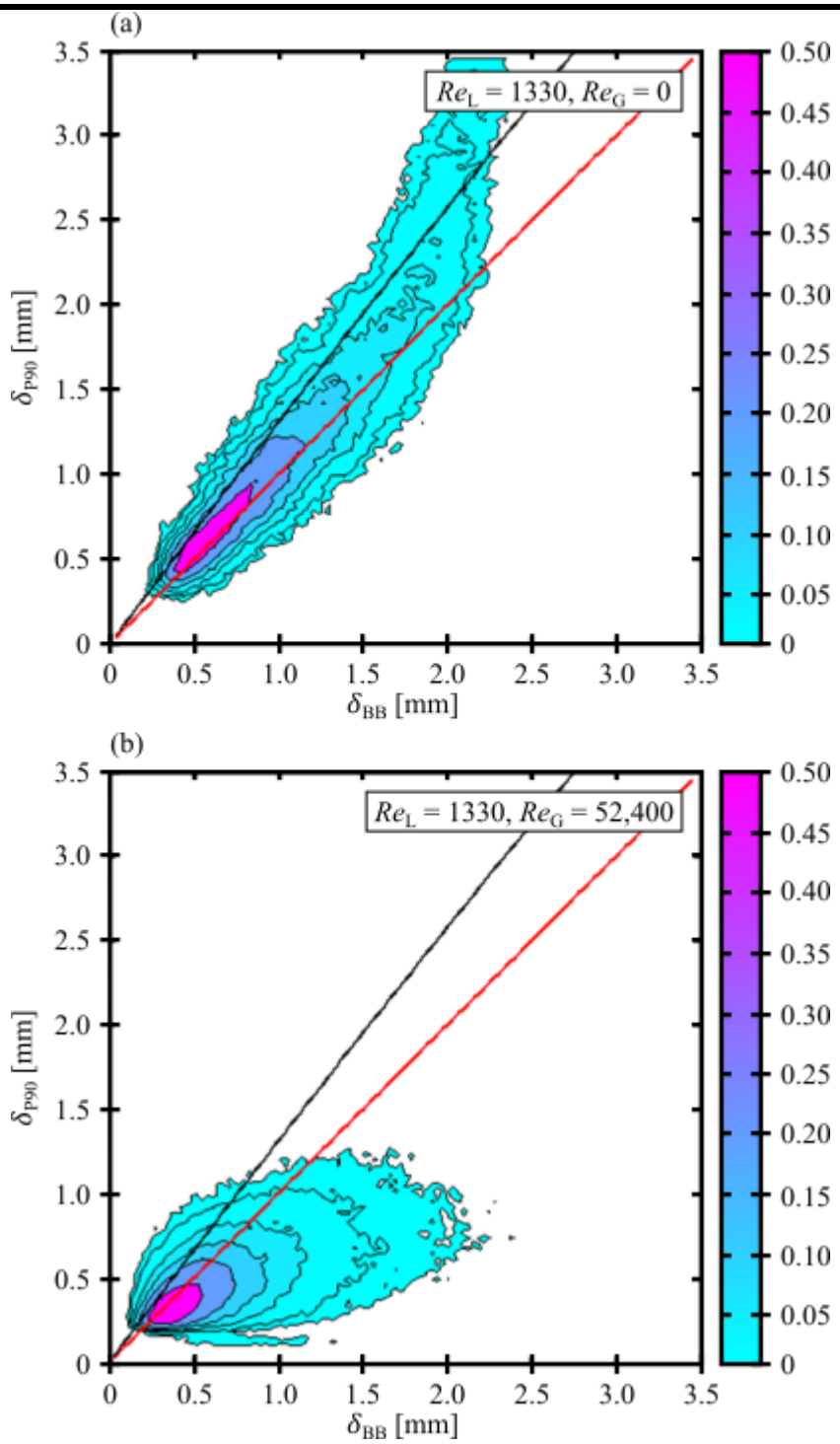


Figure 4-21 – PLIF90 and BBLIF joint probability density distributions ($P(\delta_{P90}, \delta_{BB})$) of flows at Re_L = 1330 and: (a) Re_G = 0; and (b) Re_G = 52,400. The colour-scale represents $P(\delta_{P90}, \delta_{BB})$, and the contours encompass 50 %, 80 %, 90 %, 95 %, 98 %, and 99 % of the data. The red and black-lines correspond to $\delta_{P90} = \delta_{BB}$ and predicted δ_{P90}, respectively.

4.6. Summary

In the measurement of liquid-film thickness (δ) in gas-liquid annular flows, planar laser-induced fluorescence (PLIF) and brightness-based laser-induced fluorescence (BBLIF) are the two most commonly used types of optical methods based on the principles of laser-induced fluorescence (LIF). In PLIF and BBLIF, the liquid-phase is seeded with a fluorescent dye and excited with a laser, however, the methods differ in the approach to the fluorescence emission collection and raw data treatment. In PLIF, the emitted fluorescence is collected to directly image an axial cross-section of the film; while in BBLIF, the collected fluorescence intensity signals are converted to film-thickness according to the Beer-Lambert law. Measurements of film-thickness with both LIF-based optical methods suffer from limitations due to total internal reflection (TIR) of either the fluorescent-light (in the case of PLIF) or the laser-light (in the case of BBLIF) at the gas-liquid interface (Cherdantsev et al., 2019; Häber et al., 2015;). In order to better understand the optical effects, liquid-film thickness measurements were performed in downwards air-water annular flows (Re_G = 0 – 85,000, Re_L = 140 – 1330) with the simultaneous application of PLIF and BBLIF to directly compare the ability of both methods to recover the shape of the gas-liquid interface at the same film region. In the present set of experiments, the effect of the PLIF camera observation angle (θ_P) relative to the excitation plane on the thickness measurements was also considered. One set of measurements with the standard camera alignment of θ_P = 90 °, which is referred to as PLIF90, and another set with θ_P = 70 °, which is referred to as PLIF70.

In the present work, two types of error sources were found in the PLIF measurements. The existence of the 'mirror effect' as described by Häber et al. (2015) was confirmed experimentally in smooth liquid-film regions. The emitted fluorescent-light undergoes TIR at circumferentially uniform gas-liquid interfaces and the resultant images of the film appear thicker, which leads to overestimations of the film-thickness. In addition, bright or dark-lines were occasionally observed within the liquid-film of the PLIF images. The position of these lines match the identified location

of the gas-liquid interface by BBLIF, and hence, it is assumed that this position represents the location of the true gas-liquid interface. The overestimation of the film thickness by PLIF90 and PLIF70 due to the mirror effect was evaluated in smooth films (i.e. absence of waves) and showed good agreement with the ratio of the PLIF and BBLIF recovered film-thickness (δ_P/δ_{BB}). In rough films, PLIF derived film-thickness was underestimated due to the refraction or TIR of the emitted fluorescent-light at circumferentially non-uniform gas-liquid interfaces. PLIF is less susceptible to this type of error when smaller camera observation angles (i.e. $\theta_P = 70$ °) was employed.

In flat and smooth film regions (interfacial slope angles < 45 °), BBLIF film thickness measurements were reliable. However, BBLIF was affected by a loss of signal sensitivity and saturation in thick film regions. Additionally, BBLIF was susceptible to light reflections in agitated and/or aerated flow regions due to the presence of complex or multiple interfaces, which appear with increasing frequency at higher gas and liquid flow-rates. BBLIF overestimates the local film-thickness in regions with high interfacial slopes and/or curvature that are found at the front-slope of ripple waves, edges of entrained gas bubbles, and disturbance waves. Furthermore, BBLIF underestimates the thickness in regions with multiple interfaces, and the error increases as the angle as the TIR angle is approached or exceeded.

Both PLIF and BBLIF film-thickness measurements are vulnerable to errors introduced by optical effects at the gas-liquid interface. The simultaneous application of both LIF-based optical methods was beneficial in the much improved understanding of the strengths and limitations of each technique. Despite this, non-trivial challenges remain in further minimising the film-thickness measurement errors and recovering more reliable information on the shape of complex interfacial wave phenomena. In the effort to overcome the limitations with PLIF, a new adaption of PLIF, which uses structured rather than uniform illumination, was developed. The use of the structured illumination was based on the observations of the observation of bright or dark-lines within the film of PLIF images.

CHAPTER

5. S-PLIF

The set of liquid-film thickness (δ) measurements with S-PLIF in falling liquid-film flows at $Re_G = 0$ and $Re_L \approx 150$ - 1500 is discussed in this Chapter. S-PLIF was directly compared with the PLIF approach to validate the new variation of PLIF. In addition, the mean film-thickness data of S-PLIF was compared with the BBLIF data presented in the previous Chapter, and data collected in other studies for similar flow conditions.

5.1. Introduction and problem statement

Based on the findings in the set of experiments conducted with the simultaneous application of BBLIF and PLIF (Chapter 4), the challenges with the implementation of PLIF to measure the thickness of liquid-films in gas-liquid annular flows are primarily associated with the presence of curvature at the gas-liquid interface (i.e. film free-surface). A pair of simultaneously collected raw PLIF70 and PLIF90 images of a falling-film ($Re_G = 0$) at $Re_L = 1510$ are presented in Figure 5-1. The pair of cameras were aligned at different observation angles (θ) relative to the excitation plane (i.e. laser-sheet). One of the cameras was aligned at an observation angle of $\theta_P = 70$ ° to produce the image in Figure 5-1(a), which is referred to as PLIF70; and the other camera was aligned at an observation angle of $\theta_P = 90$ °, which is referred to as PLIF90. A mirror image of the fluorescing liquid domain is projected into the camera and above the true liquid-film due to total internal reflection (TIR) of the emitted fluorescence from the excited film. This effect leads to an apparent gas-liquid interface in the PLIF images which are generally indistinguishable from the true gas-liquid interface.

The conventional approach to identify the position of the gas-liquid interface are based on either: (i) the fluorescence intensity threshold (Farias et al., 2012; Kokomoor & Schubring, 2014; Schubring et al., 2010; Zadrazil et al., 2014); or (ii) the local gradient of the fluorescence intensity profile (Charogiannis et al., 2015; 2017; Markides et al., 2016). For the sample PLIF images in Figure 5-1, the local intensity gradient approach was used to identify the gas-liquid interface, and the position of the interface as identified by PLIF70 (solid blue-line) and PLIF90 (solid cyan-line) have been superimposed on the frames. In addition, the location of the solid-liquid interface (dashed blue-line), which was acquired with the method described in Section 4.3.1 on page 122, is included in the images.

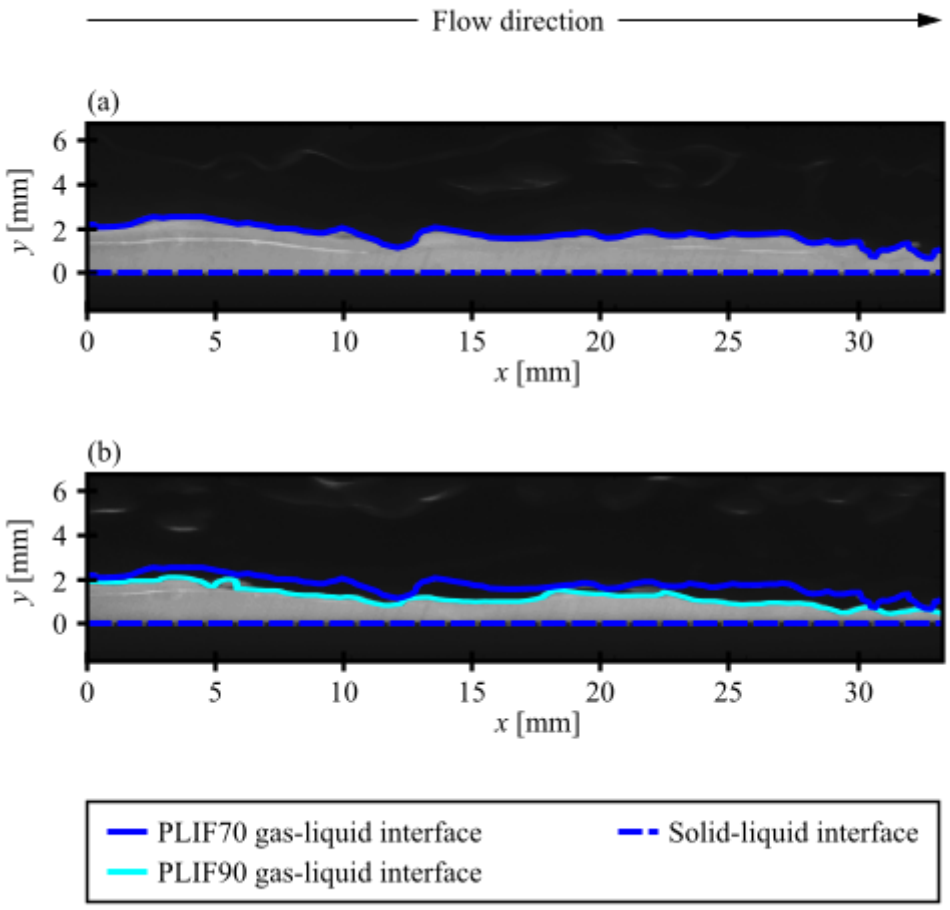


Figure 5-1 – For a falling liquid-film (i.e. $Re_G = 0$) at $Re_L = 1510$, sample raw image of: (a) PLIF70 image; and (b) PLIF90. The PLIF images have been superimposed with the position of the solid-liquid interface (dashed blue-line), and the location of the gas-liquid interface as obtained by PLIF70 (solid blue-line) and PLIF90 (solid cyan-line).

A number of observations were made in the evaluation of the PLIF images in Figure 5-1: (i) increase in the apparent liquid-film thickness (δ_{app}) with decrease in the observation angle (θ_P) of the camera relative to the illumination plane due to the increase in the spatial extent of the reflected fluorescence in the imaging plane; (ii) occasional appearance of bright-lines within the

liquid-film, such as the film region at $x = 0 – 10$ mm of the PLIF70 image and $x = 0 – 5$ mm of the PLIF90 image; and (iii) the presence of bright-lines in the liquid-film region at $x = 22 – 27$ mm of the PLIF70 image and the absence of the bright-line in the PLIF90 image in the same region. In the set of experiments presented in Chapter 4, the bright-lines were associated with the position of the true gas-liquid interface. The bright-lines were not found along the entire length of the liquid-film in the y direction, and absent in the majority of the PLIF images. Therefore, the bright-lines could not be used to systematically identify the interface. The discrepancy in the appearance of the bright-lines in the PLIF70 and PLIF90 images is probably due to the refraction or the total internal reflection (TIR) of the emitted fluorescence at the film region between the excitation and imaging planes. This effect, which is strongly dependent on the interfacial slope in the z direction, causes the illuminated film region to be 'hidden' from the camera and leads to an underestimation of the local film-thickness (δ).

In Figure 5-2, illustrations of the transverse cross-section of a gas-liquid annular flow in a pipe with qualitative ray-tracing of the emitted fluorescence from the excited liquid-film are provided to better describe the aforementioned effects on PLIF with a camera observation angle of $\theta_P = 90\,°$. The illustrations demonstrate the two principal errors which can occur in the identification of the gas-liquid interface for the thickness measurements of films with: (a) axially flat and circumferential symmetry (i.e., uniform circumferential curvature) in Figure 5-2(a); and (b) axially flat and circumferential asymmetry (i.e., non-uniform circumferential curvature) in Figure 5-2(b). The locations of Points A, B and C indicate the sources or origins of three fluorescence rays emitted from the film along the illumination plane in the y direction. The positions of Points A and C are at the near-wall and far-wall boundaries of the illuminated film, respectively. Therefore, the length between Points A and C represents the true local liquid-film thickness, which is projected into the camera by Rays A1 and C1.

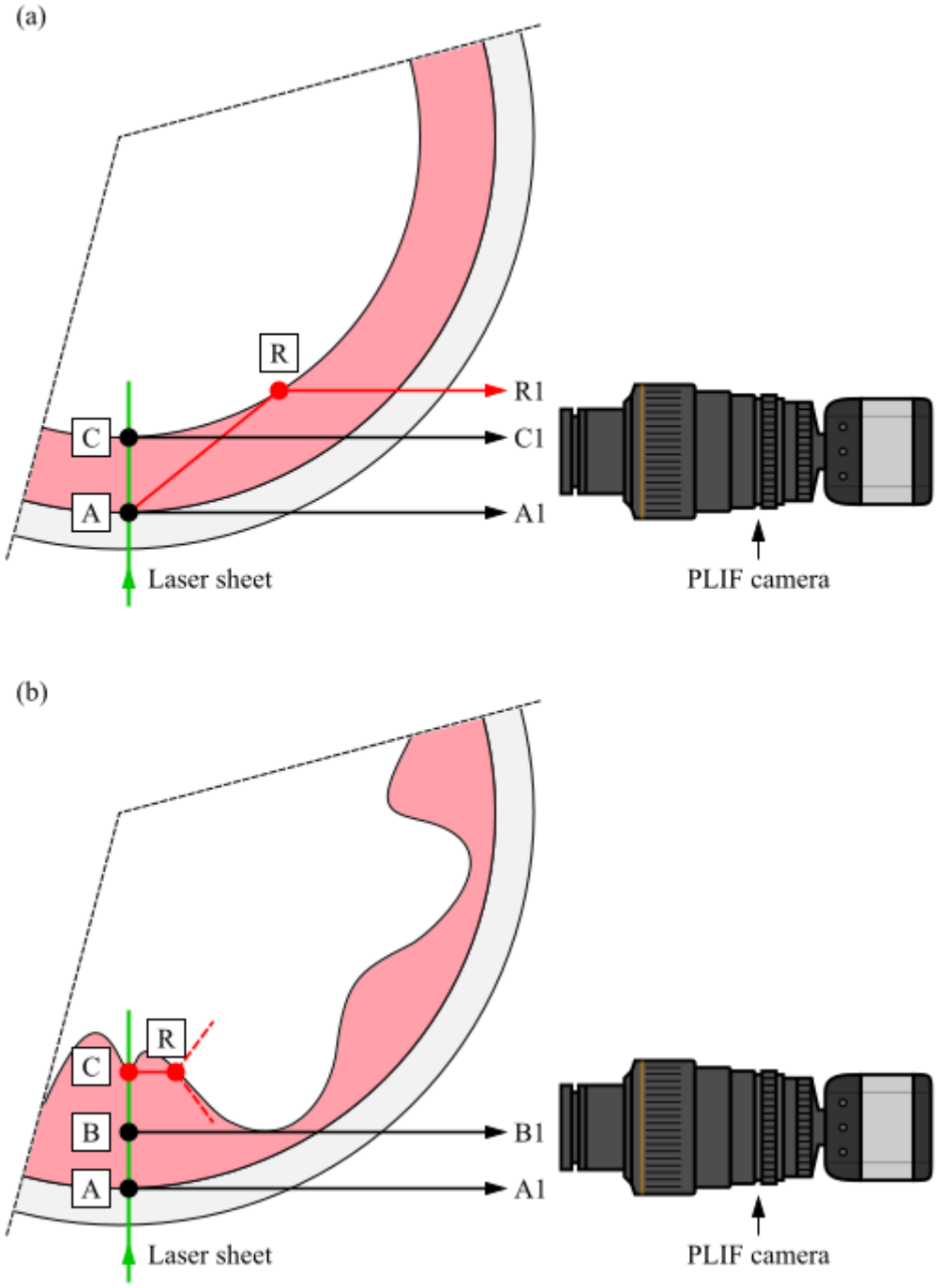


Figure 5-2 – Illustrations of the main sources of errors in the liquid-film thickness measurements by the PLIF technique: (a) Error Source I (ES-I) – identification of a larger liquid-film thickness due to total internal reflection (TIR) in a circumferentially uniform liquid-films, (b) Error Source II (ES-II) – identification of a smaller liquid-film thickness due to refraction or TIR in a circumferentially non-uniform liquid-film.

For the circumferentially uniform liquid-film in Figure 5-2(a), Ray R1 is the emitted fluorescence ray at Point A, which is reflected towards the camera at the gas-liquid interface at Point R. This source of error (ES-I) leads to an overestimated value of the local liquid-film thickness (A1R1 > AC). If Ray R1 undergoes total internal reflection (TIR) at the gas-liquid interface and the fluorescence intensity of Ray R1 is similar in magnitude with Rays A1 and C1, the ES-I error is more pronounced and difficult to identify and correct. For the circumferentially non-uniform liquid-film in Figure 5-2(b), the emitted fluorescence ray at Point C does not reach the camera due to refraction or TIR of the ray at the gas-liquid boundary at Point R. This source of error (ES-II) leads to in an underestimated value of the local liquid-film thickness (A1B2 < AC). In the measurements of Chapter 4, ES-I errors was more pronounced at a camera observation angle of $\theta_P = 70$ ° (i.e. PLIF70) for flat and smooth liquid-film regions; while ES-II errors was more pronounced at an observation angle of $\theta_P = 90$ ° (i.e. PLIF90).

In the application of the PLIF approach to obtain liquid-film thickness (δ) data of gas-liquid annular flows, the use of structured illumination rather than uniform illumination is proposed to address the challenges associated with the occurrence of ES-I errors. The employment of structured illumination is common in microscopic imaging studies (Elson et al., 2002; Gustafsson, 2000; Neil et al., 1997); and in the studies of sprays (Berrocal et al., 2008; Kristensson et al., 2008; Mishra et al., 2014) in which the ratio of the fluorescence to scattering intensity signal is used to determine the Sauter mean-diameter (SMD) of droplets.

The proposed adaptation of PLIF, which is referred to as structured planar laser-induced fluorescence (S-PLIF), was mainly implemented in falling liquid-films (i.e. $Re_G = 0$) and a few cases of liquid-films with gas-shear. The investigated range of flow conditions are provided in Tables 5-1 to 5-2. The experimental matrix was comprised of 14 data-points: 2 gas flow-rates and 12 liquid flow-rates. The investigated range of liquid volumetric flow-rate was $Q_L = 0.83$ – 8.28 L/min, which corresponds to liquid superficial velocities and liquid Reynolds numbers of j_L

= 0.017 – 0.172 m/s and Re_L = 147 – 1510. The definition of the liquid superficial velocity was $j_L = 4Q_L/\pi D_p^2$; while the liquid Reynolds number was defined as $Re_L = Q_L/\pi D_p \upsilon_L$, where υ_L is the kinematic viscosity of water. The investigated gas volumetric flow-rate range was Q_G = 500 – 100 L/min, which corresponds to gas superficial velocities of j_G = 0 – 20.7 m/s and gas Reynolds numbers of Re_G = 0 – 48,300. The gas superficial velocity was $j_G = 4Q_G/\pi D_p^2$, which is approximately equivalent to the bulk gas-phase velocity in annular flows with thin liquid-films. The definition of the gas Reynolds number was $Re_G = 4Q_L/\pi D_p \upsilon_G$, where υ_G is the kinematic viscosity of air. The temperature of the liquid-phase was $T_L \approx 20 \pm 2$ °C for the majority of the measurements.

A photograph of film-thickness (δ) measurements with S-PLIF is provided in Figure 5-3, and the configuration of the optics for the application of S-PLIF is discussed in detail in Section 3.2.3 on page 98. In this set of experiments, a pair of cameras was employed to simultaneously collect images of the flow at camera observation angles of θ_S = 70 ° and θ_S = 90 ° in order to investigate the effect and occurrence of ES-II errors on the collected images. The S-PLIF images were processed with S-PLIF and PLIF image processing algorithms to simultaneously obtain S-PLIF and PLIF film-thickness data. The PLIF and S-PLIF image processing algorithms are explained in Sections 4.2 and 5.2, respectively. For falling liquid-film flows at and $Re_L \approx 150 – 1500$, the effectiveness of S-PLIF is discussed through direct comparisons of the data acquired by S-PLIF (δ_S) and PLIF (δ_P). In addition, the present set of δ_S data were also compared with the data obtained with BBLIF (δ_{BB}) in Chapter 4, since it was collected over a similar range of flow conditions and in the same flow facility. In Section 5.3.1, the mean film-thickness ($\langle\delta\rangle$) and standard deviation of the film-thickness (σ_δ) are compared; while the probability density distributions of the film-thickness data are given in Section 5.3.2. While the demonstration of S-PLIF was primarily on falling-films, the capability of S-PLIF to correctly identify interfaces of highly agitated films is examined in Section 5.4. The uncertainties in the S-PLIF data are discussed in Section 5.5. Finally, a summary of the S-PLIF measurements is presented in Section 5.6.

Table 5-1 – List of the investigated gas flow conditions in the film-thickness measurements with S-PLIF.

Gas volumetric flow-rate	**Gas superficial velocity**	**Gas Reynolds number**
Q_G	j_G	Re_G
L/min	**m/s**	**–**
0	0	0
500	10.4	22,100
1000	20.7	48,300

Table 5-2 – List of the investigated liquid flow conditions in the film-thickness measurements with S-PLIF.

Liquid volumetric flow-rate	**Liquid superficial velocity**	**Liquid Reynolds number**
Q_L	j_L	Re_L
L/min	**m/s**	**–**
0.83	0.017	147
1.25	0.026	222
1.66	0.034	296
2.43	0.050	433
3.20	0.066	565
4.10	0.085	721
5.04	0.104	881
5.84	0.121	1020
6.64	0.138	1150
7.45	0.154	1290
8.01	0.17	1360
8.27	0.171	1420
8.28	0.172	1510

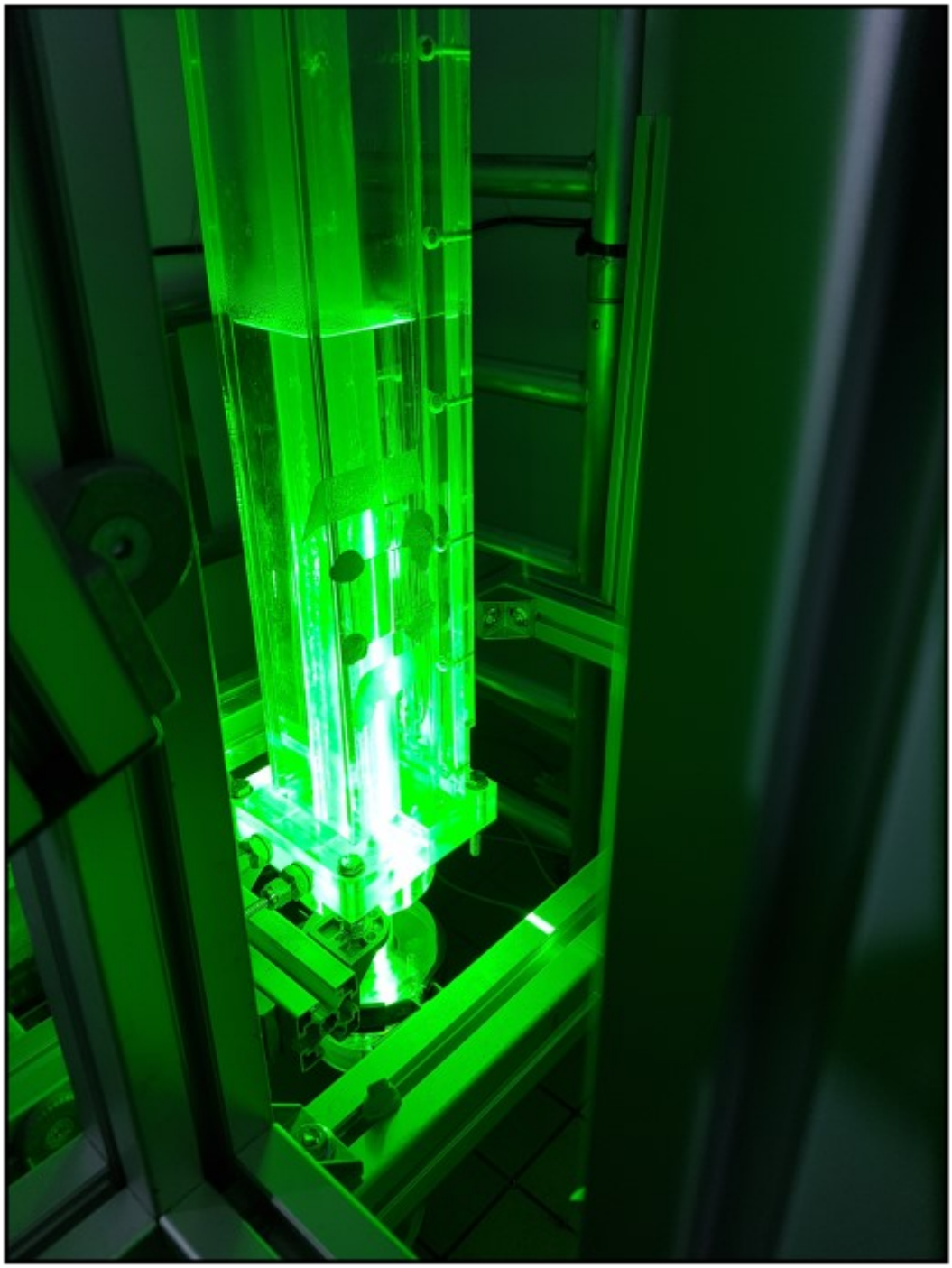


Figure 5-3 – Photograph of the application of S-PLIF to measure film-thickness in falling liquid-film flows. The investigated range of flow conditions with the proposed methodology was $Re_G \approx 0$ – 48,000 and $Re_L \approx 150$ – 1500.

5.2. S-PLIF image processing

Similar to PLIF, the fluorescing liquid domain in the S-PLIF images ($I_S(x, y, t)$) represents the axial liquid-film cross-section in the x (longitudinal) and y (radial) directions. Therefore, the extraction of liquid-film thickness (δ) data in the images is based on the ability to identify the near-wall (i.e. solid-liquid) and far-wall (i.e. gas-liquid) boundaries. The method of locating the solid-liquid interface is discussed in Section 5.2.1, and the method of locating the gas-liquid interface is discussed in Section 5.2.2. Due to the use of a structured illumination to excite he liquid-film, the emitted fluorescence collected by the pair of cameras was comprised of a pattern of parallel-lines, which extended from the solid-liquid boundary to the apparent gas-liquid boundary. In the visual inspection of the S-PLIF images, the direction of the parallel-lines changed within the liquid-film as the emitted fluorescence is reflected at the true gas-liquid interface. This major observation was the basis of the S-PLIF image processing algorithm to identify the position of the gas-liquid interface.

The current set of collected S-PLIF images were also processed with PLIF image processing algorithms to simultaneously obtain PLIF δ data. The PLIF image processing algorithm is discussed in detail in Section 4.3.2 on page 124. The image processing algorithm of the S-PLIF images were developed in-house with the MATLAB software. The raw S-PLIF images were initially corrected for perspective distortions with the LaVision DaVis software, and the spatial resolution of the frames was determined to be ≈ 27.0 μm/pixel. Therefore, each pair of parallel-lines occupied ≈ 8 pixels along the image domain. The amplitude of the fluorescence signal modulation was 20 %, which provided sufficient contrast between the lines and permitted sufficient light in the dark regions of the illuminated liquid-film. This was particularly important for the possible use of fluorescent particles to simultaneously conduct particle image or tracking velocimetry (PIV or PTV) measurements with the S-PLIF technique.

5.2.1. Solid-liquid interface

In the employment of the PLIF technique in Chapter 4, the position of the solid-liquid interface was determined with the use of the calibration-target images as described in Section 4.2.1 on page 122. However, systematic errors could be induced with this approach by the possible misalignment of the target and excitation plane, or the edge of the target and inner wall of the test-section. An alternative method was the direct use of the flow images (Charogiannis et al., 2015; 2017). For the current set of S-PLIF images, the utilization of 'reference' images was the selected approach to locate the position of the solid-liquid interface. The same images would be used in the identification of the gas-liquid interface as explained in the next section. For this approach, the test-section of the flow-loop system was flooded with the working fluid (i.e. the water seeded with Rhodamine 6G dye) and excited with the structured illumination as depicted in Figure 3-17 on page 102. A sequence of 100 reference images were collected with the pair of cameras and the images were corrected for perspective distortions in the LaVision DaVis software. Finally, an average reference image was produced with the corrected raw images. A sample frame of a reference image is shown in Figure 5-4(a). For every image column at a given x value, the fluorescence intensity profiles along the y axis of the images were examined in the following steps to identify Points S1 to S3 as demonstrated in Figure 5-4(b):

1) First-order polynomial fits were applied to the set of fluorescence signals before and after the maximum intensity, $J_{max}(x)$ to determine the intercept, and hence, Point S1.

2) The fluorescence signal gradient was locally tracked to identify the position of Point S2, which is the location at which the emitted fluorescence by the working fluid was diffusely reflected by the FEP pipe wall.

3) The y-coordinate of the solid-liquid interface was determined to be Point S3, which is the mid-point between Points S1 and S2.

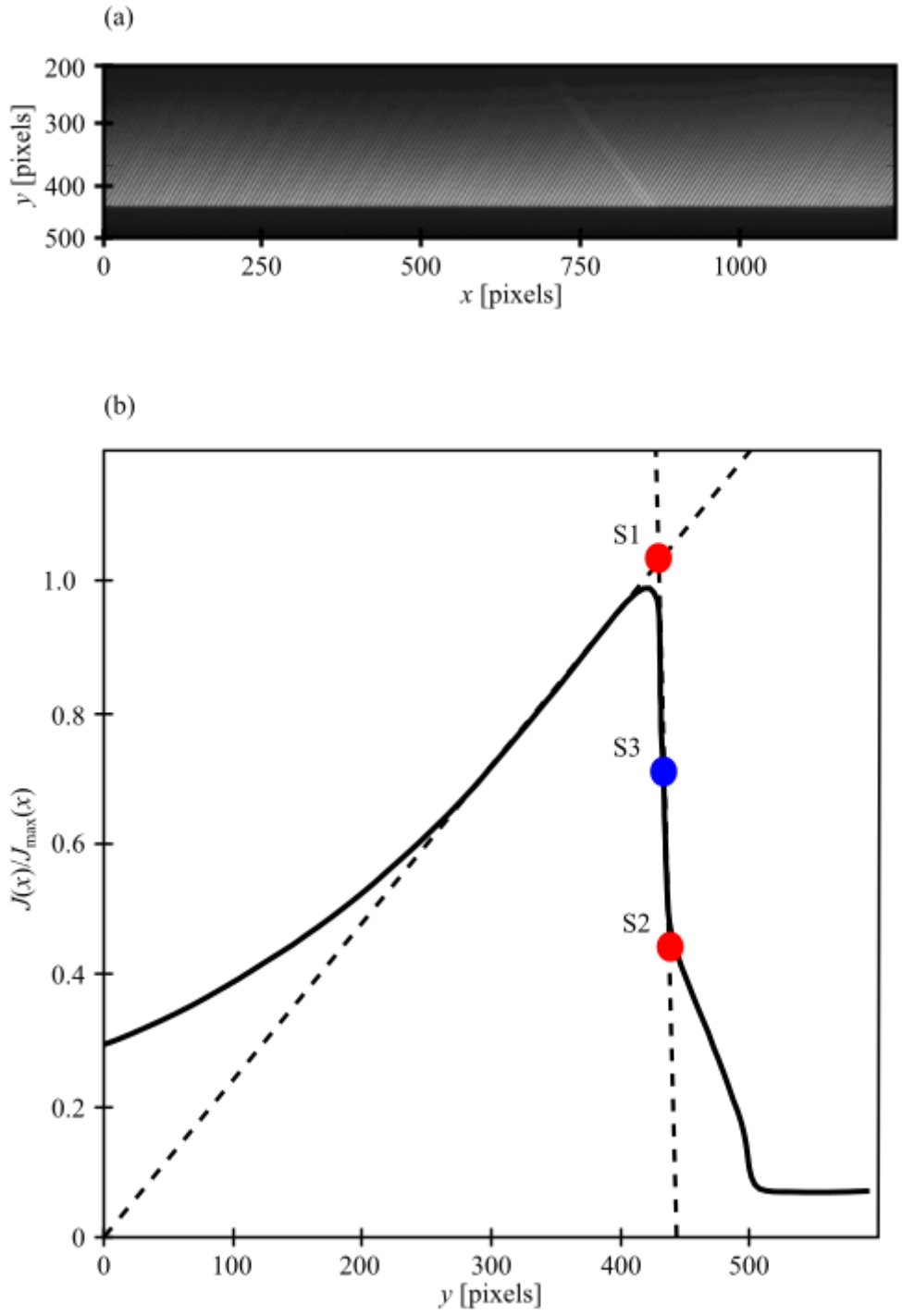


Figure 5-4 – Identification of the solid-liquid interface in the S-PLIF images: (a) sample frame of a raw reference image; and (b) fluorescence intensity profile along the *y* axis of the reference image in (a).

5.2.2. Gas-liquid interface

Following the perspective distortion corrections of the raw S-PLIF images with the LaVision DaVis software, the images were subsequently were processed with custom-built MATLAB algorithms to identify the position of the gas-liquid interface. The image processing routine for each S-PLIF image is demonstrated with a single instantaneous raw frame of a falling liquid-film at Re_L = 1150 in Figure 5-5. The routine comprised of the following steps:

1) The 'salt-and-pepper' noise in the raw image was removed with a 5 × 5 median filter. This non-linear filter was chosen as it did not affect the fluorescence intensity variation caused by the structured illumination.

2) The variation in the energy of the laser-sheet due to the Gaussian profile of the laser-beam was corrected by normalizing the filtered frame with the maximum intensity (J_{max}) to produce the image in Figure 5-5(a). The $J_{max}(x)$ values were obtained from the average of the fluorescence intensity profiles at each x.

3) Based on the filtered and normalized image, directional gradients were calculated to generate the gradient-direction image in Figure 5-5(b). Steps 1 to 3 were also applied to the reference image to produce a reference gradient-direction image.

4) The absolute difference between the gradient-direction frames of the flow image and the reference image was found to create the frame in Figure 5-5(c).

5) The gas-liquid interface was identified by applying a threshold value on the image in Figure 5-3(c). The signal value was ≈ 0 in the liquid domain, and in the area outside of the liquid domain, the signal value increased by 2 orders of magnitude.

6) The image was inspected for outliers, and a moving median filter was applied to the signal to produce the image in Figure 5(d).

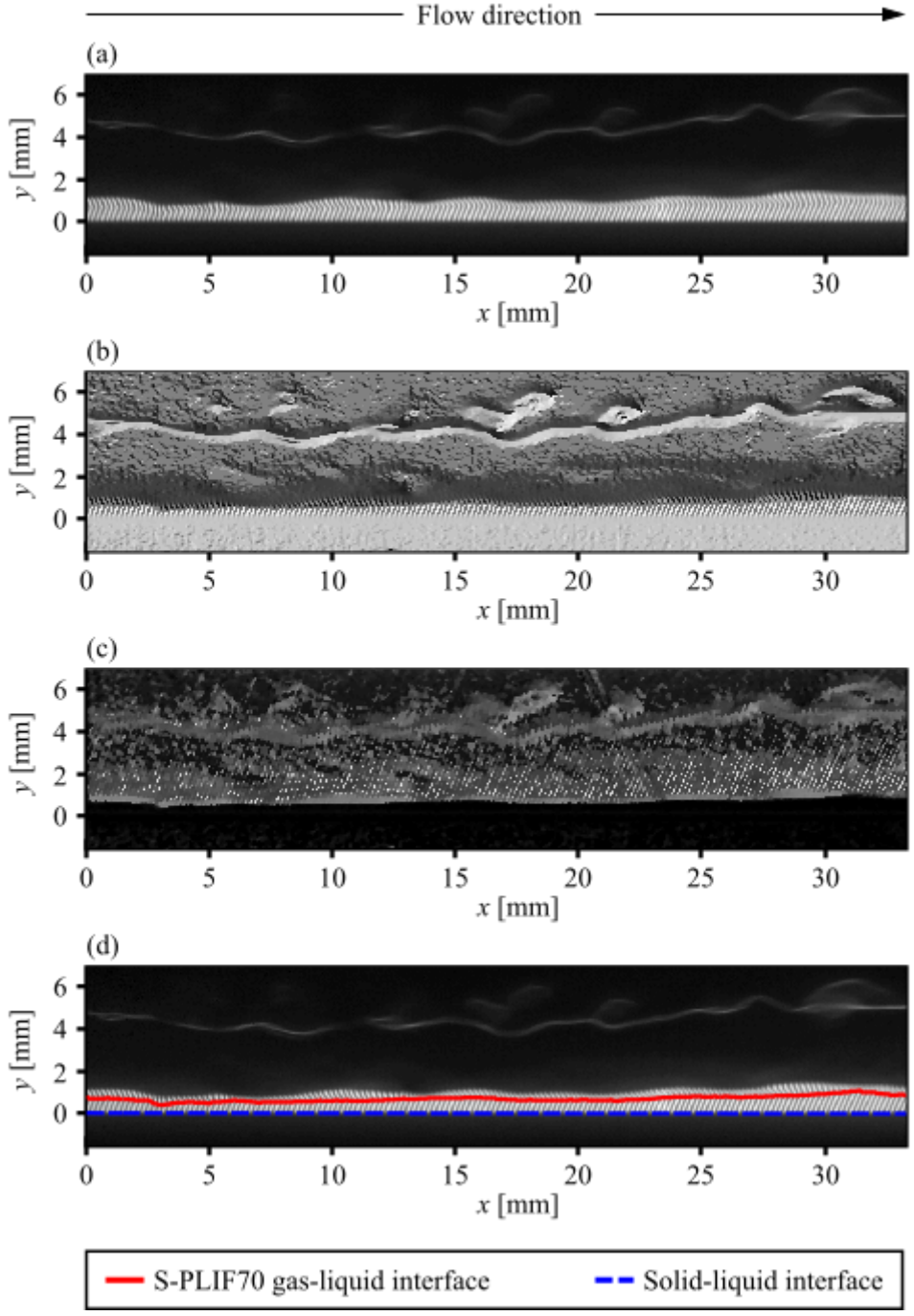


Figure 5-5 – Identification of the gas-liquid interface in the S-PLIF images: (a) median filter and laser-sheet correction applied on a raw S-PLIF70 frame of a falling film at $Re_L = 1150$; (b) a gradient-direction frame of (a); (c) absolute value of the difference between the frame in (b) and the gradient-direction frame of the reference image; and (d) frame (a) with the identified position of the gas-liquid (solid red-line) and solid-liquid (dashed blue-line) interfaces.

5.3. Quantitative analysis

For the investigated range of liquid flow conditions in falling-films, the liquid-film thickness data acquired by PLIF (δ_P) and S-PLIF (δ_S) are provided in this Section. In Section 5.3.1, the mean liquid-film thickness ($\langle\delta\rangle$) of PLIF and S-PLIF are compared with the $\langle\delta\rangle$ data obtained by Karapantsios et al. (1989), Karapantsios & Karabelas (1995), Zadrazil et al. (2014), and BBLIF in Chapter 4. In addition, the standard deviation of the liquid-film thickness (σ_δ) of PLIF and S-PLIF are compared with the data collected BBLIF data presented in Chapter 4. Finally, the probability density distributions of the liquid-film thickness data are presented in Section 5.3.2.

5.3.1. Statistical moments

For falling liquid-films at $Re_G = 0$ and $Re_L \approx 150 - 1500$, a plot of the mean liquid-film thickness ($\langle\delta\rangle$) of PLIF70, PLIF90, S-PLIF70, and S-PLIF90 as a function of the liquid Reynolds number (Re_L) is provided in Figure 5-6(a), which includes the $\langle\delta\rangle$ data acquired by BBLIF in Chapter 4. The $\langle\delta\rangle$ data of BBLIF, PLIF90 and S-PLIF70 are in good agreement with each other. The mean relative deviation between the BBLIF and S-PLIF70 $\langle\delta\rangle$ data is 4 %, and the mean relative deviation between the BBLIF and PLIF90 $\langle\delta\rangle$ data is 6 %. However, the S-PLIF70 $\langle\delta\rangle$ data lie consistently higher than PLIF90.

In the theoretical study by Häber et al. (2015), the overestimation of film-thickness by PLIF90 is ≈ 30 % for smooth liquid-film regions due to total internal reflection (TIR) and ES-I errors. However, Häber et al. (2015) assumed annular flows was axisymmetric (i.e. symmetric in respect to an axis). The analysis did not consider the three-dimensionality of the flow, which causes underestimations of δ_{P90} due to ES-II errors as observed in Chapter 4. The effect of ES-II was examined by comparing the deviations of the $\langle\delta\rangle$ data acquired by S-PLIF70 and SPLIF90.

S-PLIF70 can correctly identify the gas-liquid interface; while the overestimation of δ due to ES-I errors are suppressed in S-PLIF90, however, it is still subjected to ES-II errors. The mean relative deviation between S-PLIF70 and S-PLIF90 was 27 %. The maximum relative deviation between S-PLIF70 and S-PLIF90 was – 34 % at $Re_L \approx 1500$, while the minimum was 19 % at $Re_L = 565$. If the overestimation of the δ_{P90} due to ES-I errors is ≈ 30 %, the effects of ES-I and ES-II should effectively cancel out each other in time-averaged data. Therefore, the BBLIF, S-PLIF70 and PLIF90 data should be in good agreement, which is observed in the plot of Figure 5-6(a).

In Figure 5-6(b), similarly limited mean relative deviations are observed between the BBLIF data in Chapter 4, the PLIF data of Zadrazil el al. (2014), and the LIF data by Karapantsios et al. (1989) and Karapantsios & Karabelas (1995). It should be noted that the PLIF90 data obtained in the simultaneous application of PLIF and BBLIF in Chapter 4 show greater deviations in comparison with the PLIF90 and S-PLIF70 data, and the PLIF data of Zadrazil et al. (2014). This discrepancy is probably due to the inaccuracies in the identification of the solid-liquid interface, which can induce systematic errors in the PLIF data. Based on the configuration of the current optical magnification, a 4 pixel shift in the solid-liquid boundary corresponds to a deviation in the mean film-thickness of > 100 μm or ≈ 10 % for a film with $\langle\delta\rangle = 1$ mm. The mean deviation between the current set of PLIF70 and S-PLIF70 $\langle\delta\rangle$ data is 69 %, and the mean deviation between the PLIF70 and BBLIF $\langle\delta\rangle$ data in Chapter 4 is 62 %; which is in good agreement. The higher mean deviations between PLIF70 and the S-PLIF70 and BBLIF $\langle\delta\rangle$ data can be linked to the increased spatial extent of the TIR regions in the imaging plane of the PLIF70 camera, which leads to greater ES-I errors; and the substantial suppression of refraction or TIR at the three-dimensional (3-D) gas-liquid interface, which reduces ES-II errors.

The good agreement of the mean liquid-film thickness data obtained by PLIF90 and S-PLIF70 is due to the PLIF camera observation angle of $\theta_P = 90$ ° relative to the illumination plane. When the observation angle of the PLIF camera was $\theta_P < 90$ °, the agreement between the two

sets of data would be invalid. In reality, the observation angle of the camera might have to be $\theta_P < 90$ ° due to the physical constraints of the available experiment space. The effects of ES-I and ES-II errors do not cancel each other out in either statistical interpretations of temporal fluctuations in the liquid-film thickness data with the use of metrics such as standard deviation, or isolated interpretations with the use of local and time-resolved data. Therefore the reliability of PLIF with $\theta_P < 90$ ° is compromised, which is evident in the deviation between the PLIF70 and PLIF90 σ_δ data in Figure 5-7.

For falling-films at $Re_G = 0$ and $Re_L \approx 150 - 1500$, a plot of the standard deviation of the liquid-film thickness (σ_δ) data acquired as a function of Re_L is presented in Figure 5-7. The plot includes the data of PLIF70, PLIF90, S-PLIF70, S-PLIF90, and the BBLIF data presented in Chapter 4. The σ_δ data of PLIF and S-PLIF increase near-monotonically with the increase of Re_L, however, the PLIF σ_δ data are consistently higher than the S-PLIF σ_δ data. This observation is expected due to the inverse effects of the two optical phenomena which cause ES-I and ES-II errors on the measurements of local film-thickness; and hence, accentuates the discrepancy observed in the trends. The mean relative deviation between the PLIF70 and PLIF90 data and the PLIF70 and S-PLIF70 data is ≈ 20 % and ≈ 50 %, respectively. The ES-I errors in S-PLIF90 have a negligible effect on the σ_δ data of S-PLIF90 in comparison with the data acquired with S-PLIF70, which is in contrast with the observations in the $\langle\delta\rangle$ data. In the visual inspection of the liquid-film thickness time-traces obtained from the S-PLIF70 and S-PLIF90 data, S-PLIF90 display lower δ values in the region of base-films and region of thicker wavy films. In the assumption that the ES-I errors are taken into account by the application of structured illumination, the mismatch in the data is caused by ES-II errors.

In the direct evaluation of the liquid-film thickness time-traces for the current set of data, ES-II errors appear to similarly affect the S-PLIF δ data along the entire liquid-film topology. The BBLIF data in Chapter 4 is in good agreement with the S-PLIF data sets with the exception of

falling-films at $Re_L \approx 1050$. In the set of experiments presented in Chapter 4, a steep increase in σ_δ was found until $Re_L \approx 800$, and subsequently a drop and a further increase in σ_δ at $Re_L \approx 1300$. For the current set of data at $Re_L \approx 800 - 1050$, the trend of the σ_δ as a function of Re_L is more resembling of the data collected by Karapantsios et al. (1989) and Karapantsios and Karabelas (1995); and additionally the trends observed in Chapter 4 for liquid-films with gas-shear.

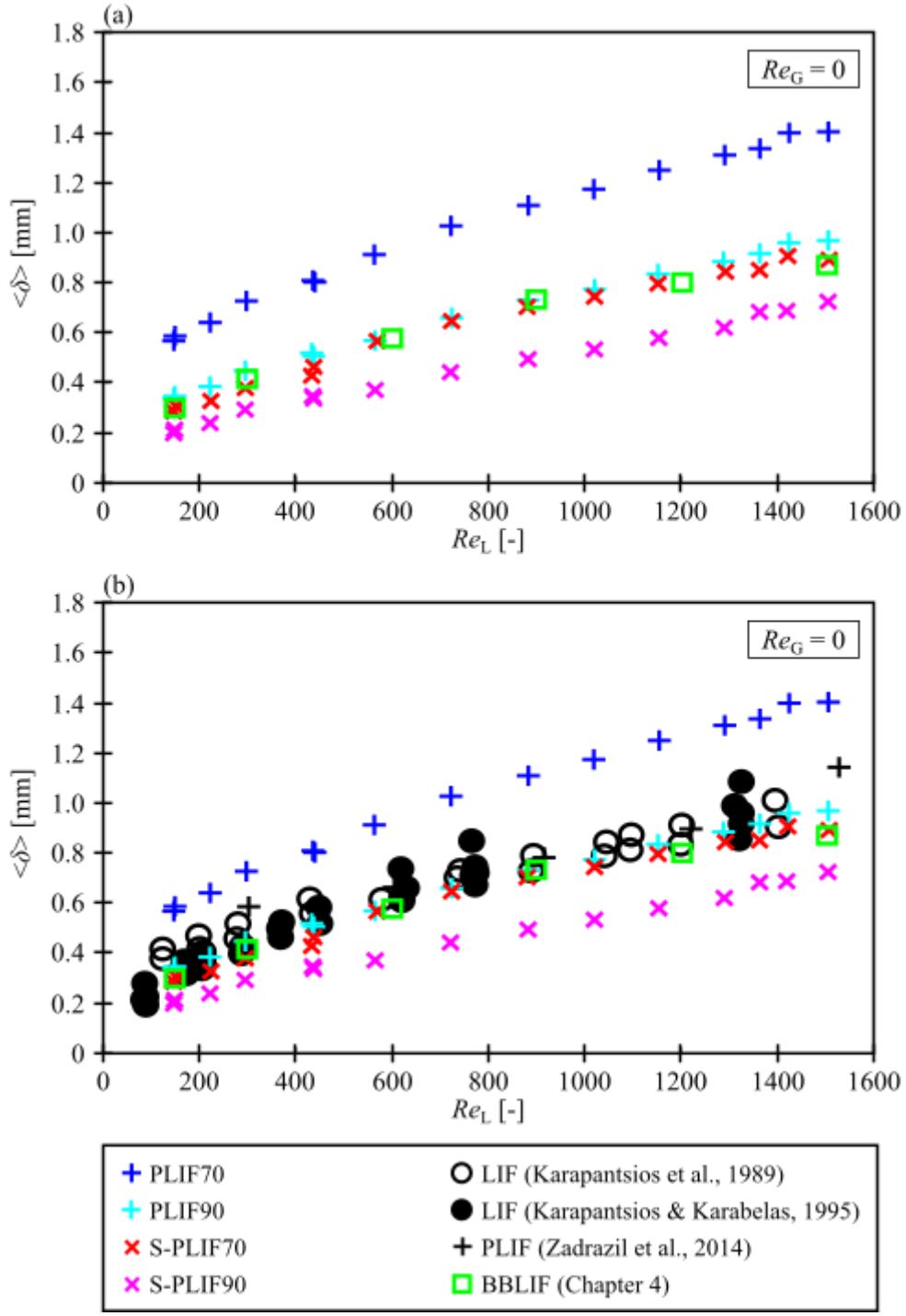


Figure 5-6 – For falling liquid-films (i.e. $Re_G = 0$), comparison of the mean film-thickness ($\langle\delta\rangle$) data obtained by: (a) PLIF70, PLIF90, S-PLIF70, S-PLIF90 and BBLIF (Chapter 4); (b) PLIF70, PLIF90, S-PLIF70, S-PLIF90, Karapantsios et al. (1989), Karapantsios and Karabelas (1995), Zadrazil et al. (2014), and BBLIF (Chapter 4).

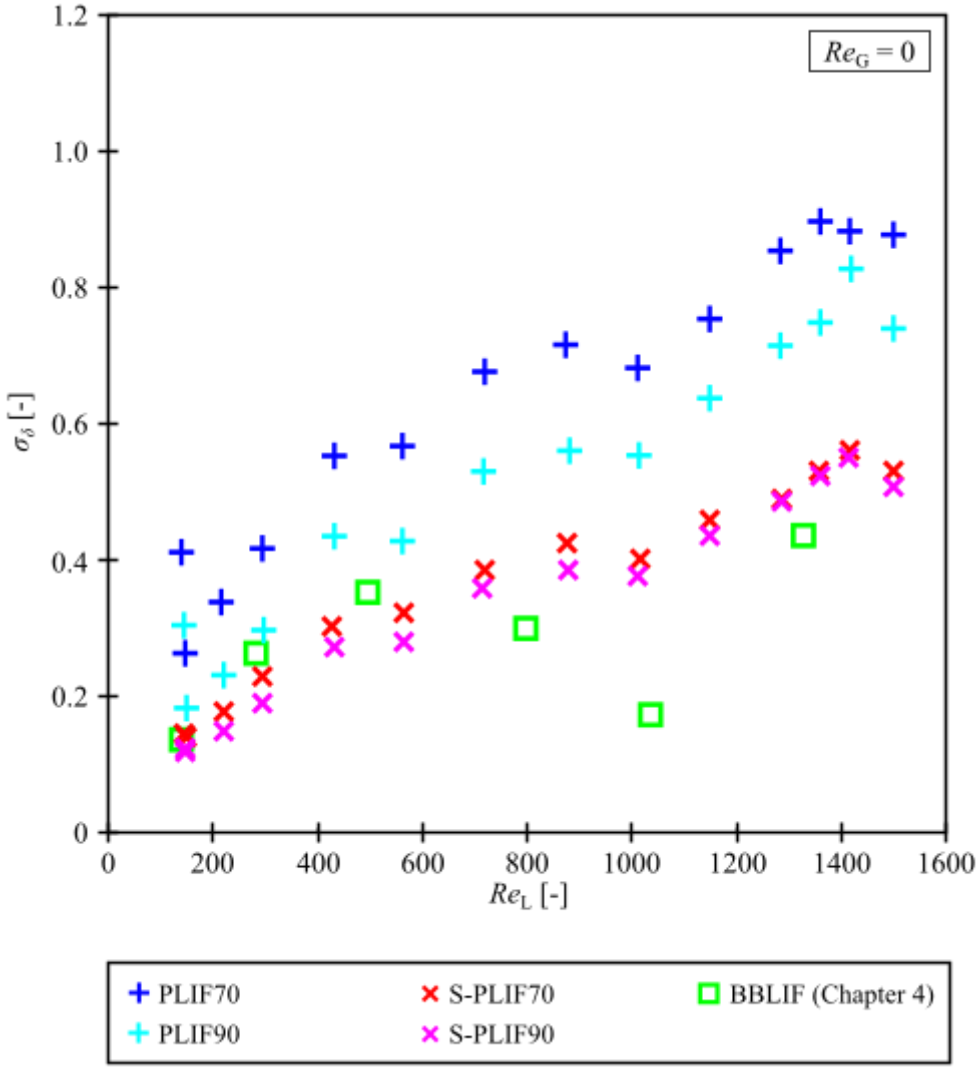


Figure 5-7 – For falling liquid-films (i.e. $Re_G = 0$) at $Re_L \approx 150 - 1500$, a plot of the standard deviation of liquid-film thickness (σ_δ) as a function of Re_L, which includes the data acquired by PLIF70, PLIF90, S-PLIF70, S-PLIF90, and BBLIF (Chapter 4).

5.3.2. Probability density distributions

For a falling-film flow at $Re_L \approx 1500$, plots of the local and instantaneous liquid-film thickness data of PLIF70 (δ_{P70}), PLIF90 (δ_{P90}), and S-PLIF90 (δ_{S90}) as a function of the local and instantaneous film thickness data of S-PLIF70 (δ_{S70}) are presented in Figure 5-8. Based on the bivariate distributions of the δ values obtained with PLIF and S-PLIF, the colour scheme of the contour-lines in each plot represent the normalized probability of finding a specific pair of δ data. In addition, the black-lines in the plots represent $\delta_{S70} = \delta_{S90}$, $\delta_{S70} = \delta_{P90}$, and $\delta_{S70} = \delta_{P70}$ in Figures 5-8(a), 5-8(b), and 5-8(c), respectively. In the generation of the plots, 25 values of δ were randomly selected per image pair from the set of 500 image runs.

In Figure 5-8(a), the majority of the δ_{S90} data lie below the black-line (i.e. the values of δ_{S90} are generally lower than δ_{S70}). The δ data with the highest probability correspond to the substrate-film regions, since large amplitude interfacial waves are seldom encountered in this type of flow. In Figure 5-8(b), the highest probability contour-lines are found within the black-line ($\delta_{S70} = \delta_{S90}$) as the effects which cause ES-I and ES-II errors frequently cancel each other out in PLIF90; and as discussed earlier in Section 5.3.1, this is the reason for the good agreement between the δ_{BB}, δ_{P90}, and δ_{S70} data, which is demonstrated in Figure 5-6(a). Finally, in Figure 5-8(c), the δ_{P70} data lie consistently higher than δ_{S70}, and hence, the large deviations between the two data sets is due to the increased spatial extent of TIR regions which introduces more ES-I errors in the PLIF70 images.

In each plot, the lack of data near the two axes (i.e. thin liquid-films with $\delta < 100$ μm) was due to the modulation transfer function (MTF) of the used optical arrangement in the current work, which limits the measurable spatial frequency. Based on the similar optics used by Markides & Mastorakos (2006), the effective spatial resolution, which is the ability of relevant optical elements (e.g. camera, lens) in the optical path between the camera senor and the illumination

plane to resolve spatial gradient (contrast) information, was determined to be 4 – 6 pixels. As a result, sharper intensity gradients (i.e. higher spatial frequency), which correspond to very thin liquid-films with $\delta < 100$ μm, are not expected to be resolved. This limitation can be overcome to an extent by the employment of either a camera with a higher resolution and a greater number of pixels, a better quality lens, and/or a smaller region of interrogation (ROI).

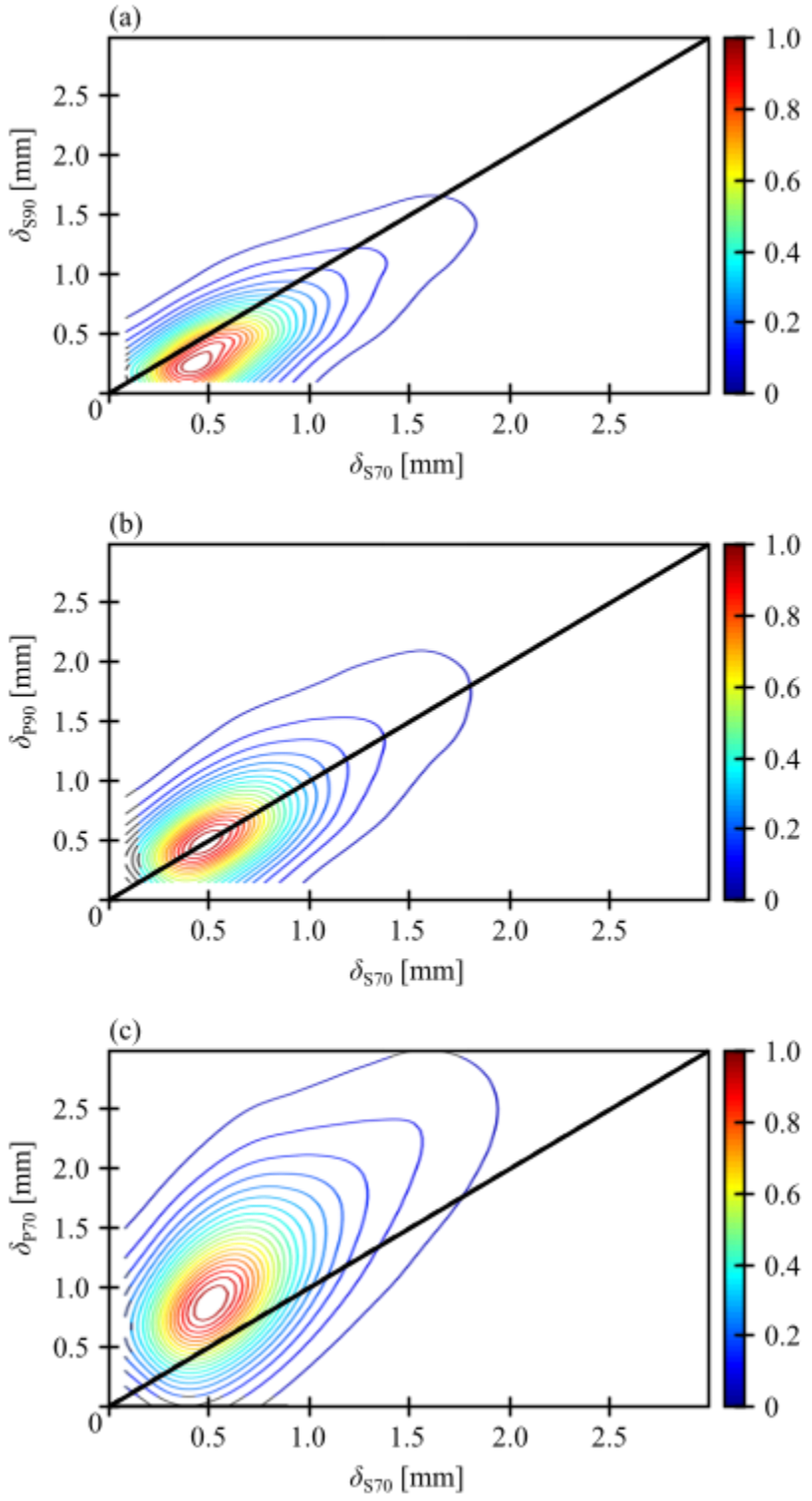


Figure 5-8 – Contour plots of the joint probability distributions of the local and instantaneous film-thickness data obtained by S-PLIF70 (δ_{S70}) against: (a) S-PLIF70 (δ_{S90}); (b) PLIF90 (δ_{P90}); and (c) PLIF70 (δ_{P70}).

5.4. Liquid-films with gas-shear

The demonstration of the S-PLIF technique was focused on falling liquid-film flows (i.e. $Re_G = 0$) in vertical pipes. In this section, the capability of S-PLIF to correctly identify the gas-liquid interface of highly agitated and rough liquid-films is examined. In Figure 5-9(a), an instantaneous raw S-PLIF70 image of a large amplitude interfacial wave is presented, which is superimposed with the identified position of the gas-liquid interface by S-PLIF70 (solid red-line) and the corresponding position of S-PLIF90 (dashed black-line) gas-liquid interface in the S-PLIF90 image. In addition, the solid-liquid interface is represented by the dashed blue-line. At the liquid-film region of $x = 0 – 15$ mm, good agreement was observed between S-PLIF70 and S-PLIF90, which indicates a limited loss of information by S-PLIF90 due to ES-II errors. The ES-II errors are commonly accompanied with a lack of reflected light towards the collection optics, which was found in very thin film regions in the S-PLIF images.

Gas bubble entrainment in liquid-films with gas-shear is frequent as shown in Figures 5-9(b) and 5-9(c). For PLIF and S-PLIF, the presence of entrained gas bubbles between the excitation and imaging planes continuously conceals the location of the true gas-liquid interface, which leads to abrupt fluctuations in the liquid-film thickness profile. In other liquid-film regions, the pattern of the structured illumination is conserved in the S-PLIF images, and consequently, the S-PLIF processing algorithms can successfully acquire the interface position. The application of BBLIF in flows with similar flow conditions is also associated with limitations, since the emitted fluorescence from the film is reflected at the interfaces of out-of-plane bubbles and into the camera; and results in peaks in the film-thickness profile. In Figure 5-9(b), the entrained gas bubble density is relatively low, and gas bubbles within the illumination plane cast a shadow. Furthermore, the identification of the true gas-liquid interface with S-PLIF is mostly reliable. Therefore, the additional advantage of applying structured illumination rather than uniform illumination is the ability to identify out-of-plane gas bubbles based on the presence of the original

or reflected pattern of parallel-lines above the gas bubbles.

For a given Re_L, film regions with smooth gas-liquid interfaces become more scarce as the entrained gas bubble density increases with increasing Re_G. Therefore, abrupt fluctuations in the local liquid-film thickness is frequently observed. These regions can be identified relatively easily by tracking the local gradient of the interface, and hence, the relevant film-thickness data can either be neglected or interpolated. Therefore, the employment of S-PLIF provides more reliable results than PLIF, and also allows for better interpretations of the collected flow images. For a flow at even higher Re_G that is shown in Figure 5-11(d), the three-dimensionality of the flow suppresses any total internal reflections (TIR) at the gas-liquid boundary and reflections of the structured illumination pattern almost disappear completely in the S-PLIF images. The position of the gas-liquid interface is interpreted as the location of the disappearance of the imposed pattern at the gas-liquid boundary by the S-PLIF processing routines. In these types of flow conditions (i.e. films with high gas-shear), the liquid-film thickness data obtained by BBLIF suffers with substantial and systematic overestimations (often exceeding 100 %) due to TIR at the boundaries of in-plane and out-of-plane gas bubbles, which contribute to the collected fluorescence intensity by the camera (as observed in the BBLIF images and data in Chapter 4). In contrast, PLIF provides more reliable information in the vicinity of entrained gas bubbles, however, the identification of bubbles located between the illumination and imaging planes is far from trivial; and the position of the gas-liquid interface becomes ambiguous.

In the S-PLIF images, the gas-liquid interface of liquid-film regions with uninterrupted films can be identified with a high degree of certainty, and a number of out-of-plane bubbles can be potentially neglected by tracking the pattern of parallel-lines above the gas bubbles found in the images. However, it should be noted that it is necessary to improve the robustness of the processing algorithm beyond the capability that is demonstrated in this Chapter to investigate liquid-films with highly agitated gas-liquid interfaces and high entrained gas bubble densities. In

future applications of S-PLIF, one of the potential alterations that needs to be considered to the methodology is the increase in the amplitude of the fluorescence signal modulation (i.e. the contrast) between the dark and bright regions of the structured illumination. This can be achieved by decreasing the distance between the Ronchi ruling plate and pipe wall, or by collimating the laser-light. The reason for this modification stems from the diffuse background excitation and fluorescence due to reflections contributed by numerous gas-liquid interfaces present within the flow, which leads to ‘degradations’ in the imaged modulation amplitude.

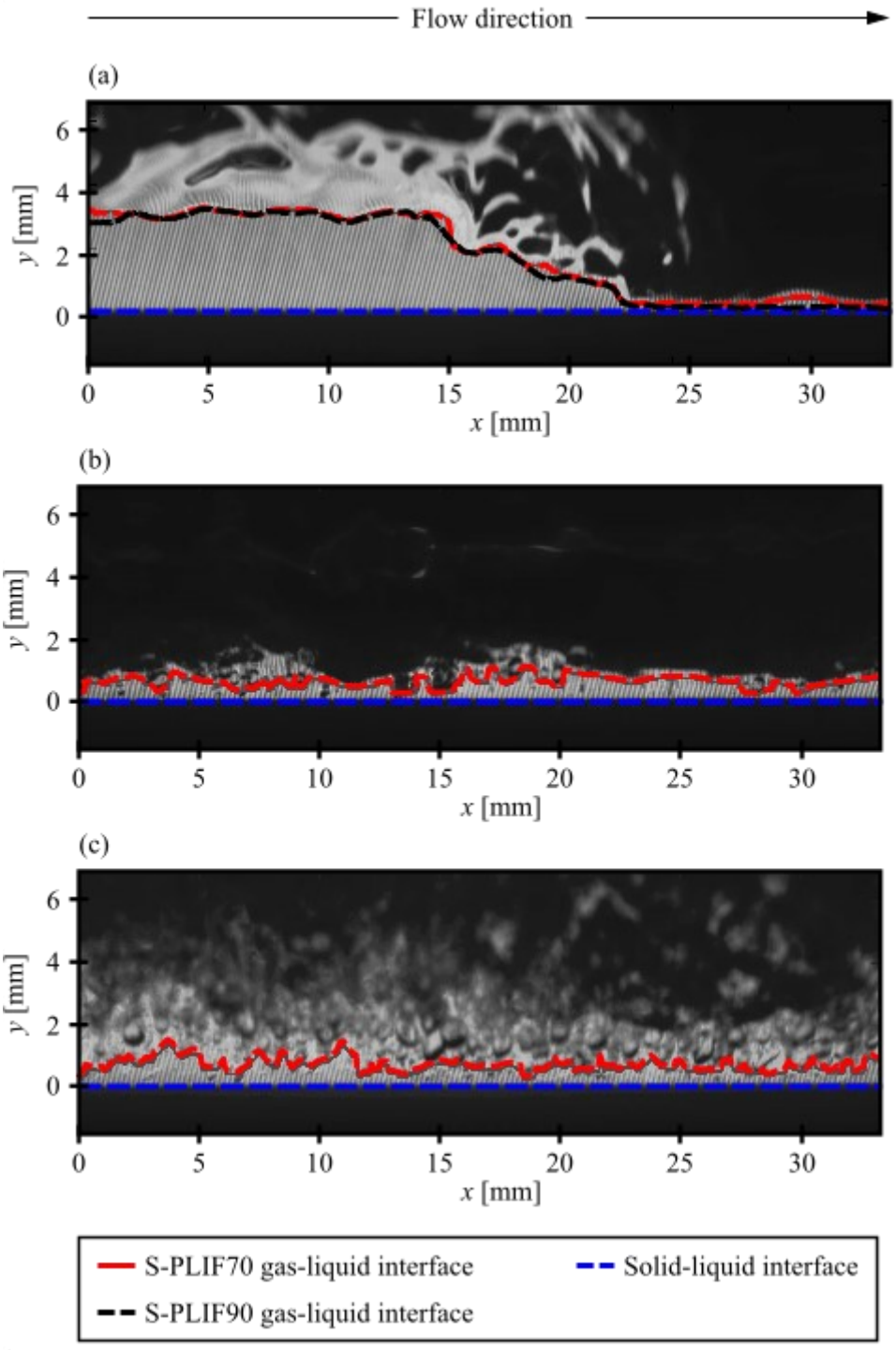


Figure 5-9 – Raw S-PLIF70 frames of liquid-films with gas-shear at: (a) $Re_G = 0$ and $Re_L = 1510$; (b) $Re_G = 22{,}100$ and $Re_L = 1360$; and (c) $Re_G = 48{,}300$ and $Re_L = 1360$. The solid-liquid interface (dashed blue-line), and the gas-liquid interface obtained by S-PLIF70 (solid red-line) and S-PLIF90 (dashed black-line) are superimposed on each frame.

5.5. Uncertainty considerations

In co-current gas-liquid annular flows, estimations of the uncertainty of instantaneous local and time-averaged liquid-film thickness data with optical methods. The primary reason for this is the fact that alternative optical methods also suffer from errors due to issues predominantly caused by total internal reflection (TIR), which affect different optical techniques in various degrees, and dependant on numerous factors, such as the flow regime. For example, the influence of TIR on BBLIF data for smooth liquid-film regions is relatively modest, however, the application of BBLIF becomes more challenging for liquid-films with agitated surfaces and entrained gas bubbles. In contrast, the PLIF data is compromised for smooth liquid-film regions and improves with increasing Re_G as the mirror effect is suppressed.

Similar to PLIF, the uncertainty of the S-PLIF δ data is associated with the identification of the gas-liquid interface in smooth and rough film regions, and hence, different sources of error. In addition, relevant studies in literature focus on the identification of the gas-liquid interface position, however, finding the solid-liquid interface location is non-trivial. This can contribute to significant uncertainties in the δ data. Underlying these issues are the: (i) finite laser-sheet thickness; (ii) observation angle of the camera (i.e. $\theta_P = \theta_S = 70$ °); and (iii) utilization of a translucent pipe wall material in the current experimental configuration due to the application of a refractive index matching approach in the design of the test-section.

Nevertheless, uncertainties in relation to the location of the solid-liquid interface should be systematic, and hence, calibration exercises should be performed to appreciably minimise this type of uncertainty. This set of exercises could comprise of measurements in a number of flows with laminar films (i.e. low Re_L and no gas-shear), where the expected δ values match the Nusselt values. In the current work, methods described by Charogiannis et al. (2015; 2017) were employed to obtain the position of the solid-liquid interface. The uncertainties of these methods

have been thoroughly examined, and consequently, confident that the processing algorithm to obtain the solid-liquid interface produces an error of < 1 pixel, which is in good agreement with the aforementioned research efforts. Nevertheless, a mean film-thickness of $\langle\delta\rangle$ = 500 – 1000 μm corresponds to an error of ≈ 5.0 – 2.5 %.

The accuracy of the gas-liquid interface identification is dependent on the employed methodology to locate the position of the shift in the pattern (which occurs at the interface), and on a number of experimental parameters. For the current set of S-PLIF images, an image gradient approach was implemented, and the optical parameters that affect the accuracy of the gas-liquid interface identification are primarily the level of the camera noise and the amplitude of the fluorescence modulation. For the first parameter, cameras with higher bit-depth and lower noise levels can be used to enhance the accuracy; while the use of a transparent pipe wall material and/or collimator optics to deal with the second optical parameter.

Given that a set of credible and simultaneous measurements with known uncertainty is not available, for a liquid-film thickness range of δ = 500 – 1000 μm, the upper limit of the instantaneous liquid-film thickness data was estimated to be < 10 %; while it was < 5 % for the average liquid-film thickness data. Provided that S-PLIF is not as sensitive to camera noise at low values of δ and does not suffer from reduced sensitivity at higher values of δ (e.g. above large amplitude waves), the upper limit values are equivalent to the values acquired by BBLIF on smooth liquid-film regions with similar optical equipment (Chapter 4). In addition, S-PLIF can more reliably obtain the position of the gas-liquid interface in liquid-films regions with steep interfacial slopes and entrained gas bubbles than either BBLIF or PLIF.

5.6. Summary

PLIF and BBLIF have been employed extensively to recover the thickness data of liquid-films in gas-liquid annular flows. However, recent studies have shown that the reliability of both methods is compromised due to optical effects at the gas-liquid interface. In PLIF, two main sources of errors affect the film-thickness measurements: (i) ES-I errors due to total internal reflection (TIR) of fluorescent-light at circumferentially uniform interfaces; and (ii) ES-II errors due to refraction or TIR of fluorescent-light at circumferentially non-uniform interfaces. In this Chapter, a novel variation of PLIF is presented, which is referred to as S-PLIF. S-PLIF was developed to overcome the limitations associated with PLIF in order to maintain the distinct advantage of directly imaging the axial cross-section of liquid-films (e.g. simultaneous application of temperature or velocity diagnostics). The S-PLIF technique relies on a periodic modulation of the laser-light intensity along the region of interrogation (ROI) to generate fluorescence images with a pattern of alternating bright and dark regions. The identification of the position of the true gas-liquid interface is based on the refraction, and hence, the direction change of the structured fluorescence pattern. The image processing methodology to obtain the location of the true gas-liquid interface is detailed, and demonstrated in falling -film flows in a vertical pipe at $Re_L \approx 150$ - 1500.

The SPLIF liquid-film thickness data are compared to PLIF data acquired simultaneously with conventional PLIF image processing algorithms, and time-averaged film-thickness data obtained in other studies that have used different experimental techniques and an identical range of investigated flow conditions. For flat and smooth regions of liquid-films with no gas-shear, the time-averaged data of SPLIF match with BBLIF, which was obtained in the same flow facility. This highlights the extent of the effects of ES-I and ES-II errors on the PLIF measurements in these flows. In addition, the effect of the camera observation angle on the S-PLIF data was investigated. A pair of cameras were aligned at $\theta_S = 70$ ° and $\theta_P = 90$ ° relative to the excitation plane. S-PLIF performed better at $\theta_S = 70$ ° due to the suppression of ES-II errors caused by

refraction or TIR of the emitted fluorescence at the three-dimensional gas-liquid interface.

The capability of the S-PLIF approach was also demonstrated for a few flow conditions in liquid-films with gas-shear, which are characterised by the presence of agitated film surfaces and entrained gas bubbles. In this type of liquid-film regions, S-PLIF provides more reliable data than both BBLIF and PLIF, and also allows for more accurate interpretations of the collected flow images (e.g. distinction between in/out-of-plane bubbles, uninterrupted liquid-film regions, etc.). For smooth regions of the liquid-film with film thicknesses of δ = 500 – 1000 μm, the upper limits of the instantaneous and time-average liquid-film thickness data were estimated to be < 10 % and < 5 %, respectively.

CHAPTER

6. MFoR-BBLIF

The application of the moving frame-of-reference brightness-based laser-induced fluorescence (MFoR-BBLIF) technique on downwards air-water annular flows at Re_G = 39,500 – 79,000 and Re_L = 286 – 1320 is discussed in this Chapter. The current set of experiments was performed to primarily verify the potential of the moving frame-of-reference (MFoR) approach, which implements a dynamic region of interrogation (ROI) rather than a static ROI in standard flow measurements in order to investigate interfacial phenomena with large development lengths. Therefore, MFoR-BBLIF was used to measure the individual disturbance wave velocities u_{DW} as function of downstream distance from the test-section inlet (s) in this work.

6.1. Introduction and problem statement

In general, the vast majority of experimental methods that have been used to investigate various flow phenomena have had a fixed or static region of interrogation (ROI). For example, the ROI position of the measurements with simultaneous PLIF and BBLIF (in Chapter 4) was ≈ 100 L/D (i.e. ≈ 3.24 m) downstream of the test-section inlet; while it was ≈ 125 L/D (i.e. ≈ 4.05 m) in the the measurements with S-PLIF (in Chapter 5). Furthermore, a number of studies have implemented different experimental methods at multiple ROI positions downstream of the channel inlet to investigate the axial development of disturbance wave characteristics (e.g. circumferential coherence, liquid-film thickness, wave frequency, wave velocity) in gas-liquid annular flows,: (i) conductance probes (Hall Taylor et al., 1963; Wolf et al., 2001; Zhao et al., 2013); (ii) laser-focus displacement (LFD) method (Hazuku et al., 2008); and (iv) brightness-based laser-induced fluorescence (BBLIF) technique (Alekseenko et al. 2015).

Inherent limitations exist with static ROI measurements to investigate interfacial wave phenomena with large development lengths (i.e. large amplitude disturbance waves) due to the unknown instantaneous information before-and-after the ROI position, and the short interrogation time of individual waves. In optical methods (e.g. BBLIF or PLIF), the static ROI length covers a liquid-film region in the x (i.e. flow) direction in a single measurement. However, this primarily depends on the used optics, which typically limits the ROI length to several centimetres. Therefore, the integration of a moving-frame-of-reference (MFoR) approach to non-intrusive optical methods is proposed to have a dynamic or moving ROI in order to increase the interrogation time and interrogate as a function of distance.

In the present work, MFoR was applied to BBLIF, which is referred to as moving-frame-of-reference brightness-based laser-induced fluorescence (MFoR-BBLIF), and used to investigate the axial development of individual disturbance wave velocities in downwards annular flows. In

MFoR-BBLIF, the optics were installed on a linear actuator system to physically move the optical measurement system, and hence, the ROI position along the entire test-section length. The motion of dynamic ROI was from the top of the test-section to the bottom with varying set velocities, which was dependent on the flow condition and u_{DW} data of Webb & Hewitt (1975). The dynamic ROI velocity profiles are provided in Section 3.2.4 of Chapter 3 on page 103. The images were qualitatively analysed to observe relevant interfacial wave phenomena, and processed to recover individual disturbance wave velocities (u_{DW}) as a function of downstream distance from the test-section inlet (s).

Lists of the investigated gas and liquid flow conditions are provided in Tables 6-1 and 6-2, respectively. The investigated gas volumetric flow-rate range was Q_G = 900 – 1800 L/min. This corresponds to gas superficial velocities and gas Reynolds numbers of j_G = 18.7 – 37.3 L/min and Re_G = 39,500 – 79,000, respectively. The gas superficial velocity was defined as $j_G = 4\ Q_G/\pi D_p^2$, which is near-equivalent to the bulk gas-phase velocity in annular flows with thin films. The definition of the gas Reynolds number was $Re_L = 4Q_G/\pi D_p \upsilon_G$, where υ_G is the kinematic viscosity of air. The investigated range of liquid volumetric flow-rate was Q_L = 1.7 – 8.0 L/min, which corresponds to a superficial liquid velocities and liquid Reynolds numbers of j_L = 0.02 – 0.17 L/min and Re_L = 286 – 1320, respectively. The definition of liquid superficial velocity was $j_L = 4\ Q_L/\pi D_p^2$; while the liquid Reynolds number was $Re_L = Q_L/\pi D_p \upsilon_L$, where υ_L is the liquid kinematic viscosity. The temperature of the liquid-phase was $T \approx 20$ °C ± 3 °C for the majority of the measurements.

Photographs of the MFoR-BBLIF set-up and a MFoR-BBLIF measurement are provided in Figures 6-1 and 6-2, respectively. The experimental configuration of MFoR-BBLIF is described in Section 3.2.4 of Chapter 3. The MFoR approach was integrated with BBLIF as the non-intrusive optical method uses a line-of-sight approach to the fluorescence emission collection, and the physical dimensions of the optical configuration is more compact than PLIF. However, the

MFoR-BBLIF images were only used to recover the u_{DW} data due to the aforementioned limitations with BBLIF in Chapter 4. For each investigated flow condition, ≈ 10 experimental runs (ER) were performed to ensure a sufficient number of disturbance waves were observed in the moving ROI. The MFoR-BBLIF image processing routine to generate *x*-*t* matrices and recover the disturbance wave velocities (u_{DW}) are explained in Section 6.2. In Section 6.3, a qualitative analysis is presented of the instantaneous raw MFoR-BBLIF images, and the u_{DW} data is discussed in Section 6.4. Finally, a summary of the MFoR-BBLIF measurements is given in Section 6.5.

Table 6-1 – List of the investigated gas flow conditions in the dynamic ROI measurements with MFoR-BBLIF.

Gas volumetric flow-rate	**Gas superficial velocity**	**Gas Reynolds number**
Q_G	j_G	Re_G
L/min	**m/s**	**–**
900	18.7	39,500
1350	28.0	59,200
1800	37.3	79,000

Table 6-2 – List of the investigated liquid flow conditions in the dynamic ROI measurements with MFoR-BBLIF.

Liquid volumetric flow-rate	**Liquid superficial velocity**	**Gas Reynolds number**
Q_L	j_L	Re_L
L/min	**m/s**	**–**
1.7	0.35	286
5.0	1.04	826
8.0	1.66	1320

(a)

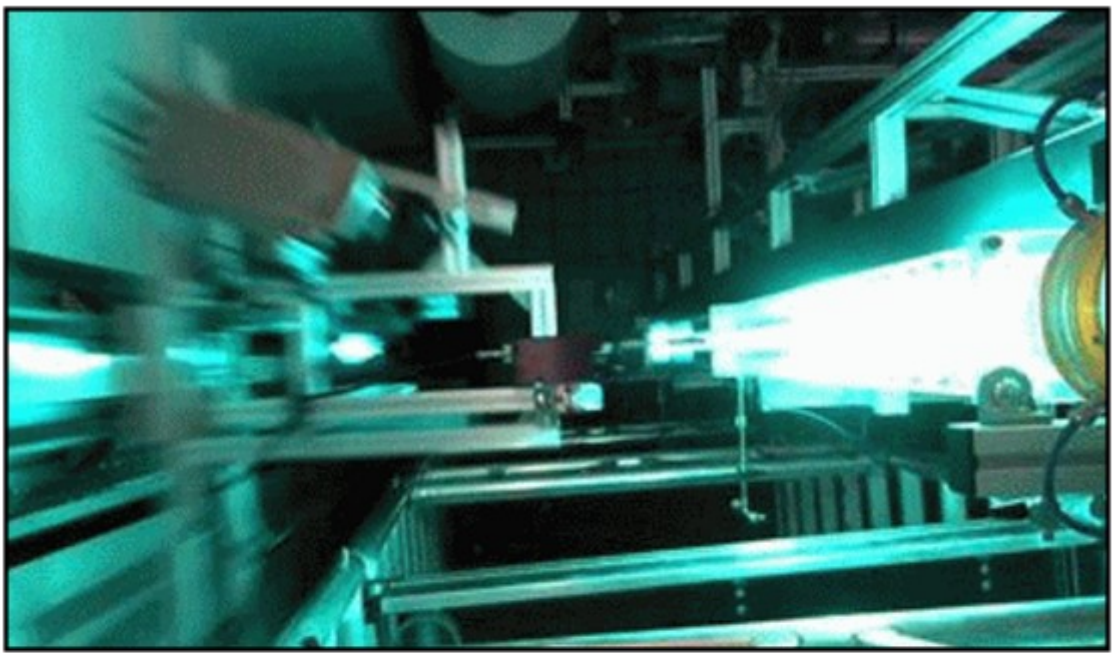


(b)



Figure 6-1 – Photographs of the MRoF-BBLIF set-up to investigate the axial development of individual disturbance waves in downwards annular flows at Re_G = 39,500 – 79,000 and Re_L = 286 – 1320: (a) top-view; and (b) side-view.

(a)



(b)

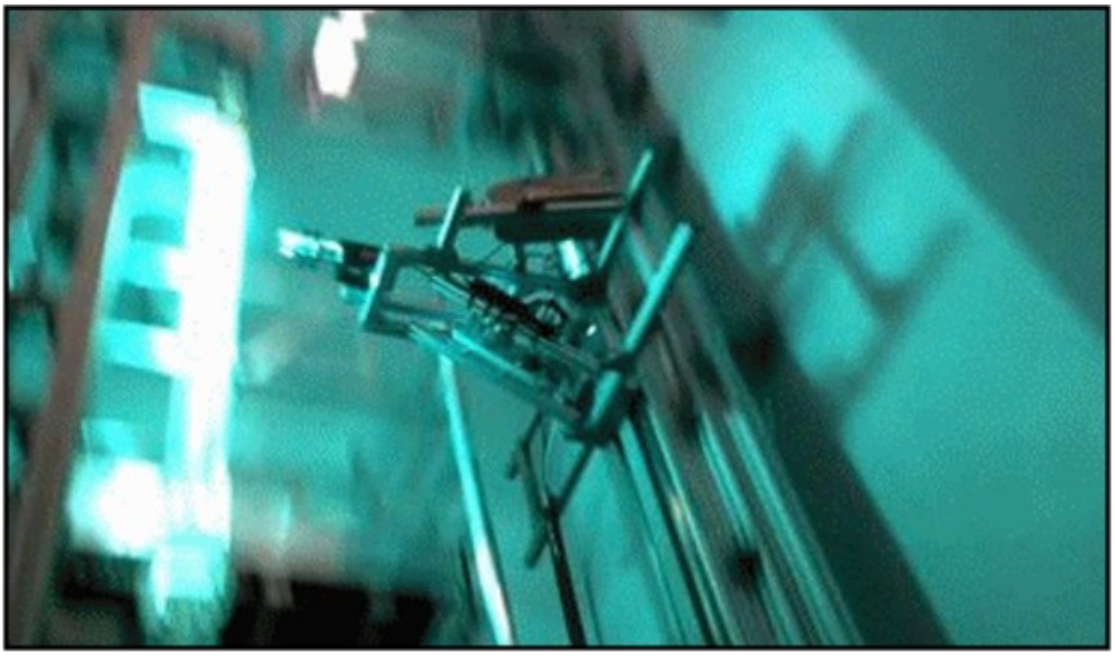


Figure 6-2 – Photographs of a MRoF-BBLIF measurement to investigate the axial development of individual disturbance wave velocities (u_{DW}) in downwards annular flows at Re_G = 39,500 – 79,000 and Re_L = 286 – 1320: (a) top-view; and (b) side-view.

6.2. MFoR-BBLIF image processing

Each experimental run (ER) of a MFoR-BBLIF measurement produced ≈ 15,000 – 25,000 instantaneous raw images, which was dependent on the flow condition and the set velocity profile of the dynamic region of interrogation (ROI). The spatial resolution of the MFoR-BBLIF images was 245 μm/pixel in the flow (x) direction. Similar to BBLIF, the fluorescence signals in the MFoR images ($I_M(x, z, t)$) represent the liquid-film region in the x (longitudinal) and z (transverse) directions. For the set of images collected during an ER, a MFoR-BBLIF image processing algorithm, which was built in-house with the MATLAB software, was employed to: (i) generate a spatiotemporal (x-t) matrix; (ii) identify individual disturbance waves and their positions; and (iii) determine the wave velocity of identified disturbance waves (u_{DW}). The image processing routine is demonstrated with the images collected in ER4 of a flow at Re_G = 59,200 and Re_L = 286, which comprised of the following steps:

1) In each instantaneous raw image, the position of the central-line of the fluorescing liquid domain along the x axis was identified and gathered to construct a spatiotemporal (x-t) matrix. In Figure 6-3(a), the x-t matrix of ER4 at t = 0.4469 – 1.4469 s is presented. A single bright-region at each t value represents an individual disturbance wave. Since the dynamic ROI is moving down the test-section with a constant velocity, the position of the bright-region can shift along the x axis. A left-to-right shift indicates a disturbance wave faster than the moving ROI, and hence, a right-to-left shift indicates a disturbance wave slower than the ROI.

2) The dark-regions in the x-t matrix, which extend across the entire x axis, was a consequence of the de-synchronization between the high-speed camera and laser system; which lead to a natural division of the x-t matrix into multiple segments ($S(x, t)$). The size of each segment was similar as the frequency ($f_{d\text{-}s}$) and time duration ($t_{d\text{-}s}$) of the de-

synchronization were consistent ($f_{d\text{-}s} \approx 17.7$ Hz and $t_{d\text{-}s} \approx 0.00025$ s). The individual segments of the (x-t) matrix are depicted as dashed red-squares in Figure 6-3(b).

3) The (x-t) matrix was visually inspected to identify the presence of disturbance waves in each S, and subsequently, determine whether the identified wave in consecutive segments were separate or identical. For example, in Figure 6-3(b), the disturbance waves at $t = 0.4521$ s – 0.5933 s and $t = 0.6768$ s – 1.5084 s are separate waves.

4) In each S, the locations of the front-slope of the disturbance wave, $S(x_1, t_1)$ and $S(x_2, t_2)$ was found as demonstrated in Figures 6-3(c) and 6-4(a), and the gradient between the two positions corresponds to the disturbance wave velocity in relation to the moving ROI (u_{DWR}) at $S(x_3, t_3)$. Therefore, a negative u_{DWR} value indicated a disturbance wave moving slower than the ROI; while a disturbance wave moving faster than the dynamic ROI would give a positive u_{DWR} value.

5) Since the linear velocity profile of the dynamic ROI (u_{AC}) as a function of time (t) was obtained in the set of calibration exercises described in Section 3.2.3 of Chapter 3, the disturbance wave velocity (u_{DW}) at $S(x_3, t_3)$ is defined as $u_{DW} = u_{AC} + u_{DWR}$. In addition, the downstream distance of the disturbance wave from the test-section inlet (s) at $S(x_3, t_3)$ was calculated based on the known movement parameters of the moving ROI.

6) In Figure 6-4(b), a plot of u_{DW} as a function of s is presented in Figure 6-4(b). The solid-black circle-markers and the dashed black-lines indicate the u_{DW} value in each S and an identical disturbance wave, respectively. As depicted in the plot, the disturbance wave at $t = 0.6768$ s – 1.5084 s was within the dynamic ROI of the optical measurement system for $s = 1.63$ m.

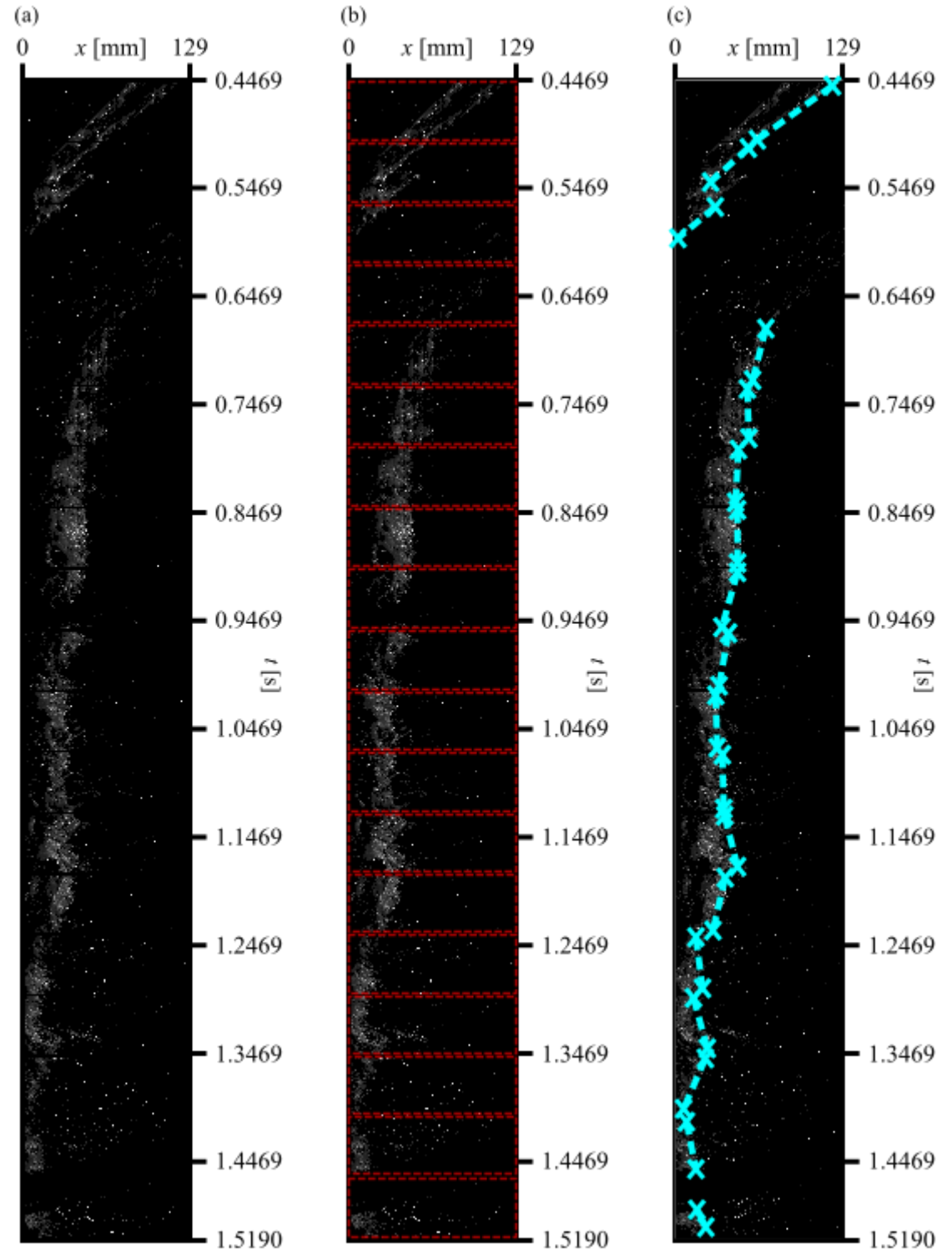


Figure 6-3 – In ER4 of a flow at Re_G = 59,200 and Re_L = 286: (a) *x*-*t* matrix at t = 0.4469 s – 1.5190 s; (b) segments (*S*) represented as dashed red-squares; and (c) positions of the front-slope of identified waves (cyan cross-markers) in each *S*.

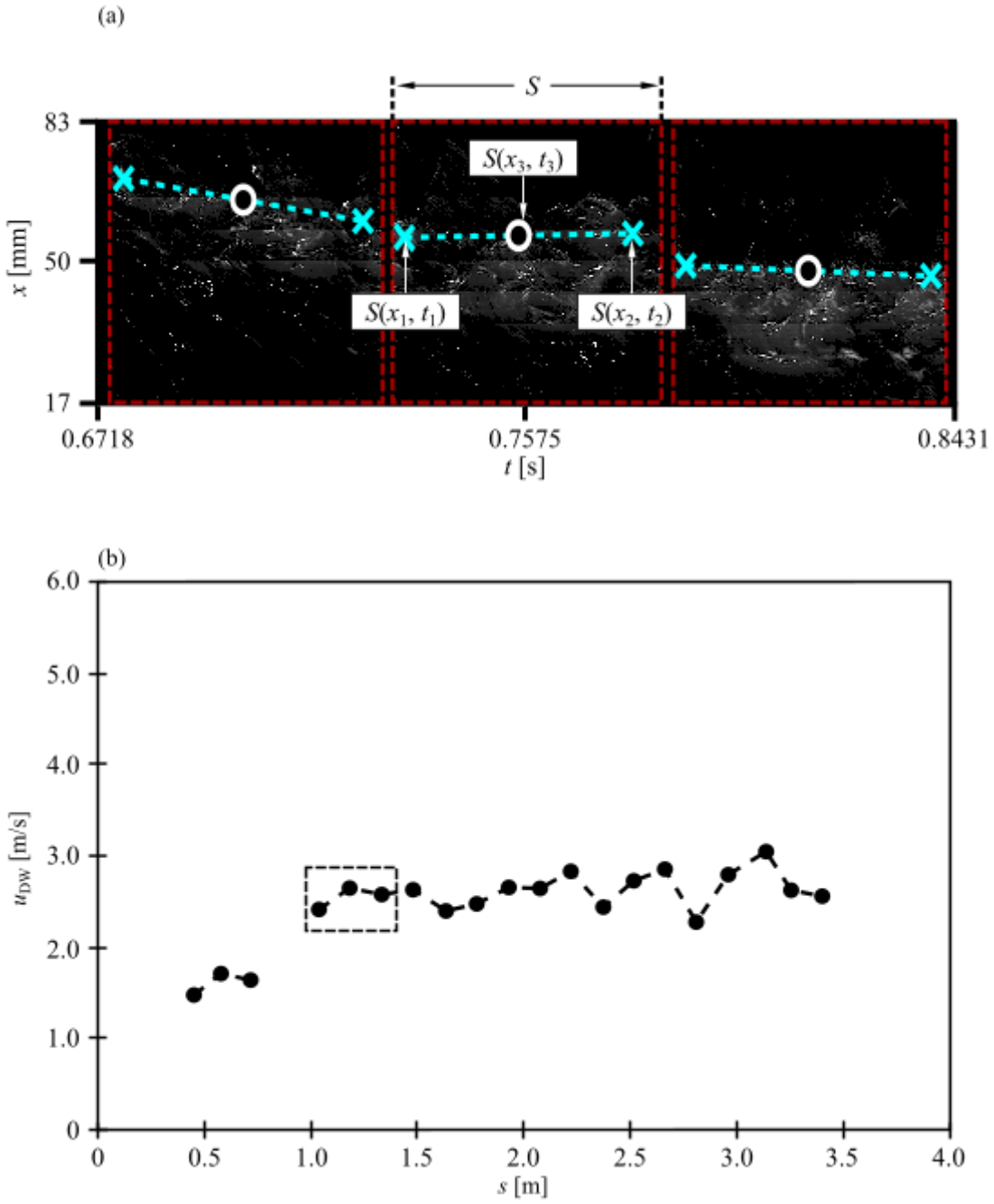


Figure 6-4 – In ER4 of a downwards annular flow at Re_G = 59,200 and Re_L = 286: (a) *x*-*t* matrix at t = 0.6718 s – 0.8431 s, which shows an identical disturbance wave in the three consecutive segments and the identified positions of the front-slope of the wave; and (b) plot of u_{DW} as a functions of s, which highlights (in the dashed black-square) the u_{DW} values extracted from the *x*-*t* matrix in (a).

6.3. Qualitative analysis

One of the significant advantages of the MFoR-BBLIF approach is the increase in the interrogation time of the various features (e.g. disturbance waves) and phenomenon present in gas-liquid annular flows; which was evident in the qualitative analysis of the collected instantaneous raw images and the *x-t* matrices generated in the current set of measurements. For a downwards annular flow at Re_G = 79,000 and Re_L = 1320, the *x-t* matrix of ER5 at t = 0.8324 – 0.9619 s and five of the corresponding raw MFoR-BBLIF frames at given t values are presented in Figure 6-5. For the aforementioned gas-liquid flow condition, the continuous coalescence of disturbance waves, liquid droplet deposition, liquid droplet and gas bubble entrainment was observed in the sequence of collected images.

In Figure 6-5, the time duration between the Frames (a) and (e) was t = 0.8481 s – 0.9524 s and corresponds to a distance of $s \approx 0.41$ m. In Frame (a), an individual or single disturbance wave (DW1) travels down the channel, and the entire liquid-film is covered with fast and slow-moving small amplitude interfacial waves (i.e. ripples or ripple waves). In agreement with the observations made by Cherdantsev et al. (2014), the slow ripples slid to the film-substrate behind the large amplitude wave; while the fast ripples travelled over the top of DW1 to the wave-front, and in most occasions, lead to the entrainment of liquid droplets into the gas core. In addition, both the bag and ligament break-up mechanisms of liquid droplet entrainment were observed in the flow. Liquid droplets with varying sizes and velocities moved primarily in the axial direction of the flow, some of which deposited onto the liquid-film.

Both craters and furrows, which are the liquid droplet deposition mechanisms described by Cherdantsev et al. (2017), were observed. In their experimental study of droplet impacts onto gas-sheared liquid-films, the occurrence of either mechanism was dependent on the impact angle of the droplet. Asymmetric craters appear at large impact angles, which creates secondary liquid

droplets; furrows appear at low impact angles, which leads to the entrainment of gas bubbles in the liquid-film. A number of the droplets appeared to fragment into multiple droplets with smaller sizes during process of deposition, which agrees with the findings of Cherdantsev et al. (2017).

Further downstream of the channel (≈ 0.14 m), DW1 approaches a second disturbance wave (DW2) as shown in Frame (b) at t = 0.8850 s, which is highly likely due to the u_{DW} value of DW1 being greater than u_{DW} value of DW2. Therefore, the difference between the u_{DW} values of the two disturbance waves eventually leads to wave coalescence and occurs in Frame (c) at t = 0.9124 s. Based on the negligible shift of the bright-region along the x axis of the x-t matrix, the coalesced wave (DW3) appears to travel with the same velocity as DW1 Frame (d) at t = 0.9324 s, which is in agreement with the observations of Hall et al. (1963). In addition, the generation of a large number of liquid droplets was observed as a consequence of the wave coalescence. Since the wave velocity is proportional to the height of the wave (Pashniak, 1969), Wilkes et al. (1983) assumed that the entire liquid volume of the slower disturbance wave (i.e. DW2) is entrained into the gas-phase during the coalescence; since an increase in the liquid volume, and hence, the height of the disturbance wave would lead to a different wave velocity in comparison with DW1. DW3 continues to propagate through the channel and approaches a third disturbance wave (DW4) in Frame (e) at t = 0.9524 s. In the subsequent frames, DW3 coalesces with DW4 and more liquid entrainment was observed. In wave coalescence model of Wilkes et al. (1983), the liquid droplet entrainment due to wave coalescence can significantly contribute to the total entrainment occurring in gas-liquid annular flows.

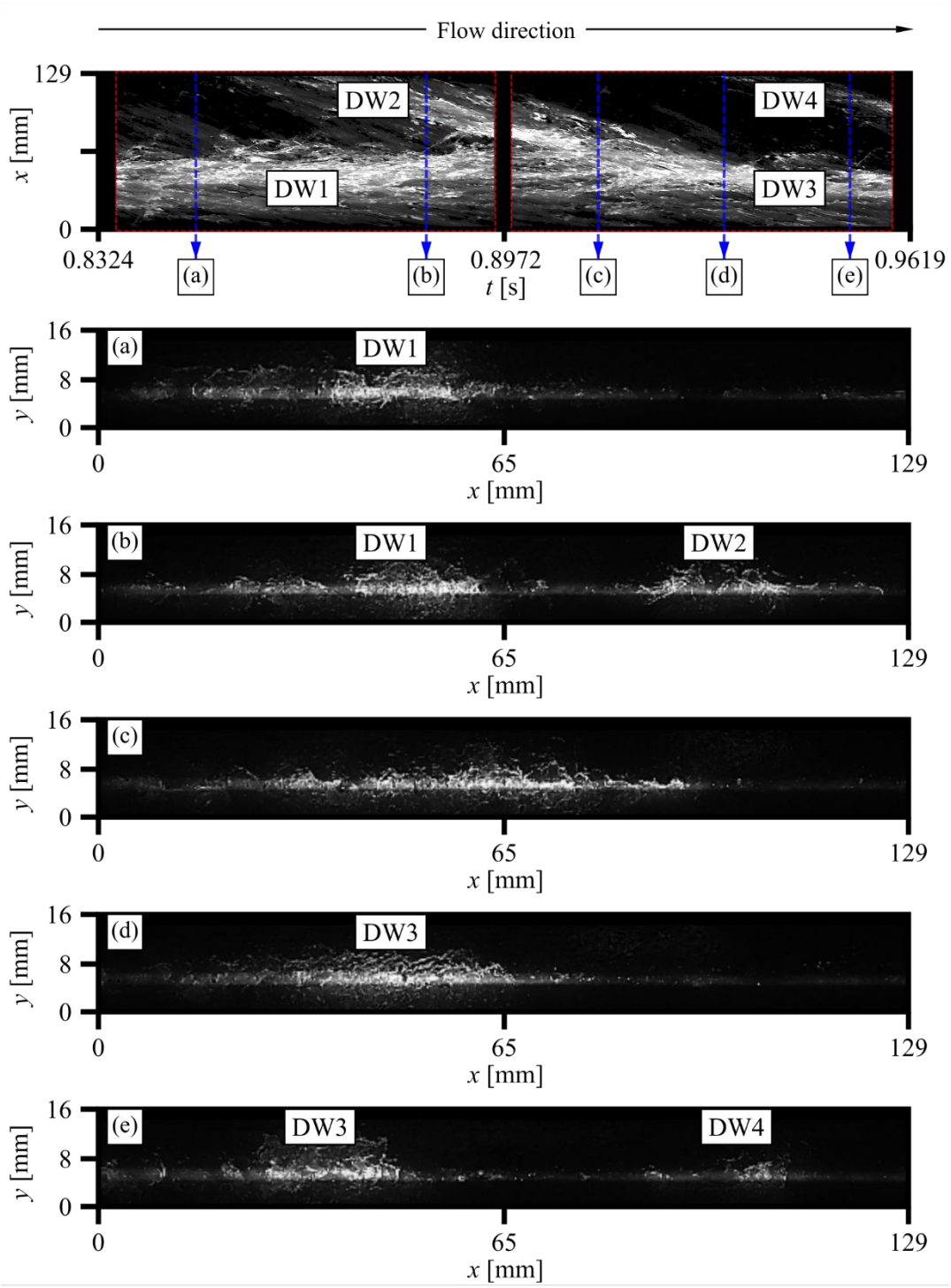


Figure 6-5 – For a flow at $Re_G = 79{,}000$ and $Re_L = 1320$, observation of disturbance wave coalescence in the *x*-*t* matrix of ER5 at $t = 0.8324$ s – 0.9619 s and the corresponding frames at: (a) $t = 0.8481$ s – DW1; (b) $t = 0.8850$ s – DW1 and DW2; (c) $t = 0.9124$ s – coalescence of DW1 and DW2; (d) $t = 0.9324$ s – DW3; and (e) $t = 0.9524$ s – DW3 and DW4.

6.4. Disturbance wave velocities

For the range of investigated gas and liquid flow conditions in the current set of experiments, the individual disturbance wave velocities (u_{DW}) as a function of downstream distance from the test-section inlet (s) are presented in Figures 6-6 to 6-8. In each plot, the solid and empty circle-markers represent the u_{DW} values acquired in each relevant segment (S) of a x-t matrix of a given experimental run (ER) and flow condition. In addition, the different colours and markers indicate different experimental runs, and the dashed-lines indicate identical disturbance waves. Since the primary objective of the present experiments was to develop and verify the potential of the MFoR-BBLIF methodology, the number of individual disturbance waves identified in each measurement was deemed insufficient for statistical analysis of the u_{DW} data. However, a number of noticeable trends can still be observed within the plots provided:

1) In general, the u_{DW} values increase with increasing Re_G and Re_L along the entire length of the test-section, however, the influence of Re_L seems to be greater than Re_G. This observation was expected as an increase in Re_G leads to thicker liquid-films (δ), and consequently, greater wave height, which is proportional to the wave velocity (Pashniak, 1969).

2) For a given gas and liquid flow condition, the u_{DW} values increase with s. The increase of the u_{DW} values is more significant in initial pipe diameters (L/D) due to the high acceleration of disturbance waves at the initial stages of their development (Alekseenko et al., 2015). In the majority of the flow conditions, the u_{DW} values appear to reach a near-constant value as the individual disturbance waves approach a downstream distance of $s \approx 3.0$ m (e.g. Figure 6-6(b)). A similar trend was reported by Wolf et al. (2001) for upwards annular flows. For a range of Re_L and a constant Re_G, Wolf et al. (2001) found that the wave velocity reached a near-constant value at $s > 125\ L/D$, which

corresponds to $s > 4.05$ m in the current experimental set-up, and attributed the observation on the balance between the decrease in liquid-film thickness (δ) and the increase in gas velocity.

3) The deviation of the u_{DW} values at a given s value is significant for downwards annular flows at $Re_G = 79{,}000$ and $Re_L = 826$, $Re_L = 59{,}200$ and $Re_L = 1320$, and $Re_L = 79{,}000$ and $Re_L = 1320$. These flow conditions correspond to flows in the 'regular wave' regime. The gas-liquid interface is highly agitated and the rate of liquid droplet entrainment is very high, which could cause pressure gradient fluctuations along the axial length of the channel.

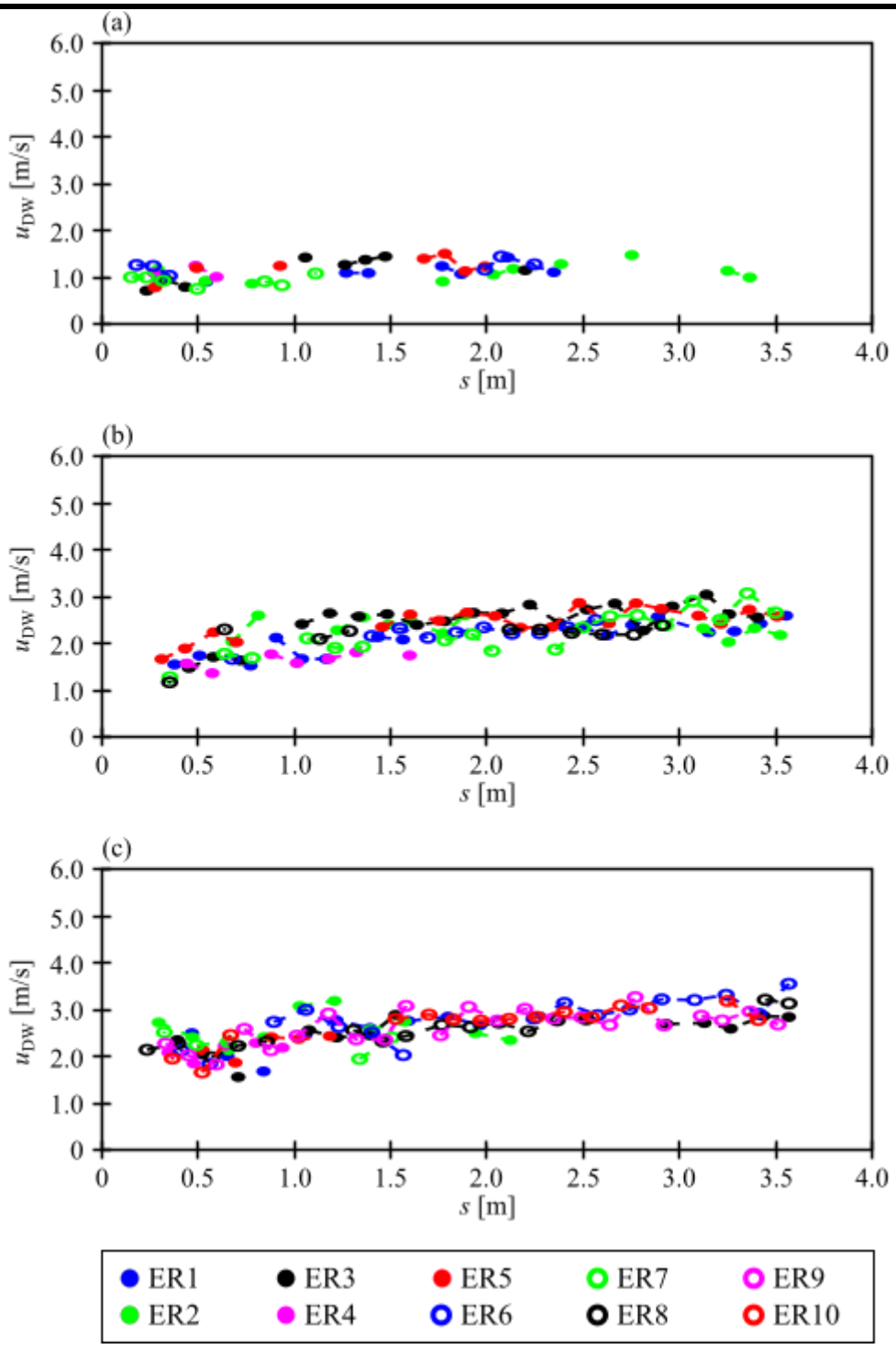


Figure 6-6 – Plots of u_{DW} as a function of s for downwards co-current gas-liquid annular flows at Re_L = 286 and: (a) Re_G = 39,500; (b) Re_G = 59,200; and (c) Re_G = 79,000. The different colours and markers indicate a different experimental run (ER), and the dashed-lines indicate an identical wave in each ER.

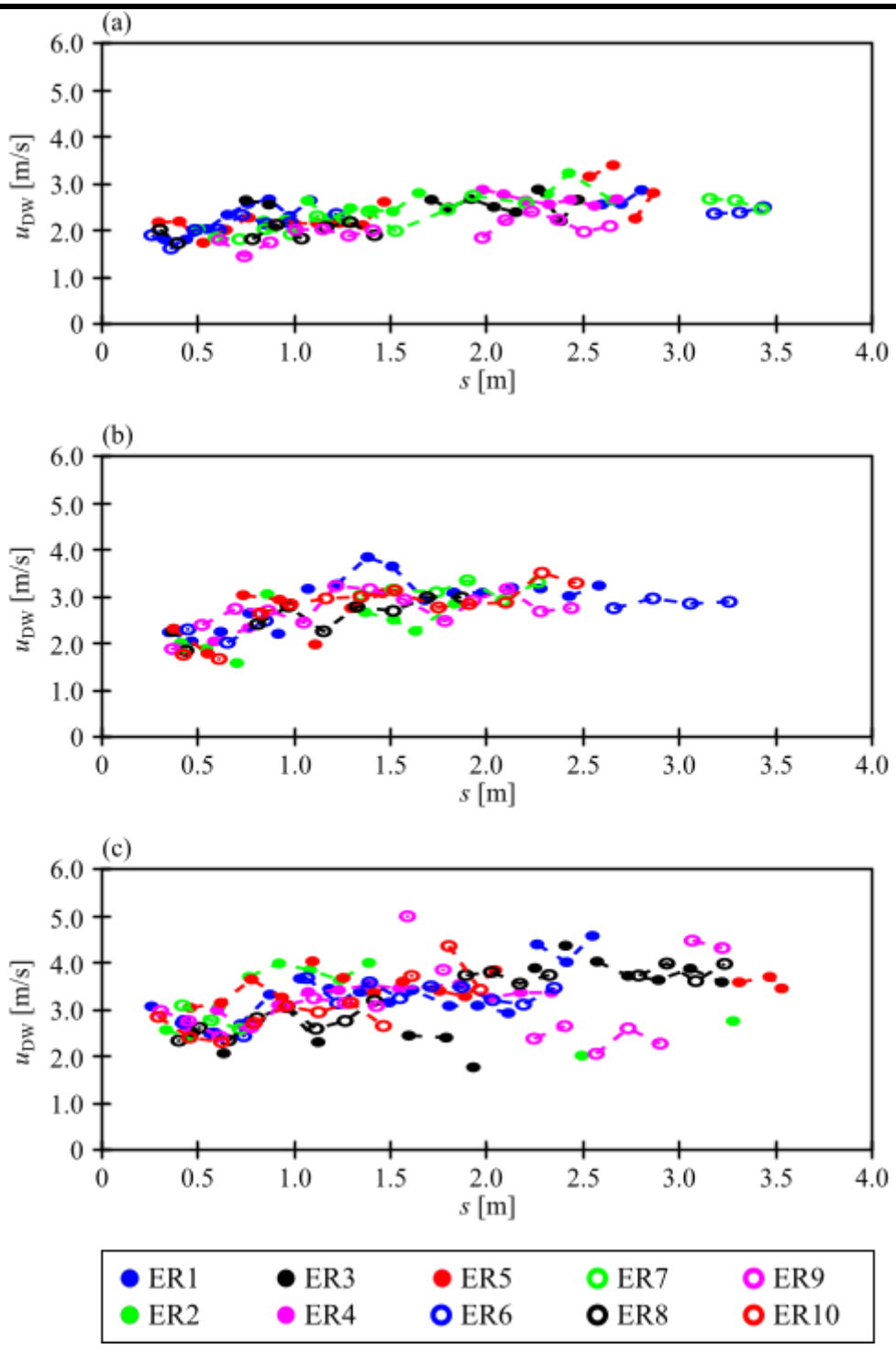


Figure 6-7 – Plots of u_{DW} as a function of s for downwards co-current gas-liquid annular flows at Re_L = 826 and: (a) Re_G = 39,500; (b) Re_G = 59,200; and (c) Re_G = 79,000. The different colours and markers indicate a different experimental run (ER), and the dashed-lines indicate an identical wave in each ER.

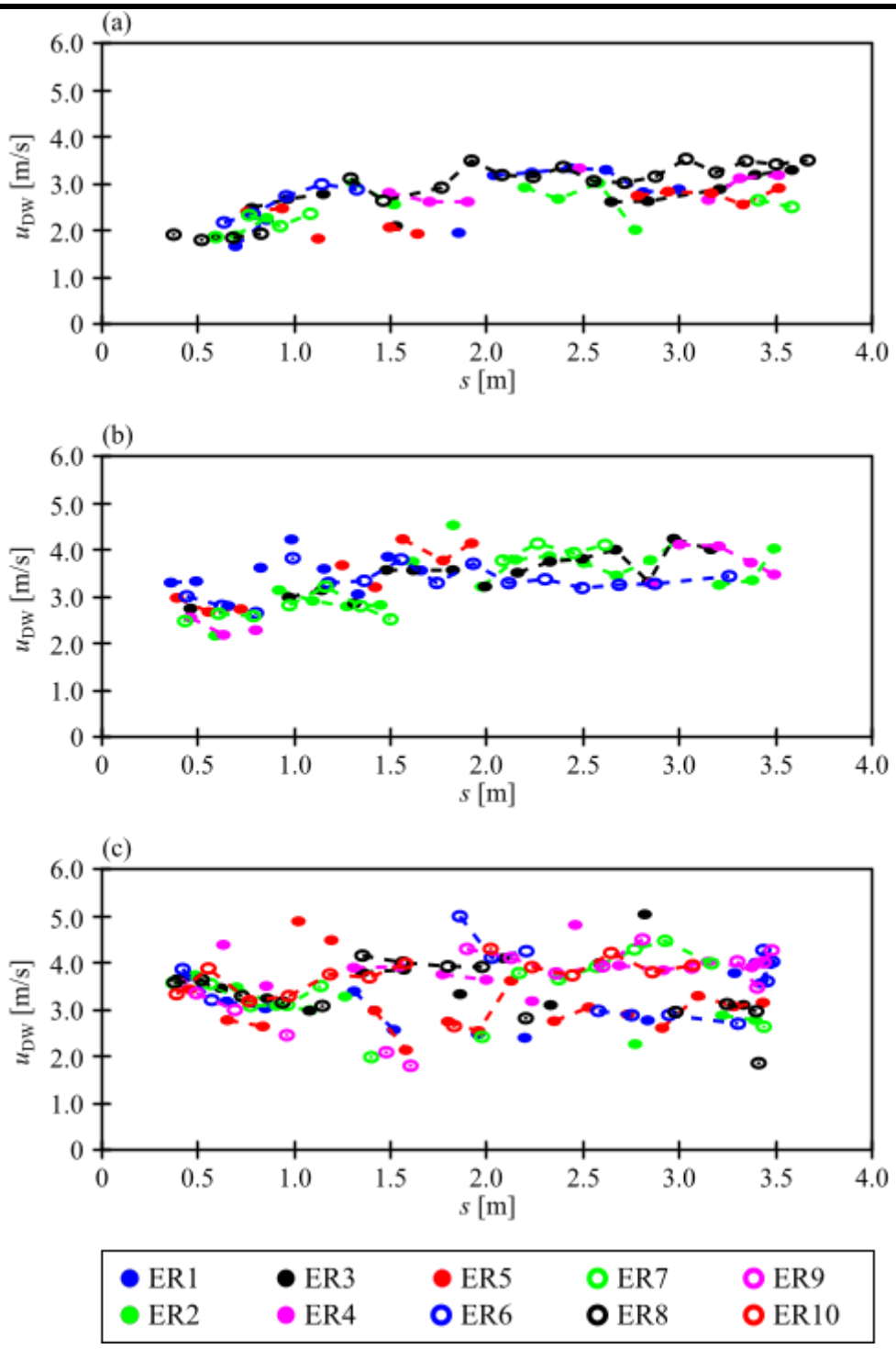


Figure 6-8 – Plots of u_{DW} as a function of s for downwards co-current gas-liquid annular flows at Re_L = 1320 and: (a) Re_G = 39,500; (b) Re_G = 59,200; and (c) Re_G = 79,000. The different colours and markers indicate a different experimental run (ER), and the dashed-lines indicate an identical wave in each ER.

6.5. Summary

MFoR-BBLIF was developed to conduct dynamic ROI measurements on interfacial phenomena with large development lengths, such as disturbance waves. Standard flow measurements have a static ROI, which limits the interrogation time of individual waves. The novel experimental method was demonstrated in annular flows to investigate the axial development of disturbance waves. The optical measurement system, and hence, the ROI position physically traversed down the entire test-section length in order to significantly increase the duration of individual disturbance wave interrogation, and to continuously investigate the wave characteristics as a function of downstream distance.

The MFoR-BBLIF images were qualitatively analysed to phenomenologically observe the various phenomena relevant to large amplitude waves (e.g. liquid droplet entrainment, wave coalescence), and quantitatively analysed to recover the individual disturbance wave velocities (u_{DW}) as a function of distance downstream from the test-section inlet (s). While the method was applied to disturbance waves in annular flows, the moving-frame-of-reference (MFoR) approach is also extremely promising for studying the downstream evolution of other interfacial phenomena of multiphase flows with large development lengths, such as the Taylor bubbles or liquid slugs in slug flow. In the current set of experiments, only the u_{DW} data was obtained from the images. However, future work will be aimed at the extraction of other wave characteristics (e.g. film thickness) of single waves as they propagate through the channel, as well as, a systematic study of disturbance wave coalescence and fast and slow ripple wave generation by individual disturbance waves.

CHAPTER

7. Conclusions

Optical methods based on the principles of laser-induced fluorescence (LIF) have been previously employed to perform space and time-resolved measurements of liquid-film thickness, which is one of the key flow quantities, in annular flows. LIF-based methods vary in the approach used for the collection of the emitted fluorescence and the image processing to recover the film-thickness data. One of the most commonly used variations is planar laser-induced fluorescence (PLIF). A distinct advantage of PLIF is the collection of instantaneous images of the fluorescence emission which directly represent the axial cross-section of the liquid-film (i.e. x and y directions). Therefore, PLIF can be integrated with other similar measurement approaches to simultaneously investigate different flow quantities at the same region of interrogation (ROI), such as particle image or tracking velocimetry (PIV or PTV) to obtain the velocity fields within the film (e.g. Charogiannis et al., 2015; Zadrazil et al., 2014). However, Häber et al. (2015) predicted theoretically that the reliability of the PLIF film-thickness measurement can be compromised in

smooth liquid-film regions due to the 'mirror effect' caused by total internal reflection (TIR) of the emitted fluorescent-light at uniform circumferential gas-liquid interfaces.

Brightness-based laser-induced fluorescence (BBLIF) is another frequently used variation, which uses a line-of-sight approach to collect the fluorescence emission (i.e. x and z directions) from the film. Therefore, BBLIF can be more readily used to conduct three-dimensional (3-D) measurements. In BBLIF, the collected fluorescence intensity signals or 'brightness' are converted to film-thickness in accordance with the Beer-Lambert law (Alekseenko et al., 2014). Liquid-film thickness measurements with BBLIF are affected by the interfacial slope, which introduces errors that increase gradually with steepness and become significant as the incidence angle of the laser-light approaches the critical angle of total internal reflection (TIR); typically 40 – 45° in water-air systems.

In order to better confirm the optical effects on both methods, spatiotemporally resolved film-thickness measurements in the same flow interrogation region was performed by PLIF and BBLIF simultaneously in downwards annular flows at $Re_G = 0 – 85{,}100$ and $Re_L = 140 – 1320$. The ability of both LIF-based optical methods to recover the shape of the gas-liquid interface was directly compared to determine the limitations of each one. In addition, the effect of the angle between the PLIF camera and the laser sheet on the thickness measurements was also considered. One set of experiments was performed with an angle of 90 °, which is referred to as PLIF90, and another set was performed with an angle of 70 °, which is referred to as PLIF70.

In the simultaneous PLIF and BBLIF experiments, two principal error sources were found in PLIF based on the circumferential curvature of the gas-liquid interface: (i) ES-I and (ii) ES-II. ES-I errors occur in flat and smooth films with uniform circumferential interfaces, where the emitted fluorescent-light endures total internal reflection (TIR). The films appear thicker in the images, and hence, the local PLIF obtained thickness in smooth film regions is overestimated, which validates the findings of Häber et al. (2015). In addition, bright or dark-lines were

occasionally observed within the smooth films. The position of these lines was in good agreement with the identified position of the gas-liquid interface by BBLIF, which suggests that the location of the bright or dark-lines indicate position of the true interface. The overestimation of the PLIF90 and PLIF70 derived film-thickness data was evaluated for flat films (i.e. absence of waves), which agreed with the ratio of the PLIF and BBLIF obtained film-thickness (δ_P/δ_{BB}). ES-II errors occur in rough films with significant wave activity. The local PLIF derived film-thickness was underestimated due to refraction or reflection of the emitted fluorescent-light at circumferentially non-uniform gas-liquid interfaces along with line-of-sight of the camera. Smaller camera observation angles relative to the excitation plane make PLIF less susceptible to this type of error.

While BBLIF was found to be reliable for thickness measurements in flat and smooth films regions (free-surface angles $\leq 40 - 45$ ° from the horizontal), measurements with the method exhibited errors in more complex film regions. BBLIF is affected by a loss of signal sensitivity and saturation in thick film regions. In addition, the approach is vulnerable to light reflections at complex or multiple interfaces in film regions with agitated surfaces (i.e. rough) and/or aeration (i.e. presence of entrained gas bubbles), which occur with increasing frequency at higher flow conditions. BBLIF locally overestimates the film-thickness of film regions with high interfacial slopes and/or curvature, which for example, can be found at the front-slope of fast-moving ripple waves and the edges of entrained bubbles. The LIF-based optical method can also locally underestimate the thickness in regions with multiple gas-liquid interfaces. The film-thickness underestimation becomes progressively worse as the critical TIR angle is approached or exceeded.

Based on the findings of the simultaneous PLIF and BBLIF measurements, a novel variation of PLIF, which is referred to as structure planar laser-induced fluorescence (S-PLIF), was developed to overcome the limitations associated with the PLIF approach and maintain the benefit of direct imaging of the axial cross-section of the flow. The S-PLIF relies on a periodic modulation of the laser-light intensity along the film interrogation region to generate fluorescence images

with a pattern of alternating bright and dark-regions. The identification of the true gas-liquid interface position is based on the reflection, and hence, the change of direction of the structured fluorescence pattern within the liquid-film. S-PLIF was demonstrated on mainly falling liquid-film flows at $Re_G = 0$ and $Re_L \approx 150 – 1500$ in a vertical pipe. The S-PLIF derived film-thickness data were compared with the standard PLIF derived data, which were acquired simultaneously with S-PLIF, and the mean liquid-film thickness collected in previous studies with other experimental techniques employed in the same flow conditions.

For flat and smooth film regions with no gas-shear, results from S-PLIF matched with BBLIF data acquired from the simultaneous PLIF and BBLIF measurements. This highlights the extent of the effect of the ES-I and ES-II errors on PLIF in this type of flows. In addition, the effect of the S-PLIF camera observation angle was also investigated by employing a pair of cameras at 90 ° and 70 ° angles to the laser, referred to as S-PLIF90 and S-PLIF70, respectively. The performance of S-PLIF70 was better than S-PLIF90 due to the suppression of the ES-II errors caused by the refraction or TIR of the emitted fluorescence at the three-dimensional (3-D) gas-liquid interface. Finally, the capability of the S-PLIF approach was demonstrated on liquid-films with gas-shear, which are characterised by the presence of entrained gas bubbles in the film. S-PLIF provided more reliable δ data than both PLIF and BBLIF. Furthermore, S-PLIF allowed for more accurate interpretations of the collected flow images, such as the distinction between in/out-of-plane entrained gas bubbles.

The vast majority of experimental methods employed in annular flow studies use a fixed region of interrogation (ROI) to investigate the disturbance wave characteristics. However, disturbance waves have large development lengths (Wolf et al., 2001), and a static ROI can limit the interrogation time of individual waves. Furthermore, the instantaneous wave information of the wave before-and-after the ROI position is not collected. In order to investigate the downstream development of disturbance waves, the ROI position has to be altered in each set of measurements.

Therefore, the moving-frame-of-reference brightness-based laser-induced fluorescence (MFoR-BBLIF) technique was developed to conduct measurements with a dynamic ROI, which is created with the use of a linear actuator system to physically move the optical measurements system along the entire test-section length. MFoR-BBLIF was demonstrated in downwards annular flows to obtain phenomenological observations of interfacial phenomena and individual disturbance wave velocities (u_{DW}) as a function of downstream distance from the channel inlet (s).

While S-PLIF has been applied to downwards annular flows to demonstrate the ability of this novel PLIF approach to reliably identify the position of the gas-liquid interface of liquid-films with gas-shear, only a few flow conditions were investigated due to the primary objectives of the S-PLIF measurements. Therefore, a set of experiments with a wide range of flow conditions (i.e. $Re_G \approx 0 – 85{,}000$, $Re_L \approx 150$ - 1500) would be beneficial to further validate S-PLIF as a more accurate tool for film-thickness measurements in these flows.

Furthermore, the moving-frame-of-reference approach implemented on a non-intrusive LIF-based optical method was extremely promising for studying the downstream evolution of individual disturbance waves in annular flows. The various phenomena relevant to these waves (e.g. wave coalescence, droplet entrainment, droplet deposition) were continuously observed as individual waves propagated through the channel. In the current MFoR-BBLIF measurements, BBLIF was chosen due to the more physically compact optical configuration of BBLIF than PLIF. Only the downstream development of disturbance wave velocities were obtained due to the various aforementioned limitations with the current stand-alone BBLIF in highly agitated and aerated films. To obtain other wave characteristics (e.g. film thickness), further investigation of the BBLIF set-up (e.g. BBLIF camera observation angle and dye concentration) is necessary. Even though ≈ 10 experimental runs were performed for each investigated flow condition, the number of identified waves was deemed insufficient to acquire statistical u_{DW} data. Therefore, it would be useful for an extended number of experimental runs to be used over a wider range of

flow conditions.

While the MFoR approach with a dynamic ROI has demonstrated a significant advantage over conventional static ROI measurements, MFOR has the potential to open new manners in which the downstream evolution of individual interfacial phenomena with large development lengths in different multiphase flows (e.g. disturbance waves in annular flow, liquid slugs in plug or slug flow) are investigated. Nevertheless, further development of the techniques is required. Future work should be aimed at the extraction of other wave characteristics of individual disturbance waves; as well as, a systematic study of disturbance waves coalescence and the generation of fast and slow-moving ripples by individual disturbance waves. Combinations of this technique with planar measurements, e.g. S-PLIF, but also PIV or PTV would also be crucial in minimising errors in the measurement of wave dynamics but also obtaining velocity-field information.

References

Adomeit, P. & Renz, U. (2000) Hydrodynamics of three-dimensional waves in laminar falling films. *International Journal of Multiphase Flow.* 26, 1183–1208. Available from: doi:10.1016/S0301-9322(99)00079-8

Alekseenko, S.V., Aktershev, S.P., Bobylev, A.V., Kharlamov, S.M. & Markovich, D.M. (2015a) Nonlinear forced waves in a vertical rivulet flow. *Journal of Fluid Mechanics.* 770, 350–373. Available from: doi:10.1017/jfm.2015.170

Alekseenko, S.V., Antipin, V.A., Cherdantsev, A.V., Kharlamov, S.M. & Markovich, D.M. (2009) Two-wave structure of liquid film and waves interrelation in annular gas-liquid flow with and without entrainment. *Physics of Fluids.* 21 (6), 061701. Available from: doi:10.1063/1.3151999

Alekseenko, S.V., Antipin, V.A., Guzanov, V.V., Kharlamov, S.M., Markovich, D.M. (2005) Three-dimensional solitary waves on falling liquid film at low Reynolds numbers. Phys. Fluids 17 (12), 121704. Available from: doi:10.1063/1.2158428

Alekseenko, S., Cherdantsev, A., Cherdantsev, M., Isaenkov, S., Kharlamov, S. & Markovich, D. (2012) Application of a high-speed laser-induced fluorescence technique for studying three-dimensional structure of annular gas-liquid flows. *Experiments in Fluids.* 53 (1), 77–89. Available from: doi:10.1007/s00348-011-1200-5.

Alekseenko, S.V., Cherdantsev, A.V., Heinz, O.M., Kharlamov, S.M. & Markovich, D.M. (2013) Analysis of spatial and temporal spectra of liquid film surface in annular gas–liquid flow. *Experiments in Fluids.* 54 (9), 1590. Available from: doi:10.1007/s00348-013-1590-7

Alekseenko, S.V., Cherdantsev, A.V., Heinz, O.M., Kharlamov, S.M. & Markovich, D.M. (2014) Analysis of spatial and temporal evolution of disturbance waves and ripples in annular gas-liquid

flow. *International Journal of Multiphase Flow.* 67, 122–134. Available from: doi:10.1016/j.ijmultiphaseflow.2014.07.009

Alekseenko, S.V., Cherdantsev, A.V., Cherdantsev, M.V., Isaenkov, S.V., Markovich, D.M. (2015b) Study of formation and development of disturbance waves in annular gas–liquid flow. *International Journal of Multiphase Flow.* 77, 65–75. Available from: doi:10.1016/j.ijmultiphaseflow.2015.08.007

Ambrosini, W., Forgione, N. & Oriolo, F. (2002) Statistical characteristics of water film falling down a flat plate at different inclinations and temperatures. *International Journal of Multiphase Flow*. 28, 1521–1540. Available from: doi:10.1016/S0301-9322(02)00039-3

An, J.S., Cherdantsev, A.V., Zadrazil, I. & Markides, C.N. (2020) Study of disturbance wave development in downwards annular flows with a moving frame-of-reference brightness-based laser induced fluorescence method. *Experiments in Fluids*. *Submitted for publication*.

Arnold, C.R. & Hewitt, G.F. (1967) *Further developments in the photography of two-phase gas-liquid flow*. UKAEA. Report number: AERE-R5318.

Asali, J.C., Hanratty, T.J. & Andreussi, P. (1985) Interfacial drag and film height for vertical annular flow. *AIChE Journal*. 31 (6), 895-902. Available from: doi:10.1002/aic.690310604

Azzopardi, B.J. (1983) *Mechanisms of entrainment in annular two-phase flow*. UKAEA. Report number: AERE-R 11068.

Azzopardi, B.J. (1985) Drop sizes in annular two-phase flow. *Experiments in Fluids*. 3 (1), 53-59. Available from: doi:10.1007/BF00285271

Azzopardi, B.J. (1986) Disturbance waves frequencies, velocities and spacing in vertical annular two-phase flow. *Nuclear Engineering and Design.* 92 (2), 121–133. Available from: doi:10.1016/0029-5493(86)90240-2

Azzopardi, B.J. (1997) Drops in annular two-phase flow. *International Journal of Multiphase Flow*. 23 (7), 1-53.

Azzopardi, B.J. (2006) *Gas-Liquid Flows*. Connecticut, Begell House.

Azzopardi, B.J., Taylor, S. & Gibbons, D.B. (1983) Annular two-phase flow in large diameter pipes. *Proceedings of the International Conference on Physical Modelling of Multi-Phase Flow, 19-21 April 1983, Coventry, England, 256-267*.

Barbosa, J.R. Jr., Hewitt, G.F. & Richardson, S.M. (2003) High-speed visualisation of nucleate boiling in vertical annular flow. *International Journal of Heat and Mass Transfer.* 46 (26), 5153–5160. Available from: doi:10.1016/S0017-9310(03)00255-2

Belt, R.J., Van't Westende, J.M.C., Prasser, H.M. & Portela, L.M. (2010) Time and spatially resolved measurements of interfacial waves in vertical annular flow. *International Journal of Multiphase Flow*. 36 (7), 570–587. Available from: doi:10.1016/j.ijmultiphaseflow.2010.03.004

Berrocal, E., Kristensson, E., Richter, M., Linne, M. & Aldén, M. (2008) Application of structured illumination for multiple scattering suppression in planar laser imaging of dense sprays. *Optics Express*. 16 (22), 17870–17881. Available from: doi: 10.1364/OE.16.017870

Bhagwat, S.M. & Ghajar, A.J. (2012) Similarities and differences in the flow patterns and void fraction in vertical upward and downward two-phase flow. *Experimental Thermal and Fluid Science.* 39, 213-227. Available from: doi:10.1016/j.expthermflusci.2012.01.026.

Bonn, D., Rodts, S., Groenink, M., Rafai, S., Shahidzadeh-Bonn, N. & Coussot, P. (2008) Some applications of magnetic resonance imaging in fluid mechanics: Complex flows and complex Fluids. *Annual Review of Fluid Mechanics.* 4040, 209–233. Available from: doi: 10.1146/annurev.fluid.40.111406.102211

Bouyahiaoui, H., Azzi, A., Zeghloul, A., Hasan, A.H., Al-Sarkhi, A. & Parsi, M. (2020) Vertical

upward and downward churn flow: Similarities and differences. *Journal of Natural Gas Science and Engineering.* 73, 103080. Available from: doi:10.1016/j.jngse.2019.103080

Brauner, N., Maron, D.M. & Toovey, I. (1987) Characterization of the interfacial velocity in wavy thin films flow. *International Communications in Heat and Mass Transfer*. 14 (3), 293-302. Available from: doi:10.1016/0735-1933(87)90030-3

Castrejón-García, R., Castrejon-Pita, R., Martin, G.D. & Hutchings, I.M. (2011) The shadowgraph imaging technique and its modern application to fluid jets and drops. *Revista Mexicana de Física*. 57 (3), 266-275. Available from: https://www.researchgate.net/publication/262465475_The_shadowgraph_imaging_technique_and_its_modern_application_to_fluid_jets_and_drops [Accessed 7th January 2020].

Cengel, Y. and Cimbala, J. (2006) *Fluid Mechanics: Fundamentals and Applications*. London, McGraw-Hill.

Charogiannis, A., An, J.S. & Markides, C.N. (2015) A simultaneous planar laser-induced fluorescence, particle image velocimetry and particle tracking velocimetry technique for the investigation of thin liquid-film flows. *Experimental Thermal and Fluid Science.* 68, 516–536. Available from: doi:10.1016/j.expthermflusci.2015.06.008

Charogiannis, A., An, J.S., Voulgaropoulos, V. & Markides, C.N. (2019) Structured planar laser-induced fluorescence (S-PLIF) for the accurate identification of interfaces in multiphase flows. *International Journal of Multiphase Flow*, 118, 193-204. Available from: doi:10.1016/j.ijmultiphaseflow.2019.06.002

Charogiannis, A., Denner, F., van Wachem, B.G.M., Kalliadasis, S. & Markides, C.N. (2017) Detailed hydrodynamic characterization of harmonically excited falling-film flows: A combined experimental and computational study. *Physics Review Fluids.* 2 (1), 014002. Available from: doi:10.1103/PhysRevFluids.2.014002

Charogiannis, A., Denner, F., van Wachem, B. G.M., Kalliadasis, S. & Markides, C.N. (2018a) A combined experimental and computational study of the heat transfer characteristics of falling liquid-films. *3rd Thermal and Fluids Engineering Conference (TFEC), 4-7 May 2018, Fort Lauderdale, USA*

Charogiannis, A., Denner, F., Wachem, B.G.M., Kalliadasis, S., Scheid, B., Markides, C.N. (2018b) Experimental investigations of liquid falling films flowing under an inclined planar substrate. *Physics Review Fluids.* 3, 114002. Available from: doi:10.1103/PhysRevFluids.3.114002

Charogiannis, A. & Markides, C.N. (2014) Experimental Study of Falling Films by Simultaneous Laser-Induced Fluorescence, Particle Image Velocimetry and Particle Tracking Velocimetry. *17th International Symposium on Applications of Laser Techniques to Fluid Mechanics, 07-10 July, Lisbon, Portugal*.

Charogiannis, A. & Markides, C.N. (2016). Application of planar laser-induced fluorescence for the investigation of interfacial waves and rivulet structures in liquid film flowing down inverted substrates. *Interfacial Phenomena and Heat Transfer*. 4 (4), 235-252. Available from: doi:10.1615/InterfacPhenomHeatTransfer.2017019587

Charogiannis, A. & Markides, C.N. (2017). Application of laser-induced fluorescence, particle velocimetry and infrared thermography to heated falling-film flows. *ASME 2017 Heat Transfer Summer Conference, 9-12 July 2017, Washington, USA*.

Charogiannis, A. & Markides, C.N. (2019) Spatiotemporally resolved heat transfer measurements in falling liquid-films by simultaneous application of planar laser-induced fluorescence (PLIF), particle tracking velocimetry (PTV) and infrared (IR) thermography. Experimental Thermal and Fluid Science. 107, 169-191. Available from: doi:10.1016/j.expthermflusci.2018.11.001

Chen, Z.Q., Hermanson, J.C., Shear, M.A. & Pedersen, P.C. (2005) Ultrasonic monitoring of

interfacial motion of condensing and non-condensing liquid films. *Flow Measurement and Instrumentation.* 16 (6), 353–364. Available from: doi:10.1016/j.flowmeasinst.2005.06.002

Cherdantsev, A.V., An, J.S., Charogiannis, A. & Markides, C.N. (2018) Cross-validation of PLIF and BBLIF towards the detailed study of gas-sheared liquid films in downward annular flows. *19th International Symposium on Applications of Laser and Imaging Techniques to Fluid Mechanics, 16-19 July 2018, Lisbon, Portugal*.

Cherdantsev, A.V., An, J.S., Charogiannis, A. & Markides C.N. (2019) Simultaneous application of two laser-induced fluorescence approaches for film thickness measurements in annular gas-liquid flows. *International Journal of Multiphase Flow*. 119, 237-258. Available from: doi:10.1016/j.ijmultiphaseflow.2019.07.013

Cherdantsev, A.V., Hann, D.B. & Azzopardi, B.J. (2014) Study of gas-sheared liquid film in horizontal rectangular duct using high-speed LIF technique: Three-dimensional wavy structure and its relation to liquid entrainment. *International Journal of Multiphase Flow.* 67, 52–64. Available from: doi:10.1016/j.ijmultiphaseflow.2014.08.003

Cherdantsev, A.V., Hann, D.B., Hewakandamby, B.N. & Azzopardi, B.J. (2017) Study of the impacts of droplets deposited from the gas core onto a gas-sheared liquid film. *International Journal of Multiphase Flow.* 88, 69–86. Available from: doi:10.1016/j.ijmultiphaseflow.2016.09.015

Clark, W.W., Campbell, G.B., Hills, J.H. & Azzopardi, B.J. (2001) Viscous effects on the interfacial structure of falling liquid film/co-current gas systems. *Proceedings of the 4th International Conference on Multiphase Flow, 27 May – 1 June 2001, New Orleans, USA*.

Chu, K.J. & Dukler, A.E. (1974) Statistical characteristics of thin, wavy films: Part II. Studies of the substrate and its wave structure. *AIChE Journal.* 20 (4), 695–706. Available from: doi:10.1002/aic.690200410

Chu, K.J. & Dukler, A.E. (1974) Statistical characteristics of thin, wavy films: Part III. Structure of the large waves and their resistance to gas flow. *AIChE Journal.* 21 (3), 583-593. Available from: doi:10.1002/aic.690210323

Damsohn, M. & Prasser, H.M. (2009) High-speed liquid film sensor for two-phase flows with high spatial resolution based on electrical conductance. *Flow Measurement and Instrumentation.* 20 (1), 1–14. Available from: doi:10.1016/j.flowmeasinst.2008.06.006

Duarte, F.J. (2003) *Tunable Laser Optics*. New York, Elsevier. Available from: doi:10.1016/B978-0-12-222696-0.X5047-9 [Accessed 12th January 2018].

Dupont, J., Mignot, G., Zboray, R. & Prasser, H.M. (2016) Infrared film thickness measurement: Comparison with cold neutron imaging. *Journal of Nuclear Science and Technology.* 53 (5), 673-681. Available from: doi:10.1080/00223131.2015.1102779

Elson, D.S., Siegel, J., Webb, S.E.D., Lévěquefort, S., Parsons-Karavassilis, D., Cole, M.J., French, P.M.W., Davis, D.M., Lever, M.J., Juškaitis, R., Neil, M.A.A., Sucharov, L.O. & Wilson, T. (2002) Wide-field fluorescence lifetime imaging with optical sectioning and spectral resolution applied to biological samples. *Journal of Modern Optics.* 49 (5–6), 985–995. Available from: doi:10.1080/09500340110109377

Enrique Julia, J., Liu, Y., Hibiki, T. & Ishii, M. (2013) Local flow regime analysis in vertical co-current downward two-phase flow. *Experimental Thermal and Fluid Science.* 44, 345–355. Available from: doi:10.1016/j.expthermflusci.2012.07.006

Farias, P.S.C., Martins, F.J.W.A., Sampaio, L.E.B., Serfaty, R. & Azevedo, L.F.A. (2012) Liquid film characterization in horizontal, annular, two-phase, gas–liquid flow using time-resolved laser-induced fluorescence. *Experiments in Fluids.* 52(3), 633–645. Available from: doi:10.1007/s00348-011-1084-4

Fischer, F. & Hampel, U. (2010) Ultra fast electron beam X-ray computed tomography for two-

phase flow measurement. *Nuclear Engineering and Design.* 240 (9), 2254–2259. Available from: doi:10.1016/j.nucengdes.2009.11.016

Gustafsson, M.G.L. (2000) Surpassing the lateral resolution limit by a factor of two using structured illumination microscopy. *Journal of Microscopy.* 198 (2), 82–87. Available from: doi:10.1046/j.1365-2818.2000.00710.x

Häber, T., Gebretsadik, M., Bockhorn, H. & Zarzalis, N. (2015) The effect of total reflection in PLIF imaging of annular thin films. *International Journal of Multiphase Flow.* 76, 64–72. Available from: doi:10.1016/j.ijmultiphaseflow.2015.06.009

Hall Taylor, N.S., Hewitt, G.F. & Lacey, P.M.C. (1963) The motion and frequency of large disturbance waves in annular two-phase flow of air-water mixtures. *Chemical Engineering Science.* 18 (8), 537–552. Available from: doi:10.1016/0009-2509(63)85014-9

Hall Taylor, N.S. & Nedderman, R.M. (1968) The coalescence of disturbance waves in annular two phase flow. *Chemical Engineering Science.* 23 (6), 551–564. Available from: doi:10.1016/0009-2509(68)89003-7

Han, H., Zhu, Z. & Gabriel, K. (2006) A study on the effect of gas flow rate on the wave characteristics in two-phase gas–liquid annular flow. *Nuclear Engineering and Design.* 236 (24), 2580–2588. Available from: doi:10.1016/j.nucengdes.2006.03.015

Hann, D.B., Cherdantsev, A.V. & Azzopardi, B.J. (2018) Study of bubbles entrapped into a gas-sheared liquid film. *International Journal of Multiphase Flow.* 108, 181-201. Available from: doi:10.1016/j.ijmultiphaseflow.2018.07.001

Hazuku, T., Takamasa, T. & Matsumoto, Y. (2008) Experimental study on axial development of liquid film in vertical upward annular two-phase flow. *International Journal of Multiphase Flow.* 34 (2), 111–127. Available from: doi:10.1016/j.ijmultiphaseflow.2007.10.008

Hewitt, G.F. & Hall Taylor, N.S. (1970) *Annular two-phase flow*. Oxford, Pergamon Press.

Hewitt, G.F. & Lovegrove, P.C. (1969) *Frequency and velocity measurements of disturbance waves in annular two-phase flow*. UKAEA. Report number: AERE-R4304.

Hewitt, G.F., Lovegrove, P.C. & Nicholls, B. (1964) *Film thickness measurement using a fluorescence technique I: Description of the method*. UKAEA. Report number: AERE-R4478.

Hewitt, G.F., Jayanti, S. & Hope, C.B. (1990) Structure of thin liquid films in gas-liquid horizontal flow. *International Journal of Multiphase Flow.* 16 (6), 951–957. Available from: doi:10.1016/0301-9322(90)90100-W

Hewitt, G.F. & Nicholls, B. (1969) *Film thickness measurement in annular two-phase flow using a fluorescence spectrometer technique*. UKAEA. Report number: AERE-R4506.

Hurlburt, E.T. & Newell, T.A. (1996) Optical Measurement of Liquid Film Thickness and Wave Velocity in Liquid Film Flows. *Experiments in Fluids.* 21 (5), 357–362. Available from: doi:10.1007/BF00189056

Ishii, M. & Grolmes, M.A. (1975) Inception criteria for droplet entrainment in two-phase concurrent flow. *AIChE. Journal.* 21 (2), 308–318. Available from: doi:10.1002/aic.690210212

James, P.W., Hewitt, G.F. & Whalley, P.B. (1980) *Droplet motion in two-phase flow*. UKAEA. Report number: AERE-R9711.

Jepson, D.M., Azzopardi, B.J. & Whalley, P.B. (1989) The effect of gas properties on drops in annular flow. *International Journal of Multiphase Flow.* 15 (3), 327–339. Available from: doi:10.1016/0301-9322(89)90004-9

Karapantsios, T.D. & Karabelas A.J. (1995) Longitudinal characteristics of wavy falling films. *International Journal of Multiphase Flow.* 21 (1), 119–127. Available from: doi:10.1016/0301-

9322(94)00048-O

Karapantsios, T.D., Paras, S.V. & Karabelas, A.J. (1989) Statistical characteristics of free falling films at high Reynolds numbers. *International Journal of Multiphase Flow.* 15 (1), 1–21. Available from: doi:10.1016/0301-9322(89)90082-7

Karimi, G. & Kawaji M. (1999) Flow characteristics and circulatory motion in wavy falling films with and without counter-current gas flow. *International Journal of Multiphase Flow*. 25 (6–7), 1305-1319. Available from: doi:10.1016/S0301-9322(99)00044-0

Karimi, G. & Kawaji M. (2000) Flooding in vertical counter-current annular flow. *Nuclear Engineering and Design*. 200 (1–2), 95-105. Available from: doi:10.1016/S0029-5493(99)00331-3.

Kharlamov, S.M., Guzanov, V.V., Bobylev, A.V., Alekseenko, S.V. & Markovich, D.M. (2015) The transition from two-dimensional to three-dimensional waves in falling liquid films: Wave patterns and transverse redistribution of local flow rates. *Physics of Fluids.* 27 (11), 114106. Available from: doi:10.1063/1.4935958

Kline, S.J., Reynolds, W.C., Schraub, F.A. & Runstadler, P.W. (1967) The structure of turbulent boundary layers. *Journal of Fluid Mechanics.* 30 (4), 741–773. Available from: doi:10.1017/S0022112067001740

Knutsen, A.N., Lawson, J.M., Dawson, J.R. & Worth, N.A. (2017) A laser sheet self-calibration method for scanning PIV. *Experiments in Fluids*. 58: 145. Available from: doi:10.1007/s00348-017-2428-5

Kokomoor, W. & Schubring, D. (2014) Improved visualization algorithms for vertical annular flow. *Journal of Visualization.* 17 (1), 77–86. Available from: doi:10.1007/s12650-013-0191-0

Kristensson, E., Berrocal, E., Richter, M., Pettersson, S.G. & Aldén, M. (2008) High-speed structured planar laser illumination for contrast improvement of two-phase flow images. *Optics Letters.* 33 (23), 2752–2754. Available from: doi:10.1364/OL.33.002752

Lecompte, S., An, J.S., Charogiannis, A., De Paepe, M. & Markides, C.N. (2017) Simultaneous capacitive probe and planar laser-induced fluorescence measurements in downwards gas-liquid annular flow. *9th World Conference on Experimental Heat Transfer, Fluid Mechanics and Thermodynamics, 12-15 June 2017, Iguazu Falls, Brazil*.

Lel, V.V., Al-Sibai, F., Leefken, A. & Renz, U. (2005) Local thickness and wave velocity measurement of wavy films with a chromatic confocal imaging method and a fluorescence intensity technique. *Experiments in Fluids.* 39 (5), 856–864. Available from: doi:10.1007/s00348-005-0020-x

Lin, R., Wang, K., Liu, L., Zhang, Y. & Dong, S. (2020) Application of the image analysis on the investigation of disturbance waves in vertical upward annular two-phase flow. *Experimental Thermal and Fluid Science*. 114, 110062. Available from: doi:10.1016/j.expthermflusci.2020.110062

Lindon, J.C. (ed.), Tranter, G.E. (ed.) & Koppenaal, D.W. (ed.) (2010) *Encyclopedia of Spectroscopy and Spectrometry*. 2nd Edition, Amsterdam, Elsevier.

Liu, J., Paul, J.D. & Gollub, J.P. (1993) Measurements of the primary instabilities of film flows. *Journal of Fluid Mechanics.* 250, 69–101. Available from: doi:10.1017/S0022112093001387

Markides, C.N. & Charogiannis, A. (2016). Application of planar laser-induced fluorescence for the investigation of interfacial waves and rivulet structures in liquid films flowing down inverted substrates. *Interfacial Phenomena and Heat Transfer*. 4 (4), 235-252. Available from: doi:10.1615/InterfacPhenomHeatTransfer.2017019587.

Markides, C.N. & Mastorakos., E. (2006) Measurements of scalar dissipation in a turbulent plume with planar laser-induced fluorescence of acetone. *Chemical Engineering Science.* 61 (9), 2835–2842. Available from: doi:10.1016/j.ces.2005.10.040

Markides, C.N., Mathie, R. & Charogiannis, A. (2016) An experimental study of spatiotemporally resolved heat transfer in thin liquid-film flows falling over an inclined heated foil. *International Journal of Heat and Mass Transfer.* 93, 872–888. Available from: doi:10.1016/j.ijheatmasstransfer.2015.10.062

Martin, C.J. (1983) Annular two-phase flow. DPhil thesis. University of Oxford.

Mathie, R., Charogiannis, A. & Markides, C.N. (2014) Combined PLIF-IR thermal measurements of wavy film flows undergoing forced harmonic excitation. *10th International Conference on Heat Transfer, Fluid Mechanics and Thermodynamics, 14-16 July 2014, Orlando, USA*.

Mathie, R. & Markides, C.N. (2013) Heat transfer augmentation in convecting film flows. *ASME 2013 Heat Transfer Summer Conference collocated with the ASME 2013 7th International Conference on Energy Sustainability and the ASME 2013 11th International Conference on Fuel Cell Science, Engineering and Technology, 14-19 July 2013, Minneapolis, USA*.

Mathie, R., Nakamura, H. & Markides, C.N. (2013) Heat transfer augmentation in unsteady conjugate thermal systems – Part II: Applications. *International Journal of Heat and Mass Transfer*. 56 (1–2), 819-833. Available from: doi:10.1016/j.ijheatmasstransfer.2012.09.017

Mishra, Y.N., Kristensson, E. & Berrocal. E. (2014) Reliable LIF/Mie droplet sizing in sprays using structured laser illumination planar imaging. *Optics Express.* 22 (4), 4480–4492. Available from: doi:10.1364/OE.22.004480

Mudawar, I.A. & El-Masri, M.A. (1986) Momentum and heat transfer across freely falling turbulent liquid films. *International Journal of Multiphase Flow.* 12 (5), 771–790. Available from: doi:10.1016/0301-9322(86)90051-0

Nakoryakov, V.E., Pokusaev, B.G. & Alekseenko, S.V. (1976) Stationary two dimensional rolling waves on a vertical film of liquid. *Journal of Engineering Physics.* 30(5), 517-521. Available from: doi:10.1007/BF00863656

Neil, M.A.A., Juškaitis, R. & Wilson., T. (1997) Method of obtaining optical sectioning by using structured light in a conventional microscope. *Optics Letters.* 22 (24), 1905–1907. Available from: doi:10.1364/OL.22.001905

Nusselt, W. (1916) *Die Oberflächenkondensation des Wasserdampfes*. Z. Vereines Deutscher Ingenieure. 60, 541–546.

Ohba, K. & Nagae, K. (1993) Characteristics and behavior of the interfacial wave on the liquid film in a vertically upward air-water two-phase annular flow. *Nuclear Engineering and Design.* 141 (1–2), 17–25. Available from: doi:10.1016/0029-5493(93)90088-Q

Pan, L.M., He, H., Ju, P., Hibiki, T. & Ishii, M. (2015) Experimental study and modeling of disturbance wave height of vertical annular flow. *International Journal of Heat and Mass Transfer.* 89, 165–175. Available from: doi:10.1016/j.ijheatmasstransfer.2015.05.073

Pashniak, D.W. (1969) An investigation of the interfacial disturbances in vertical two phase flow. PhD thesis. University of Washington.

Pham, S.H., Kawara, Z., Yokomine, T. & Kunugi, T. (2014) Detailed observations of wavy interface behaviors of annular two-phase flow on rod bundle geometry. *International Journal of Multiphase Flow.* 59, 135–144. Available from: doi:10.1016/j.ijmultiphaseflow.2013.11.004

Rodríguez, D.J. & Shedd, T.A. (2004) Entrainment of gas in the liquid film of horizontal, annular, two-phase flow. *International Journal of Multiphase Flow.* 30 (6), 565-583. Available from: doi:10.1016/j.ijmultiphaseflow.2004.04.011

Schubring, D., Ashwood, A.C., Shedd, T.A. & Hurlburt, E.T. (2010) Planar laser-induced

fluorescence (PLIF) measurements of liquid film thickness in annular flow. Part I: Methods and data. *International Journal of Multiphase Flow.* 36 (10), 815–824. Available from: doi:10.1016/j.ijmultiphaseflow.2010.05.007

Schubring, D. & Shedd, T.A. (2011) A model for pressure loss, film thickness & entrained fraction for gas–liquid annular flow. *International Journal of Heat and Fluid Flow.* 32 (3), 730–739. Available from: doi:10.1016/j.ijheatfluidflow.2011.02.010

Sekoguchi, K., Takeishi, M. & Ishimatsu, T. (1985) Interfacial structure in vertical upward annular flow. *Journal of the Flow Visualization Society of Japan.* 6, 239–255. Available from: doi:10.3154/jvs1981.5.Supplement_61

Settles, G.S. (2001) *Schlieren and Shadowgraph Techniques: Visualizing Phenomena in Transparent Media*. Heidelberg, Springer.

Setyawan, A., Indarto & Deendarlianto (2016) The effect of the fluid properties on the wave velocity and wave frequency of gas-liquid annular two-phase flow in a horizontal pipe. *Experimental Thermal and Fluid Science.* 71, 25–41. Available from: doi:10.1016/j.expthermflusci.2015.10.008

Sharaf, S., Da Silva, M., Hampel, U., Zippe, C., Beyer, M. & Azzopardi, B. (2011) Comparison between wire mesh sensor and gamma densitometry void measurements in two-phase flows. *Measurement Science and Technology.* 22 (10), 104019. Available from: doi:10.1088/0957-0233/22/10/104019

Spedding, P.L., Woods, G.S., Raghunathan, R.S. & Watterson, J.K. (1998) Vertical Two-Phase Flow: Part I: Flow Regimes. *Chemical Engineering Research and Design*. 76 (5), 612-619. Available from: doi:10.1205/026387698525298

Takamasa, T. & Hazuku, T. (2000) Measuring interfacial waves on film flowing down a vertical plate wall in the entry region using laser focus displacement meters. *International Journal of Heat*

and Mass Transfer. 43 (15), 2807-2819. Available from: doi:10.1016/S0017-9310(99)00335-X

Takamasa, T. & Kobayashi, K. (2000) Measuring interfacial waves on film flowing down tube inner wall using laser focus displacement meter. *International Journal of Multiphase Flow*. 26 (9), 1493-1507. Available from: doi:10.1016/S0301-9322(99)00099-3

Takenaka, N., Asano, H., Fujii, T. & Matsubayashi, M. (1998) Three-dimensional visualization of void fraction distribution in steady two-phase flow by thermal neutron radiography. *Nuclear Engineering and Design.* 184 (2–3), 203–212. Available from: doi:10.1016/S0029-5493(98)00197-6

Usui, K. & Sato, K. (1989) Vertically downward two-phase flow, (I) Void distribution and average void fraction. *Journal of Nuclear Science and Technology.* 26 (1989), 670–680. Available from: doi:10.1080/18811248.1989.9734366

van Eckeveld, A.C., Gotfredsen, E., Westerweel, J. & Poelma, C. (2018) Annular two-phase flow in vertical smooth and corrugated pipes. *International Journal of Multiphase Flow.* 109, 150–163. Available from: doi:10.1016/j.ijmultiphaseflow.2018.07.004

van Maanen, H.R.E & Fortuin, J.M.H (1983) Experimental determination of the random lump-age distribution in the boundary layer of the turbulent pipe flow using laser-Doppler anemometry. *Chemical Engineering Science*. 38 (3), 399-424. Available from: doi:10.1016/0009-2509(83)80158-4

Van der Meulen, G.P. (2012) Churn-annular gas-liquid flows in large diameter vertical pipes. PhD thesis. University of Nottingham.

Vasques, J., Cherdantsev, A., Cherdantsev, M., Isaenkov, S. & Hann, D. (2018) Comparison of disturbance wave parameters with flow orientation in vertical annular gas-liquid flows in a small pipe. *Experimental Thermal and Fluid Science*. 97, 484-501. Available from: doi:10.1016/j.expthermflusci.2018.03.020

Vlachogiannis, M. & Bontozoglou, V. (2001) Observations of solitary wave dynamics of film flows. *Journal of Fluid Mechanics.* 435, 191–215. Available from: doi:10.1017/S0022112001003688

Wang, Z. & Gabriel, K.S. (2005) The influence of film structure on the interfacial friction in annular two-phase flow under microgravity and normal gravity conditions. *Microgravity Science and Technology.* 16 , 264-268. Available from: doi:10.1007/BF02945988

Webb, D. & Hewitt, G.F. (1975) Downwards co-current annular flow. *International Journal of Multiphase Flow* 2 (1), 35–49. Available from: doi:10.1016/0301-9322(75)90027-0

Wegener, J.L. & Drallmeier, J.A. (2010) Measurement of thin liquid film characteristics using laser focus displacement instruments for atomization applications. *ILASS-Americas 22nd Annual Conference on Liquid Atomization and Spray Systems, 16-19 May 2010, Cincinnati, USA*.

Wilkes, N.S., Azzopardi, B.J. & Thompson, C.P. (1983) Wave coalescence and entrainment in vertical annular two-phase flow. *International Journal of Multiphase Flow* 9 (4), 383–398. Available from: doi:10.1016/0301-9322(83)90095-2

Wolf, A. (1995) Film Structure of Vertical Annular Flow. PhD thesis. University of London (Imperial College London).

Wolf, A., Jayanti, S. & Hewitt, G.F. (2001) Flow development in vertical annular flow. *Chemical Engineering Science*. 56 (10), 3221-3235. Available from: doi:10.1016/S0009-2509(00)00546-7

Woodmansee, D.E. & Hanratty, T.J. (1969) Mechanism for the removal of droplets from a liquid surface by a parallel air flow. *Chemical Engineering Science.* 24 (2), 299–307. Available from: doi:10.1016/0009-2509(69)80038-2

Yu, L.M., Zeng, A.W. & Yu K.T. (2006) Effect of interfacial velocity fluctuations on the

enhancement of the mass-transfer process in falling film flow. *Industrial & Engineering Chemistry Research*. 45 (3), 1201-1210. Available from: doi:10.1021/ie050855q

Zadrazil, I., Matar, O.K. & Markides, C.N. (2014) An experimental characterization of downwards gas–liquid annular flow by laser-induced fluorescence: Flow regimes and film statistics. *International Journal of Multiphase Flow.* 60, 87–102. Available from: doi:10.1016/j.ijmultiphaseflow.2013.11.008

Zadrazil, I. & Markides, C.N. (2014) An experimental characterization of liquid films in downwards co-current gas–liquid annular flow by particle image and tracking velocimetry. *International Journal of Multiphase Flow.* 67, 42–53. Available from: doi:10.1016/j.ijmultiphaseflow.2014.08.007

Zadrazil, I., An, J.S., Cherdantsev, A. & Markides, C.N. (2016) Development of LIF techniques applied to gas-liquid annular flows. *18th International Symposium on Applications of Laser and Imaging Techniques to Fluid Mechanics, 4-7 July 2016, Lisbon, Portugal*.

Zhao, Y., Markides, C.N., Matar, O.K. & Hewitt, G.F. (2013) Disturbance wave development in two-phase gas–liquid upwards vertical annular flow. *International Journal of Multiphase Flow.* 55, 111–129. Available from: doi:10.1016/j.ijmultiphaseflow.2013.04.001